Springer Proceedings in Earth and Environmental Sciences

Sergei Votyakov
Daria Kiseleva
Viktor Grokhovsky
Yuliya Shchapova *Editors*

Minerals: Structure, Properties, Methods of Investigation

Proceedings of the 10th All-Russian Youth Scientific Conference

Springer

Springer Proceedings in Earth and Environmental Sciences

The series Springer Proceedings in Earth and Environmental Sciences publishes proceedings from scholarly meetings and workshops on all topics related to Environmental and Earth Sciences and related sciences. This series constitutes a comprehensive up-to-date source of reference on a field or subfield of relevance in Earth and Environmental Sciences. In addition to an overall evaluation of the interest, scientific quality, and timeliness of each proposal at the hands of the publisher, individual contributions are all refereed to the high quality standards of leading journals in the field. Thus, this series provides the research community with well-edited, authoritative reports on developments in the most exciting areas of environmental sciences, earth sciences and related fields.

More information about this series at http://www.springer.com/series/16067

Sergei Votyakov • Daria Kiseleva •
Viktor Grokhovsky • Yuliya Shchapova
Editors

Minerals: Structure, Properties, Methods of Investigation

Proceedings of the 10th All-Russian Youth Scientific Conference

Springer

Editors
Sergei Votyakov
Institute of Geology and Geochemistry
Urals Branch of Russian Academy
of Sciences
Yekaterinburg, Russia

Daria Kiseleva
Institute of Geology and Geochemistry
Urals Branch of Russian Academy
of Sciences
Yekaterinburg, Russia

Viktor Grokhovsky
Ural Federal University
Yekaterinburg, Russia

Yuliya Shchapova
Institute of Geology and Geochemistry
Urals Branch of Russian Academy
of Sciences
Yekaterinburg, Russia

ISSN 2524-342X ISSN 2524-3438 (electronic)
Springer Proceedings in Earth and Environmental Sciences
ISBN 978-3-030-49467-4 ISBN 978-3-030-49468-1 (eBook)
https://doi.org/10.1007/978-3-030-49468-1

This Springer imprint is published by the registered company Springer Nature Switzerland AG
The registered company address is: Gewerbestrasse 11, 6330 Cham, Switzerland

Preface

This volume of Springer Proceedings in Earth and Environmental Sciences contains selected papers presented at the 10th Anniversary Geoscience Conference for Young Scientists "Minerals: Structure, Properties, Methods of Investigation," which took place during May 27–31, 2019, at the Institute of Geology and Geochemistry, Ural Branch of Russian Academy of Sciences, Ekaterinburg, Russia.

The conference was organized by the Institute of Geology and Geochemistry, UB RAS, in cooperation with the Ural Federal University named after B. N. Yeltsin and the Institute of Mineralogy, UB RAS, and held under the auspices of the commission for X-ray diffraction, crystal chemistry, and spectroscopy of the Russian Mineralogical Society.

The central idea behind the conference program is the application of contemporary physicochemical methods of analysis to the study of terrestrial and extraterrestrial minerals.

More than 100 participants, including young scientists, postgraduates, and students, as well as members of the Russian Academy of Sciences, professors, doctors, and candidates of sciences, represented academic and industrial institutes from Moscow, St. Petersburg, Kazan, Ekaterinburg, Miass, Novosibirsk, Irkutsk, Omsk, Tomsk, Perm, Syktyvkar, Apatity, Petropavlovsk-Kamchatsky, Ulan-Ude, Simferopol, and elsewhere.

Plenary sessions were held for four days over three sections "crystal chemistry of minerals," "typomorphism and methods for studying minerals," and "meteorites, asteroids, comets." More than 50 oral reports, including 12 plenary lectures of invited specialists, and more than 50 posters were presented. Participants discussed relevant issues of crystal chemistry and mineral typomorphism, structural studies, physical and chemical and technological properties of minerals, nanoscale formations and inclusions, techno- and biogenic objects, non-crystalline mineral matter, and the problems in applied mineralogy.

Dr. Anna Vymazalová (Czech Geological Survey, Prague, Czech Republic) had visited the conference within SGA Keynote Speaker Program sponsored by Society of Geology Applied to Mineral Deposits (SGA). Her research interests are focused on ore and experimental mineralogy, precious metals (PGE) and their formation, the genesis of mineral deposits and various aspects associated with exploitation and processing of deposits, as well as on detailed experimental investigation of ternary

systems involving PGE, intermetalides and chalcogenides, their phase relations, and mineralogical application. She has been also actively involved in a description of about twelve new platinum-group minerals. Dr. Anna Vymazalová gave a keynote lecture "Platinum-group minerals, new and traditional."

During the conference, excursions were organized to the "Geoanalyst" Center for Collective Use of the UB RAS and the museum of scientific mineral collections of the IGG UB RAS.

A visiting scientific session dedicated to the memory of Prof. Vadim N. Bykov, one of the founders of the Conference for Young Scientists "Minerals: Structure, Properties, Methods of Investigation," was held at the Institute of Mineralogy, Urals Branch of RAS, Miass, Chelyabinsk region. The session was devoted to the application of vibrational spectroscopy in the studies of silicate melts and natural minerals. Professor Vadim Bykov was a great authority in the field of experimental mineralogy, geochemistry, and physics of minerals. The major direction of his research was the study of structure and properties of disordered mineral-forming systems such as magmatic melts and glasses. He was Head of the Laboratory of Experimental Mineralogy and Physics of Minerals and Founder of South-Ural Center for Collective Use to study mineral substance, and since 2002 he had become Deputy Director of the Institute of Mineralogy, UB RAS. Vadim Bykov will always be remembered and appreciated by his friends, colleagues, and students as an outstanding person whose invincible will and vital power, as well as curiosity in both science and everyday life, would lead to the achievement of the set goals.

The participants of the field trip had a chance to visit the Natural Science Museum of the Ilmensky State Reserve, one of the few geological and mineralogical reserves in the world. The first collections of minerals and rock specimens were started in 1925 soon after the reserve's foundation. The museum currently holds 30000 items, with about 9000 of them on display. Besides mineralogical collections, the museum possesses one of Russia's largest biological dioramas (full circle composite model scenery around a large display hall).

Post-conference field trip included a visit to a large number of genesis-specific deposits and mineralization points. However, the beginning of the trip was marked by a visit to an archaeological site—ancient sanctuary, inhabited since Paleolithic, located near the Lake Allaki among the granite outcrops, where the fragments of parietal art were preserved.

The geological part of the field trip began with a visit to the "Pyataya (5th) Versta" corundum deposit in the area of Kasli town framed by the Vishnevogorsky alkaline massif. The striking representative of granitoid pegmatite veins in the Ilmenogorsky alkaline massif was Mine No. 242 on the territory of the Ilmensky State Reserve (Miass) with crystals of aquamarines and topazes. The participants were rewarded for complicated access to a site with graphic (Hebraic) granite samples from the graphic part of the vein and the small crystals of blue beryls. Sapphire crystals were found in the micaites of Mine No. 418.

The ancient complexes of the Bashkir Meganticlinorium can be seen from the Black Mountain ("Chernaya Skala") observation point of the world-famous Taganay National Park. Here, in the Precambrian strata along the "living" fault,

quartzites creep into amphibolites. Acquaintance with the early history of the Urals continued in the Urals largest Kusa–Kopan stratified intrusion revealing one of the riftogenic fragments of the territory development. Within the intrusion, there are many mineral mines concentrated in the skarn xenoliths of host carbonate rocks. Clinochlore, epidote, and garnet samples were collected from the Zelentsovskaya mine.

The tour ended with a visit to the alkaline pegmatites of the "Kurochkin Log" mine and the quarries with carbonatite veins of the Vishnevogorsky deposit where rare-metal mineralization could be found.

This proceedings volume contains the full texts of 8 invited plenary lectures and of 30 young scientist papers presented at the conference. All the papers have been subjected to peer review by at least two referees.

Ekaterinburg, Russia

Sergei Votyakov
Daria Kiseleva
Yuliya Shchapova
Viktor Grokhovsky

Acknowledgements

On behalf of the Organizing Committee of the 10th Geoscience Conference for Young Scientists “Minerals: Structure, Properties, Methods of Investigation,” we would like to thank all the invited speakers, session chairs, and participants for making the conference successful. We also would like to express our gratitude to Irina Vlokh for the linguistic assistance.

The conference was supported by the Society for Geology Applied to Mineral Deposits (SGA) and sponsored by Ural’skoe Byuro PerkinElmer (PerkinElmer Ural Bureau), Ekaterinburg, and Nytek Instruments, Moscow.

About this Book

All papers published in this volume of Springer Proceedings in Earth and Environmental Sciences "Minerals: Structure, Properties, Methods of Investigation—10th Geoscience Conference for Young Scientists, Ekaterinburg, Russia, May 27–31, 2019" have been peer-reviewed over the course of processes administered by the proceedings editors. Reviews by expert referees conformed to the professional and scientific standards expected of a proceedings journal published by Springer.

Contents

Zoned Olivines in Metallurgical Slags of the Bronze Age: Electron Microscopy and Raman Mapping

Maksim N. Ankushev, Elizaveta A. Pankrushina, and Ivan A. Blinov

Abstract

In this work, we studied the zoned olivine crystals from historical metallurgical slags by means of hyperspectral Raman mapping and Raman spectroscopy. As a result, we detected 3 crystal zones: central, intermediate and peripheral. The most important was the "gap" area within the intermediate zone with a Raman band typical for olivine. This defective area was formed due to quick melt crystallization and crystal absorption of glass microparticles and non-structural impurities.

Keywords

Slags · Olivine · Raman mapping · Bronze Age · Ancient metallurgy

1 Introduction

The study of mineralogical and geochemical features of historical metallurgical slags allows the problem of the primary ore protolith genesis and metallurgical process in the Bronze Age to be solved. The mineralogical focus of the work is on the examination of the structures, morphology and geochemical features of newly-formed slag minerals from the viewpoint of igneous and pyrogenic rock

M. N. Ankushev (✉) · I. A. Blinov
Institute of Mineralogy SU FRC MG UB RAS, Ilmensky Reserve, 456317 Miass, Russia
e-mail: ankushev_maksim@mail.ru

E. A. Pankrushina
Zavaritsky Institute of Geology and Geochemistry UB RAS, 15 Akademika Vonsovskogo Str., 620016 Ekaterinburg, Russia

S. Votyakov et al. (eds.), *Minerals: Structure, Properties, Methods of Investigation*,
Springer Proceedings in Earth and Environmental Sciences,
https://doi.org/10.1007/978-3-030-49468-1_1

analogues. The main mineral of the Bronze Age slags in the Southern Urals is olivine, which morphology and geochemical features have been studied earlier (Ankushev et al. 2018a). However, the structural features and crystallization process from the melt are not yet entirely figured out.

As previously stated by (Ankushev et al. 2018b), the isomorphic Fe-Mg miscibility in olivines affects the position and full weight at half maximum (FWHM) of the most intensive Raman spectra of olivine bands (about 815 and 840 cm^{-1}), and fayalite zone without olivine Raman spectra is detected in the historical metallurgical slags.

This work is aimed at studying the olivine crystal zonality from the historical metallurgical slags using Raman spectroscopy. The main tasks are to detect the chemical composition of different olivine crystal zones using SEM data and to perform the Raman mapping of zoned olivine crystal.

2 Materials and Methods

The olivine composition was determined by means of a Tescan Vega 3 SBU scanning electron microscope equipped with Oxford Instruments X-act EDS spectrometer (IM SU FRC MG UB RAS, analyst I.A. Blinov). The olivine formulae were calculated by anionic method based on the 4 O atoms per formula.

Hyperspectral Raman maps and Raman spectra were obtained using high resolution Horiba Jobin Yvon LabRam HR800 Evolution Raman spectrometer equipped with Olympus BX-FM optical microscope (IGG UB RAS, analyst E.A. Pankrushina), a grating with 1800 grooves per millimeter, Ar and He-Ne-laser (laser radiation wavelength of 514 and 633 nm, respectively); the system was operated in confocal mode, and 100× objective (numerical aperture 0.9) was used.

Hyperspectral Raman maps were obtained using an automated x, y motorized stage that mechanically moves the sample; a Raman spectrum was obtained at each position.

3 Results and Discussion

For the research we used a Cr-spinel-containing metallurgical slag fragment from the well-studied Kamenny Ambar Bronze Age settlement (Multidisciplinary… 2013). The sample was related to the cultural layer of Sintashta.

Olivine forms large euhedral, and often zoned crystals in the fragments of Cr-containing slags. These metallurgical slags from the Kamenny Ambar settlement are presented by fragments with porphyry structure; the bulk of slag is composed of newly-formed crystals of olivine, magnetite and glass; sometimes metallic Cu inclusions occur. The relic minerals are serpentine and Cr-spinel. The olivine/glass ratio is approximately 4:1.

The olivine forms prismatic euhedral grains, often with zoning and skeletal crystals. In reflected light on the grain peripherals, we observed a light rim with an elevated Fe content as compared to the central grain parts. The olivine is represented by fayalite (Table 1), but forsterite minal amount can be increased in the central crystal parts (Ankushev et al. 2018a).

The following vibration modes are predicted by group-theoretical analysis: $\Gamma = 11A_g + 11B_{1g} + 7B_{2g} + 7B_{3g} + 10A_u + 9B_{1u} + 13B_{2u} + 13B_{3u}$, where u subscript corresponds to infrared active vibrations, and g – to Raman active vibrations (Kolesov et al. 1996). For fayalite and forsterite, the positions of vibrational Raman modes are different (see Kolesov et al. 1996). Lattice modes are typical for the range up to 350 cm^{-1}. The modes of 416 cm^{-1} in forsterite and 370 cm^{-1} in fayalite are characteristic of $\nu_4(SiO_4)$ antisymmetric bending vibrations. The range of 500–650 cm^{-1} is due to $\nu_4(SiO_4)$ symmetric bending vibrations; and the modes at 824 cm^{-1} in forsterite and at 815 cm^{-1} in fayalite correspond to $\nu_1(SiO_4)$ symmetric stretching vibration. The range of 830–1000 cm^{-1} is related to $\nu_1(SiO_4)$ antisymmetric stretching vibrations (Kolesov et al. 1996).

Hyperspectral Raman Maps of Spectral Parameter Distribution

$\nu_1(SiO_4)$ Raman bands at ~815 and 840 cm^{-1} have been chosen for mapping, because their spectral parameters (amplitude, weight, peak position) vary for grains.

$\nu_1(SiO_4)$ Symmetric Stretching Vibration at ~815 cm^{-1}

For **3260r/718** sample, the central and partially peripheral zones are characterized by the position of this band at ~815 cm^{-1} (Fig. 1). The intermediate zone is characterized by an absence of this mode. Its FWHM in the central and peripheral zones is stable and reaches 10–15 cm^{-1}. As we approach the intermediate zone, the peak becomes wider up to 25 cm^{-1}. At the center of the intermediate zone, the peak is not recorded and its width is equal to zero. The highest intensity (2800–2400 arbitrary units) of this vibrational mode is in the central area having the highest forsterite amount. As we approach the crystal borders, the intensity gradually decreases to zero in the "gap" area of the intermediate zone. At the crystal peripheral, the intensity is 500–1000 arbitrary units.

Zoning is also observed for **4027/718** sample, where we have detected at least three zones: central, intermediate and "gap" zone. The central zone is the most crystalline area with narrow (up to 23 cm^{-1}) and intensive bands. The peak position is ~817 cm^{-1}. An intensity decrease is observed (up to 400 arbitrary units) in the intermediate zone; FWHM varies between 15 and 25 cm^{-1} from the central to intermediate zones, respectively. The 3rd zone is the "gap" area, which is characterized by an absence of this mode (which can be seen on the intensity map).

$\nu_1(SiO_4)$ Symmetric Stretching Vibration at ~840 cm^{-1}

For **3260r/718** sample, the central zone is characterized by a minor irregularity of the vibrational mode position ranging between 840 and 845 cm^{-1}. In the intermediate zone, we have observed an absence of this mode. At the peripheral zone, where the mode appears again, its position is at ~840 cm^{-1}. The peak width both in the central and peripheral zones is constant (35 cm^{-1}). As we approach the

Table 1 The composition of zoned olivine from the Kamenny Ambar settlement metallurgical slags of the Bronze Age (3214/718 sample)

№	Analysis area	SiO_2	FeO	MgO	CaO	Calculated mineral formulae	Minerals, %
1	Core	30.34	63.5	6.16	n/d	$(Fe_{1.73}Mg_{0.3})_{2.03}Si_{0.98}O_4$	$Fa_{85.26}Fo_{14.74}$
2	Core	30.38	61.32	8.30	n/d	$(Fe_{1.65}Mg_{0.4})_{2.05}Si_{0.98}O_4$	$Fa_{80.57}Fo_{19.43}$
3	Core	31.36	62.61	5.08	0.29	$(Fe_{1.7}Mg_{0.25}Ca_{0.01})_{1.96}Si_{1.02}O_4$	$Fa_{86.92}Fo_{12.57}La_{0.52}$
4	Intermediate zone	31.00	64.76	3.96	0.28	$(Fe_{1.77}Mg_{0.19}Ca_{0.01})_{1.97}Si_{1.01}O_4$	$Fa_{89.73}Fo_{9.78}La_{0.50}$
5	Intermediate zone	31.31	64.51	3.90	0.29	$(Fe_{1.76}Mg_{0.19}Ca_{0.01})_{1.96}Si_{1.02}O_4$	$Fa_{89.81}Fo_{9.68}La_{0.52}$
6	Rim	30.69	67.69	1.30	0.33	$(Fe_{1.88}Mg_{0.06}Ca_{0.01})_{1.96}Si_{1.02}O_4$	$Fa_{96.11}Fo_{3.29}La_{0.60}$
7	Rim	30.60	67.01	1.42	0.41	$(Fe_{1.87}Mg_{0.07}Ca_{0.01})_{1.96}Si_{1.02}O_4$	$Fa_{95.64}Fo_{3.61}La_{0.75}$

Note Analyses were carried out using VEGA3 TESCAN SEM scanning electron microscope (analyst I.A. Blinov) at the Institute of Mineralogy of SU FRC MG UB RAS. n/d – element is not detected. The basis of O atoms per formulae is 4

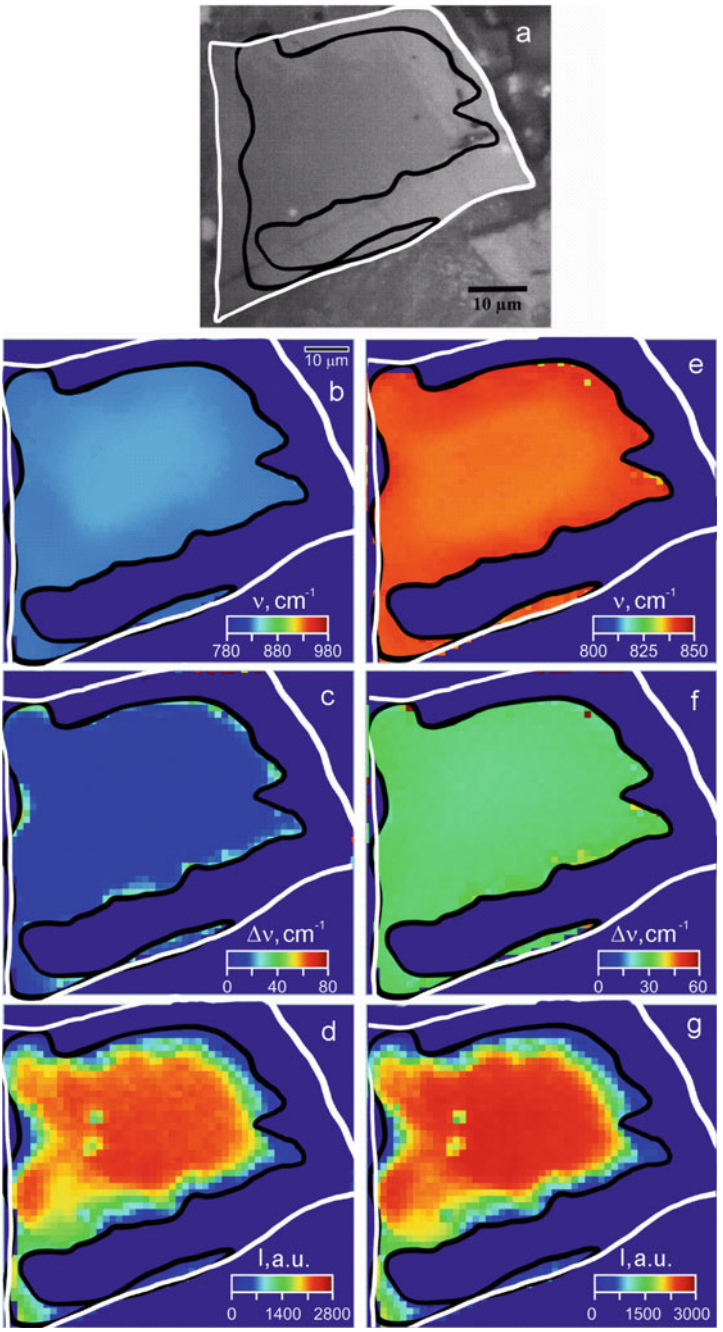

Fig. 1 A zoned olivine grain, **3260r/718** sample: optical image (**a**), 2D hyperspectral Raman maps of spectral parameter distribution of olivine grain for bands ~815 (**b**, **c**, **d**) and 840 (**d**, **e**, **f**) cm^{-1} (b, d – peak position; c, e – FWHM; d, f – intensity)

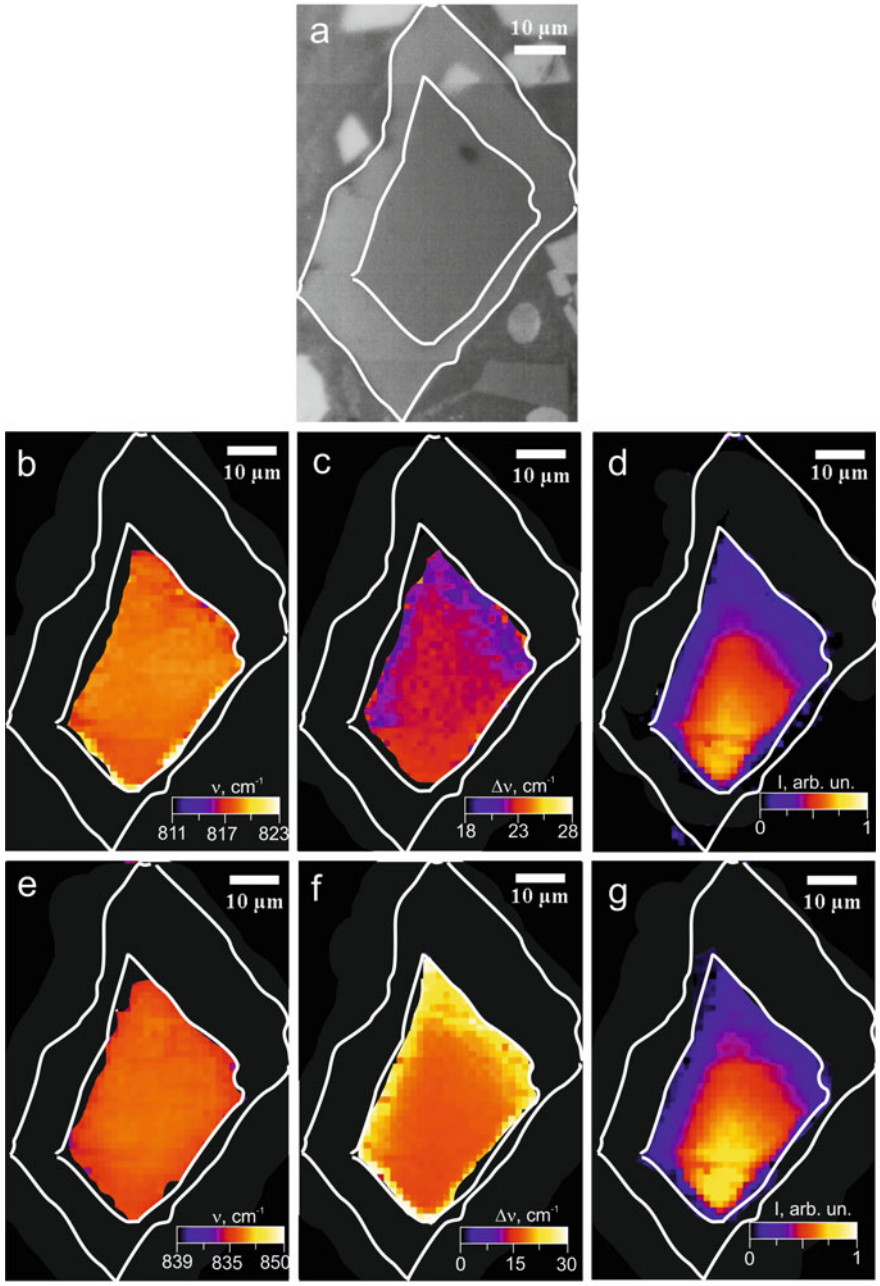

Fig. 2 A zoned olivine grain, **4027/718** sample: optical image (**a**), 2D hyperspectral Raman maps of spectral parameter distribution of olivine grain for bands ~815 (**b**, **c**, **d**) and 840 (**d**, **e**, **f**) cm^{-1} (b, d – peak position; c, e – FWHM; d, f – intensity)

intermediate zone, the peak becomes wider up to 40 cm^{-1}; then we observe the "gap" with an absence of the mode. The intensity is characterized by a maximum value (3000–2800 arbitrary units) in the crystal center and it gradually decreases to 400–600 arbitrary units at a distance from the center. In the middle of the intermediate zone, the intensity becomes equal to zero. In the peripheral zone, the intensity is 600–1000 arbitrary units.

To confirm the observed effect, we have mapped the zoned crystal from another sample. For **4027/718** sample, the peak position in the central and intermediate zones is almost equal and reaches 846 cm^{-1} (Fig. 2). The amplitude from central to intermediate parts varies from 700 to 200 arbitrary units, while FWHM varies slightly (from 20 to 23 cm^{-1}). In the peripheral zone, we have observed the absence of this vibrational mode.

4 Conclusions

As a result of zoned olivine mapping, we have detected 3 crystal zones in Raman spectrum: central, intermediate and peripheral. The central zone had been forming for a long time and is characterized by an elevated forsterite amount; consequently, the typical bands of olivine Raman spectra are most pronounced and high-intensity. The most important is the "gap" area in the intermediate zone, where the typical olivine peaks are observed. Probably, this zone is formed due to the melt cooling and its crystallization into glass-like substrate, which is a part of the crystal. Thin peripheral zone is characterized by the typical Raman bands for olivine, but they are of low intensity and may be caused by small olivine crystallites formed on the crystal borders. Further research of olivine crystal structural features will be carried out by the EBSD (electron backscatter diffraction) method.

Acknowledgements The study of the mineralogical features of historical metallurgical slags was supported by the Russian Science Foundation (Grant No. 16-18-10332). Raman spectroscopy was performed as a part of the topic No. AAAA-A18-118053090045-8 of the IGG UB RAS state assignment.

References

Ankushev MN, Artemyev DA, Blinov IA. Elementy-primesi v zonal'nyh olivinah metallurgicheskih shlakov bronzovogo veka na Yuzhnom Urale. Mineralogiya. 2018a;4(1):55-67. [Ankushev MN, Artemyev DA, Blinov IA. Trace elements in zoned olivines from the Bronze Age metallurgical slags at the Southern Urals. Mineralogy. 2018a;4(1):55–67 (In Russ.)].

Ankushev MN., Pankrushina EA., Mikheeva AV. Ramanovskaya spektroskopiya zonal'nyh olivinov v drevnih metallurgicheskih shlakah Yuzhnogo Urala. Ural'skaya mineralogicheskaya shkola. 2018;24:13-18. [Ankushev MN., Pankrushina EA., Mikheeva AV. Raman spectroscopy of zoned olivines from historical metallurgical slags. Ural Mineralogical School. 2018b;24:13–18 (In Russ.)].

Kolesov BA, Tanskaya JV. Raman spectra and cation distribution in the lattice of olivines. Mater. Res.Bull. 1996;31(8):1035–1044. https://doi.org/10.1016/S0025-5408(96)00085-2

Multidisciplinary investigations of the Bronze Age settlements in the Southern Trans-Urals (Russia). Krause R & Koryakova LN (eds.). Bonn: Habelt; 2013.

PT-Parameters of the Egitinsky Fluorite Deposit (Trans-Baikalia, Russia)

Natalia N. Ankusheva, Roza A. Badmatsyrenova, and Sayana B. Tsydypova

Abstract

The structures and conditions of fluorite ore formation of the Egitinsky deposit in Trans-Baikalia were examined through the geological and mineralogical evidences and fluid inclusion study. The fluorite ores were formed due to the filling of fractures and cavities and, to a lesser degree, by replacing the Ca-bearing host rocks. The productive assemblage consisted of 3 ore types and included the same minerals in different proportions. The main ores of the Egitinsky deposit were formed at temperatures ranging from 400 to 300 °C due to Na-K-Mg-chloride fluids with the involvement of metamorphic and magmatic fluids.

Keywords

Fluorite deposits · Fluid inclusions · Formation stages

N. N. Ankusheva (✉)
Institute of Mineralogy SU FRC MG UB RAS, 1 Ilmensky Reserve, 456317 Miass, Russia
e-mail: ankusheva@mail.ru

N. N. Ankusheva
South Ural State University, 10 8 Iyulya str., 456304 Miass, Russia

R. A. Badmatsyrenova
Geological Institute SB RAS, 6 Sakhayanovoy str., 670047 Ulan-Ude, Russia
e-mail: brose@ginst.ru

R. A. Badmatsyrenova
Buryat State University, 24a Smolina str., 670000 Ulan-Ude, Russia

S. B. Tsydypova
Institute of Geochemistry SB RAS, 1a Favorskogo str., 650033 Irkutsk, Russia
e-mail: brose@ginst.ru

S. Votyakov et al. (eds.), *Minerals: Structure, Properties, Methods of Investigation*,
Springer Proceedings in Earth and Environmental Sciences,
https://doi.org/10.1007/978-3-030-49468-1_2

1 Introduction

The epithermal fluorite deposits are widespread in Trans-Baikalia, Eastern Mongolia and NW China. One of the richest is the Egitinsky deposit related to the quartz-carbonate-fluorite type with CaF_2 content ranging from 5 to 95% (average 52.09%), $CaCO_3$ from 1.77 to 43% (average 6.9), and SiO_2 from 7.96 to 53.54% (average 26.42).

The Egitinsky deposit was discovered in 1974. Its prospecting had started in the same year and finished in 1977 (Bulnaev 1981; Lastochkin et al. 2018). In 1978–1986, the exploration work including the reserve estimation was conducted and approved by the USSR GKZ (State Commission on Mineral Reserves). The Egitinsky deposit provides 8.4% of a total fluorite production in Russia.

The Egitinsky ore field is represented by a xenolith of Late Cambrian volcano-sedimentary rocks embedded in Late Paleozoic granitoids (Fig. 1). The Paleozoic and Mesozoic dykes of various compositions are developed across the deposit. In the eastern part, Late Carbonaceous coarse-grained rocks occur and overlap with other sediments including the ore bodies. They are 5–50 m thick and composed of pebble and boulder-pebble conglomerates.

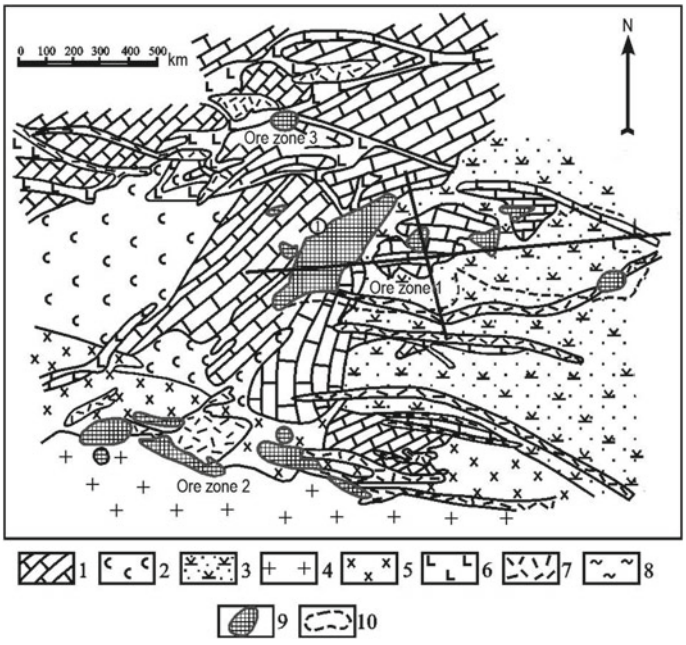

Fig. 1 The geological scheme of the Egitinsky deposit (modified after [Mikhailov 2000]). 1—limestones, 2—scarns, hornfels, 3—dacite breccia, 4—granites, 5—quartz syenites, 6—dolerites, 7—trachyrhyolites, 8—argillizites, 9—fluorite ore bodies, 10—the projection of the 1st ore vein on the surface

During the exploration work at the Egitinsky deposit, 23 ore bodies and several small ore lenses have been discovered and assessed. They are grouped into 3 ore zones. The largest 1st ore zone is situated in the central part of the deposit. It is 940 m long, up to 400 m thick, and up to 270 m deep. The 2nd ore zone with industrial mineralization is located 400 m south from the 1st ore area. It is 1 km long and about 100 m thick with a depth of 250 m. The 3rd ore zone is situated 200 m north from the 1st ore zone. It is 600 m long, 100–150 m thick, and about 230 m deep.

More than 10 ore bodies have been discovered in the 1st ore zone, among them No. 1 and 2 ore bodies contain balance ores, while No. 2, 7 and 8 ore bodies contain off-balance ores. The remaining ore bodies (No. 4, 6, 9, 21, 22, and 23) are small lenses.

As a part of the 2nd ore area, only No. 15 ore body contains balance ores, and No. 17, 18, 24 and 61 ore bodies contain off-balance ores. The 3rd ore area is even less significant and consists of 7 ore bodies, and only two of them—No. 10 and 55—contain off-balance ores. The morphology of ore bodies is complicated: the larger ones are tabular deposits, and small bodies are lens-shaped.

The aim of this study is to examine the PT-conditions of fluorite ore formation and to remodel the ore-forming processes and reveal the role of different factors responsible for the ore formation.

2 Materials and Methods

An Olympus BX 52 polarizing microscope equipped with a digital camera was used to study the optical characteristics of minerals.

The chemical composition was identified by a LEO 1430 VP scanning electron microscope with INCA-Energy 300 EDS spectrometer at the Geological Institute SB RAS (Ulan-Ude).

Microthermometric measurements were conducted by a Linkam TMS-600 heating/freezing stage mounted on Olympus BX 51 microscope. All measurements were performed in nitrogen medium. The standard deviation of the measured temperature depended on the absolute temperature and did not exceed ± 1 °C in every case for temperatures above 80 °C and ≤ 0.1 °C for the measurements at temperatures between −20 and 80 °C. The salt composition of fluid was determined according to (Davis et al. 1990; Spencer et al. 1990). The salinities of fluids were calculated using final melting temperatures according to (Bodnar and Vityk 1994).

3 Results and Discussion

The ore bodies of the Egitinsky deposit are composed of breccia with limestone and argillized rock fragments cemented by quartz-fluorite aggregates. Massive ores are found along with breccias. Streaky-disseminated ores have limited distribution and are developed over the rocks of alumino-silicate composition. The texture of these ores transforms into breccia-like in intensively fractured zones with widespread veinlets. The main ore minerals are fluorite, quartz and calcite; the minor minerals are clayey minerals, feldspar, Fe hydroxides, and F-apatite. Magnetite, hematite, goethite, ilmenite, rutile, titanite, pyrite, chalcopyrite, galena, sphalerite, monazite, zircon, thorite, amphibole, pyroxene, biotite, chlorite, garnet, vesuvianite, and tourmaline are found in single grains.

The chemical composition of ores from the Egitinsky deposit is characterized by an increased content of CaF_2 and lower amounts of SiO_2, $CaCO_3$ and Al_2O_3. Other components are found as traces. According to the phase analysis, CaF_2 is mainly related to fluorite. The average fluorite content in ores of the main ore bodies is similar. The variation coefficient of fluorite content across the sections is indicative of its irregular distribution in ores. Proceeding from the same data, SiO_2 is represented in half by ore quartz. The rest of fluorite is confined to Al-Si fragments of ore rock and minerals. $CaCO_3$ is characteristic of breccia ores from the contact parts of ore body areas, where metasomatic processes are fragmented. $CaCO_3$ content in the central parts of ore bodies does not exceed 5–10%. The main $CaCO_3$ sources are unsubstituted limestone fragments. Al_2O_3 is related to clayey minerals, mica and feldspar, and ranges between 0.37 and 14.70% (average 5.4%). Phosphorus is considered an undesirable impurity in ores and its content ranges from tenths and hundredths of a percent, while in the western part of the 1st ore zone, its content reaches 2.8%. Generally, P_2O_5 content in ores does not exceed 0.7%. The mineralogical and geochemical report (Bulnaev 1981) indicates that P is related to F-apatite and berlinite, a rare secondary aluminophosphate, which forms thin patina on F-apatite surface and replaces it.

The primary and pseudosecondary bi-phase (VL) fluid inclusions in fluorite from massive fluorite and quartz-fluorite veins of the Egitinsky deposit have been studied using a microthermometric technique (200 measurements). The studied fluid inclusions are 20–30 μm in size and have an isometric shape with crystal elements (Fig. 2a). According to (Roedder 1978; Kerkhof and Hein 2001), these inclusions can be classified as primary and pseudosecondary. The primary fluid inclusions are located separately in the central areas of fluorite grains and are characterized by similar phase ratios, while pseudosecondary fluid inclusions are confined to the fractures in fluorite, which appeared during its formation.

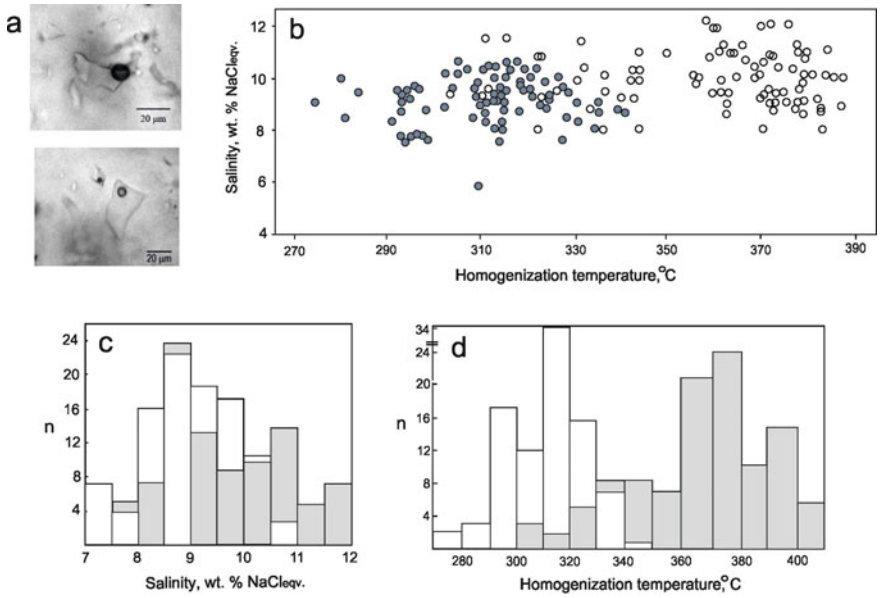

Fig. 2 The fluid inclusion data for the fluorite from the Egitinsky deposit. **a**—primary fluid inclusions in fluorite; **b**—the plot of homogenization temperature *vs.* salinity; **c**, **d**—the histograms of salinity **c** and homogenization temperatures **d** distribution. White color shows massive fluorite ores; grey color shows quartz-fluorite ores

The eutectic temperatures of fluid inclusions in fluorite from massive fluorite ores form two ranges as follows: −31…−37 °C and −22…−25 °C that correspond to K-Mg-Na±Fe chloride fluid with carbonate impurities (Davis et al. 1990; Spenser et al. 1990]. The vapor bubbles occupy about 20–30% of inclusion volume. These temperatures characterize NaCl-KCl fluid with possible Mg impurity. In addition, we have determined rare eutectic temperatures close to −26 °C that indicate the presence of $CaCl_2$ in the fluid (Spenser et al. 1990).

For most inclusions, the final melting temperatures range between −5 and −8.3 °C corresponding to salinities between 8 and 12 wt% $NaCl_{eqv}$ with a peak at 8.5–9 wt%. The homogenization temperatures are 300–400 °C with a peak of 370–380 °C (Fig. 2c, d).

Fluid inclusions in fluorite from quartz-fluorite ores demonstrate the eutectic temperatures ranging from −38 to −33 °C and −22 to −28 °C, which suggests a Na-K-Mg chloride fluid. In most inclusions, the final melting temperatures range between −4.6 and −7.2 °C, corresponding to a salinity of 5.5–10 wt% $NaCl_{eqv}$. The homogenization temperatures are 270–340 °C with a peak of 310–320 °C (see Fig. 2c, d).

Fluorite in veins is fractured and traced by bi-phase (VL) secondary fluid inclusions about 5 μm in size. However, due to the small size, we cannot determine the fluid salinity and composition. The homogenization temperatures are 240–300 °C. The temperatures of secondary fluid inclusions suggest that the filling of fractures in fluorite was simultaneous with the formation of the latest fluorite aggregates. In addition, we observed the co-existing monophase gas and liquid inclusions up to 5 μm in size. The coexisting monophase gas and liquid inclusions and more concentrated bi-phase inclusions are indicative of a heterogeneous fluid.

The formation of the Egitinsky deposit is noted to be multistage (Korotayev et al. 1986). The ore process is caused by the flow of siliceous-fluoride hydrothermal fluids enriched with F, Ca, Si, Na, K, Al, and Fe into the fault zone. They are responsible for the formation of violet and fine- and medium-grained fluorite in the main ore bodies. In the deposit, the resumed tectonic processes have triggered the partial crushing of ore bodies and near-ore argillized and silicified metasomatic rocks.

Due to the detailed study of mineral assemblages and their replacement over time, we have noted that the mineral formation includes 3 following stages: massive fluorite, quartz-fluorite and siliceous-carbonate. The first massive fluorite stage deals with the main metasomatic ore bodies and mineralized zones in Al-Si rocks. The mineral formation of this stage occurs from water-Mg-K-Na-chloride fluid with salinity of 8–12 wt% $NaCl_{eqv}$ at temperatures decreasing from 400 to 300 °C (Table 1).

The second quartz-fluorite stage begins with the formation of a small amount of fine-grained "porcelain-like" quartz followed by weak colorless veinlets of coarse-columnar fluorite 1–2 cm in size. The latter is subordinate with respect to the first stage, but more common in ore zones than "porcelain-like" quartz. Fluorite-II forms the most of streaky, druzy, cockade-, frame-like and disseminated ores and contains the microinclusions of clayey minerals, calcite and sericite. The quartz-fluorite mineral assemblages are formed at higher temperatures ranging

Table 1 Fluid inclusion data of fluorite from the Egitinsky deposit

Ore stage	n	T_{eut}, °C, (salts)	T_{fm}, °C	C, wt% $NaCl_{eqv}$	T_{hom}, °C
Massive fluorite (3 samples)	110	–23…–35 (NaCl-KCl ±$MgCl_2$)	–5.0…–8.3	8–12	300–400
Quartz-fluorite (3 samples)	95	–23…–37 (NaCl-KCl-$MgCl_2$)	–4.6…–7.2	5.5–10	270–340

Note T_{eut}—first melting temperature; T_{fm}—final melting temperature; C—salinity; T_{hom}—homogenization temperature; n—number of measurements

between 270 and 340 °C due to Na-Mg-K chloride fluid with the salinity of 5–10 wt %. $NaCl_{eqv}$ (see Fig. 2b, and Table 1).

The final carbonate-siliceous stage is responsible for $nSiO_2 \cdot mH_2O$ products. Chalcedony quartz and opal, occurring at this stage, form thin veinlets, small lenses and nodules in ores and host rocks.

We have compared our fluid inclusion data to similar data for different fluorite deposits of Trans-Baikalia (Vinokurov et al. 2014). The salt composition of fluids responsible for fluorite veins from the Garsonui and Streltsovsky deposits is close to ours: at eutectic temperatures, Na, K, and Mg chlorides are found in the ore-forming fluid. However, homogenization temperatures and salinity vary considerably. For the Garsonui deposit, these parameters are similar to ours, but vary widely: 230–380 °C and 5–17% $NaCl_{eqv}$, respectively. Similar formation conditions are determined for the Suran hydrothermal fluorite deposit in the Southern Urals (Krupenin et al. 2012). At this deposit, the higher salinity of ore-forming fluids is caused by the mixing of seawater with evaporitic brines.

Similar to our experience, complex Na-Ca-Mg chloride fluids with widely varying salinities (12–15, up to 20 wt%) have been examined at hydrothermal fluorite and barite-fluorite deposits in Germany, Tunis and Iran (Trinkler et al. 2005; Rajabzaden 2007; Bejaoui et al. 2013). The temperatures of fluorite formation at these deposits do not exceed 250 °C, which is caused by hot magmatic fluids produced by the host intrusive.

The presence of calcite in ores indicates that $CaCl_2$ content can be significant in the fluid (0.1 mol per 1 kg of H_2O). According to (Morgunov 2006), the calcite/fluorite assemblage is stable at $CaCl_2$ concentration of 10^{-2} mol/kg H_2O and more. Calcium and fluorine, necessary for fluorite formation, occur in a magmatic fluid (massive fluorite ores) and exogenic calcium fluid (fluorite-siliceous-carbonate or quartz-fluorite ores).

4 Conclusions

The obtained sequence of mineral formation is in agreement with fluid inclusion data and shows that ores of the Egitinsky deposit were formed at temperatures ranging from 400 to 300 °C due to Na-K-Mg-chloride fluids. The specific temperature range corresponds to the completion of each stage and the beginning of the following stage. A narrow range of fluid temperatures and salinity gives evidence to the stability of mineral formation conditions and/or weak flow of hydrothermal fluids. The higher salinity and temperatures of mineral formation of massive fluorite ores may be caused by the mixing of metamorphic fluids accompanied by fluid dehydration or hot deep fluids produced by adjacent granitoids. The Mg and Ca sources may be host limestones containing Mg-carbonates.

Acknowledgements The study was supported by the Russian Foundation for Basic Research (Grant No. 12-05-31204).

References

Bejaoui J, Salah Bouhlel S, Barca D. Geology, Mineralogy and Fluid inclusions investigation of the Fluorite deposit at Jebel Kohol, Northeastern Tunisia. Periodico di Mineralogia. 2013: 82 (2), 217–237. https://doi.org/10.2451/2013PM0013

Bodnar RJ, Vityk MO. Interpretation of microthermometric data for H_2O–NaCl fluid inclusions. Fluid inclusions in minerals: methods and applications. Pontignana-Siena. 1994: 117–130.

Bulnaev KB. Osobennosti obrazovaniya i razmeshcheniya flyuoritovyh formaciy Zabaykal'ya. Evolyuciya endogennyh processov i orudeneniya v Zabajkal'e. Ulan-Ude: BF SO AN SSSR. 1981: 101–109. [Bulnaev KB. The peculiarities of formation and localization of fluorite formations of Trans-Baikalia. The evolution of endogenic processes and ore formation in Trans-Baikalia. Ulan-Ude: BF SO AN SSSR. 1981: 101–109 (in Russ.)].

Davis DW, Lowenstein TK, Spenser RJ. Melting behavior of fluid inclusions in laboratory-grown halite crystals in the systems NaCl-H_2O, NaCl-KCl-H_2O, NaCl-$MgCl_2$-H_2O and $CaCl_2$-NaCl-H_2O. Geochimica Et Cosmochimica Acta. 1990; 54 (3): 591–601. https://doi.org/10.1016/0016-7037(90)90355-O

Korotayev IP, Divina LV, Vinogradov PK. Egitinskoe mestorozhdenie flyuorita. Geologiya i genezis flyuoritovyh mestorozhdeniy. Vladivostok. 1986: 108–117. [Korotayev IP, Divina LV, Vinogradov PK. Egitinsky fluorite deposit. Geology and genesis of fluorite deposits. Vladivostok. 1986: 108–117 (in Russ.]

Krupenin MT, Prokhaska V, Ronkin YuL. Priroda ftora i rudoobrazuyushchih rastvorov flyuoritovogo mestorozhdeniya Suran (Bashkirskiy meganticlinoriy) po dannym izucheniya lantanoidov, flyuidnyh vklyucheniy i Sr-Nd sistematiki // Litosfera. 2012: 5, 126–144 [Krupenin MT, Prokhaska V, Ronkin YuL. The genesis of fluorine and ore-forming fluids of Suran fluorite deposit (Bashkir meganticlinorium): lanthanoids, fluid inclusions and Sr-Nd systematics // Lithosphere. 2012: 5, 126–144 (In Russ)].

Lastochkin EI, Ripp GS, Tsydenova SD, Posokhov VF. Epitermal'nye flyuoritovye mestorozhdeniya Zapadnogo Zabajkal'ya. Izv. Sib. otd. Sekcii nauk o Zemle RAEN. 2018; 41/2 (63): 41–53. [Lastochkin EI, Ripp GS, Tsydenova SD, Posokhov VF. Epithermal fluorite deposits of the Western Trans-Baikalia. The News of Siberian Branch of the Earth Sciences RANS. 2018; 41/2 (63): 41–53 (In Russ.)]

Morgunov KG. Razvitie programmnogo obespecheniya i termodinamicheskih baz dannyh dlya modelirovaniya geohimicheskih processov s uchastiem mikrokomponentov. Avtoref. dis. k.g.-m.n. Novosibirsk, OIGGM SO RAN. 2006: 16. [Morgunov KG. The development of the software and thermodynamic base for modelling of geochemical processes involving microcomponents. Abstract of PhD (geol.-min. sci.) thesis. Novosibirsk, UIGGM SB RAS. 2006: 16 (in Russ.)]

Rajabzaden MA. A fluid inclusion study of a large MVT barite-fluorite deposit Komshechen, Central Iran. Iranian Journal of Science & Technology. 2007: 31, 73–87

Roedder E. Flyuidnye vklyucheniya v mineralah. Moskva: Mir, 1978: 1, 360 [Roedder E. Fluid inclusions in minerals. Moscow: Mir, 1978: 1, 360. (In Russ)]

Spenser RJ, Moller N, Weare JN. The prediction of mineral solubilities in mineral waters: a chemical equilibrium model for the Na-K-Ca-Mg-Cl-SO_4 system at temperatures below 25°C. Geochimica Et Cosmochimica Acta. 1990; 54 (3): 575–590. https://doi.org/10.1016/0016-7037(90)90354-N

Trinkler M, Moneske T, Thomas R. Constraints on the genesis of yellow fluorite in hydrothermal barite-fluorite veins of the Erzgebirge, Eastern Germany: evidence from optical absorption spectroscopy, REE data, and fluid inclusion investigations. The Canadian Mineralogist. 2005: 43, 883–898. https://doi.org/10.2113/gscanmin.43.3.883.

Van Kerkhof AM, Hein UF. Fluid inclusion petrography. Lithos. 2001; 55, 27–47. https://doi.org/10.1016/S0024-4937(00)00037-2

Vinokurov SF, Golubev VN, Krylova TL, Prokof'ev VY. RZE i flyuidnye vklyucheniya v zonal'nyh flyuoritah Vostochnogo Zabajkal'ya: raspredelenie i geohimicheskoe znachenie. Geohimiya. 2014: 8, 715–731 [Vinokurov SF, Golubev VN, Krylova TL, Prokof'ev VY. REE and fluid inclusions in zoned fluorites from Eastern Transbaikalia: Distribution and geochemical significance. Geochemistry International. 2014: 52(8), 654–669 (In Russ.)] https://doi.org/10.1134/S0016702914060093

XRF Analysis of Elemental Composition of Archaeological Coins from Mangup, Crimea

Anna V. Antipenko, Igor A. Nauhatsky, Elena M. Maksimova, Tatiana N. Smekalova, and Valeriy E. Naumenko

Abstract

The results of the study of coins from Mangup town (Crimea) archeological excavations in 2018 are presented. The aim of the study is the precise determination of coin alloy composition by X-ray fluorescence analysis using Rigaku Supermini200 high-power benchtop sequential wavelength dispersive X-ray fluorescence spectrometer. Based on the data obtained, it can be concluded that the use of lead ligature was not an exclusive characteristic of the Chersonesos Mint, caused by the metal shortage in the Crimea. It is possible that the lowest-denomination coins were produced from alloys with abnormally high lead content in Chersonesos and other mints of the Byzantine Empire.

Keywords

X-ray fluorescence analysis · Alloy composition · Crimea numismatics · Mangup town

1 Introduction

Mangup fortress is located in the South-western part of the Inner ridge of the Crimean Mountains. Its study is important for solving a number of difficult issues in the history of medieval Taurica, in particular, political, commercial and cultural relations with Byzantium (Gertsen 1990; Gertsen 2003). The authority of the

A. V. Antipenko · I. A. Nauhatsky · E. M. Maksimova (✉) · T. N. Smekalova · V. E. Naumenko
V.I. Vernadsky Crimean Federal University, 4 Vernadsky ave., 295033 Simferopol, Crimea, Russia
e-mail: maksimovaem@cfuv.ru

S. Votyakov et al. (eds.), *Minerals: Structure, Properties, Methods of Investigation*,
Springer Proceedings in Earth and Environmental Sciences,
https://doi.org/10.1007/978-3-030-49468-1_3

Byzantine power in the Crimea was carried out primarily through the old town centers—Chersonesos and Bosporus (Aybabin and Khayredinova 2017). The South-western Crimean town of Mangup was connected with the territory of Chersonesos. Probably, the monetary circulation between the two medieval towns was in close cooperation.

The aim of the work was to determine the precise composition of coin alloys by X-ray fluorescence (XRF) analysis. A comprehensive study of the numismatic material included the definition of the issuer, date, place of issue and the denomination of the coins.

2 Materials and Methods

60 samples from archeological excavations of Mangup settlement were analyzed in 2018 using the equipment of the Institute of Physics and Technology, V.I. Vernadsky Crimean Federal University. The samples included 3 coins of the Eastern Roman Empire and 18 coins of the Byzantine Empire (Fig. 1).

According to the existing experience (Smekalova 2018; Chernykh 2009), coin research methodology was developed using a Rigaku Supermini200 high-power benchtop sequential wavelength dispersive X-ray fluorescence (WDXRF) spectrometer providing high spectral resolution for overlapping peaks. The automatic sample changer for 12 samples provided non-destructive sample handling in vacuum. High powered (200 W) X-ray tube contributed to high sensitivity for light elements (Na, Mg, Ca, Si, Al, P, etc.). The composition of the analyzed samples was determined by comparison with the reference spectra. The information on the alloy composition was obtained from the entire surface of the coin.

A specific feature of this study was the presence of patina on the samples. Therefore, the mechanical cleaning of coins from patina and soil contamination was carried out prior to analysis and the elemental composition both of the contamination material and cleaned coin was determined. This allowed the protocol of the final sample composition to be clarified using the content of matrix elements (P, S, K, Na, Ca, Si).

Coins contamination, their difference in size and weight has led to the need for additional equipment to fix the samples in the spectrometer. It protected the spectrometer from the entry of foreign particles and preserved the vacuum of the instrumental measuring system.

3 Results and Discussion

According to the developed methodology, the coins of the Eastern Roman Empire and Byzantine Empire were examined; the measurement results are presented in Table 1.

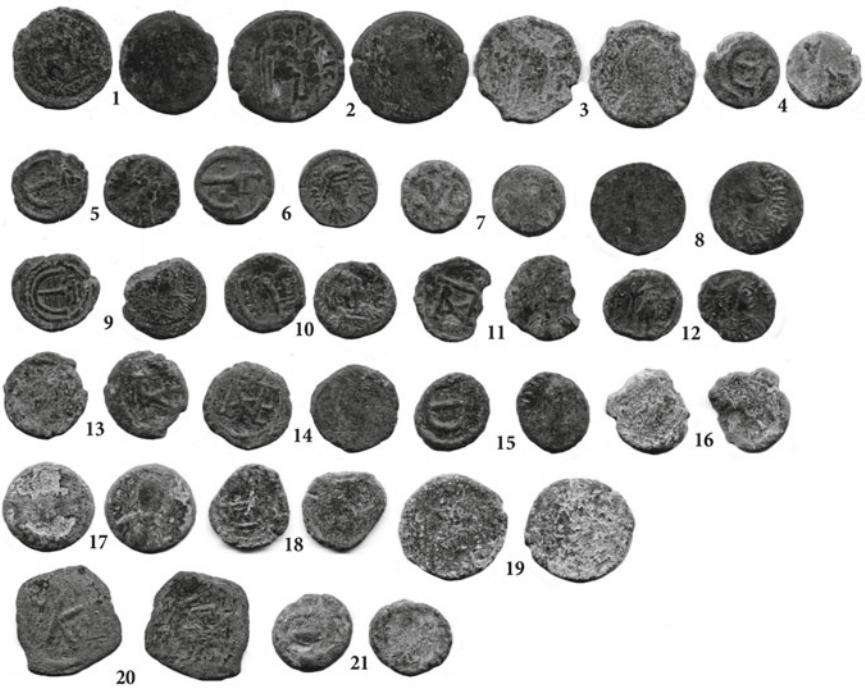

Fig. 1 Description of samples: 1—Collection inventory (CI) 258 Eastern Roman Empire. Arkadius (383–408 AD). Mint: Antioch, Officina "A"; 2—CI 27 Eastern Roman Empire. Leo I (457–474 AD). Mint: Chersonesos; 3—CI 84. Eastern Roman Empire. Zeno (474–491 AD); 4—CI 27 Byzantine Empire. Anastasius I (491–518 AD). Mint: Constantinople. Pentanummium; 5—CI 9 Byzantine Empire. Anastasius I (491–518 AD). Mint: Constantinople. Pentanummium; 6—CI 61 Byzantine Empire. Anastasius I (491–518 AD). Mint: Constantinople. Pentanummium; 7—CI 86 Byzantine Empire. Justin I (518–527 AD). Pentanummium; 8—CI 133 Byzantine Empire. Justinian I (527–565 AD). Decanummium; 9—CI 93 Byzantine Empire. Justinian I (527–565 AD). Pentanummium; 10—CI 40 Byzantine Empire. Justinian I (527–565 AD). Mint: Chersonesos. Pentanummium; 11—CI 10 Byzantine Empire. Justinian I (527–565 AD). Mint: Chersonesos. Pentanummium; 12—CI 257 Byzantine Empire. Justinian I (527–565 AD). Mint: Chersonesos. Pentanummium; 13—CI 76 Byzantine Empire. Justinian I (527–565 AD). Mint: Chersonesos. Pentanummium; 14—CI 145 Byzantine Empire. Justinian I (527–565 AD). Mint: Chersonesos. Pentanummium; 15—CI 66 Byzantine Empire, late V—early VI century AD Pentanummium; 16—CI 256 Byzantine Empire, late V—early VI century AD (?); 17—CI 166 Byzantine Empire, late V—early VI century AD Pentanummium; 18—CI 114; 19—CI 269 Byzantine Empire, late V—early VI century AD Pentanummium; 20—CI 5, Byzantine Empire, late VII—early VIII century AD semifollis; 21—CI 116 Byzantine Empire, late V—early VI century AD Pentanummium

The great amount of "copper" coins of small denominations of Arcadius, Leo I, Zeno and Anastasius I times is characteristic of the Chersonesos numismatic material of the V—VI centuries (Guruleva 2018). Chersonesos is considered to cease producing its own coins under the power of Emperor Gallien (253–268 AD),

Table 1 The chemical composition of coins of the Eastern Roman Empire and Byzantine Empire from the archeological excavations of Mangup town in 2018

No.	CI no.	Weight, g	Elemental composition, wt%											
			Cu	Pb	Sn	Zn	Fe	Ag	As	Mn	Sb	Ni	Ti	Other
1	25	2.58	37.0	54.5	2.4	–	5.1	0.5	–	–	–	–	0.4	0.1
2	27	4.19	35.3	43.4	12.6	0.2	6.3	–	1.0	0.1	–	0.2	0.2	0.8
3	84	4.84	25.6	49.6	16.8	–	5.4	–	0.6	–	0.6	–	0.8	0.8
4	87	2.06	51.1	30.5	9.2	–	5.3	1.5	–	–	–	–	0.7	0.8
5	9	2.14	32.3	59.7	2.7	–	4.9	–	–	–	–	0.4	–	–
6	61	1.97	42.3	42.0	9.6	–	5.0	–	–	0.2	0.6	0.1	–	–
7	86	2.17	8.7	85.8	4.1	–	1.1	–	–	–	–	–	–	0.3
8	133	3.93	97.4	1.5	–	–	0.5	0.3	–	–	–	0.1	–	0.2
9	93	2.14	67.0	8.3	14.2	1.5	7.2	0.7	–	0.1	–	0.2	0.7	–
10	40	2.15	24.9	53.3	14.4	0.5	4.3	–	–	–	0.6	0.6	0.4	1.0
11	10	1.13	35.9	42.4	5.9	0.2	12.6	–	0.9	0.1	0.7	0.2	0.9	0.2
12	257	2.1	36.4	50.3	8.0	0.5	3.6	–	–	0.1	0.5	0.1	–	0.5
13	76	1.78	23.1	55.8	12.3	0.3	6.0	–	–	0.1	–	0.1	0.8	1.0
14	145	2.24	22.1	54.4	9.1	1. 1	11.1	0.9	–	–	–	0.3	1.1	–
15	66	1.85	48.6	37.7	5.3	0.1	5.7	1.4	–	–	1.1	0.2	–	–
16	256	2.92	21.2	69.0	6.0	0.1	2.5	–	–	–	–	0.1	0.5	0.6
17	166	2.67	50.9	40.7	3.9	0.1	3.7	0.4	–	–	–	0.1	0.3	0.2
18	114	1.79	24.1	70.8	3.8	0.7	1.0	–	–	–	–	0.2	–	–
19	269	3.91	7.1	73.0	16.0	0.1	1.7	–	–	0.1	0.7	–	0.3	1.1
20	5	2.02	90.8	6.5	–	–	2.0	–	–	–	–	0.5	0.3	–
21	116	2.23	11.5	82. 3	3.1	–	2.1	1.1	–	–	–	–	–	–

and resumed its activity during the reign of Emperor Zeno (474–491 AD) (Anokhin 1977). It is possible that already under his predecessor—Leo I (457–474 AD)—the needs of the town in monetary circulation determined the issue of a "copper" coin of small denomination. The basis for this assumption is a number of characteristics of the Chersonesos Mint products. Certain types of coins of this time have a high percentage of tin or lead in the alloy composition and a layered structure (Korshenko 2000). The coin of Leo I belongs to the early Byzantine bronzes, which a number of researchers attribute to the Chersonesos mintage (Sidorenko 2011) (Fig. 1, coin No. 2) from the "SALUS REI PUBLICAE" (The Welfare of the Republic") series, below is the name of Mint "CON".

The studies of the chemical composition of coins of the Eastern Roman Empire (Table 1, lines 1–3) of the times of Arcadius, Leo I and Zeno have shown that they are made of three-component bronze, which main alloy component is lead (up to 49%) with fairly high tin values (up to 16.7%). The presence of arsenic and titanium is also observed. Nickel and manganese impurities and zinc traces are present in the coin minted in the Chersonesos (Table 1, line 2).

Under Anastasius I Dikor (491–518 AD), a monetary reform was carried out in the Byzantine Empire (512 AD), and new "nominally copper" coins were put into circulation, which smallest denomination was pentanummium. In the Northern Black Sea region, both small pre-reform coins of this ruler and new coins, pentanummi and decanummi, were actively used (Guruleva 2018), but the Chersonesos coins produced under the reign of Anastasius I are not known (Anokhin 1977). Three coins of this denomination, minted in Constantinople (Table 1, lines 4–6), are made of three-component bronze, which contains a large amount of lead (30–59%) and tin (2–9%). The composition of the KO 87 coin (Table 1, line 4) has a small amount of silver (1.5%), which presence in a "copper" coin can be explained either by its ore origin or by the smelting of silver-containing waste.

Under Justin I and Justinian I, the inflow of coins from Constantinople and other cities of the Empire to Taurica decreases, as the Chersonesos mint is actively functioning and meeting the demands of the home market (Guruleva 2018). The pentanummium of Justin I (Table 1, line 7) is more than half lead. The decanummium of Justinian I (Table 1, line 8) is made of copper with low lead content (1.45%) and the traces of silver and nickel. It is believed that the only denomination minted in Chersonesos was pentanummium. The excavation materials on the Mangup plateau in 2018 include 5 coins of this mint (Table 1, lines 10–14). All of them are made of three-component bronze, which main alloy components are lead (42–55%) and tin (5–14%). It is interesting that zinc and nickel traces are found in these products in all cases. However, the set of trace elements is different for each coin. The Byzantine coins (Table 1, lines 15–19) of the same denomination, but without precise attribution, are made of an alloy of a similar formulation (Cu+Pb+Sn) with traces of zinc and nickel, and in two cases—of silver (Table 1, lines 15, 16). The KO 116 coin (Table 1, line 21) is different having a higher lead content (over 80%). The Byzantine semifollis (Table 1, line 20) is made of leaded bronze.

4 Conclusion

Based on the data obtained, it can be concluded that the use of lead ligature was not an exclusive characteristic of the Chersonesos Mint, caused by the metal shortage in the Crimea. It is possible that the lowest-denomination coins were made of alloys with abnormally high lead content, in this and other mints of the Byzantine Empire, while the semifolles were made of better quality bronze with a lead content within 7%.

It can be assumed that the traces of zinc in the pentanummium of Chersonesos mintage indicate the use and repeated melting of coins of the Roman time, for which production the brass and multicomponent zinc-containing alloys were actively used.

Acknowledgements The studies of the composition of coin alloys were supported by the Russian Science Foundation (grant No. 18-18-00193 "The initial period of the history of money: the transition from a coin of a full metallic value to a sign of conventional value". The excavations on the site of Mangup and the description of the coins were supported by the Russian Foundation for Basic Research (grant No. 19-09-00124 "The palace complex of the Mangup fortress—the residence of the rulers of the principality of Theodoro in the South-Western Crimea. The problems of chronology, planning and architectural reconstruction of the monument").
The authors are grateful to A.V. Yakushechkin for the description and attribution of coins.

References

Anokhin VA. Monetnoye delo Khersonesa (IV v. do n.e. - XII v. n. e.). Kiyev. 1977. [Anokhin VA. The coinage of Chersonesos (4-th century BC – 12-th century AD). Kiev. 1977. (In Russ.)]

Aybabin AI, Khayredinova EA. Krymskiye goty strany Dori (seredina III-VII v.). – Simferopol': OOO "Antikva". 2017; 368. [Aybabin AI, Khayredinova EA. Crimean goths of the Dori country (the middle of the III-VII centuries). Simferopol: Antiqua LLC, 2017; 368. (In Russ.)]

Chernykh EN, Lun'kov VY. Metodika rentgeno-fluorestsentnogo analiza medi i bronz v laboratorii Instituta arkheologii. Analiticheskiye issledovaniya. 2009; 78-83. [Chernykh EN, Lunkov VYu. X-ray fluorescence analysis of copper and bronze in the laboratory of the Institute of Archeology. Analytical Studies. 2009; 78-83. (In Russ.)]

Gertsen AG. Doros-Feodoro (Mangup): ot rannevizantiyskoy kreposti k feodal'nomu gorodu. Antichnaya drevnost' i sredniye veka. 2003; 34: 94-112 [Gertsen AG. Doros-Theodoro (Mangup): from the early Byzantine fortress to the feudal city. Antiquity and the Middle Ages. 2003; 34: 94-112 (In Russ.)]

Gertsen AG. Krepostnoy ansambl' Mangupa. Materialy po arkheologii, istorii i etnografii Tavrii. 1990; I: ss. 87-166, 242-271. [Gertsen AG. Mangup fortress ensemble. Materials on archeology, history and ethnography of Tavria. 1990; I: pp. 87-166, 242-271 (In Russ.)]

Guruleva VV. Osnovnyye problemy numizmatiki Kryma vizantiyskoy epokhi. Trudy Gosudarstvennogo Ermitazha. Materialy i issledovaniya Otdela numizmatiki. 2018; 94: 61-80. [Guruleva VV. The main problems of the numismatic of the Crimea of the Byzantine era. Works of the State Hermitage. Materials and Research of the Numismatics Department. 2018; 94: 61-80. (In Russ.)]

Korshenko AN. Rimskiye monety chekanki Khersonesa. Vos'maya Vserossiyskaya numizmaticheskaya konferentsiya. Moskva, 17-21 aprelya, 2000: tezisy dokladov i soobshcheniy. 2000; ss. 34-36. [Korshenko AN. Roman coins minted by Chersonesos. Eighth All-Russian Numismatic Conference. Moscow, April 17-21, 2000: Abstracts of reports and communications. 2000; pp. 34-36. (In Russ.)]

Sidorenko VA. Monetnoye delo srednevekovogo Khersona V-VII vv. n.e. Vizantiyskiy seminar "ΧΕΡΣΩΝΟΣ ΘΕΜΑΤΑ: imperiya i polis". Tezisy dokladov soobshcheniy III Mezhdunarodnogo Vizantiyskogo seminara. Sevastopol'. 2011; ss. 25-30. [Sidorenko VA. Coin business of medieval Chersonesos in V-VII centuries AD. Byzantine seminar "ΧΕΡΣΩΝΟΣ ΘΕΜΑΤΑ: Empire and policy". Abstracts of reports from the III International Byzantine Seminar. Sevastopol. 2011; pp. 25-30. (In Russ.)]

Smekalova TN. Evolution of composition of monetary alloys of ancient Greek states on the Black Sea shores, basing on the data of X-ray-fluorescent spectroscopy with the example of Bosporos Cimmerian. Crystallography Reports. 2018; 63(6): 1043-1050

Influence of Seymchan Meteorite Structure on the Growth and Properties of Carbon Nanotubes

Anastasia S. Begunova, Grigoriy A. Yakovlev, Robert V. Kamalov, Elizaveta A. Pankrushina, and Victor I. Grokhovsky

Abstract

Carbon nanotubes (CNTs) were synthesized by chemical vapor deposition (CVD). The Seymchan meteorite (metal part) was used as a substrate due to its nanoscale structure and areas with different Ni content. The thermal oxidation experiment with the Seymchan sample was carried out to estimate the oxidation result during the CVD. The study of the samples by scanning electron microscopy and Raman spectroscopy showed that they were covered with Fe_2O_3 nanorods (30 nm in diameter). After the CVD process, the oxide nanocrystals and CNTs covered the sample. The structural composition affected the growth and morphology of CNTs. The least disordered CNTs were obtained on a taenite surface (an average diameter was 10 nm).

Keywords

CNT · CVD · Meteorite · Seymchan · Raman

A. S. Begunova (✉) · G. A. Yakovlev · R. V. Kamalov · V. I. Grokhovsky
Ural Federal University, 19 Mira str., 620002 Ekaterinburg, Russia
e-mail: n.s.begun@gmail.com

E. A. Pankrushina
Zavaritsky Institute of Geology and Geochemistry UB RAS, 15 Akademika Vonsovskogo str., 620016 Ekaterinburg, Russia

S. Votyakov et al. (eds.), *Minerals: Structure, Properties, Methods of Investigation*, Springer Proceedings in Earth and Environmental Sciences,
https://doi.org/10.1007/978-3-030-49468-1_4

1 Introduction

Carbon nanotubes (CNTs) are the most common carbon nanomaterial that is currently synthesized in many ways on various substrates (Kumar and Ando 2010). It is known that few examples of multi-walled carbon nanotubes (MWCNT) are found in nature, including meteorites (Rümmeli et al. 2011). In this study, carbon nanotubes were synthesized using chemical vapor deposition (CVD). It is the most popular method of producing CNTs nowadays, in which the thermal decomposition of a carbon-containing vapor is achieved in the presence of a metal catalyst. The CVD method requires a metal substrate, and Fe, Co, Ni are commonly used, because of high carbon solubility in these metals and high carbon diffusion rate at high temperatures (Ding et al. 2008).

In this study, the Seymchan meteorite samples served as substrates for CVD experiments. The metal part of Seymchan has a Widmanstätten structure that was formed during very slow cooling, about 7.1 K/Myr (Yang et al. 2010). This structure consists of kamacite (α-(Fe, Ni) alloy with Ni content of about 7 wt%), taenite (γ-(Fe, Ni) alloy with Ni content of 20–45 wt%), plessite (a fine-grained mixture of the kamacite and taenite minerals), and schreibersite ($(Fe, Ni)_3P$ iron and nickel phosphide) (Buchwald 1975). Since the Seymchan meteorite samples possessed submicrostructure, we assumed that they could be an acceptable substrate for CVD growth. The aim of our work was to reveal the influence of the structural composition of the meteorite surface on CNT growth and properties.

2 Materials and Methods

The Seymchan meteorite samples were prepared using standard metallographic procedures: grinding, polishing, and etching with 1.5% nital. Sample 1 was etched for 15, 10, 5, and 0 min to reach a different surface structure. Sample 2 was etched for 10 min. The structural composition of the samples was investigated using Zeiss Axiovert 40 MAT optical microscope, then the areas of analysis were marked, and the samples were observed by scanning electron microscopy (SEM) and energy-dispersive X-ray spectroscopy (EDS) with Zeiss Sigma VP.

There were two different experiments using a “CVDomna” commercial equipment for carbon nanotube growth. The first one dealt with the synthesis of CNTs using ethanol pyrolysis, the second was carried out to explore the influence of the thermal oxidation process during CVD. In the experiments, the samples were placed into the reaction chamber and then heated to 600 °C at a pressure of 1 kPa. After the heating, the vapor-gas mixture passed into the reaction chamber, and after 10 min the sample was cooled to 400 °C at a pressure of 1 kPa and then cooled under ambient air. Table 1 shows the parameters of both experiments.

Table 1 Experimental parameters

Sample	Experiment	Vapor-gas mixture	Pressure of mixture	Duration
Sample 1	Ethanol pyrolysis	C_2H_5OH (95%) + air	15 kPa	10 min
Sample 2	Thermal oxidation	H_2O (distilled) + air	15 kPa	10 min

The samples were observed using SEM. The morphology of synthesized structures was analyzed by Raman spectroscopy. The results of Raman spectroscopy were obtained in UB RAS Common use center "Geoanalyst" using a LabRam HR 800 Evolution spectrometer equipped with the confocal Olympus BX-FM microscope. The lateral resolution was 1–2 μm, and the excitation wavelength was 514.5 nm. Spectra were collected by means of backscattering geometry. A diffraction grating of 600 gr/mm and an electrically cooled CCD detector were used for recording. The obtained spectra were compared with databases (Database of Raman spectroscopy 2019) and with the spectra of MWCNT obtained earlier (Bokobza and Zhang 2012; Zaine et al. 2014). According to López-Lorente et al. (2014) the MWCNT spectrum contained a G-band around 1600 cm^{-1}, which was the tangential mode, and a D-band around 1350 cm^{-1}, which indicated the presence of some disorder in the structure, while a series of radial breathing mode, characterizing single-walled carbon nanotubes, were not present in the MWNT spectra.

3 Results and Discussion

The observation of samples using the scanning electron microscopy before the experiments showed that etching treatment revealed structural elements with sizes in the range from 60 to 250 nm. Figure 1 shows a kamacite surface after etching for 15 (Fig. 1a) and 10 min (Fig. 1b).

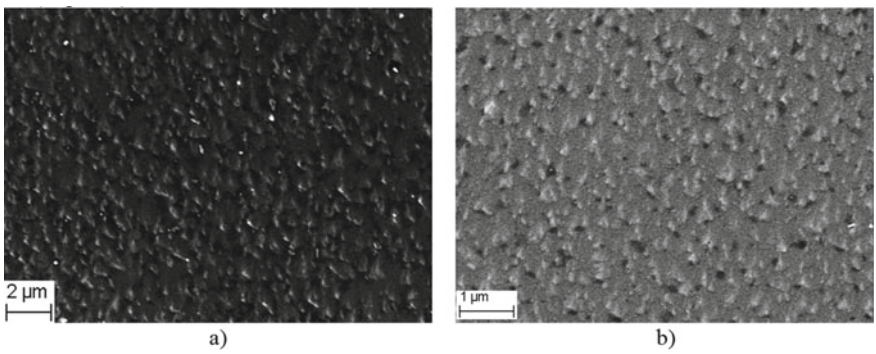

Fig. 1 SEM images of etched kamacite: **a** 15 min; **b** 10 min

The observation of samples after CVD showed that thin nanorods and some prisms covered their surface. Different initial structures contributed to the formation of different morphology of nanorods. Figures 2, 3, 4 and 5 demonstrate the analysis areas before and after the experiment. Synthesized on various surfaces, the structures differ in diameter, growth direction, and morphology.

The influence of an etching time of substrate etching on nanorod growth was detected. Longer etching time resulted in more nanorods per unit surface area. The type of structure affected the diameters of the obtained units. The diameters of nanorods were measured and plotted in Fig. 6. The average diameter of nanorods obtained on kamacite was 15 nm, plessite—15 nm, taenite—10 nm, and schreibersite—15 nm. Thus, average diameters were almost the same.

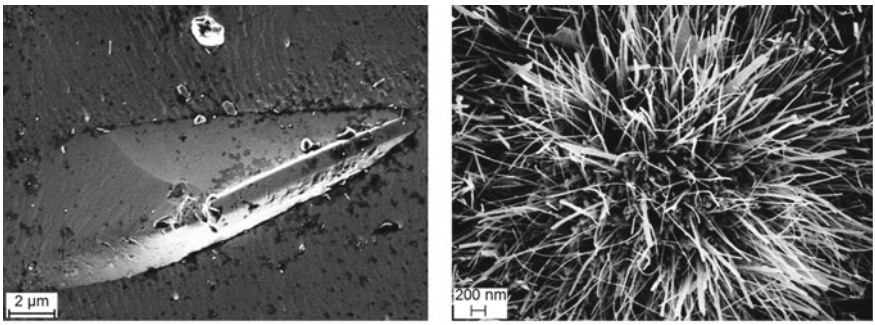

Fig. 2 SEM images of the schreibersite area: **a** before CVD; **b** after CVD

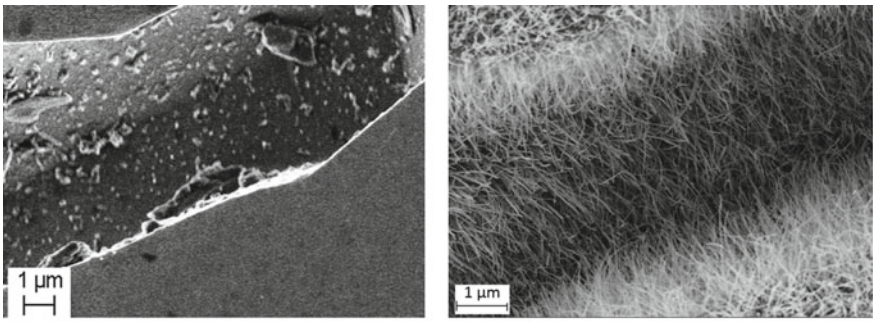

Fig. 3 SEM images of the taenite rim: **a** before CVD; **b** after CVD

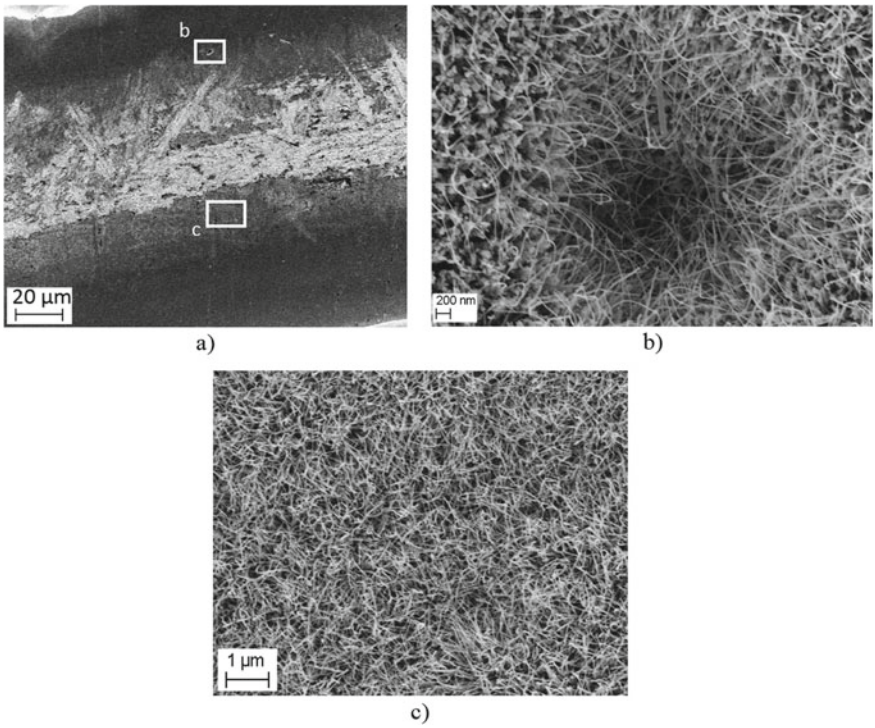

Fig. 4 SEM image of the plessite area **a** before CVD (b and c locations are marked by rectangles); **b**, **c** after CVD

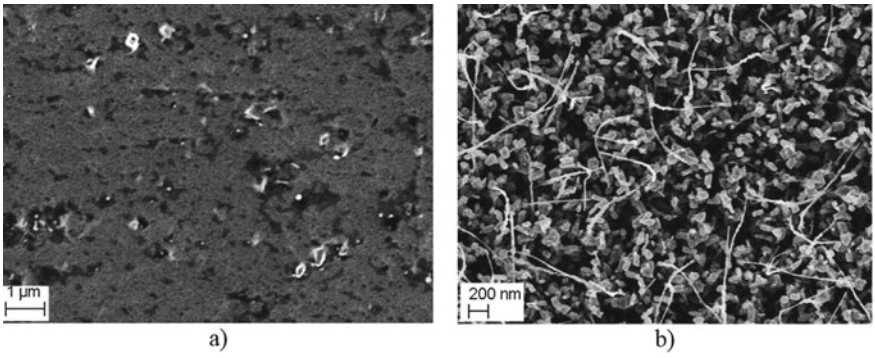

Fig. 5 SEM image of the kamacite area: **a** before CVD; **b** after CVD

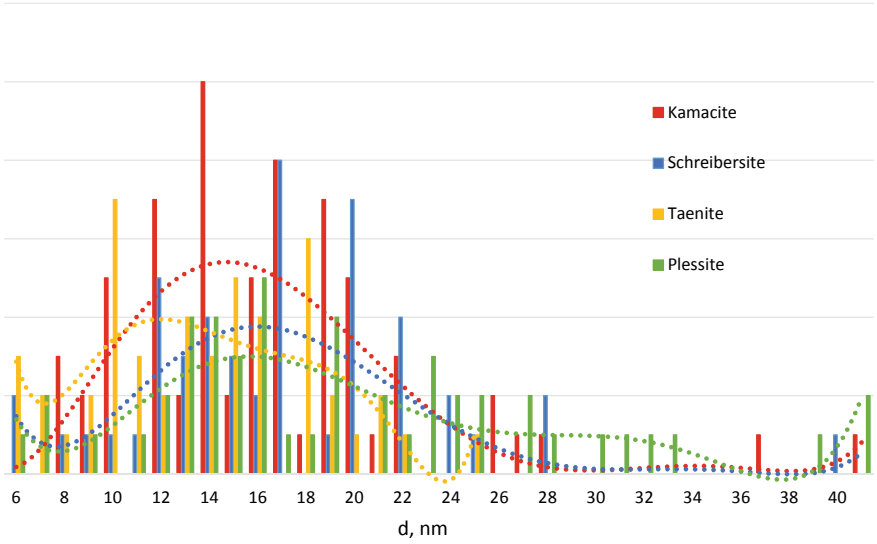

Fig. 6 The diameters of nanorods synthesized on different initial structures of the Seymchan meteorite

The second experiment had no carbon source. Sample 2 was thermally oxidized. According to Vincent et al. (2012), during the thermal oxidation of iron foil, thin Fe_2O_3 nanorods were formed. SEM observation of Sample 2 showed nanorods on its surface. The average diameter of oxide nanorods was 30 nm (Fig. 7). Thereby it was confirmed that oxidation took place during the synthesis of CNTs using CVD. Furthermore, the shape of the oxides was the same as that of the CNTs. Scanning electron microscopy does not allow CNTs to be distinguished from oxide rods, and CNTs are too small to be defined using EDS.

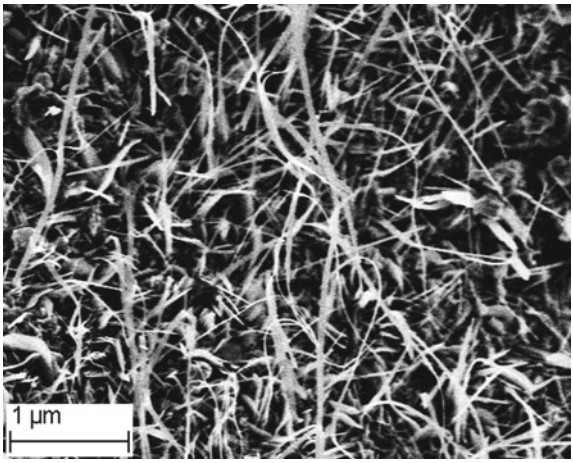

Fig. 7 SEM image of the surface of oxidized Sample 2

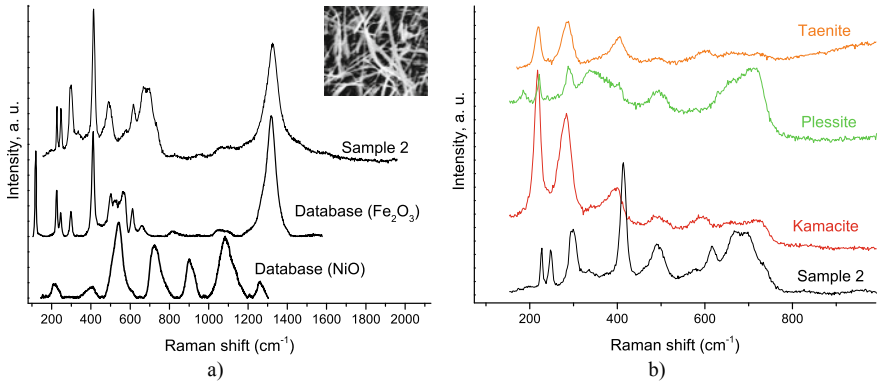

Fig. 8 Raman spectra: **a** Sample 2 and Fe_2O_3 from database (Database of Raman spectroscopy 2019); **b** Sample 1 (above) and Sample 2 (below). The insert shows the SEM image of the measured surface

The Raman study of Sample 2 and the comparison with database data showed that its surface was covered with hematite (Fe_2O_3) (Database of Raman spectroscopy 2019). Figure 8 shows Sample 2 and database spectra. Comparing the spectra, one can conclude that oxide nanorods, which were obtained by thermal oxidation, consisted of mostly Fe_2O_3, the content of NiO could not be estimated from these spectra. The Raman study of Sample 1 showed that its surface was covered by both Fe_2O_3 and CNTs. Figure 9 shows spectra obtained on Sample 1 (taenite, plessite, kamacite), the spectrum of Sample 2 was included for comparison. It can be seen that iron oxides were obtained on Sample 1, and the iron oxide content was higher on the surface of kamacite (it contained more iron than taenite or plessite).

Figure 9 shows the carbon modes of the Sample 1 spectra. It should be noted that the FWHM of the D band rises with increasing Ni content of the initial surface (wider in kamacite spectrum). Disordering in carbon nanotube morphology and contamination by amorphous carbon can be estimated using G/D intensity ratio (López-Lorente et al. 2014). FWHM of peaks also matters, but the investigation of Sample 2 showed that one of the Fe_2O_3 peaks and D-band could overlap (1320 and 1350 cm^{-1}, respectively), so FWHM is not the parameter for estimation.

The I_G/I_D intensity ratios of G- and D-bands of CNT spectra obtained on the different surfaces were calculated and comprised 1.08 for taenite, 1.00 for plessite, and 0.96 for kamacite. Thereby the least disordered CNTs were obtained on the taenite surface. Whether the reason is related to a high content of nickel or to the structure of the taenite, remains an open question.

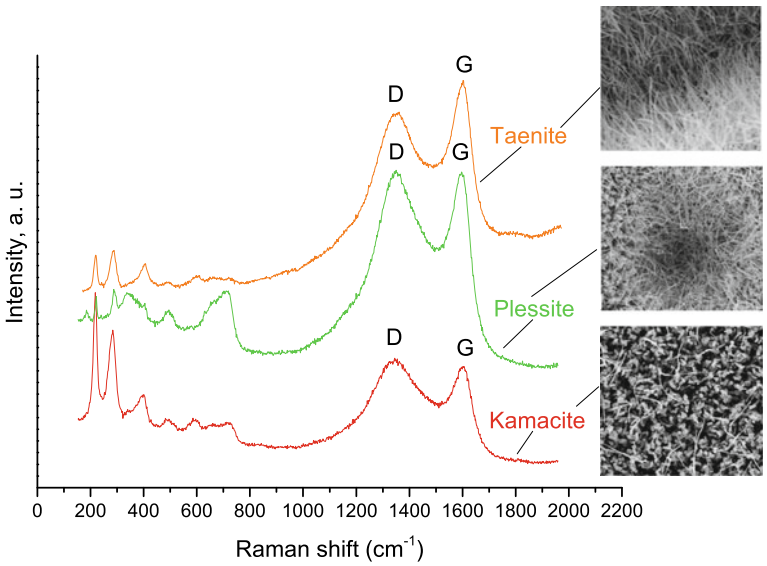

Fig. 9 Raman spectra of Sample 1. The insert shows the SEM image of the measured surface

4 Conclusions

In this report, the study of the surface structural composition influence on the CNT synthesis and morphology was presented. The analysis using SEM and Raman spectroscopy showed that:

- Carbon nanotubes and nanorods of iron oxides were synthesized on the whole surface of Sample 1. It was defined using SEM and confirmed by Raman spectroscopy.
- The oxidation process also occurred during CNT synthesis. It was confirmed by the experiment of thermal oxidation. Fe_2O_3 nanorods with an average diameter of 30 nm covered the surface of Sample 2 after the experiment.
- Etching increased an active surface area, so we obtained more CNTs.
- After the CVD various initial surface structures were covered by different nanomaterials: schreibersite—60 nm oxide crystals, 60 nm width ribbons, CNTs with average diameters of 15 nm. The CNT growth direction was perpendicular to the edges of the schreibersite; taenite formed 50 nm oxide crystals and vertical arrays of CNTs with average diameters of 10 nm. The least disordered CNTs were obtained with $I_G/I_D = 1.08$; plessite formed 50 nm oxide crystals and curved CNTs with average diameters of 15 nm; kamacite—50 nm oxide crystals, curved CNTs with average diameters of 15 nm, the quantity of CNTs was 5 times less than on taenite and plessite.

Acknowledgements The reported study was funded by RFBR, project number 19-32-90243. Raman measurements were carried out as part of the IGG UB RAS state budget theme No. AAAA-A18-118053090045-8.

References

Bokobza L, Zhang J. Raman spectroscopic characterization of multiwall carbon nanotubes and of composites. Express Polym Lett. 2012;7:601-8. https://doi.org/10.3144/expresspolymlett.2012.63.

Buchwald VF. Primary Structures of Iron Meteorites. Handbook of Iron Meteorites. Oakland: The Regents of the University of California; 1975. p. 115-124.

Database of Raman spectroscopy. University of Arizona. 2019. http://rruff.info. Accessed 13 June 2019.

Ding F, Larsson P, Larsson JA, et al. The importance of strong carbon-metal adhesion for catalytic nucleation of single-walled carbon nanotubes. Nano Lett. 2008;8:463-8. https://doi.org/10.1021/nl072431m.

Kumar M, Ando Y. CVD of CNT: A Review on Growth Mechanism and Mass Production. J. Nanosci. Nanotechnol. 2010;10:3739-58. https://doi.org/10.1166/jnn.2010.2939.

López-Lorente AI, Simonet BM, Valcárcel M. Raman spectroscopic characterization of single walled carbon nanotubes: influence of the sample aggregation state. Analyst. 2014;139:290-8. https://doi.org/10.1039/C3AN00642E.

Rümmeli MH, Bachmatiuk A, Börrnert F, et al. Synthesis of carbon nanotubes with and without catalyst particles. Nanoscale Res. Lett. 2011;6:303. https://doi.org/10.1186/1556-276X-6-303.

Vincent T, Gross M, Dotan H, Rothschild A. Thermally oxidized iron oxide nanoarchitectures for hydrogen production by solar-induced water splitting. Int. J. Hydrog. Energy. 2012;37:8102-9. https://doi.org/10.1016/j.ijhydene.2011.08.088.

Yang J, Goldstein JI, Scott ERD. Main-group pallasites: Thermal history, relationship to IIIAB irons, and origin. Geochim. Cosmochim. Acta. 2010;74:4471–92. https://doi.org/10.1016/j.gca.2010.04.016.

Zaine IS, Napiah NAM, Yusof AM, et al. Study on Dispersion and Characterization of Functionalized MWCNTs Prepared by Wet Oxidation. Appl. Mech. Mater. 2014;661:8-13. https://doi.org/10.4028/www.scientific.net/AMM.661.8.

Scandium, Yttrium and Lanthanids in the Beryl of the Sherlovaya Gora Deposit

Alena A. Borzenko and Georgiy A. Yurgenson

Abstract

For the first time, a comparative study of the content of iron, scandium, yttrium and lanthanide impurities was carried out using the example of 58 differently colored beryl crystals of the Sherlovaya Gora deposit in the South-Eastern Transbaikalia. Significant variations in the average values of the contents of scandium, yttrium and iron in the beryl crystals of Sherlovaya Gora have been found. A comparative analysis of the ratios of the content of scandium and iron in the color varieties of beryl has shown an existing tendency towards their positive correlation. Based on this, two groups of crystals, differing in scandium and iron levels, have been found typical for the iron content up to 1200 ppm and scandium to 100 ppm (Group 1: yellow, green-blue and olive-green crystals and only 17% of green ones) and for the iron content up to 700 ppm and scandium from 120 to 240 ppm (Group 2: green (60%) and blue (35%) crystals). A tendency towards higher content of heavy lanthanides in comparison with light ones has been revealed. The exception is lanthanum in green, blue and yellow crystals, the content of which is close to a clarke or higher (up to 48 ppm). For the studied beryl crystals, the europium minimum is not typical. The distribution of yttrium in beryl crystals has not yet been revealed.

Keywords

Beryl · Iron · Scandium · Yttrium · Lanthanides · Isomorphism · Sherlovaya Gora

A. A. Borzenko (✉) · G. A. Yurgenson (✉)
Institute of Natural Resources, Ecology and Cryology SB RAS, 16a Nedorezova Str., Chita 672014, Russia
e-mail: avonanik@mail.ru

G. A. Yurgenson
e-mail: yurgga@mail.ru

S. Votyakov et al. (eds.), *Minerals: Structure, Properties, Methods of Investigation*, Springer Proceedings in Earth and Environmental Sciences,
https://doi.org/10.1007/978-3-030-49468-1_5

1 Introduction

Beryl is an island silicate of beryllium and aluminum, $Be_3Al_2Si_6O_{18}$, a number of varieties of which since ancient times have been used as a noble and expensive gemstone. It is known that Sc^{3+}, Cr^{3+}, Fe^{3+}, Fe^{2+}, Mg, Ca, Mn, Ti^{3+}, V^{3+}, Ga^{3+}, Ge^{4+}, B, P can be present as isomorphic impurities in beryl, as shown in the scheme of isovalent isomorphism of $Sc^{3+}VI \rightarrow Al^{3+}VI$ (Minerals 1981). Moreover, it is known for its blue scandium variety, bazzite (Demartin 2000). It is also assumed that Y and Yb are located in the structural channels (Minerals 1981).

Among the beryl crystals of Sherlovaya Gora, its almost colorless varieties are developed: blue and green-blue of different color intensity (aquamarines), green, yellow-green and typical heliodors of different intensity of yellow and orange color. Transitional to heliodors, olive-green beryls, the nature of the color of which has not been studied at all, are also recognized. Single crystals of green color, corresponding to emeralds of average quality by the content of chromium and vanadium, were found (Yurgenson et al. 2017). Sherlovaya Gora beryl crystals are often heterogeneous. For many of them, a regular change in color in the form of its longitudinal or transverse zonality with respect to the c axis in the crystal, which depends on the distribution of impurities, is characteristic.

Earlier, the authors carried out a comparative study of the content of scandium in variously colored beryl crystals of the Sherlovogorsk ore field. Its connection with the Fe^{3+} content has been established. It has been revealed that the maximum concentrations of scandium are typical for blue beryl crystals (Yurgenson et al. 2017). However, the work was performed on a relatively small number of samples, which required further research. Due to the fact that the content of rare-earth elements in beryl of Sherlovaya Gora has not been studied, this article presents the primary results of the study of their distribution in beryl crystals of various colors.

2 Materials and Methods

Using an ICP MS method, ICM40B, the content of iron, scandium, yttrium and lanthanides in 58 beryl crystals of various colors and their fragments was studied. The analytical sensitivity for rare earth elements was 0.1 ppm. Sherlovaya Gora beryl crystals are often heterogeneous. The zonality, expressed as a change in multi-colored zones, alternating both along the c axis and perpendicular to it, creates a transverse and longitudinal color zonality, which is reflected in changes in the composition of trace elements. The samples were crushed manually in a quartz mortar with a pure rock crystal pestle.

3 Results and Discussion

The results of these studies are presented in Table 1 and Fig. 1.

The table data analysis shows significant variations in average values of the content of scandium, yttrium and iron. This is also evidenced by the standard deviation. In this case, the iron content predominates over that of scandium

Table 1 Statistical characteristics of the content of Sc, Y and Fe in Sherlovaya Gora beryl crystals

Color	n	Element content and its statistical characteristics, ppm					
		Scandium		Yttrium		Iron	
		x	σ	x	σ	x	σ
Colorless	2	82.5	77.5	0.7	0.15	3900	700
Pale blue	8	107.5	57.4	1.7	2.9	4787	1709
Light blue	11	74.2	72.7	7.8	6.3	5609	1117
Bright blue	2	70.0	0	0.5	0	10250	1050
Transitional (greenish-blue)	7	46.6	28.2	3.7	2.1	5986	1561
Pale blue	7	148.6	57.4	1.3	1.9	4671	1077
Green	13	55.3	56.3	5.9	4.1	4454	1196
Yellow	4	41.0	22.3	3.8	2.3	6325	642
Olive	2	115.0	25	0.5	0	8900	1000

Note n—number of samples, x—average content, σ—standard deviation

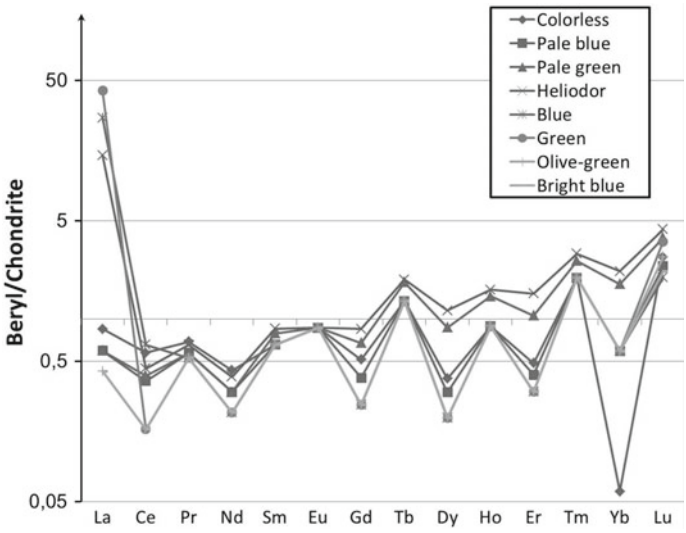

Fig. 1 Distribution of lanthanides in beryl crystals

(31 times for green and 154 times for yellow crystals) and yttrium (from 719 to 20,500 times, regardless of whether the crystals belong to a particular color variety). This means that the contribution of iron to the color is significantly greater in comparison with scandium and, especially, with yttrium.

The distribution of rare-earth elements in beryl crystals of different colors is shown in Fig. 1. The content of lanthanides in the beryl crystals of Sherlovaya Gora is extremely unevenly distributed. In general, there is a certain tendency towards an increase in the content of heavy lanthanides in comparison with light ones, which we previously found for ferberite crystals of this field (Yurgenson et al. 2017). The exception is lanthanum in green, blue and yellow crystals, the content of which is close to a clarke or higher (up to 48 ppm). La, Pr, Nd, Sm, Eu, Gd in all color varieties of beryl have concentrations of less than 1 ppm, and Tb, Tm and Lu in all studied samples are in quantities close to or exceeding their clarks.

The europium minimum is not observed, but instead a minimum for ytterbium in colorless and pale blue crystals is clearly manifested. These initial data on the content of lanthanides in beryl provide the basis for special studies.

A comparative analysis of the ratios of the content of scandium and iron in the color varieties of beryl (Fig. 2) has shown a tendency towards their positive correlation.

However, as can be seen in the same figure, two groups of crystals emerged, differing in the content of scandium and iron. The iron content up to 1200 ppm and scandium up to 100 ppm are typical for the first group, while Fe up to 700 ppm and Sc from 120 to 240 ppm are characteristic of the second group. The first group includes all yellow, green-blue and olive-green crystals and only 17% of green ones, while the second one consists only of green (60%) and blue (35%) crystals.

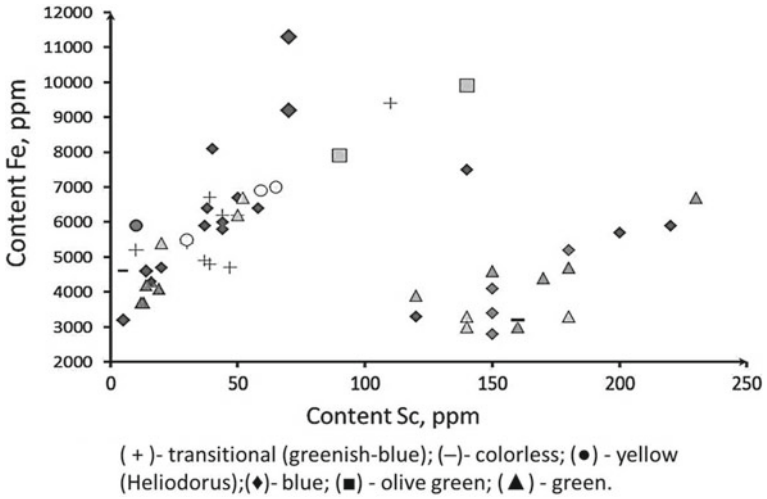

Fig. 2 Two trend ratios of iron and scandium concentrations in beryl crystals of different colors

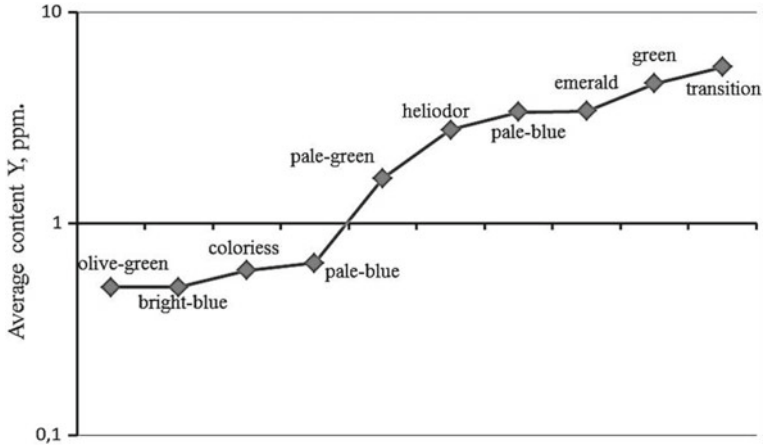

Fig. 3 Variability of yttrium content in variously colored beryl crystals

Only one is colorless. This feature of the distribution of color varieties of beryl crystals over two groups of Sc and Fe correlation has revealed their different role in the formation of beryl crystals of different colors and requires further study.

Figure 3 shows the variability of the content of yttrium in beryl crystals of different colors.

The distribution of yttrium in beryl crystals, as can be seen in Fig. 3, has not yet revealed a connection between its content and beryl crystals of a certain color, and requires further study.

4 Conclusions

1. The limits of variations in the content of scandium in beryl crystals of the Sherlovaya Gora and the direct relationship between the impurities of iron and scandium in them have been found.
2. A tendency towards higher concentrations of heavy lanthanides in beryl crystals has been revealed.
3. For the studied beryl crystals, the europium minimum is not typical.

References

Demartin F, Gramaccioli CM, Pilati T. Structure refinement of bazzite from pegmatitic and miarolitic occurrences. Canadian Mineralogist. 2000;38:1419-1424.

Mineraly. Spravochnik. T. III. – M.: Nauka, 1981. 614 s. [Minerals. Reference book. Vol. III. M.: Nauka, 1981. 614 p. (in Russ.)]

Yurgenson G, Bychkov A, Kononov O & Popova J. REE in wolframites from Sherlova Gora gems mine (Transbaikalia, Russia). Goldschmidt 2017, Paris 13-18 Aug. 2017. Goldschmidt Abstracts. 2017. P. 4443.

Yurgenson GA, Limberova VV, Borzenko AA. Skandii v berille Sherlovogorskogo rudnogo polya v Yugo-Vostochnom Zabaikal'e. Kulaginskie Chteniya: tekhnika i tekhnologiya proizvodstvennykh protsessov. Ch.2. Chita: ZabGU. 2017. S.200– 206 [Yurgenson GA, Limberova VV, Borzenko AA. Scandium in the beryl of Sherlova Mountain ore field in South-Eastern Transbaikalia. Kulaginskie Chteniya: technics and technology of industrial processes. P.2. Chita: ZabGU. 2017. P. 200– 206. (in Russ.)]

A Special Role of Spectrophotometry in the Study of Asteroids and Meteorite Analogs

Vladimir V. Busarev, Andrey M. Sobolev, Victor I. Grohovsky, and Nikolai A. Kruglikov

Abstract

The significance of spectrophotometry among other optical methods for the assessment of chemical and mineral composition of asteroids and other solid celestial bodies is discussed. Laboratory studies of analogs of these bodies, such as meteorites and common minerals, expand the limits of our knowledge of extraterrestrial matter as a whole. However, the modern collections of meteorites are incomplete because of the rigid selection of falling space matter by terrestrial atmosphere. To solve this problem, wider spectral investigations of asteroids, as well as the search and study of new meteorites, including micrometeorites and meteorites after modeling the processes of space weathering, and space dust are necessary. We consider possibilities to move forward in this direction.

Keywords

Asteroids · Spectroscopy · Meteorites · Minerals · Space dust

V. V. Busarev (✉)
Sternberg Astronomical Institute (SAI MSU), Lomonosov Moscow State University, 13 University Ave., 119234 Moscow, Russia
e-mail: busarev@sai.msu.ru

A. M. Sobolev
Institute of Natural Sciences and Mathematics, Ural Federal University, 51 Lenin Ave., 620075 Ekaterinburg, Russia

V. I. Grohovsky · N. A. Kruglikov
Institute of Physics and Technology, Ural Federal University, 19 Mira Str., 620002 Ekaterinburg, Russia

N. A. Kruglikov
Institute of Metal Physics, Ural Branch of Russian Academy of Sciences, 18 S. Kovalevskoy Str., 620108 Ekaterinburg, Russia

S. Votyakov et al. (eds.), *Minerals: Structure, Properties, Methods of Investigation*, Springer Proceedings in Earth and Environmental Sciences,
https://doi.org/10.1007/978-3-030-49468-1_6

1 Introduction

Photometry, spectrophotometry (spectroscopy) and polarimetry are the traditional optical methods of remote sensing of atmosphereless solid celestial bodies (SCBs). However, in case of the presence of some SCB exosphere, the data obtained via these methods are subject to significant distortions. These methods are independent and mutually complementary. Light scattering on surface particles (down to the smallest size) allows not only the shape, structure and porosity of the particles, but also their chemical and mineral composition to be determined. Photometry and polarimetry are most effective in the determination of the SCB structural parameters (from macro to micro scale), but these methods are ambiguous in attempts to find the elemental composition of solid matter. It may be illustrated by an example of such photometric parameter as the geometric albedo (p_v). While p_v characterizes the reflectivity of solid matter and correlates with its melting temperature (a brighter substance, as a rule, has a higher melting point), fresh ices (with the highest p_v values) have the lowest melting point and, conversely, graphite has the highest melting point but minimal p_v values. At the same time, spectrophotometry allows the chemical, mineralogical, and structural properties of the SCB surface to be assessed reliably.

2 Main Results of Spectral Study of Asteroids and Their Analogs

Reflectance spectrophotometry of the lunar surface and some asteroids in the wavelength range of 0.4–1.0 μm along with an extensive laboratory study of their possible analogs in 60's and 70's of the 20th century has clearly shown the method plausibility (e.g., (Adams and McCord 1970; McCord et al. 1970)). Spectral and geochemical studies of meteorites—probable fragments of asteroids—and the most common minerals have shown that the features of their reflectance spectra (RS) in the range of ~200–2500 nm contain direct information about the chemistry and mineralogy of the substance in the form of mineralogical absorption bands (ABs). In particular, it has been found that in the range of 350–1000 nm there are two strongest ABs in the silicate substance: the electron charge-transfer band of oxygen-metal with a minimum in the ultraviolet (UV) range, centered at 200 nm, and pyroxene-olivine with a minimum at ~1000 nm. The more intense UV band depends mainly on the oxidation state of the silicate material, and its long-wave wing determines the slope and shape of the RS of powdered silicates in the entire visible range (Loeffler et al. 1974; Burns 1993). AB at 1000 nm, which originates from spin-allowed electron transitions in Fe^{2+} cations in the crystal field, is a superposition of ABs, characteristic of such common minerals as orthopyroxene (AB centered at 900 nm), clinopyroxene (centered at 1000 nm) and olivine (centered at 1010 nm) (Adams 1975; Platonov 1976; Bakhtin 1985; Khomenko and Platonov 1987). The Fe^{2+} cation (in the $3d^6$ electron configuration) also yields a

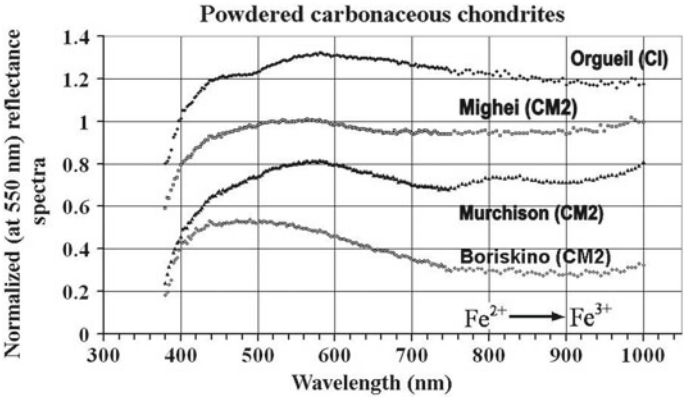

Fig. 1 RS of carbonaceous chondrites

series of weak ABs in crystalline pyroxenes (400–700 nm) and olivines (400–650 nm) (Bakhtin 1985; Khomenko and Platonov 1987), which are important for refining the chemical-mineralogical interpretation of asteroid RS. ABs at 700–900 nm (originated due to $Fe^{2+} \rightarrow Fe^{3+}$ electron charge transfer (Burns 1993; Bakhtin 1985; Burns 1972) and at 440 nm (electronic transitions in Fe^{3+} in the crystal field and/or $Fe^{3+} \rightarrow Fe^{3+}$ electron charge transfer) (Busarevet al. 2008) are characteristic of a hydrated or highly oxidized matter and are observed in RS of carbonaceous chondrites (Fig. 1) and similar hydrated silicates, such as serpentines (Fig. 2) (Dodd 1981; Jarosewich 1990). It makes the spectral shape partially or completely concave in the range of 500–1000 nm (Busarev and Taran 2002). It's interesting that with elevated Fe_2O_3 content (having such AB) in terrestrial pyroxenes and olivines, this band can even mask their diagnostic AB at 1000 nm (Adams 1975).

The strongest of the mentioned spectral features are seen in the averaged reflectance spectra for asteroid taxonomic (systematic) classes of the first spectral classification by Tholen (Fig. 3) (Tholen and Barucci 1989). The classification was performed by the method of "principal components" using the data of the 8-color survey (with 8 light filters distributed in the range of 0.35–1.0 μm) (ECAS) of ~600 asteroids (Zellner et al. 1985), which allowed 14 asteroid spectral types to be distinguished (Tholen and Barucci 1989). The information about p_v of the asteroids was required only to differentiate 3 of those classes (E, M and P) with very similar RS. By that time, there were already several other classifications of asteroids via different sets of parameters (*U-B*, *B-V*, *V-R*, p_v, linear polarization, etc.), by which it was possible to identify only a few taxonomic classes of asteroids and, furthermore, without a clear understanding of their physical meaning. Tholen's spectral classification of asteroids (Tholen 1984) and mineralogical interpretation of the spectral classes using the characteristics of meteorites and common minerals (Tholen 1984; Gaffey et al. 1989) has given such understanding. It is important to

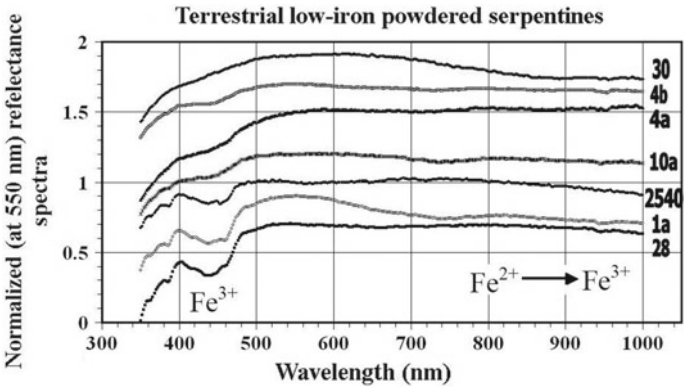

Fig. 2 RS of serpentines

note that two of the principal classification components turned out to be corresponding to the colors characterizing the shape of wings (and intensity) of the strongest ABs at 0.2 and 1.0 μm in reflectance spectra of silicate matter. Another considerable achievement was the division of all asteroids into two large groups according to Tholen's spectral classes: with predominantly low-temperature mineralogy (the left part of Fig. 3 excluding M and E classes) and with high-temperature mineralogy (the right part of Fig. 3). The gray background in Fig. 3 shows the reflectance spectra of primitive type asteroids with close low-temperature mineralogy (Gaffey et al. 1989).

Moreover, the calculation of heliocentric asteroid distributions of each of the Tholen's classes made it possible to assess the temperature and other physicochemical parameters of their parent bodies formation in the early Solar system (Bell et al. 1989) (Fig. 4 demonstrates the number of asteroids of certain types versus semi-major axis of asteroid orbit in Astronomical Units). The heliocentric distributions of asteroids of different spectral classes in the main asteroid belt clearly demonstrate that the objects with high-temperature mineralogy shift to the center and those with low-temperature mineralogy shift from the center of Solar system. Such a specific structure of the main asteroid belt made it one of the principal criteria for checking the validity of any modern cosmogonic models.

The principal component analysis was also used in the following spectral classifications of asteroids by Bus and Binzel (2002) (through the data of CCD-based spectroscopic survey in nearly the same wavelength range for ~1500 asteroids) and by DeMeo et al. (2009) (who applied the same visible-range data for asteroids (Bus and Binzel 2002) and near infra-red (IR) data up to 2.5 μm for a considerable part of the bodies). Despite these advantages of the last classification (2009), a relatively little progress has been achieved in refining chemical-mineralogical interpretation of taxonomic classes, taking into account weaker absorption bands in the asteroid reflectance spectra and the subsequent introduction of additional spectral subclasses.

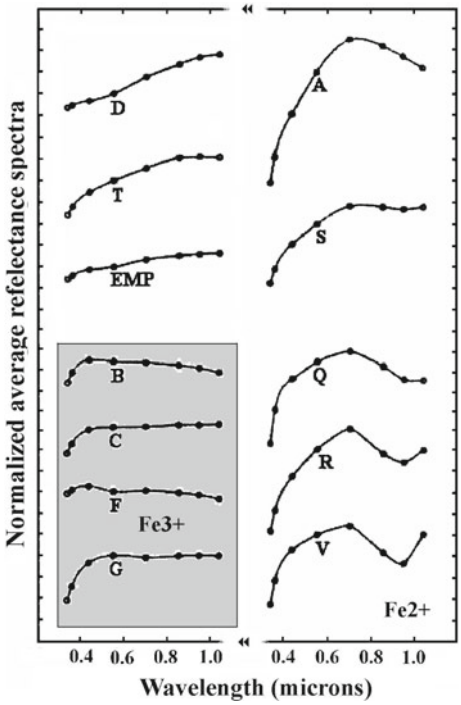

Fig. 3 Averaged RS of different asteroid spectral types by Tholen and Barucci (1989)

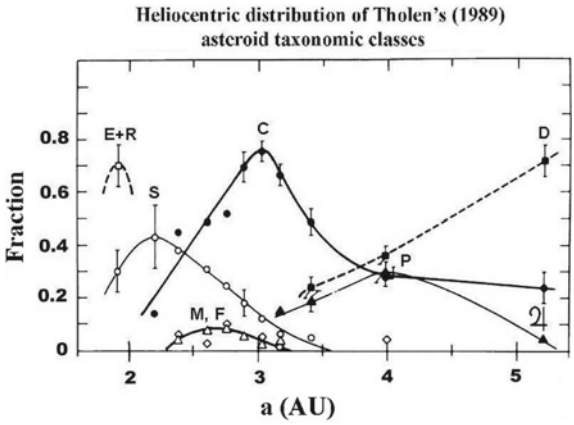

Fig. 4 Heliocentric distributions of Tholen's asteroid spectral types (Bell et al. 1989). Parameter "a" is semi-major axis of asteroid orbit in AU

Attention should be drawn to some important issues, which, apparently, in some conditions, cast doubt on the reliability of the obtained spectrophotometric data on asteroids. These are the main factors affecting the shape of RS of powdered samples, namely, the size of particles, different phase angles (at the same particle sizes), sample temperature, and the influence of irradiation simulating the "maturation" of silicate matter in space conditions. These effects were demonstrated in laboratory conditions on reflectance spectra of meteorite samples (Figs. 5, 6, 7 and 8).

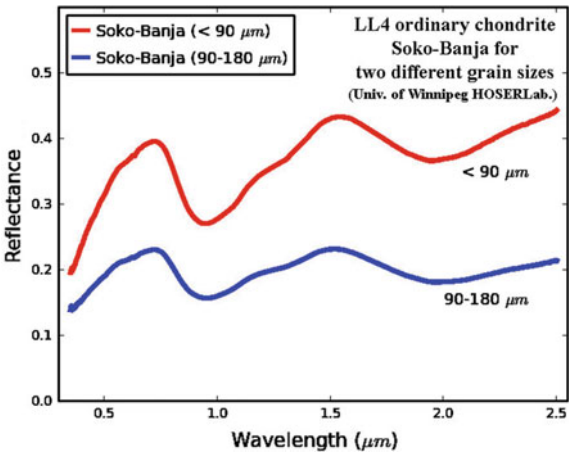

Fig. 5 RS of two LL4 samples of various sizes (Reddy et al. 2016)

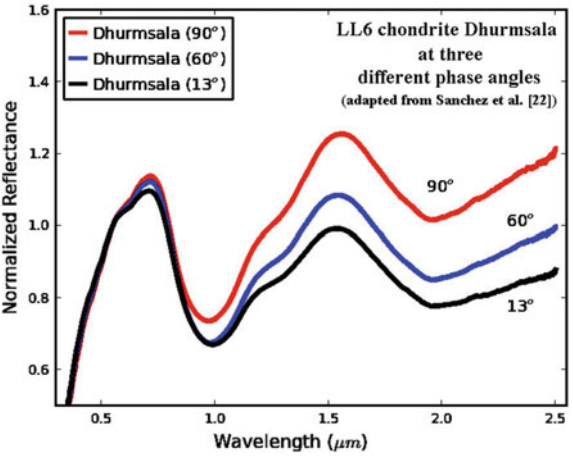

Fig. 6 RS of three LL6 samples at various phase angles (Sanchez et al. 2012)

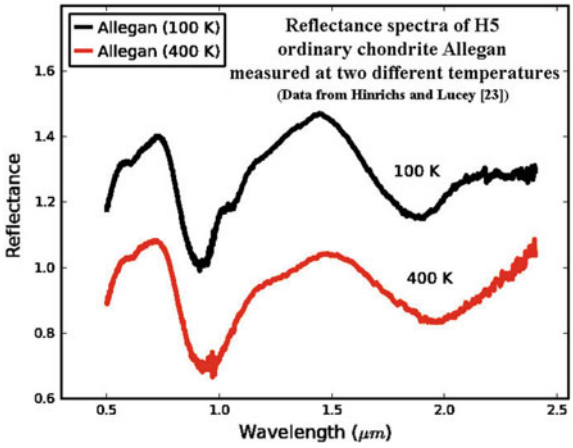

Fig. 7 RS of two H5 samples at 100 and 400 K (Hinrichs and Lucey 2002)

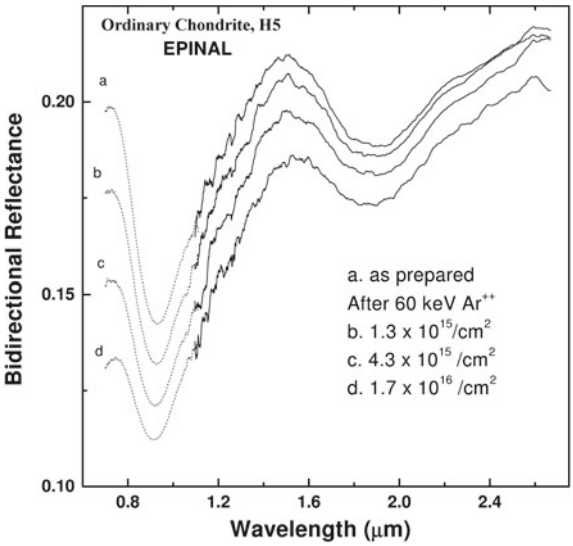

Fig. 8 RS of four H5 samples irradiated by Ar^{++} (Strazzulla et al. 2006)

From these results it follows that changes in the RS shape of ordinary chondrites do not exceed ~30% (Figs. 5 and 6) (Reddy et al. 2016; Sanchez et al. 2012) for a typical size range of the smallest particles on asteroid surface and for usual phase angle variations during asteroid spectral observations (predominately within $\sim 5 \div 30°$). Spectral changes caused by the irradiation of ordinary chondrites by particle fluxes, simulating space weathering (predominantly by solar wind) at time-scales of the order of 10^5 years at a distance of about 1 AU from the Sun (Fig. 8) (Strazzulla et al. 2006) are even less. Pulse-laser treatment simulating the action of the micrometeorite flux usually leads to relatively small spectral changes of powdered olivine and pyroxene samples (Yamada et al. 1999), but the spectral changes are considerably greater for carbonaceous chondrites, especially in the case of sample desiccation and disappearance of characteristic phyllosilicate ABs (e.g. Thompson et al. 2019).

Thus, from the mentioned results it follows that the described spectral changes induced by variations of particle sizes, phase angles and weathering conditions do not shift the wavelength position of characteristic ABs of silicate matter and, consequently, do not prevent its identification (with this or that degree of accuracy). However, a definitely negative factor for the spectrophotometric study of asteroids is the temperature growth, which increases the vibrations of atoms and molecules of the solid matter and causes AB shifts in the infrared range (Fig. 7) (Hinrichs and Lucey 2002). It indicates, apparently, an undesirable extension of the present asteroid spectral classification to IR.

3 Conclusion and Plans for the Future

Generally, there are two considerable challenges in the investigations of asteroids. First, a very small number of known bodies (about several thousand out of ~ 894 thousand only in the main-belt (IAU Minor Planet International Centre 2019)) has been covered by spectrophotometric measurements allowing their spectral classes and chemical-mineral composition to be estimated. Second, there is a considerable incompleteness of our knowledge of the diversity of solid matter in the Solar system and beyond. A high selectivity (ablation) of terrestrial atmosphere in respect to falling meteorite matter at space velocities (>11 $km \cdot s^{-1}$) is a reason of the paucity of meteorite collections. However, micron-sized porous cosmic dust is not subjected to ablation while passing through the Earth's atmosphere and reaches the Earth's surface quite smoothly preserving its original composition (e.g. Basiuk et al. 1999; Plane 2012). The study of such and similar particles show that the diversity of their compositions is about three times greater than that of meteoritic analogs of asteroids (Bradley 2003; Vernazza et al. 2015).

To solve this problem, wider spectrophotometric investigations of asteroids as well as the search and more thorough analysis (via spectral, electron-probe, Mössbauer, X-ray phase and other methods) of new meteorites, including micrometeorites, and space dust are necessary. We are considering the possibility of combining our technical and other capabilities in the future study of extraterrestrial matter.

References

Adams JB. Interpretation of visible and near-infrared diffuse reflectance spectra of pyroxenes and other rock-forming minerals. In: Karr C, editor. Infrared and Raman spectroscopy of lunar and terrestrial minerals. New York: Academic Press; 1975. pp. 91–116.

Adams JB, McCord TB. Remote sensing of lunar surface mineralogy: Implications from visible and near-infrared reflectivity of Apollo 11 samples. Proceedings of "Apollo 11 Lunar Science Conference". 1970;3:1937–1945.

Basiuk VA, Douda J, Navarro-Gonzalez R. Transport of extraterrestrial biomolecules to the earth: Problem of thermal stability. Adv. Space Res. 1999;24:505–514.

Bell JF, Davis DR, Hartmann WK, Gaffey MJ. Asteroids: The big picture. In: Binzel RP, Gehrels T, Mattews MS, editors. Asteroids II. Tucson: Univ. of Arizona Press; 1989, pp. 921–945.

Burns RG, Huggins FE, Abu-Eid RM. Polarized Absorption Spectra of Single Crystals of Lunar Pyroxenes and Olivines. Moon, 1972;4:93–102.

Burns RG. Mineralogical applications of crystal field theory. New York: Cambridge Univ. Press, 1993.

Bus SJ, Binzel RP. Phase II of the Small Main-Belt Asteroid Spectroscopic Survey. A Feature-Based Taxonomy. Icarus, 2002;158:146–177.

Busarev VV, Barabanov SI, Rusakov VS, Puzin VB, Kravtsov VV. Spectrophotometry of (32) Pomona, (145) Adeona, (704) Interamnia, (779) Nina, (330825) 2008 XE3, and 2012 QG42 and laboratory study of possible analog samples. Icarus, 2015;262:44–57.

Busarev VV, Taran MN. On the spectral similarity of carbonaceous chondrites and some hydrated and oxidized asteroids. Proc. of "Asteroids, Comets, Meteors 2002", Berlin: ESA-SP-500. 2002, pp. 933–936.

DeMeo FE, Binzel RP, Slivan SM, Bus SJ. An extension of the Bus asteroid taxonomy into the near-infrared. Icarus, 2009;202:160–180.

Dodd RT. Meteorites - A petrologic-chemical synthesis. Cambridge: Cambridge Univ. Press, 1981.

Bradley JP. Interplanetary Dust Particles. In: Davis AM, editor. Treatise on Geochemistry. Elsevier; 2003. V.1, pp. 689–711.

Gaffey MJ, Bell JF, Cruikshank DP. Reflectance spectroscopy and asteroid surface mineralogy. In: Binzel RP, Gehrels T, Mattews MS, editors. Asteroids II. Tucson: Univ. of Arizona Press; 1989, pp. 98–127.

Hinrichs JL, Lucey PG. Temperature-dependent near-infrared spectral properties of minerals, meteorites, and lunar soil. Icarus. 2002;155:169–180.

IAU Minor Planet International Centre: https://minorplanetcenter.net/mpc/summary. Accessed 08 Jun 2019.

Jarosewich E. Chemical analyses of meteorites: A compilation of stony and iron meteorite analyses. Meteoritics, 1990;25:323–337.

Khomenko VM, Platonov AN. Porodoobrazuyushchie pirokseny: opticheskie spektry, okraska i pleokhroizm. Kiev: Naukova dumka, 1987. [Khomenko VM, Platonov AN. Rock-forming pyroxenes: Optical spectra, color and pleochroism. Kiev: Naukova Dumka, 1987 (In Russ.)].

Loeffler BM, Burns RG, Tossel JA et al. Charge transfer in lunar materials: Interpretation of ultraviolet-visible spectral properties of the moon. Proc. of the Fifth Lunar Conf. (Supplement 4. Geochimica et Cosmochimica Acta). 1974;3:3007–3016.

McCord TB, Adams JB, Johnson TV. Asteroid Vesta: Spectral reflectivity and compositional implications. Science. 1970;168:1445–1447.

Plane JMC. Cosmic dust in the earth's atmosphere. Chem. Soc. Rev. 2012;41:6507–6518.

Platonov AN. Priroda okraski mineralov. Kiev: Naukova dumka, 1976. [Platonov AN. The nature of minerals' coloring. Kiev: Naukova dumka, 1976 (In Russ.)].

Bakhtin AI. Porodoobrazuyushchie silikaty: opticheskie spektry, kristallokhimiya, zakonomernosti okraski, tipomorfizm. Kazan': Izdat. Kazanskogo un-ta, 1985. [Bakhtin AI. Rock-forming silicates: Optical spectra, crystal chemistry, color regularities, typomorphism. Kazan: Izdat. Kazan. University, 1985 (In Russ.)].

Reddy V, Sachez JA, Thirouin A. et al. Challenges in Physical Characterization of Dim Space Objects: What can we learn from NEOs. Proc. of Advanced Maui Optical and Space Surveillance Technologies Conference (AMOS). http://amostech.com/TechnicalPapers/2016/Poster/Reddy.pdf. Accessed 07 Jun 2019.

Sanchez JA, Reddy V, Nathues A, Cloutis EA, Mann P, Hiesinger H. Phase reddening on near-Earth asteroids: Implications for mineralogical analysis, space weathering and taxonomic classification. Icarus. 2012;220:36–50.

Strazzulla G, Brunetto R, Gomis O, Leto G, Orofino V. Ion irradiation of solids of planetological interest. Mem. S.A.It. Suppl. 2006;9:157–160.

Tholen DJ. Asteroid taxonomy: From cluster analysis to photometry. PhD. thesis. Tucson: University of Arizona, 1984.

Tholen DJ., Barucci MA. Asteroid taxonomy. In: Binzel RP, Gehrels T, Mattews MS, editors. Asteroids II. Tucson: Univ. of Arizona Press; 1989, pp. 298–315.

Thompson MS, Loeffler MJ, Morris RV, Keller LP, Christoffersen R. Spectral and chemical effects of simulated space weathering of the Murchison CM2 carbonaceous chondrite. Icarus. 2019;319:499–511.

Vernazza P, Marsset M, Beck P. et al. Interplanetary dust particles as samples of icy asteroids. Astrophys. J. 2015;806:204–213.

Yamada M, Sasaki S, Nagahara H. et al. Simulation of space weathering of planet-forming materials: Nanosecond pulse laser irradiation and proton implantation on olivine and pyroxene samples. Earth Planet. Space. 1999;51:1255–1265.

Zellner B, Tholen DJ, Tedesco EF. The eight-color asteroid survey: Results for 589 minor planets. Icarus. 1985;61:355–416.

Apatite Saturation Thermometry of the Kozhim Granite Massif (the Subpolar Urals)

Yulia V. Denisova

Abstract

Saturation thermometry based on the rock level of the substance organization occupies a special place among the variety of existing methods for determining temperature. This method allows the individual accessory minerals to be used as natural geothermometers. When studying the rocks of the Kozhim massif, M. Fishman and his colleagues found that the temperature of rock formation did not exceed 720 °C. In the present work, apatite saturation thermometry was used to confirm the temperature regime of the rocks under consideration. Using Watson and Bea formulas, the saturation temperatures for apatite and apatite-containing rocks were estimated from 722 to 856° C. The obtained temperature range was similar to the temperatures obtained earlier by the author using evolutionary crystal morphological analysis for the zircon of the studied massif.

Keywords

Apatite · Granite · The Kozhim massif · The Subpolar Urals · Watson · Bea

1 Introduction

Currently, many different geothermometers are used to determine the temperature of rock formation, such as isotopic geothermometers (oxygen geothermometer, argon geothermometer, etc.), mineral equilibrium geothermometers (Barth-Ryabchikov

Y. V. Denisova (✉)
Institute of Geology of the Komi Science Centre of the Ural Branch of the Russian Academy of Sciences, 54 Pervomayskaya str., Syktyvkar 167000, Russia
e-mail: yulden777@yandex.ru

S. Votyakov et al. (eds.), *Minerals: Structure, Properties, Methods of Investigation*,
Springer Proceedings in Earth and Environmental Sciences,
https://doi.org/10.1007/978-3-030-49468-1_7

two-feldspar geothermometer, Kudo-Weil geothermometer, Oftedal biotite geothermometer, Buddington-Linsley-Tugarinov magnetite geothermometer, Harker-Tuttle-Graf-Goldsmith calcite geothermometer, Perchuk garnet-biotite geothermometer, Arnold pyrrhotite geothermometer, Kullerud sphalerite geothermometer, etc.), saturation geothermometers (Watson geothermometer, Montel geothermometer), crystal-morphology thermometer (Pupin thermometer), etc. Some of the above methods allow the accessory minerals (zircon, apatite, garnet, monazite) to be used as geothermometers providing a more comprehensive approach to the study of rock features (Denisova 2018).

The aim of the work is to determine the temperature of the Kozhim granite formation by means of apatite saturation thermometry.

The Kozhim massif is exposed in the limb part of the Lyapin anticlinorium (the Subpolar Urals) and is located in the basins of Ponyu, Oseyu and Epkoshor streams. It is the group of elongated granitic bodies related to one interstratal intrusion breaking through the sediments of Middle Riphean Puyva suite. Kozhim granites are highly cataclized (Mahlaev 1996; Pystin et al. 2008). The rocks of this massif, which have the greatest degree of preservation of the primary structure and appearance, are represented by dense gneiss-like medium-grained rocks of pink color with a greenish-gray tint. The mineral composition of granites is represented by potassium-sodium feldspar, plagioclase, quartz, biotite, and muscovite. Zircon, apatite, allanite, titanite, fluorite, garnet, monazite, etc. are found among the accessory minerals of the rocks of the Kozhim massif (Fishman et al. 1968). Accessory apatite in the Kozhim granites is found as light yellow and semi-transparent crystals of hexagonal dipyramidal-prismatic habit. The grain size is 0.10–0.4 mm with an elongation factor of 1.5–3.5 (Fig. 1).

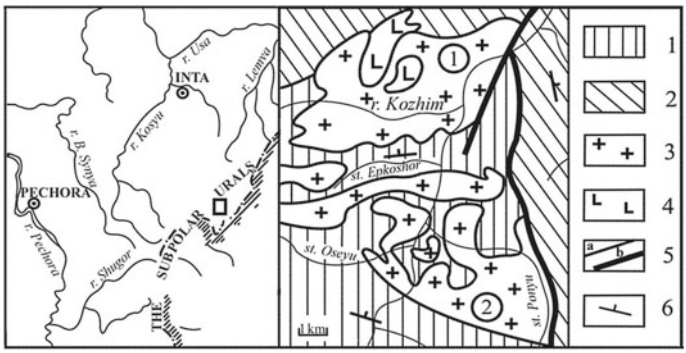

Fig. 1 The Kozhim granite massif. 1—mica-quartz shales, green orthoshales, quartzite; 2—mica-quartz shales, porphyries, porphyrites, the interlayers of marbles and quartzites; 3—granites; 4—gabbro; 5—the geological boundaries: a—stratigraphic and igneous, b—tectonic; 6—dip and strike of planar surfaces. Massifs (numerals in circles): 1—the Kuzpuayu massif; 2—the Kozhim massif

2 Methods

Saturation thermometry was used to calculate the Kozhim granite formation temperatures. The method allows the temperature for apatite and apatite-containing rock to be obtained based on the degree of phosphorus accumulation.

Watson and Harrison (1984) found the relation between the temperature of apatite and apatite-containing rock formation, the saturation level of phosphorus in the rock (required amount for the apatite formation), silicon content and temperature for metaluminous rocks (A/CNK < 1):

$$\mathrm{InD_P} = \frac{8400 + 26400 * (\mathrm{SiO_2} - \frac{1}{2})}{T^K} - 3.1 - 12.4 * (\mathrm{SiO_2} - \frac{1}{2}),$$

$$\mathrm{P_2O_5(HW)} = \frac{42}{D_p},$$

$$\mathrm{T^C} = \frac{8400 + 26400 * (\mathrm{SiO_2} - \frac{1}{2})}{\mathrm{In}(\frac{42}{P_2O_5}) + 3.1 + 12.4 * (\mathrm{SiO_2} - \frac{1}{2})} - 273.15.$$

where $\mathrm{D_P}$ is the ratio of phosphorus concentrations in apatite and the melt, $\mathrm{P_2O_5}$; $\mathrm{SiO_2}$ is the weight fraction of phosphorus oxide and silicon in the melt, wt%,

$\mathrm{T^K}$ is temperature, Kelvin,
$\mathrm{T^C}$ is temperature, Celsius

Bea et al. (1992) with colleagues contributed to the E. Watson and T. Harrison formula refinement in terms of the content of phosphorus oxide for peraluminous rocks (A/CNK > 1).

$$\mathrm{P_2O_5(Bea)} = \mathrm{P_2O_5(HW)} * e^{\frac{6429*(\mathrm{A/CNK})}{T^C - 273.15}};$$

where $A/CNK = \frac{\mathrm{Al_2O_3}}{\mathrm{CaO} + \mathrm{Na_2}O + K_2O}$

Based on the Bea's correction, the calculation formula has acquired the following form:

$$\mathrm{T^C} = \frac{8400 + 26400 * (\mathrm{SiO_2} - \frac{1}{2})}{\mathrm{In}(\frac{42}{P_2O_5}) * e^{\frac{6429*(\mathrm{A/CNK})}{T^C - 273.5}} + 3,1 + 12.4 * (\mathrm{SiO_2} - \frac{1}{2})} - 273.15.$$

Table 1 Chemical composition and formation temperatures of the Kozhim massif rock

Component, wt%	Sample									
	K-1	K-2	K-3	K-4	K-5	K-6	K-7	K-8	K-9	K-10
SiO_2	77.78	76.89	75.95	75.89	76.49	78.12	77.54	76.26	77.48	76.95
TiO_2	0.16	0.22	0.48	0.52	0.48	0.11	0.24	0.42	0.31	0.59
Al_2O_3	11.88	11.95	12.69	12.52	10.05	11.34	11.78	12.22	11.09	10.92
FeO	1.72	1.29	1.15	1.24	0.56	0.50	0.59	0.62	0.61	1.03
Fe_2O_3	0.84	1.12	0.52	1.05	0.92	1.21	0.87	1.02	0.89	0.56
MnO	0.02	0.00	0.00	0.01	0.02	0.01	0.02	0.04	0.03	0.03
MgO	0.16	0.25	0.17	0.33	0.38	0.39	0.18	0.29	0.19	0.18
CaO	0.31	0.29	0.22	0.38	0.59	0.28	0.45	0.42	0.37	0.51
Na_2O	3.65	3.33	4.22	4.02	3.08	3.15	3.22	4.51	3.01	3.89
K_2O	3.88	4.51	4.09	3.89	4.15	5.17	4.99	3.78	4.65	3.28
P_2O_5	0.01	0.03	0.02	0.02	0.03	0.02	0.01	0.01	0.03	0.02
LOI	0.05	0.29	0.59	0.15	0.75	0.62	0.39	0.98	1.02	1.23
$\sum$	100.46	100.17	100.10	100.02	97.50	100.92	100.28	100.57	99.68	99.19
H_2O^-	0.07	0.09	0.10	0.11	0.12	0.13	0.09	0.02	0.05	0.06
A/CNK	1.103	1.098	1.078	1.087	0.945	1.005	1.023	0.996	1.041	1.004
T, °C	722	798	770	764	856	836	768	770	840	826

Note Major element oxide concentrations were obtained in "Nauka" Center for Collective Use of the Institute of Geology of Komi SC UB RAS (Syktyvkar)

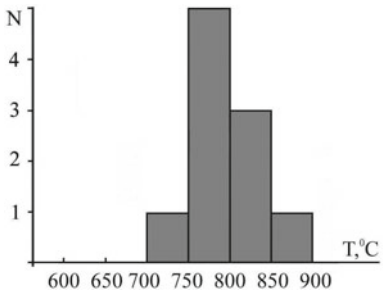

Fig. 2 Histogram of crystallization temperature distribution for apatite and apatite-containing rock

3 Results and Discussion

The temperatures of apatite and apatite-containing rock formation were determined on the basis of chemical composition of the Kozhim massif granites (Table 1).

According to the calculations, the temperature of the Kozhim granites formation is in the range from 722 to 856 °C and on average amounts to 795 °C. According to the Fishman's mineral extraction sequence for the Kozhim complex rocks, apatite crystallization began at the early stages of granitogenesis and continued until the final stage of the granite formation. Moreover, the most intense apatite crystallization occurs after the release of the feldspar bulk and simultaneously with the biotite formation. According to the temperature distribution histogram (Fig. 2), the largest amount of apatite was formed at temperatures from 750 to 800 °C. This suggests that the temperature of biotite crystallization from the Kozhim granites was also within these limits. The subject of further research on the features of the Kozhim massif granites is to verify this assumption using the Oftedal biotite and Perchuk garnet-biotite geothermometers.

4 Conclusions

The study of accessory apatite from the rocks of the Kozhim massif using Watson and Bea saturation thermometry allowed us to determine that the studied granites were high-temperature formations, formed at temperatures from 722 to 856 °C. This confirmed the author's earlier conclusions made on the basis of the morphological study of the Kozhim zircon using the analysis by J. Pupin and G. Turco: the formation of Kozhim massif occurred at a temperature of 700 to 900 °C (Denisova 2014, 2016). But at the same time, it contradicts the data of M.V. Fishman and his colleagues, who argued that the granites of the Kozhim massif were lower temperature rocks with a formation temperature not exceeding 720 °C.

Acknowledgements The work was supported by the RAS Program of fundamental research No. 18-5-5-19.

References

Bea F, Fershtater GB, Corretgé LG. The geochemistry of phosphorus in granite rocks and the effects of aluminium. Lithos.1992; 48:43-56

Denisova JuV. Apatit Nikolajshorskogo granitnogo massiva (Pripoljarnyj Ural). Vestnik Instituta geologii Komi NC UrO RAN, Syktyvkar;2018;9:24-29. [Denisova JuV. The apatite of the Nikolaishor granite massif (the Subpolar Urals). Vestnik IG Komi SC UB RAS, Syktyvkar;2018;9:24-29. (In Russ.)]

Denisova JuV. Termometrija cirkona iz granitoidov Pripoljarnogo Urala. Vestnik Instituta geologii Komi NC UrO RAN, Syktyvkar; 2016;11:11-22. [Denisova JuV. Thermometry of zircon from the granitoids of the Subpolar Urals. Vestnik IG Komi SC UB RAS, Syktyvkar;2016;11:11-22. (In Russ.)]

Denisova JuV. Tipomorficheskie i tipohimicheskie osobennosti akcessornyh cirkonov granitoidov pripoljarnogo Urala. Vestnik Instituta geologii Komi NC UrO RAN, Syktyvkar;2014;5:9-16. [Denisova JuV. Typomorphic and typochemical accessory zircon features of the Subpolar Urals granitoids. Vestnik IG Komi SC UB RAS, Syktyvkar;2014;5:9-16. (In Russ.)]

Harrison TM., and Watson EB. The behavior of apatite during crustal anatexis: Equilibrium and kinetic considerations. Geochim. Cosmochim. Acta. 1984;48:1467-1477

Mahlaev LV. Granitoidy severa Central'no- Ural'skogo podnjatija (Poljarnyj i Pripoljarnyj Ural). Ekaterinburg: UrO RAN;1996. [Mahlaev LV. Granitoids of the North of the Central Ural uplift (the Polar and the Subpolar Urals). Ekaterinburg: UrO RAN;1996. (In Russ.)]

Pystin AM., Pystina JuI. Metamorfizm i granitoobrazovanie v proterozojsko-rannepaleozojskoj istorii formirovanija Pripoljarnoural'skogo segmenta zemnoj kory. Litosfera. 2008;11:25-38. [Pystin AM., Pystina JuI. Metamorphism and granite formation in the Proterozoic - Early Paleozoic history of the formation of the Subpolar-Urals segment of the earth's crust. Litosfera. 2008;11:25-38. (In Russ.)]

Fishman MV, Yushkin NP, Goldin BA, Kalinin EP. Mineralogija, tipomorfizm i genezis akcessornyh mineralov izverzhennyh porod severa Urala i Timana. M.- L: Nauka;1968. [Fishman MV, Yushkin NP, Goldin BA, Kalinin EP. Mineralogy, typomorphism and genesis of accessory minerals of igneous rocks of the North Urals and Timan. M.- L.: Nauka;1968. (In Russ.)]

The Nature of the Enstatite Rim in Refractory Forsterite-Rich Inclusions: An EBSD Study

Kseniya A. Dugushkina, Stepan V. Berzin, and Dmitry A. Zamyatin

Abstract

Refractory forsterite-rich inclusions are a common component for different classes of chondrites. They belong to one of the first mineral formations of the solar system. Forsterite is characterized by low ferruginosity (Fa 0.2–2.0), enrichment with refractory lithophilic elements (RLE), in particular CaO 0.5–1.0%, Al_2O_3 up to 0.3%, and at the same time a sharp deficit of MnO. In some refractory forsterite-rich inclusions, a rim is observed consisting of enstatite with a thickness of 5–200 μm. The composition of the enstatite is SiO_2 (58.545 wt%), TiO_2 (0.24 wt%), Al_2O_3 (1.04 wt%), Cr_2O_3 (0.55 wt%), FeO (1.06 wt%), MgO (37.95 wt%), and CaO (0.5 wt%). The article presents the first results of studying enstatite rims of the refractory forsterite-rich inclusions from the Northwest Africa 11781 carbonaceous chondrite using electron backscatter diffraction (EBSD). As a result of the mapping, it has been established that each of the two grains of refractory forsterite is overgrown with a whole individual enstatite grain. The curvature of enstatite individuals and their disorientation up to 40º is observed along the rim.

Keywords

Carbonaceous chondrite · Refractory inclusions · Forsterite · Enstatite · EBSD

K. A. Dugushkina (✉) · S. V. Berzin · D. A. Zamyatin
A.N. Zavaritsky Institute of Geology and Geochemistry UB RAS, 15 Akademika Vonsovskogo str., 620016 Ekaterinburg, Russia
e-mail: dugushkina.kseniya@mail.ru

S. Votyakov et al. (eds.), *Minerals: Structure, Properties, Methods of Investigation*,
Springer Proceedings in Earth and Environmental Sciences,
https://doi.org/10.1007/978-3-030-49468-1_8

1 Introduction

Refractory forsterite-rich inclusions are found in non-equilibrium carbonaceous (Reid et al. 1970; Fuchs et al. 1973; Steele 1989), ordinary (Steele 1986), and R-chondrites (Pack et al. 2004). These inclusions are present both inside chondrules and in the form of isolated grains 5–500 μ in size in the chondrite matrix. The forsterite is characterized by low ferruginosity (Fa 0.2–2.0), enrichment with refractory lithophilic elements (RLE), in particular CaO 0.5–1.0%, Al_2O_3 up to 0.3%, and at the same time a sharp deficit of MnO. Refractory forsterite-rich inclusions are a common component of different classes of chondrites. According to generally accepted concepts, forsterite-rich inclusions are among the first mineral formations of the Solar System, along with calcium- and aluminum-rich inclusions (CAIs) and amoeboid olivine aggregates (AOAs). At the same time, forsterite-rich inclusions, unlike other refractory inclusions (CAIs and AOAs), are the least studied. According to the most common concepts, the formation of forsterite-rich inclusions occurred by direct condensation from a nebular gas (Steele 1986; Olsen and Grossman 1978), or by crystallization in RLE enriched droplets (protochondrules, initial generation chondrules) with further destruction of the latter and release of refractory forsterite (Pack et al. 2004; McSween 1977; Roedder 1981; Pack et al. 2005). After that, the grains of refractory forsterite appeared in the later formed chondrules and in the matrix of chondrites.

In some refractory forsterite-rich inclusions, a rim is observed consisting of enstatite with a thickness of 5–200 μm. In the literature, it is traditionally referred to as reactionary, although it has not been specifically studied. Theoretically, there are two possible ways of its formation: the overgrowing of forsterite with newly formed enstatite or the replacement of forsterite with enstatite along the perimeter. In the first case, on the surface of the original forsterite grains, obviously, there should be a zone of geometric selection of enstatite individuals, directed towards the outer border. In the second case, the border will be folded by one or more enstatite individuals, and if there is a geometric selection, it will be directed towards the center of the forsterite grain.

The aim of the work is to establish the nature of this enstatite rim. It seems that the orientation study of forsterite crystal lattice and enstatite rims with high spatial resolution, as well as their mutual orientation, will provide the information on postcrystallization effects on forsterite and establish the genesis of enstatite rims.

2 Materials and Methods

An orientation study of the crystal lattices was carried out by electron backscatter diffraction (EBSD) using a JEOL JSM-6390LV scanning electron microscope with an INCA Energy 450 X-Max80 energy dispersive spectrometer and NordlysNano Oxford Instruments EBSD system in “Geoanalytic” Common Use Center, IGG UB RAS, Ekaterinburg. The analysis of the mineral phase composition across the

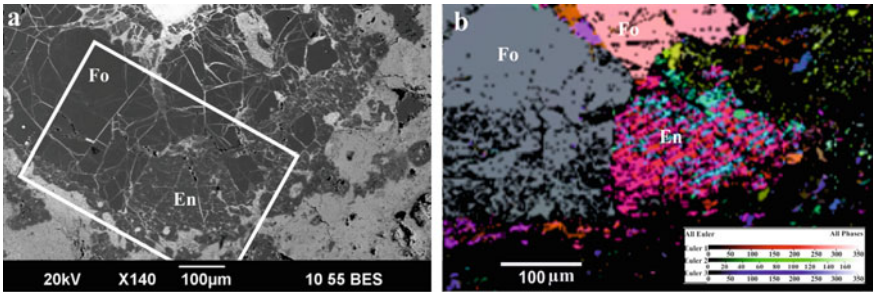

Fig. 1 Refractory forsterite-rich inclusion in Northwest Africa 11781 meteorite: **a**—back-scattered electron (BSE) image; **b**—EBSD map of mineral orientation in Euler colors

selected area was performed on elemental maps using the Aztec v3.1 software. The recording of orientation maps was made at the sample angle of 70° towards the electron beam. The processing and construction of orientation maps was performed using the CHENNEL5 software.

A large forsterite-rich inclusion of 1 mm in the NWA 11781 (CM2) meteorite was chosen for the study (Dugushkina 2018) (Fig. 1, a). Its central part was composed of several intergrown individuals of forsterite having a pronounced enstatite rim on their peripheral. The area was selected for EBSD mapping on the border of the intergrowth of two forsterite grains, surrounded by an enstatite rim.

3 Results and Discussion

As a result of mapping, it has been found that each of the two grains of refractory forsterite grains is overgrown by a whole individual enstatite grain (Fig. 1b). Forsterite is observed in the block structure and the curves of the individuals (Fig. 2b). The curvature of enstatite individuals and their disorientation up to 40º is observed along the rim. In our opinion, this indicates the enstatite rim formation by a pseudomorphic replacement of forsterite as a result of reactionary interaction with the environment. It is possible that the observed structure of the enstatite rim is associated with shock effects. However, for more reliable confirmation of this hypothesis, the data on other similar inclusions is required.

The second result of EBSD mapping is that the rim is almost entirely composed of a monoclinic variety of enstatite (clinoenstatite). In the central part of the figure there is a polysynthetic twinning, clearly visible on the map in the Euler colors (Fig. 1b).

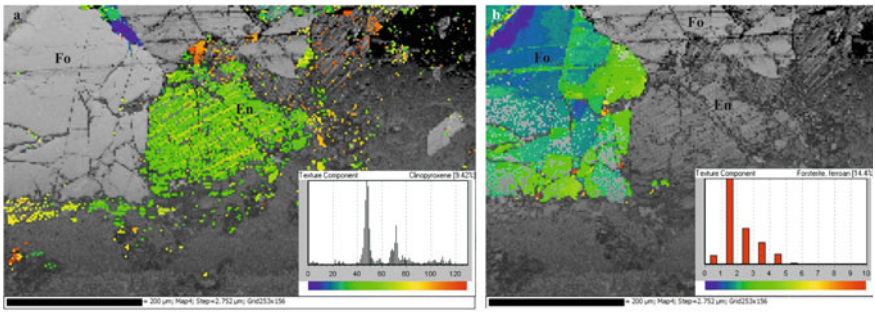

Fig. 2 Refractory forsterite-rich inclusion of Northwest Africa 11781 meteorite: **a**—the curvature of enstatite individuals and their disorientation; **b**—the block structure of forsterite

4 Conclusions

The first results of EBSD mapping of forsterite-rich inclusions are presented. The presence and structure of the enstatite rim indicates the existence of a stage of reactionary interaction with the external environment in the history of forsterite-rich inclusions after forsterite crystallization, probably during their stay in the protosolar nebulae. Only a portion of the refractory forsterite grains was subjected to the reaction and interaction. After that, the forsterite-rich inclusions, subjected and not subjected to reactionary interaction, appeared in one sample of carbonaceous chondrite. Further studies in this field will be continued.

Acknowledgements The study was funded by the Russian Foundation for Basic Research, project No. 17-05-00297 and topic No. AAAA-A18-118053090045-8 of the IGG UB RAS state assignment.

References

Dugushkina KA, Berzin SV. Novyi uglistyi khondrit iz Severo-Zapadnoi Afriki. Materialy IX Vserossiiskoi molodezhnoi nauchnoi konferentsii "Mineraly: stroenie, svoistva, metody issledovaniya". Ekaterinburg: Institut geologii i geokhimii UrO RAN, 2018. S. 24-25. [Dugushkina KA, Berzin SV. New Carbonaceous Chondrite from Northwest Africa. Proceedings of the IX All-Russian Youth Scientific Conference "Minerals: Structure, Properties, Methods of Investigation". February 5-8, 2018, Ekaterinburg, Russian, P.24-25.].

Fuchs LH, Olsen E, Jensen KJ. Mineralogy, mineralchemistry and composition of the Murchison (C2) meteorite. Smith. Contrib. Earth Sci. 1973;10:1–39.

McSween HYJr. On the nature and origin of isolated olivine grains in carbonaceous chondrites. Geochim. Cosmochim. Acta. 1977;41:411–418.

Olsen E, Grossman L. On the origin of isolated olivine grains in Type 3 carbonaceous chondrites. Earth Planet. Sci. Lett. 1978;41:111–127.

Pack A, Palme H, Shelley JMG. Origin of chondritic forsterite grains. Geochimica et Cosmochimica Acta, 2005;69:3159–3182.

Pack A, Yurimoto H, Palme H. Petrographic and oxygen-isotopic study of refractory forsterites from R-chondrite Dar al Gani 013 (R3.5-6), unequilibrated ordinary and carbonaceous chondrites. Geochimica et Cosmochimica Acta. 2004;68(5):1135–1157.

Reid AM, Bass MN, Fujita H, Kerridge JF, Frederiksson K. Olivine and pyroxene in the Orgueil meteorite. Geochim. Cosmochim. Acta. 1970;34:1253–1255.

Roedder E. Significance of Ca-Al-rich silicate melt inclusions in olivine crystals from the Murchison type II carbonaceous chondrite. Bull. Mineral. 1981;104:339–353.

Steele IM. Compositions of isolated forsterites in Ornans (CO3). Geochim. Cosmochim. Acta 1989;53:2069–2079.

Steele IM. Compositions and textures of relic forsterite in carbonaceous and unequilibrated ordinary chondrites. Geochimica et Cosmochimica Acta. 1986;50:1379–1395.

Magnetic Microspherules in Impactites and Sedimentary Rocks

Mikhail S. Glukhov, Vladimir A. Tsel'movich, Rafael Kh. Sungatullin, Rail I. Kadyrov, and Evgeniy O. Statsenko

Abstract

The structure of magnetic microspherules from impactites, evaporites, and bog peat was investigated using scanning electron microscopy and X-ray microtomography. All microspheres had a metallic luster and a textured surface. The natural origin of the studied microspherules was proven. The chemical composition of microspherules was studied; their major elements were iron and oxygen.

Keywords

Cosmic dust · Magnetic microspherules · Impactites · Evaporites · Bog peat

1 Introduction

In the second half of the 19th century, the microparticles of cosmic dust (magnetic shavings, plates and microspherules) were first discovered on the surface of the ice sheets of the Arctic (Nordenskjold 1874) and in deep oceanic clay (Murray 1876). At present, such finds have become numerous in various depositing environments:

M. S. Glukhov (✉) · R. Kh. Sungatullin · R. I. Kadyrov · E. O. Statsenko
Institute of Geology and Petroleum Technologies, Kazan Federal University, Kremlyevskaya St., 18, Kazan, Russia
e-mail: gluhov.mixail2015@yandex.ru

V. A. Tsel'movich
Borok Geophysical Observatory, Shmidt Institute of Physics of the Earth, Russian Academy of Sciences (BGO IPE RAS), Borok 142, Nekouz District, Yaroslavl Region, Russia
e-mail: tselm@mail.ru

S. Votyakov et al. (eds.), *Minerals: Structure, Properties, Methods of Investigation*, Springer Proceedings in Earth and Environmental Sciences,
https://doi.org/10.1007/978-3-030-49468-1_9

the alluvium of modern rivers, ancient sedimentary rocks, impactites, snow covers of Antarctica, etc. (Vilensky 1972; L'vov 1967; Osovetsky and Menshikova 2006; Karpov and Mokhov 2010; Sungatullin et al. 2015; Makarov et al. 2017; Tsel'movich et al. 2019; Kadyrov et al. 2018; Genge et al. 2016; Badyukov et al. 2018). The origin of these micro-objects is controversial in the scientific community. The main hypotheses are natural terrestrial, natural extraterrestrial (space) and technogenic origin (Nordenskjold 1874; Murray 1876; Vilensky 1972; L'vov 1967; Osovetsky and Menshikova 2006; Karpov and Mokhov 2010; Sungatullin et al. 2015; Makarov 2017; Tsel'movich et al. 2019; Kadyrov 2018; Genge 2016; Badyukov et al. 2018). One of the good sites for cosmic dust locations is peat, which receives mineral particles mainly from the atmosphere and therefore can serve as a good accumulator of cosmic matter (if at the moment of accumulation there are no closely located volcanoes or other mechanisms for the formation of microspheres). Peat accumulates microspheres of ablative origin with a dendrite structure, which emerge in the atmosphere of the Earth during the flight of meteoroids and micrometeorites with a well-crystallized structure, the origin of which is deep space (L'vov 1967; Tsel'movich et al. 2019). This work is devoted to the study and comparison of magnetic microspheres from modern peat, Permian evaporites and impactites.

2 Materials and Methods

The objects of study were magnetic microspherules from: (1) Obukhovsky bog peat (sampling depth 0.5 m, 52 microspherules; Yaroslavl region, Russia); (2) impactites (suevites) of the Popigai crater (2 microspherules; Russia) and Ries (10 microspherules; Germany); (3) Permian evaporites of the Kamsko-Ustinskoe gypsum deposit (25 microspherules; Russia) and the potassium-magnesium salts of the Verkhnekamskoe deposit (27 microspherules; Russia).

The material was provided by V.A. Korochantsev (suevites of the Popigai and Ries craters), a researcher of the GEOKHI named after Vernadsky (Moscow).

Before crushing the samples of the Popigai (17 × 13 × 13 mm) and Ries (12 × 9 × 7 mm) impactites and gypsum of the Kamsko-Ustinskoe deposit (6 × 3 × 3 cm), we studied them using X-ray microtomography (Phoenix V | tome | XS 240) with a nanofocus X-ray tube with a maximum accelerating voltage of 180 kV and a power of 15 W (Kazan Federal University). Next, the samples were crushed in an agate mortar. Magnetic microspherules were selected using a neodymium magnet. To study the surface of the microspherules, we used a Tescan Vega II (Borok geophysical observatory, Shmidt Institute of Physics of the Earth, Russian Academy of Sciences) and Phillips XL-30 (Kazan Federal University, operator B.M. Galiullin) electronic microscopes equipped with energy dispersive spectrometers. The survey took place at an accelerating voltage of 20 kV and a working interval of 8.9–15 mm. The probing depth was 1.0–1.5 μm, the measurement accuracy was 0.1–1%.

3 Results and Discussion

Using microtomography, we have found areas of X-ray dense minerals (iron-oxide magnetic microspheres) in some impactites (Fig. 1) and in gypsum of the Kamsko-Ustinskoe deposit (Kadyrov et al. 2018). This is a direct evidence of the natural origin of magnetic microparticles that makes it possible not to consider their technogenic origin.

During our research, scanning electron microscopy has revealed the following (Fig. 2): (1) all microspherules have an ideal spherical shape; (2) microspherule sizes from peat and evaporites are 5–150 μ; (3) microspherules from impactites are larger—50–300 μ; (4) the surface of microspherules often has a dendritic or brain-like texture, rarely the surface is represented by polygons (pentagons, hexagons) or smooth. The dependence of the surface texture of microspheres on the iron content is roughly as follows: the more iron, the smoother the surface of the microspheres.

Electron microprobe studies have shown that the main elements of microspherules are iron and oxygen. The quantitative content of iron and oxygen in the microspherules varies relative to each other and corresponds to magnetite, wustite and native iron (Table 1). Such a composition is characteristic of microspherules, which are formed during the ablation of meteorites, shock events and fall of cosmic dust (Nordenskjold 1874; Murray 1876; L'vov 1967; Sungatullin et al. 2015; Tsel'movich et al. 2019; Genge 2016; Badyukov et al. 2018). It is noteworthy that the salt microspherules belong to wustite and native iron, which may indicate the specificity of the evaporite basin and the conditions for the preservation of evaporite strata in a regenerative environment.

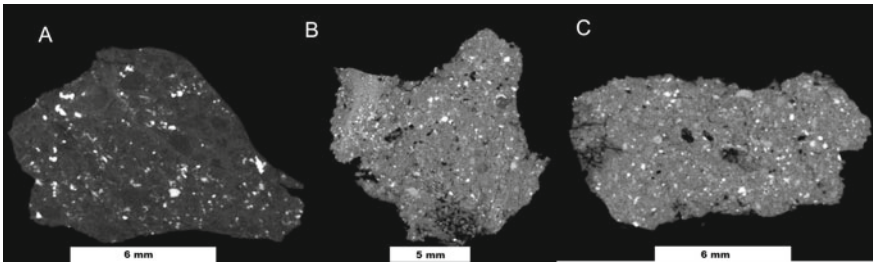

Fig. 1 Cosmic dust in impactites and sedimentary rocks (**A**—tomographic image of the gypsum sample from the Kamsko-Ustinskoe deposit (white—X-ray dense minerals), **B**—the Popigai crater, **C**—the Ries crater)

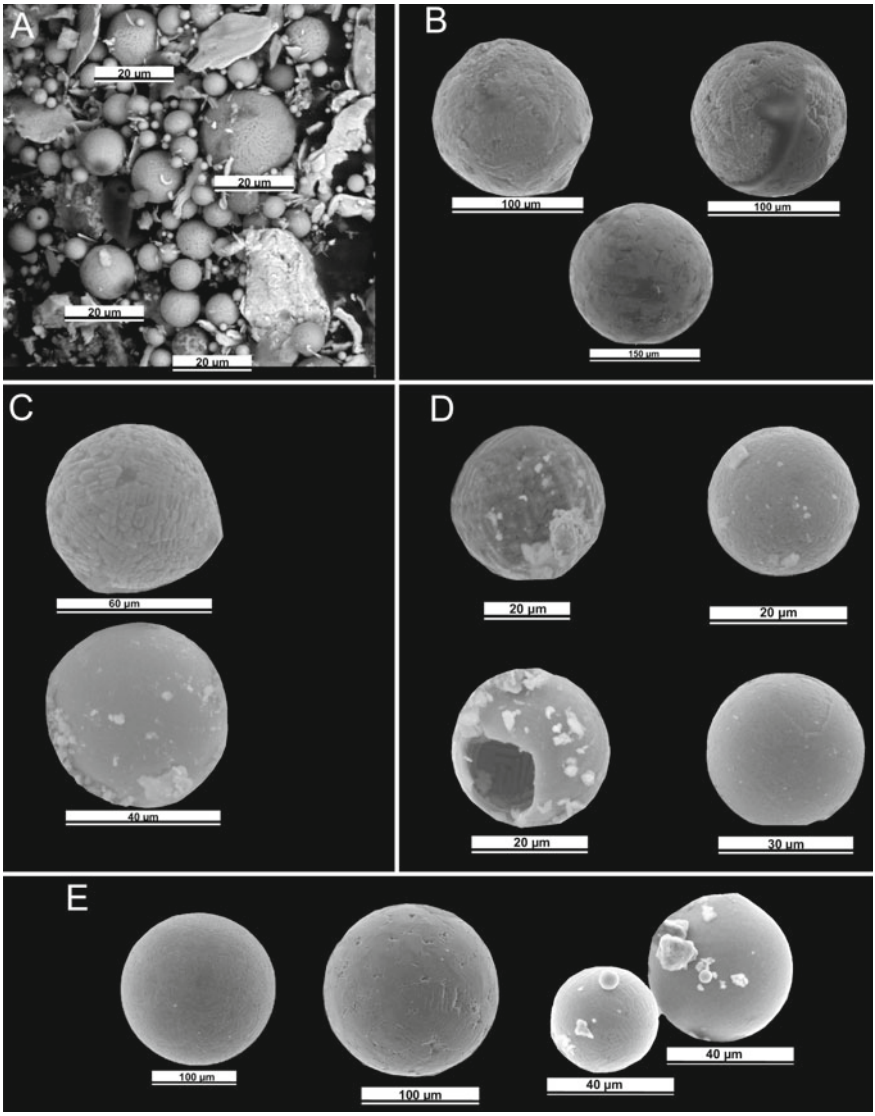

Fig. 2 Magnetic microspherules (**A**—microspherules from the Obukhovsky peat bog, **B**—microspherules from the Ries crater, **C**—microspherules from the Popigai crater, **D**—microspherules from the Verkhnekamskoe deposit, **E**—microspheres from the Kamsko-Ustinskoe deposit)

Table 1 Composition of the surface of microspherules from impactites and sedimentary rocks

Sample	Element, wt%								
	Fe	O	Cr	Al	Si	S	Ca	Mn	Total
Obukhovskoe peat bog	100	–	–	–	–	–	–	–	100
	96.38	1.42	2.20	–	–	–	–	–	100
	78.55	21.45	–	–	–	–	–	–	100
	75.25	23.14	1.61	–	–	–	–	–	100
	79.54	19.82	0.64	–	–	–	–	–	100
	73.99	24.94	1.07	–	–	–	–	–	100
	75.85	22.73	1.42	–	–	–	–	–	100
	87.39	10.55	2.06	–	–	–	–	–	100
	93.07	5.69	1.24	–	–	–	–	–	100
Popigai crater	60.45	35.90	–	1.27	1.49	0.89	–	–	100
	61.10	36.35	–	1.73	0.82	–	–	–	100
Ries crater	63.08	31.85	–	0.35	3.51	–	1.21	–	100
	59.56	35.91	–	0.44	3.28	–	0.81	–	100
	67.88	30.59	–	0.45	1.08	–	–	–	100
	70.29	29.28	–	–	0.43	–	–	–	100
	70.34	29.28	–	–	0.38	–	–	–	100
	70.22	29.20	–	–	0.58	–	–	–	100
	70.31	29.26	–	–	0.43	–	–	–	100
Kamsko-Ustinskoe deposit	90.97	5.49	–	1.18	1.83	0.53	–	–	100
	78.58	19.64	–	0.83	0.65	0.30	–	–	100
	75.68	20.52	–	2.64	0.60	0.56	–	–	100
	71.56	22.06	–	2.88	1.22	0.54	–	1.74	100
	79.71	18.62	–	1.67		–	–	–	100
Verkhnekamskoe deposit	76.85	17.09	–	5.36	0.70	–	–	–	100
	88.92	–	–	8.15	1.30	–	–	1.63	100
	74.52	18.02	–	2.99	0.80	3.67	–	–	100
	76.20	17.10	–	6.70	–	–	–	–	100
	76.90	18.42	–	1.74	2.94	–	–	–	100

Note dash—not found

We have also applied X-ray tomography and studied the internal structure of microspherules from impactites and evaporites. All microspherules have a single hollow cavity inside (Fig. 3). It proves that all the microspherules studied have a common genesis.

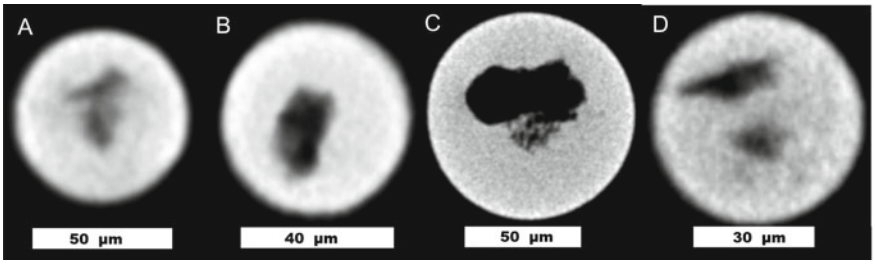

Fig. 3 Tomographic image (2D) of microspherules (**A**—the Ries crater, **B**—the Popigai crater, **C**—the Kamsko-Ustinskoe deposit, **D**—the Verkhnekamskoe deposit)

4 Conclusions

Based on the above results of the study of magnetic microspherules from impactites and sedimentary rocks, the following conclusions were made.

1. Using X-ray microtomography, the natural origin of microspherules was confirmed.
2. According to the morphology and composition of the surface of the microspherules, they can be attributed to the objects of cosmic origin.
3. We outlined the textural and chemical criteria for the separation of magnetic microspherules depending on their genesis.

Acknowledgements The work was performed as part of the Russian Government Program of Competitive Growth of Kazan Federal University.

References

Badyukov DD, Brandstetter F, Topa D. Tonkozernistyye shlakovidnyye i nepereplavlennyye mikrometeority: ikh istochniki i svyaz' s kosmicheskimi sferulami. Geokhimiya. 2018; 11: 1026–1039. [Badyukov DD, Brandstetter F, Topa D. Fine-grained slag-like and non-melted micrometheoritis: their sources and communications with space spheres. Geochemistry. 2018; 11: 1026–1039. (In Russ.)].

Genge MJ. The origins of I-type spherules and the atmospheric entry of iron micrometeoroids. Meteoritics & Planetary Science. 2016; 51 (6): 1063–1081. https://doi.org/10.1111/maps.12645.

Kadyrov R, Glukhov M, Statsenko E, Galiullin B. Enigma of Ferruginous Inclusions in Evaporites. Proceedings of the 1st Springer Conference of the Arabian Journal of Geosciences (CAJG), Tunisia (2018). Petrogenesis and Exploration of the Earth's Interior. Advances In Science, Technology & Innovation, 2019; 97-99. https://doi.org/10.13140/RG.2.2.24595.32808.

Karpov GA, Mokhov AV. Microchastitsy samorodnykh metallov, sulfidov I oksidov v andezitovykh peplakh Karymskogo vulkana. Vulcanologiya I seysmologya. 2010;3:19-35.

[Karpov GA, Mokhov AV. Microparticles of native metals, sulfides and oxides in andesitic ashes of Karymskiy volcano. Volcanology and seismology. 2010;3:19-35. (In Russ.)].

L'vov YuA. O nahozhdenii kosmicheskogo veshestva v torfe. Problema Tungusskogo meteorita. 1967; 140-144. [L'vov YuA. On the presence of space matter in the peat. Journal of Applied Problem of the Tunguska meteorite. 1967; 140-144. (In Russ.)].

Makarov AB, Osovetsky BM, Antonova IA. Magnitnye spheruly iz pochv vblizy shlakovogo otvala Nizhnetagil'skogo metallurgicheskogo combinata. Izvestiya UGGU. 2017; 48(4): 42-45. [Makarov AB, Osovetsky BM, Antonova IA. Magnetic spherules from soils near the slag dump of the Nizhny Tagil metallurgical plant. News of UGGU. 2017; 48(4): 42-45. (In Russ.)].

Murray I. On the distribution of volcanic debris over the floor of ocean. Proceedings of the Royal Society. Edinburg,1876; 9: 247–261.

Nordenskjold AE. On the cosmic dust which falls on the surface of the Earth with the atmospheric precipitation. Philosophical magazine, 1874; 48: 546.

Osovetsky BM, Menshikova EA. Prirodno-technogennye osadki. Perm: Permskiy gosudarstvenniy universitet; 2006. P. 208. [Osovetsky BM, Menshikova EA. Natural and man-made deposits. Perm: Perm state University; 2006. P. 208. (In Russ.)].

Sungatullin RH, Sungatullina GM, Glukhov MS, Osin YuN, Vorobyov VV. Vozmozhnosty ispol'zovaniya kosmicheskikh microspher pri korrelyatsii neftegazonosnykh otlozheniy. Neftyanoe Khozaystvo. 2015;2: 16-19. [Sungatullin RH, Sungatullina GM, Glukhov MS, Osin YuN, Vorobyov VV. The possibility of using space microspheres in the correlation of oil and gas deposits. Oil Industry. 2015;2: 16-19. (In Russ.)].

Tsel'movich VA, Kurazhkovsky AYu, Kazansky AYu, Shchetnikov AA, Blyakharchuk TA, Filippov DA. Issledovaniya dinamiki postupleniya kosmicheskoy pyli na zemnyu poverkhnost' po torfyanym otlozheniyam. Fizika Zemli. 2019;3. [Tsel'movich VA, Kurazhkovsky AYu, Kazansky AYu, Shchetnikov AA, Blyakharchuk TA, Filippov DA. Studies of the dynamics of space dust on the earth's surface from peat deposits. Physics of The Earth. 2019;3] (Accepted in print).

Vilensky VD. Spherichеskie microchastitsy v lednikovom pokrove Antarktidy. Meteoritika. Nauka. 1972; 31: 57-61. [Vilensky VD. Spherical microparticles in the glacial cover of Antarctica. Meteoritika. Science. 1972;31: 57-61. (In Russ.)].

Phase and Elemental Analysis of Marsa Alam 009 Ordinary Chondrite

Svetlana S. Hontsova, Elena M. Maksimova, and Igor A. Nauhatsky

Abstract

The phase and elemental composition of Marsa Alam 009 ordinary chondrite is investigated. The mineral composition of the sample corresponds to the H-type. The Fe-Ni metal is almost completely weathered, while troilite inclusions remain almost unchanged. The meteorite has a W3 weathering grade. The presence of iron oxides in the sample is associated with its long stay in the hot desert.

Keywords

Ordinary chondrite · Mineral composition · X-ray diffraction · X-ray fluorescence

1 Introduction

The substance of ordinary chondrites stores information about the different stages of the evolution of the Solar system substance. Ordinary chondrites are silicate-rich meteorites composed mostly of olivine and low calcium pyroxene with the inclusions of Fe-Ni alloy and sulfide phases. The substance differentiation by chemical composition (H, L, LL) is associated with the heliocentric distance, at which the process of nebula accretion occurs (Dodd 1981). The degree of substance differentiation in the parent body of chondrites characterizes the severity of the processes

S. S. Hontsova (✉) · E. M. Maksimova (✉) · I. A. Nauhatsky
V.I. Vernadsky Crimean Federal University, 4 Vernadsky ave., 295033 Simferopol, Russia
e-mail: sgoncova@gmail.com

E. M. Maksimova
e-mail: maksimovaem@cfuv.ru

S. Votyakov et al. (eds.), *Minerals: Structure, Properties, Methods of Investigation*,
Springer Proceedings in Earth and Environmental Sciences,
https://doi.org/10.1007/978-3-030-49468-1_10

of thermodynamic metamorphism (1–7) and is determined by the equilibrium composition of the silicate phases (Miyamoto et al. 1981). The degree of shock metamorphism (S1–S6) indicates the conditions and processes of shock transformation of the substance in the parent body (Bischoff and Stoffler 1992). The change of a substance under the influence of terrestrial conditions is characterized by the degree of weathering (W0–W6) and leads to erosion, replacement, and the formation of new minerals (Rubin 1997). It should be noted that the degree of weathering is largely determined by the environment, in which the meteorite falls. The reconstruction of structural and metamorphic evolution of extraterrestrial matter is a key issue of cosmochemistry. In this work, the chemical and mineral composition of Marsa Alam 009 ordinary chondrite were investigated.

2 Materials and Methods

The fragment of the Marsa Alam 009 meteorite was first discovered on January 11, 2015 in Al Bahr al Ahmar, Egypt (Fig. 1). This meteorite was classified as H6 ordinary chondrite having S3 shock stage and W3 weathering grade (Bouvier et al. 2017).

The phase composition of Marsa Alam 009 ordinary chondrite was investigated by X-ray diffraction (XRD) using a diffractometer with monochromatic Co Kα. The XRD investigation was performed in 2θ angles ranging from 10 to 100°. The phase composition was determined both from the powder of the whole sample and the selected magnetic part of the sample. The separation of the magnetic part from the powder of the whole sample was carried out with a neodymium magnet. The study of the meteorite elemental composition was carried out using a Rigaku Supermini200 high-power desktop wave dispersive X-ray fluorescence spectrometer of sequential action. The elemental composition was determined from the polished section of the sample and from the magnetic part selected from the powder of the whole sample. The polished section of the meteorite was prepared for the optical microscopy using the standard metallographic procedures. The sample was cut and its section was polished with diamond pastes. The sample was investigated by optical microscopy using a Micromed POLAR 3 microscope.

Fig. 1 The fragment of the Marsa Alam 009 meteorite

3 Results and Discussion

According to the X-ray fluorescence analysis of the Marsa Alam 009 sample, the following elements were identified (Table 1).

XRD showed the following phase composition of the whole Marsa Alam 009 sample: $MgSiO_3$ clinoenstatite (22.3 wt%), $(Fe,Mg)_2SiO_4$ olivine (16.9 wt%), $CaMgSi_2O_6$ diopside (12.5 wt%), $Ca_5(PO_4)Cl$ chlorapatite (11,7 wt%), γ-Fe(Ni,Co) taenite (15.9 wt%), FeS troilite (15.5 wt%), and $FeCr_2O_4$ chromite (5.3 wt%) (Fig. 2).

The following phases were detected by the X-ray phase analysis in the magnetic part of the Marsa Alam 009 fragment: Fe_3O_4 magnetite (29.1 wt%), $(Fe,Mg)_2SiO_4$ forsterite (25.2 wt%), γ-Fe(Ni,Co) taenite (22.6 wt%), FeS troilite (12.9 wt%), FeO wustite (9.3 wt%), and γ-Fe_2O_3 maghemite (0.9 wt%) (Fig. 3).

The inclusions of a Fe-Ni alloy (kamacite + taenite) and troilite with cracks filled with weathering products are found in the silicate matrix of the studied sample (Fig. 4). It can be seen that the inclusions of kamacite and taenite are more prone to terrestrial weathering. There are no significant differences in the weathering of metal phases, both near the melting crust and inside the sample. The initial Fe-Ni alloy is replaced by magnetite, wustite and maghemite as a result of terrestrial weathering. It should be noted that in the first period after the fall of meteorites in hot deserts, their main part undergoes strong weathering, after which the weathering proceeds more slowly (Bland et al. 1996). The observed degree of weathering suggests that the initial period of weathering was more humid.

Table 1 The elemental composition of the Marsa Alam 009 meteorite sample (wt%)

Chemical element	Polished section	Magnetic part
Fe	59.10	68.343
Si	13.933	–
Al	11.733	–
Mg	4.580	4.538
Ni	3.896	6.048
Ca	2.136	–
S	1.730	1.509
Cl	0.669	–
Cr	0.632	–
Mn	0.581	0.653
K	0.266	–
P	0.214	–
Na	0.145	–
Co	0.17	0.215
Ti	0.114	–

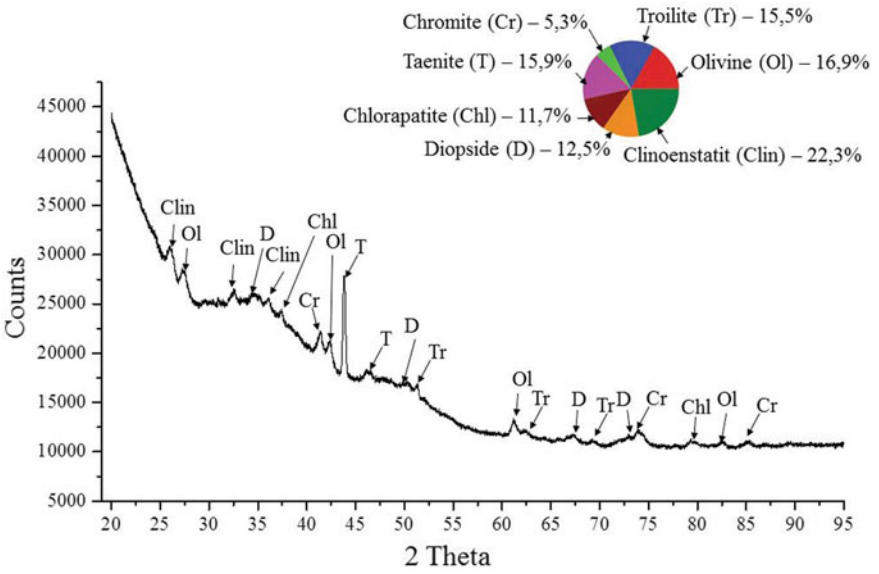

Fig. 2 X-ray diffraction pattern of the whole sample

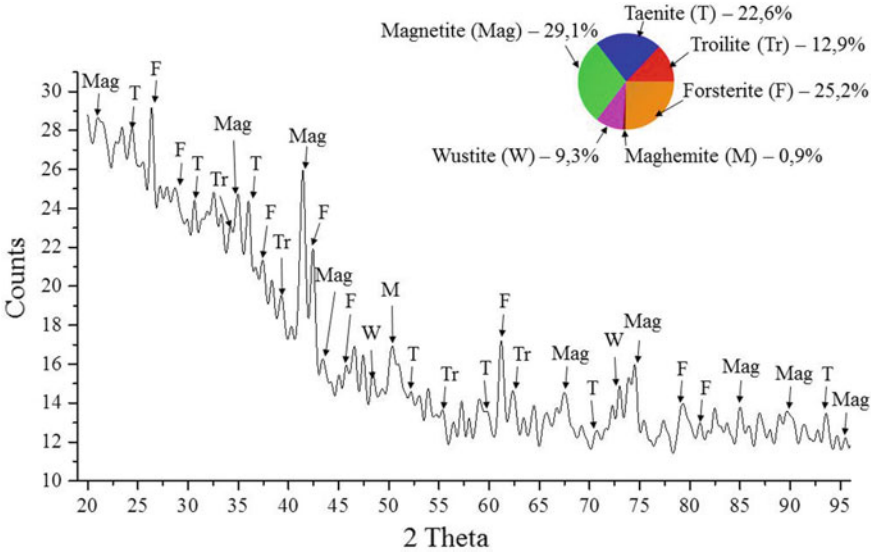

Fig. 3 X-ray diffraction pattern of the magnetic part of the sample

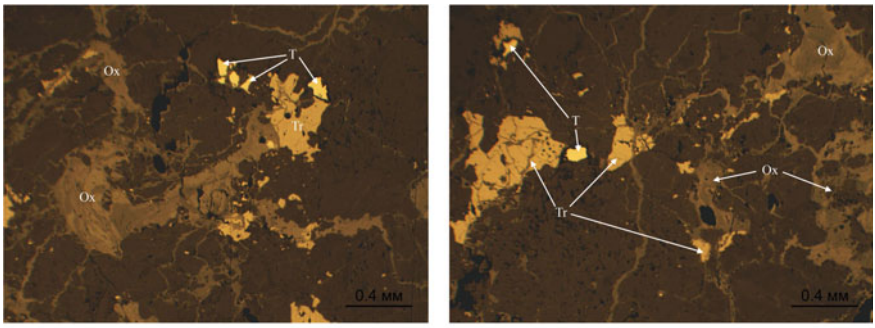

Fig. 4 Photo of inclusions in the silicate matrix (T – taenite, Tr – troilite, Ox – terrestrial weathering products)

4 Conclusions

The study of the Marsa Alam 009 ordinary chondrite by various techniques including optical microcopy, X-ray diffraction and X-ray fluorescence spectroscopy leads to conclusions:

- the phase composition of the Marsa Alam 009 corresponds to the composition of the H-type ordinary chondrites characterized by a high content of Fe (25–31 wt %);
- the metal phases of the sample are replaced by magnetite, wustite and maghemite, which are formed as a result of terrestrial effects;
- the presence of veins in Marsa Alam 009 gives evidence to shock events, which took place during the meteorite evolution;
- the observed degree of weathering suggests that the initial period of weathering was more humid.

Acknowledgements The authors are grateful to T.V. Kryachko for providing the Marsa Alam 009 sample.

References

Bischoff A, Stoffler D. Shock metamorphism as a fundamental process in the evolution of planetary bodies: information from meteorites. European Journal of Mineralogy. 1992; 4; 707–755.

Bland PA, Berry FJ, Smith TB, Skinner SJ, Pillinger CT. The flux of meteorites to the Earth and weathering in hot desert ordinary chondrite finds. Geochimica et Cosmochimica Acta. 1996; 60;11; 2053–2059.

Bouvier A, Gattacceca J, Grossman J, Metzler K. The Meteoritical Bulletin, No. 105. Meteoritics & Planetary Science. 2017; 52;11; 2411.
Dodd R. Meteorites: a Petrologic-chemical Synthesis. NY: Cambridge University press; 1981.
Miyamoto M, Fujii N, Takeda H. Ordinary chondrite parent body: An internal heating model. 12th Lunar and planetary Sci. Conf. 1981; 1145.
Rubin AE. Mineralogy of meteorite groups. Meteorit Planet Sci. 1997; 32; 231–247.

Anthropogenic Particles in the Snow Cover in the Area of the Ice Race Track

Ekaterina O. Ilgasheva, Ilya V. Yarmoshenko, Georgy P. Malinovskiy, and Andrian A. Seleznev

Abstract

The study is aimed to assess the composition and properties of solid material supply to the environment from vehicles. The study was conducted in the area of an ice race track located on the surface of a lake located at a significant distance from the stationary sources of pollution. The sampling was conducted on February 27, 2019. The samples of snow cover and ice were collected at the roadside of the track and at a distance of > 10 m from the ice race track in the winter period. The ice race track was located on Lake Baltym (north of Ekaterinburg, Sverdlovsk region, Russia). The samples of snow were melted. The solid material of the samples was separated with filter paper and dried. The particles were selected manually and photographed using an optical microscope, and then they were analyzed with a scanning electron microscope. The origin of the selected particles was determined. The particles were classified into three types:

- fragments of car tires (5 particles per 1 L of meltwater in the curb area of the ice race track),
- fragments of cast-iron brake discs (2 particles per 1 L of meltwater),
- fragments of a composite material of car brake pads.

The approximate amount of solid material supply to the lake from the ice race track during one season was estimated at the level of 40 mg/L.

E. O. Ilgasheva · I. V. Yarmoshenko · G. P. Malinovskiy · A. A. Seleznev (✉)
Institute of Industrial Ecology, Ural Branch of the Russian Academy of Sciences,
20 S. Kovalevskoy Str., 620219 Ekaterinburg, Russia
e-mail: sandrian@rambler.ru

S. Votyakov et al. (eds.), *Minerals: Structure, Properties, Methods of Investigation*,
Springer Proceedings in Earth and Environmental Sciences,
https://doi.org/10.1007/978-3-030-49468-1_11

Keywords

Automobile transport · Pollution · Snow cover · Ice · Chemical elements · Anthropogenic particles · Ice race track · Lake

1 Introduction

In recent decades, road transport has become the main source of urban pollution (Bucko et al. 2013). Road transport produces not only emissions but also mineral materials and solid particles, which are the products of corrosion and abrasion of tires, brake pads and other car parts (Pant and Harrison 2013). Heavy metals, road paint particles and mineral materials also enter the road sediments when abrading the road surface (Grant 2015; Lanzerstorfer 2018). The pollution supply from automobiles occurs all year round. In the winter season, snow cover and snow-dirt sludge on the roads accumulate pollutants from automobile traffic (Adamiec et al. 2013; Shi et al. 2014; Seleznev et al 2019).

Water and bottom sediments of the surface water bodies, which the city has in the catchment, are geochemically transformed as a result of pollution intake. Components of aquatic ecosystems are the ultimate depot for transporting pollution from non-point sources (Chen et al. 2018). The ecological state of water bodies depends on a complex of natural and anthropogenic factors when pollutants enter the water body with a material of various origins. Several authors categorize the main types of technogenic particles found in urban areas (Bucko et al. 2013; Seleznev et al. 2020). However, the great diversity of automobile materials used makes it difficult to distinguish between vehicle wear products. Friction materials of automobile brake systems are usually made from natural mineral raw materials (zircon, antimonite, aluminosilicates). Therefore, the assessment of pollution supply from vehicles in a large city is a very difficult and often impossible task.

The study was aimed to assess the composition and properties of material entering the environment during the exploitation of road transport. A special area, in which cars were the only main source of pollution, was chosen. The selected zone was characterized by the absence of material supply of natural origin, and the pollution of the study area from stationary sources was negligible. Such an area was represented by the surface of a lake, on which an ice race track was constructed in the winter period.

2 Materials and Methods

The ice race track is located on Lake Baltym (Sverdlovsk region, Russia; coordinates: 57.026608° N, 60.580374° E). The track has been functioning regularly in winters since 2008 (Fig. 1, (https://www.google.ru/maps/@57.043446,60.581969,

3a,90y,3.88h,30.83t/data=!3m8!1e1!3m6!1sAF1QipNXQkxg3B5dLnB-tuH5gF64OMmnd5zgaAuapyv7!2e10!3e11!6shttps:%2F%2Flh5.googleusercontent.com%2Fp%2FAF1QipNXQkxg3B5dLnB-tuH5gF64OMmnd5zgaAuapyv7%3Dw203-h100-k-no-pi-0-ya69.65704-ro-0-fo100!7i12000!8i6000?hl=ru)). All cars undergo technical inspection and wheel washing before entering the race track. Lake Baltym is located north of Ekaterinburg, the city with the population of approximately 1.5 million people. The lake has a saucer shape, stretched from north to south. The surface area of the lake is 7.5 km^2, the catchment area is 27 km^2. Lake Baltym has a sufficiently large water mass of over $20 \cdot 10^6$ m^3. The average depth of the lake is 3–4 m, the max is 6.5 m. The bottom topography is relatively flat with a decrease to the center. The pitfalls are located on the east and west coast. The bottom of the lake is silt with sandy areas on the eastern side (Nikolaenko 1965).

The samples of snow and crushed ice were collected by the following scheme:

- The samples were collected at 6 sampling sites located at the roadside of the ice race track. At one sampling site, two combined samples of snow and crushed ice were taken from the external (1) and internal (2) curbs relatively to the turn of the route. Snow was taken by a scoop; crushed ice was swept from the surface with a brush.
- One combined sample of snow and crushed ice was collected from the surface of a circular drift track along the entire length.
- Three sampling sites were located at the distance of > 10 m from the ice race track along the entire route. The full height of the undisturbed snow core was taken by a shovel from one site. The snow depth was < 1 m.

The volume of each sample collected at the roadside area and the circular drift track was 100 mL. The volume of the sample of the undisturbed snow core was 5 L. The coordinates of sampling sites are presented in Table 1. Examples of sampling are shown in Fig. 2.

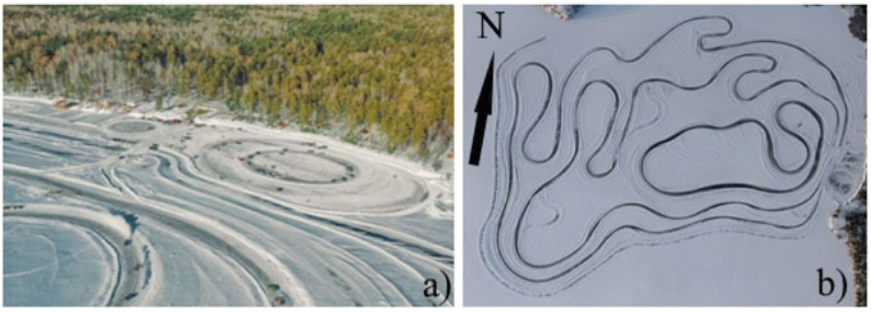

Fig. 1 The ice race track on Lake Baltym (Sverdlovsk region, Russia), view from the quadrocopter; **a** two drift tracks (round and ellipse shape) and forest on the east lakeshore, **b** the entire ice race track

Table 1 Characteristics of the studied sampling sites (coordinates and location), the volume of meltwater, and the amount of large and small particles in 10 collected samples of snow and ice in the area of Baltym ice race track

Sample number	Coordinates (N/E)	Sampling site	Volume of meltwater, ml	Number of particles > 1 mm size	Number of particles < 1 mm size
1	57.046514°/60.579201°	Roadside, external curb	58	4	Large number
2	57.04604°/60.57950°	Roadside, external curb	60	7	Insignificant
3	57.04637°/60.57527°	Roadside, external curb	54	2	Insignificant
4	57.04384°/60.57720°	Roadside, external curb	60	4	Not found
4/2	57.04384°/60.57720°	Roadside, internal curb	51	0	Not found
5	57.044521°/60.576457°	Roadside, external curb	50	2	Large number
5/2	57.044521°/60.576457°	Roadside, internal curb	55	0	Not found
6	57.044633°/60.575203°	Roadside, external curb	55	2	Not found
6/2	57.044633°/60.575203°	Roadside, internal curb	45	0	Insignificant
7	57.045393°/60.583619°	Drift track	68	5	Large number

Fig. 2 Examples of snow and crushed ice sampling in the area of Baltym ice race track: **a** samples of undisturbed snow in 5 l buckets, **b** sampling at the roadside, **c** sampling of the undisturbed snow cover

The collected samples of snow and crushed ice were melted at room temperature. The solid material of the samples was separated with filter paper and dried. The number of solid particles > 1 mm (large) and < 1 mm (small) in size was calculated in each sample using a binocular microscope. Then single visually typical particles were selected manually and photographed using a Carl Zeiss Axioplan 2 optical microscope equipped with an Olympus C-5060 digital camera. The selected particles were analyzed using a JSM-6390LV scanning electron microscope (SEM) at the Geoanalyst Common Use Center of the Ural Branch of RAS (www.geoanalyst.igg.uran.ru). The images of particles in secondary-scattered electrons and the chemical composition of particles were obtained.

3 Results and Discussion

The sampling was conducted on February 27, 2019. Sixteen samples of snow and ice were collected. All samples from the external curbs of the track contained solid particles of various sizes, including 4–12 large particles per 100 mL of meltwater. Large particles were not found in the samples from the internal curbs of the track; those samples contained a small number of particles < 1 mm in size. The snow samples collected at the sites of undisturbed snow did not have solid particles. The particles from 10 samples were analyzed using SEM. The distribution of particles of various sizes in 10 collected samples is presented in Table 1.

The solid particles found in the analyzed samples could be divided into several types. The 1st type of particles are large particles of long cylindrical shape, black, with a matte surface, elastic, 20 × 2 × 2 mm in size. The photo from the optical microscope is shown in Fig. 3. The chemical composition of this particle is given in Table 2.

Fig. 3 The 1st type particle is a large particle of long cylindrical shape (optical microscope image)

Table 2 Chemical composition of the 1st type particle (the particle from Fig. 3) in two points according to SEM-EDS analysis

Point	Element, wt%			Total, wt%
	C	Si	S	
26	86.04	11.46	1.94	99.44
42	87.44	10.08	1.48	99.00

The surface of this type of particle contains small fragments of metallic Fe and Cr (Fig. 4). The chemical composition of the fragments of metallic Fe and Cr on the surface of the 1st type particle is shown in Table 3.

The 2nd type of particles is represented by large particles of irregular shape and dark gray color, 0.5 × 0.4 × 0.3 mm in size, with strong metallic luster and high hardness. Fe predominates in the composition of the 2nd type particles; Zn and Mn are partially oxidized impurities. The photo of the 2nd type of particle from SEM is shown in Fig. 5, the chemical composition is presented in Table 4.

The 3rd type particles are fine mineral particles < 15 μm in size, consisting of clay minerals, and including fragments of brass, zirconium silicate, iron sulfide, hydromica, alloys of Fe with Ti and V. The fine mineral material was found in all 10 analyzed samples. The particles of the 3rd type in Sample 1 are shown in Fig. 6. The elemental composition of the fine mineral material in Sample 1 is presented in

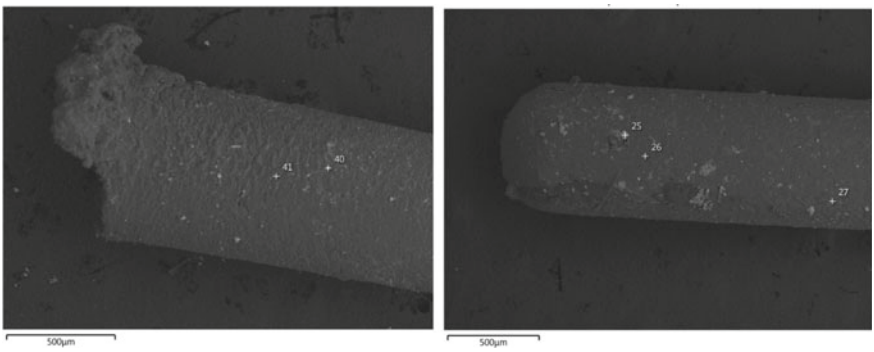

Fig. 4 The fragments of metallic Fe and Cr on the surface of the 1st type particle of long cylindrical shape (SEM image)

Table 3 Chemical composition of inclusions on the surface of the 1st type particle according to SEM-EDS analysis of the particle from Fig. 4

Point	Element, wt%		Total, wt%
	Cr	Fe	
40	98.42	0.00	98.42
27	0.00	100.00	100.00

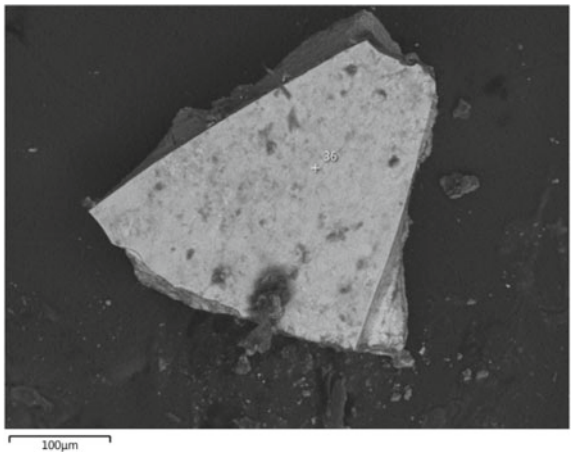

Fig. 5 The 2nd type particle of irregular shape and dark gray color (SEM image)

Table 4 Chemical composition of the 2nd type particle (from Fig. 5) according to SEM-EDS analysis

Point	Element, wt%			Total, wt%
	Mn	Fe	Zn	
36	3.99	90.81	3.97	98.77

Fig. 6 Fine mineral particles < 15 μm in size (SEM image)

Table 5: particles of zirconium silicate (spectrum 23), iron sulfide (spectrum 22), and hydromica (spectra 19 and 24). Fragments of the Fe alloy with Ti and V are also observed in the sample (spectrum 21). The total content of the components is less than 100%, taking into account the error of the device due to particle size.

One sample of snow and ice had a thin oil film of dark color after melting. The SEM photo and its elemental composition are presented in Fig. 7 and Table 6, respectively. The film contained the small particles of stainless steel with characteristic proportions of Fe, Cr, and Ni (spectra 16 and 17, Table 6). Spectrum 16 is also characterized by particles with a composition similar to the 1st type of particles. Spectrum 18 is represented by iron sulfide. Sections 14 and 15 characterize the overall chemical composition of the oil film.

The methods of visual analysis and SEM allow the origin of the studied particles to be determined with great accuracy. The operator defines the form, color, and other characteristics of the particles by the visual inspection. The SEM and EDS analyses allow the surface morphology, chemical composition of particles, and elemental composition of mixtures to be obtained. Based on all the data collected, the particles are classified into three main types (Grigoratos and Martini 2015; Kukutschová et al. 2011; Chen et al. 2012; Mosleh et al. 2004).

Table 5 Chemical composition of the fine mineral particles from Fig. 6 according to SEM-EDS analysis

Point	Element, wt%										Total, wt%
	Mg	Al	Si	S	K	Ca	Ti	V	Fe	Zr	
19	12.05	15.75	40.60	0.00	9.99	0.00	2.12	0.00	19.03	0.00	99.54
21	0.00	0.00	0.00	0.00	0.00	0.00	2.83	1.32	87.61	0.00	91.76
22	0.00	0.00	0.00	52.90	0.00	0.00	0.00	0.00	42.26	0.00	95.16
23	0.00	5.95	39.82	0.00	0.00	1.38	0.00	0.00	0.00	50.50	97.65
24	8.83	13.58	59.20	0.00	0.73	6.91	0.00	0.00	7.58	0.00	96.83

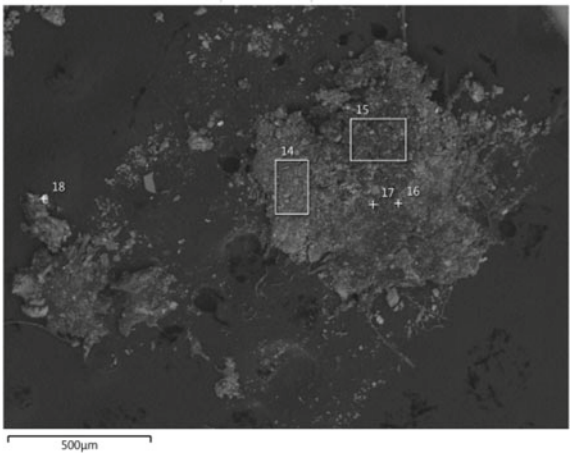

Fig. 7 A thin oil film (SEM image)

Table 6 Chemical composition of the oil film from Fig. 7 according to SEM-EDS analysis

Point	Element, wt%											Total, wt%
	C	Na	Mg	Al	Si	S	K	Ca	Cr	Fe	Ni	
14	0.00	2.18	6.77	11.78	47.43	3.27	1.01	19.29	0.00	7.83	0.00	99.55
15	0.00	0.00	5.10	6.43	23.78	18.14	1.12	34.53	0.00	8.97	0.00	98.07
16	57.44	0.00	0.00	0.00	1.19	0.50	0.00	0.00	5.54	33.84	0.28	100.00
17	0.00	0.00	0.00	0.00	0.00	0.00	0.00	0.00	14.23	82.07	0.00	100.00
18	0.00	0.00	0.00	0.00	0.00	70.78	0.00	0.00	0.00	29.22	0.00	100.00

The 1st type may be classified as fragments of car tires. Iron, nickel and chromium and other metal inclusions, chemical compounds of carbon (soot), silicon and sulfur and metals were found on the surface of the particles. The amount of such type of particles was 5 particles per 1 L of meltwater for the external curb area of the ice race track.

The 2nd type of particles is represented by the fragments of the car brake system (cast-iron brake discs); its amount was about 2 particles per 1 L of melt water.

The 3rd type (mineral material) may be related to both fragments of a composite material of car brake pads. These materials were found in all samples taken on the internal and external parts of curbs. Lubricant leak was detected only in one sample of snow and ice.

The content of large particles > 1 mm in size varies from 40 to 120 particles per 1 L of meltwater in the samples from the external curbs of the ice track. Taking the mass of one large particle for about 1 mg, the amount of solid material supply during one season will be more than 40 mg/L. The long-term supply of anthropogenic material from the ice race track to the lake water and bottom sediment is assessed at the level of > 1 g/L of meltwater (from snow and ice on route). Such supply of anthropogenic particles is similar to the supply of the urban surface sediments deposited during one year (Seleznev et al. 2019).

4 Conclusion

The study conducted in the area of the ice race track has shown that wear of brake pads, brake discs and tires is the main source of solid particles from vehicles entering the environment. The solid material does not exceed 10 m from the race track. The long-term functioning of the ice race track may result in a significant accumulation of the wear fragments of car parts containing heavy metals in the bottom sediments of Lake Baltym and a negative impact on its water inhabitants.

Acknowledgements The reported study was funded by Russian Science Foundation (grant 18-77-10024).

References

Adamiec E, Wieszała R, Strzebońska M, Jarosz-Krzemińska E. An attempt to identify traffic related elements in snow. Geology, Geophysics & Environment. 2013;39(4):317–329.

Bucko MS, Mattila O-P, Chrobak A, Ziołkowski G, Johanson B, Cuda J, Filip J, Zboril R, Pesonen LJ, Lepparanta M. Distribution of magnetic particulates in a roadside snowpack based on magnetic, microstructural and mineralogical analyses. Geophys. J. Int. 2013;195:159–175.

Chen L, Zhi X, Shen Z, Dai Y, Aini G. Comparison between snowmelt-runoff and rainfall-runoff nonpoint source pollution in a typical urban catchment in Beijing, China. Environ. Sci. Pollut. Res. https://doi.org/10.1007/s11356-017-0576-z.

Chen L-WA, Watson JG, Chow JC, Green MC, Inouye D, Dick K. Wintertime particulate pollution episodes in an urban valley of the Western US: a case study. Atmos. Chem. Phys. 2012;12:10051–10064.

Grant S. A Review of the Contaminants and Toxicity Associated with particles in Stormwater Runoff. https://doi.org/10.13140/rg.2.1.4847.1526.

Grigoratos T, Martini G. Brake wear particle emissions: A review. Environ. Sci. Pollut. Res. 2015;22:2491–2504. https://doi.org/10.1007/s11356-014-3696-8.

Kukutschová J, Moravec P, Tomášek V, Matějka V, Smolík J, Schwarz J, Seidlerová J, Šafářová K, Filip P. On airborne nano/micro-sized wear particles released from low-metallic automotive brakes. Environ Pollut. 2011;159:998–1006. https://doi.org/10.1016/j.envpol.2010.11.036.

Lanzerstorfer C. Heavy metals in the finest size fractions of road-deposited sediments. Environmental Pollution. 2018;239:522–531.

Mosleh M, Blau PJ, Dumitrescu D. Characteristics and morphology of wear particles from laboratory testing of disc brake materials. Wear. 2004;256:1128–1134.

Nikolaenko VV. Resursy poverhnostnyh vod SSSR: Gidrologicheskaya izuchennost'. T.11. Srednij Ural i Priural'e. Vyp. 2. L.: Gidrometeoizdat, 1965. (in Russian).

Pant P, Harrison RM. Estimation of the contribution of road traffic emissions to particulate matter concentrations from field measurements: A review. Atmospheric Environment. 2013;77:78–97.

Seleznev A, Yarmoshenko I, Malinovsky G, Ilgasheva E, Baglaeva E, Ryanskaya A, Kiseleva D, Gulyaeva T. Snow-dirt sludge as an indicator of environmental and sedimentation processes in the urban environment. Scientific Reports. 2019;9(1):17241.

Seleznev AA, Yarmoshenko IV, Malinovsky GP. Assessment of Total Amount of Surface Sediment in Urban Environment Using Data on Solid Matter Content in Snow-Dirt Sludge. Environ. Process. 2019. https://doi.org/10.1007/s40710-019-00383-w.

Seleznev AA, Yarmoshenko IV, Malinovsky GP, Kiseleva D, Leonova LV, Baglaeva EM, Ilgasheva EO. Anthropogenic particles in contemporary surface dirt sediments in an urban environment. Minerals: structure, properties, methods of investigation. Springer Proceedings in Earth and Environmental Sciences. 2020;221-227.

Shi X, Jungwirth S, Akin M, Wright R, Fay L, Veneziano DA, Zhang Y, Gong J, Ye Z. J. Transp. Eng. 2014;140.

https://www.google.ru/maps/@57.043446,60.581969,3a,90y,3.88h,30.83t/data=!3m8!1e1!3m6!1sAF1QipNXQkxg3B5dLnB-tuH5gF64OMmnd5zgaAuapyv7!2e10!3e11!6shttps:%2F%2Flh5.googleusercontent.com%2Fp%2FAF1QipNXQkxg3B5dLnB-tuH5gF64OMmnd5zgaAuapyv7%3Dw203-h100-k-no-pi-0-ya69.65704-ro-0-fo100!7i12000!8i6000?hl=ru

REE-Zr-U-Th-Nb-F Mineralization in Peraluminous Li-F Amazonite Granites of the Turga Massif: A New Geochemical Type of Rare-Metal Granites for Eastern Transbaikalia

Anna A. Ivanova, Elena V. Badanina, Liudmila F. Syritso, and Evgenia B. Borisova

Abstract

Unique accessory mineralization is recognized in the Turga massif of peraluminous Li-F granites in Eastern Transbaikalia. The abundance of rare LREE fluorides (fluocerite), fluorocarbonates (bastnaesite and parisite), and silicates (allanite), as well as (Y,REE,U,Th)–(Nb,Ta,Ti)-oxides (pyrochlore, samarskite) was found in the granites of this massif. The massif is characterized by a specific formation sequence manifested through a spontaneous rise in temperature at the stage of formation of microcline-albite granites with Li-siderophyllite of the main phase. This process is accompanied by the accumulation of a characteristic association of high field strength rare elements and fluorine. These features lead to a violation of the standard trend of rock evolution characteristic of the ore-bearing peraluminous granites of this region. The composition of accessory minerals and its evolution in the process of fractionation confirms the results of petrogeochemical studies of rocks and melt of this massif and provides a basis for attributing the Turga massif to a special geochemical subtype—peraluminous amazonite columbite-bearing granites of increased alkalinity with abundant Zr-REE-Th-U-Nb mineralization.

A. A. Ivanova (✉) · E. V. Badanina · L. F. Syritso · E. B. Borisova
Department of Geochemistry, Saint-Petersburg State University, Universitetskaya Emb. 7/9, 199034 Saint-Petersburg, Russia
e-mail: anna_al_ivanova@mail.ru

E. V. Badanina
e-mail: e.badanina@spbu.ru

E. B. Borisova
e-mail: jenyaborisova98@gmail.com

A. A. Ivanova · E. B. Borisova
Institute of Precambrian Geology and Geochronology, Russian Academy of Sciences, Makarova Emb. 2, 199034 Saint-Petersburg, Russia

S. Votyakov et al. (eds.), *Minerals: Structure, Properties, Methods of Investigation*, Springer Proceedings in Earth and Environmental Sciences,
https://doi.org/10.1007/978-3-030-49468-1_12

Keywords

Amazonite peraluminous Li-F granites · Eastern Transbaikalia · Accessory minerals · LREE fluorides and fluorcarbonates · Fluocerite · Bastnaesite · Allanite · REE-Y-Th-U-Zr-silicate-phosphate mineralization · (Y,REE,U,Th)–(Nb,Ta,Ti) oxides

1 Introduction

In Eastern Transbaikalia Ta deposits are associated with rare-metal Li-F amazonite granites (the Orlovka, Etyka, Achikan massifs). The Turga massif stands out on their background. Very low concentration of Li and Ta, which are ore elements conventional for such systems, is characteristic of this massif. The comparison of the whole rock composition of these massifs has revealed a number of features of the initial melt composition and the evolution ways of the Turga massif (Ivanova and Syritso 2018). The Turga intrusion is multi-formational and consists of two different age rock complexes: the Shakhtama monzodiorite-granodiorite (159.2 ± 3.7 Ma) and the Kukulbey granite-leucogranite (133.8 ± 1.2 Ma). Rare-metal mineralization is traditionally associated with the Kukulbey complex. The rocks of this complex are microcline-albite granites with Li mica and belong to the type of rare-metal peraluminous granites (Tauson 1977). The following rock differentiates are presented in the Turga massif: porphyritic biotite granites (Bt granites), microcline-albite granites with Li-siderophyllite (Li-Sdp granites), and amazonite granites with zinnwaldite (Amaz granites). The difference in the SiO_2 accumulation, a substantial increase of ferruginosity in Li-Sdp granites and REE and Zr accumulation as well as the non-linear development in the Rb-Sr coordinates of granites of the Turga massif was shown previously (Ivanova and Syritso 2018). A spontaneous rise of temperature at the stage of Li-Sdp granite crystallization (relative to earlier Bt granites) is a specific feature of the Turga massif formation. According to the data of temperature estimation by independent methods, including the distribution of Zr in the melt, Ti-in-zircon thermometry and zircon morphology, this difference is from 50 to 100 °C (Ivanova et al. 2019). There is a change in the rock geochemical specialization with the leading role of LREE, Zr, Th, U, an increase of mica ferruginosity, and an increase in F and CO_2 activity in these granites. The mineralogical distinctions of rare-metal granites of the Turga massif from the granites of the ore-bearing massifs in Eastern Transbaikalia are the absence of topaz and the typical structure of the "snow-ball quartz", incomplete evolutionary series of mica from biotite to zinnwaldite and the occurrence of ore mineralization in the form of Fe-columbite.

This paper presents the results of the accessory mineral study in the granites of the Turga massif.

2 Materials and Methods

Accessory minerals were studied in thin sections of granites and as monomineral fractions (up to 300 microns in size) from three types of granites. These minerals were studied by scanning electron microscopy. Raman spectroscopy was used to clarify the crystal chemical positions of elements in minerals. The studies were carried out at the Centre for Geo-Environmental Research and Modelling (GEOMODEL) of the Research Park of St. Petersburg State University using a Hitachi S-3400N scanning electron microscope and a Horiba Jobin-Yvon LabRam HR 800 Raman spectrometer.

3 Results and Discussion

As a result of the research, the following minerals were found in different granites of the Turga massif.

In early porphyritic Bt granites, accessory mineralization includes a set of minerals: zircon, garnet, F-apatite, fluorite, monazite, xenotime, ilmenorutile, and iron oxides.

In Li-Sdp granites, there is a sharp increase of species and chemical diversity of accessory mineralization. Along with the above minerals from Bt granites there is an abundance of minerals of LREE, U, Th, Nb, fluorides and fluorcarbonates here: Fe-columbite, pyrochlore and samarskite group minerals, cyrtolite, thorite and other minerals from the isostructural group of REE-Y-Th-U-Zr-silicate-phosphates, uraninite, (La,Ce)F_3 fluocerite, (Ce,La,Y)CO_3F bastnaesite, Ca(Ce,La)$_2$(CO_3)$_3F_2$ parisite, and (REE,Ca)$_2$(Al,Fe)$_3$[Si_2O_7][SiO_4]O[O,OH] allanite. The amount of zircon sharply increases in these granites, its habitus changes to high temperature morphology, and twins occur (Ivanova et al. 2019). The composition of zircon changes greatly, which is manifested through the abrupt rise in the ThO_2 and UO_2 contents up to 3 and 7 wt% on average, respectively, in some cases up to 15 wt%, and independent U-Th phases emerge in the form of microinclusions. Cyrtolite is predominantly developed.

A feature of the accessory mineralization of the late Amaz granites is the presence of cassiterite, sphalerite, and stibnite; the role of HREE increases—as at the rock level, there are Y-fluorite and yttrium silicates (presumably $Y_2Si_2O_7$ yttrialite).

Below we discuss some features of typochemical minerals from the Turga massif granites.

Fluorides. Fluorite is presented in all types of granites of the studied massif. In Li-Sdp granites, the volume content of fluorite increases, it develops from a number of accessory minerals to a number of secondary ones. However, while in the granites of early phases its composition corresponds to pure fluorite, Y-fluorite (Y_2O_3 content is about 5 wt%) occurs in Amaz granites. In Li-Sdp granites, fluorite replacement with fluocerite is common.

Fluocerite is presented in Li-Sdp and Amaz granites. In Li-Sdp granites, fluocerite sometimes forms well-faceted euhedral dipyramidal crystals with a size of 100–120 microns, while in Amaz granites such well-faceted crystals are not detected. Fluocerite often replaces fluorite and is replaced by bastnaesite. Its composition is quite stable (31.22–45.63 wt% Ce_2O_3, 9.06–27.44 wt% La_2O_3, 8.16–18.58 wt% Nd_2O_3, 2.57–4.79 wt% Pr_2O_3). In Amaz granites, there is a slight increase in the proportion of Th to 8.23 wt%, Ca to 2.1 wt%, Si up to 4.26 wt% among the impurities in fluocerite. The presence of oxygen up to 8 wt% is often recorded. In many cases fluocerite is replaced by bastnaesite, forming pseudomorphs of bastnaesite after fluocerite (Fig. 1a).

According to the researchers of amazonite granites of the Northern Tian Shan (Fel'dman et al. 1973), the presence of fluocerite in granitoids indicates increased alkalinity within the peraluminous petrochemical type. The authors call fluocerite "a typomorphic mineral of one of the subtypes of rare-metal granites, namely peraluminous amazonite-containing columbite-bearing granites".

Bastnaesite and parisite belong to the most recent paragenetic association. They develop mainly after fluocerite and allanite. According to the results of microprobe analysis, bastnaesite-(Ce) is mainly distributed with the content (in wt%) of the following elements: F—4.06–8.99, Ce_2O_3—31.85–50.5, Nd_2O_3—4.34–26.71, Pr_2O_3—1.91–4.93, Sm_2O_3—0–6.37, Ca—0–4.66, Y_2O_3—0–5.8, Th— 0–8.07. It is possible to assume the following sequence of mineral formation: fluorite → fluocerite → bastnaesite, as well as allanite → bastnaesite. The replacement of fluocerite occurs predominantly from the outer edge, and allanite is eroded from within by numerous cracks (Fig. 1).

Phosphates. Fluorapatite is well represented in Bt granites. In all types of granites, monazite is widespread, xenotime is less common. This is probably due to the general predominance of LREE in the composition of mineral-forming media or the special role of LREE complexes. Monazite from Bt granites has the maximum Th concentration for this massif (up to 22.82 wt%). In monazite from Li-Sdp granites,

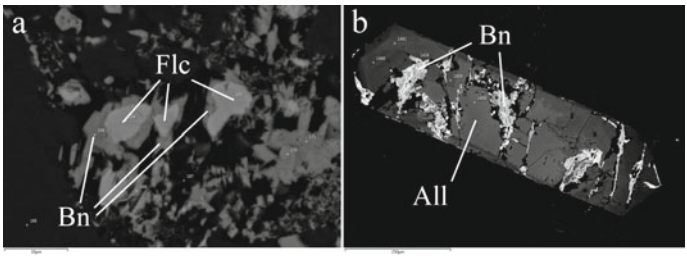

Fig. 1 The nature of the relationship between REE-minerals: **a**—replacement of fluocerite with bastnaesite; **b**—replacement of allanite with bastnaesite; Flc—fluocerite, Bn—bastnaesite, All—allanite

a growing role of LREE is noted; monazite from Amaz granites has high contents of REE and Y (Borisova et al. 2018). This fact is unusual, as the reverse trend is observed for monazite from rare-metal granite massifs (Erzgebirge, Germany) (Förster 1998).

The temperature of crystallization is estimated by the Gd distribution coefficient in coexisting monazite and xenotime (Borisova et al. 2018). For early Bt granites, the temperature ranges from 800 to 720 °C, for Li-Sdp granites >820 °C, for Amaz granites 750 ± 50 °C. The fact of increasing the crystallization temperature in Li-Sdp granites, proved by this technique, confirms our previous studies (Ivanova and Syritso 2018; Ivanova et al. 2019).

REE-Y-Th-U-Zr-Silicate-Phosphate Mineralization. Unlike typical peraluminous granites, where monazite is the main (up to 60–90%) Th and LREE concentrating mineral, and allanite and thorite are absent (Förster 2006), the granites of the Turga massif contain a large number of the latter. Zr, Th, U, REE, and Y phosphates and silicates in the form of independent phases and inclusions are found in all types of granites of the studied massif. The mineralogy of the Th-Y(HREE)-Zr-U system may be conveniently considered within the framework of isostructural intermediate solid solutions of the tetragonal thorite-xenotime-zircon-coffinite system (Förster 2006). The maximum distribution of these minerals is manifested through Li-Sdp granites. In early Bt granites there are mineral phases of huttonite group composition—(Ce,LREE)Th[PO_4]SiO_4 "cerphosphorhuttonite". In Li-Sdp granites, mainly thorite with U, Y and W admixture is developed. Thorite is often bordered by a hematite rim with an average thickness of 30 μ (Fig. 2). This phenomenon probably reflects an increase in ferruginosity at the stage of Li-Sdp granite formation, which is recorded in the whole-rock composition, and the replacement of biotite with Li-siderophyllite. There is a lot of U-Th-enriched zircon in the rock. The absence of LREE as impurities is most likely due to the formation of their own minerals. The role of HREE increases in Amaz granites, where thorite with the isomorphic admixture of xenotime predominates. Zircon is enriched in hafnium.

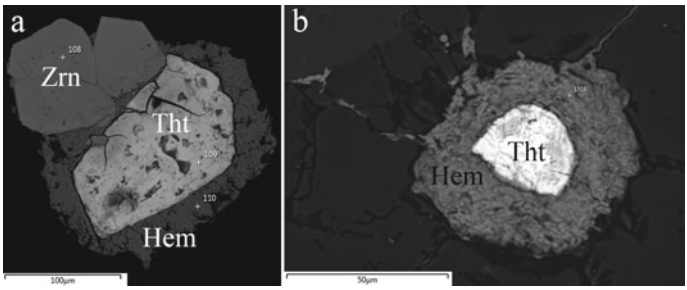

Fig. 2 Thorite with hematite rim: **a**—frequent association with zircon; **b**—thorite with hematite in feldspar; Tht—thorite, Zrn—zircon, Hem—hematite

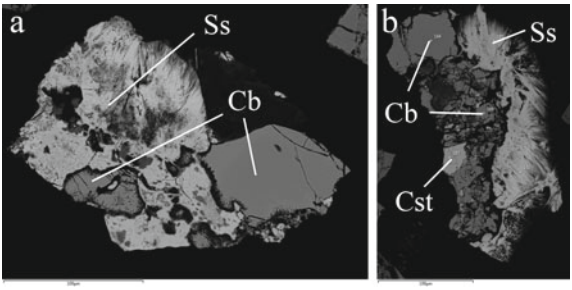

Fig. 3 Columbite and samarskite group minerals (ishikawaite?) from amazonite granites: Cb—columbite, Cst—cassiterite, Ss—samarskite group mineral

Columbite-Tantalite Group Minerals (CGM) and (Y,REE,U,Th)–(Nb,Ta,Ti) Oxides. In the Turga massif, the CGMs are represented exclusively by $Fe^{2+}Nb_2O_6$ ferrocolumbite with a low Mn and Ta content. In contrast to the Turga massif, the CGMs within the known ore-bearing massifs of the region are characterized by the presence of columbite-tantalite and microlite with a high Mn and Ta content (Melcher et al. 2017). Columbite from Li-Sdp granites shows some variation in Mn/(Mn + Fe) = 0.22 ± 0.09 at constant Ta/(Ta + Nb) = 0.04 ± 0.02, and columbite from Amaz granites – in Ta/(Ta + Nb) = 0.09 ± 0.06 at constant Mn/(Mn + Fe) = 0.27 ± 0.02. The crystals don't have zoning. Titanium (up to 2.9 wt% TiO_2, average 1.2) and tungsten (up to 5.4 wt% WO_3, average 2.2) prevail among the impurities, sometimes tin is present (up to 0.8 wt% SnO_2) (mainly in Li-Sdp granites). The veins of wolframoixiolite (?) in columbite are found.

Based on the method of (Y,REE,U,Th)–(Nb,Ta,Ti) oxide identification according to the canonical variables (Ercit 2005), we have found the presence of minerals from pyrochlore and samarskite groups in Li-Sdp and Amaz granites of the Turga massif. These minerals ($UFeNb_2O_8$ ishikawaite (?)) are often associated with columbite, the relationship between them is ambiguous (Fig. 3). At the same time, microlite is more typical for the ore-bearing massifs of this region, while samarskite is more typical for the granites from the Turga massif.

4 Conclusions

Mineralogical and geochemical studies give reason to believe that a specific set of minerals can, along with the geochemical characteristics of rocks, be a prerequisite for referring the Turga massif granites to a special subtype—peraluminous amazonite

columbite-bearing granites of increased alkalinity with abundant Zr-REE-Th-U-Nb mineralization. This mineralization can be considered typomorphic for a fundamentally new subtype of rare-metal granites in Transbaikalia region.

Acknowledgements Electron-microprobe analysis and Raman spectroscopy were carried out at the Centre for Geo-Environmental Research and Modelling (GEOMODEL) of the Research Park of St. Petersburg State University, by employees Natalia S. Vlasenko and Vladimir N. Bocharov. The study was supported by the Russian Foundation for Basic Research, project No.18-05-00957.

References

Borisova EB, Ivanova AA, Badanina EV. Aktsessornye mineraly Turginskogo massiva amazonitovykh granitov v Vostochnom Zabaikal'e. Novoe v poznanii protsessov rudoobrazovaniya: Vos'maya Rossiiskaya molodezhnaya nauchno-prakticheskaya Shkola, Moskva, 26-30 noyabrya 2018. Sbornik materialov - Elektron. dan. (1 fail: 45 MB) - M.: IGEM RAN, 2018. [Borisova EB, Ivanova AA, Badanina EV. Accessory minerals of the Turginsky massif of amazonite granites in Eastern Transbaikalia. New in the knowledge of the processes of ore formation: The Eighth Russian Youth Scientific and Workshop, Moscow, November 26-30, 2018. Proceedings. - Electron. Data. (1 file: 45 Mb) - IGEM RAN: Moscow, 2018. (in Russ.)].

Ercit TS. Identification and alteration trends of granitic-pegmatite-hosted (Y, REE, U, Th) – (Nb, Ta, Ti) oxide minerals: a statistical approach. The Canadian Mineralogist. 2005;43:1291 – 1303.

Fel'dman LG, Surkov BK, Stolyarova TI. Flyuotserit iz redkometal'nykh granitov Severnogo Tyan'-Shanya i nekotorye dannye k geneticheskoi mineralogii ftoridov redkozemel'nykh ehlementov. Trudy mineralogicheskogo muzeya. Vypusk 22. Novye dannye o mineralakh SSSR. Nauka: Moskva, 1973. 216 s. [Fel'dman LG, Surkov BK, Stolyarova TI. Fluocerite from the rare-metal granites of the Northern Tien Shan and some data on genetic mineralogy of rare-earth fluorides. Mineralogical Museum transactions. Issue 22. New data on USSR minerals. Nauka: Moscow, 1973. 216 p. (in Russ.)].

Förster H-J. The chemical composition of REE-Y-Th-U rich accessory minerals from peraluminous granites of the Erzgebierge-Fichtelgebirge region, Germany. Part I: The monazite (Ce) – brabantite solid solution series. American Mineralogist. 1998;83:259-272.

Förster H-J. Composition and origin of intermediate solid solutions in the system thorite-xenotime-zircon-coffinite. Lithos, 2006;88:35–55. https://doi.org/10.1016/j.lithos.2005.08.003.

Ivanova AA, Syritso LF, Badanina EV, Sagitova AM. Zircon from the Turga multiphase massif with amazonite granites (Eastern Transbaikalia) and its petrogenetic significance. Geol. Ore Deposits. 2019;61:707–721. https://doi.org/10.1134/S1075701519080051

Ivanova AA, Syritso LF. Geokhimicheskie predposylki bezrudnosti Turginskogo massiva amazonitovykh granitov v Vostochnom Zabaikal'e. Voprosy estestvoznaniya. Irkutsk. 2018;3(17):64-70. [Ivanova AA, Syritso LF. Geochemical preconditions for the barrenness of the Turginsky massif of amazonite granites in Eastern Transbaikalia. Voprosy estestvoznaniya. Irkutsk. 2018;3(17):64-70. (in Russ.)].

Melcher F, Graupner T, Gäbler H-E, Sitnikova M, Oberthür T, Gerdes A, Badanina E, Chudy T. Mineralogical and chemical evolution of tantalum–(niobium–tin) mineralisation in pegmatites and granites. Part 2: Worldwide examples (excluding Africa) and an overview of global metallogenetic patterns. Ore Geology Reviews. 2017;89:946-987. https://doi.org/10.1016/j.oregeorev.2016.03.014.

Tauson LV. Geokhimicheskie tipy i potentsial'naya rudonosnost' granitoidov. M., Nauka, 1977, 280 s. [Tauson LV. Geochemical types and ore-bearing potential of granitoids. Moscow, Nauka, 1977, p. 279 (in Russ.)].

FTIR, XRF and Powder XRD Experimental Study of Charoite: Crystal Chemical Features of Two Associated Generations

Ekaterina V. Kaneva, Tatiana A. Radomskaya, Roman Yu. Shendrik, Victor M. Chubarov, Alena A. Amosova, and Mikhail A. Mitichkin

Abstract

A collection sample of charoite rock from the Murun massif (Russia) was examined. Based on the textural and structural features, it was concluded that the sample comprised two charoite generations: the earliest one, so-called "block", and the second one, "schistose-goffered". A small amount (1–2 g) of each phase was used for sequential X-ray diffraction, X-ray fluorescence and FTIR absorption analyses. The obtained results allowed us to reveal some crystal chemical features of the early and later generations of the charoite specimen under study.

Keywords

Charoite · The Murun massif · Crystal chemistry · FTIR

1 Introduction

Charoite, $(K,Sr,Ba,Mn)_{15\text{-}16}(Ca,Na)_{32}[Si_{70}(O,OH_{180}](OH,F)_4 \cdot nH_2O$, is a unique valuable jewelry-ornamental stone, found only in alkaline rocks of the Murun massif (Yakutia, Russia). The mineral was originally described in 1978 (Rogova et al. 1978), and the crystal structure of charoite was solved only in 2009 using the

E. V. Kaneva (✉) · T. A. Radomskaya · R. Yu. Shendrik · V. M. Chubarov · A. A. Amosova · M. A. Mitichkin
Vinogradov Institute of Geochemistry SB RAS, 1A Favorsky str., 664033 Irkutsk, Russia
e-mail: kev604@mail.ru

E. V. Kaneva · T. A. Radomskaya · V. M. Chubarov
Irkutsk National Research Technical University, 83 Lermontov str., 664074 Irkutsk, Russia

S. Votyakov et al. (eds.), *Minerals: Structure, Properties, Methods of Investigation*,
Springer Proceedings in Earth and Environmental Sciences,
https://doi.org/10.1007/978-3-030-49468-1_13

methods of automatic electron diffraction tomography (ADT) and precession electron diffraction (PED) (Rozhdestvenskaya et al. 2010). Two polytypes with different unit cell parameters were identified: monoclinic "charoite-96" (Rozhdestvenskaya et al. 2010) and monoclinic, but with a pseudorhombic cell, "charoite-90" (Rozhdestvenskaya et al. 2011). In addition, there are other partially ordered and disordered polytypes ("charoite-2a" and "charoite-d" (Rozhdestvenskaya et al. 2011)), which are extremely rare. The crystal structure of charoite contains three different types of silicon-oxygen chains attached to a ribbon of Ca- and Na-octahedra extending along the [001] direction. The cavities formed in the structure are occupied by (K,Sr,Ba,Mn)-cations and H_2O molecules.

2 Materials and Methods

The sample under study is a piece of charoite rock that was polished on one side, 6.5 × 4.0 × 1.0 cm in size. It is composed of two generations of charoite (Fig. 1). The first, earliest generation (~75 vol.% of the sample) is the so-called "block" charoite (according to Vorob'ev (2008)). The aggregate is composed of densely accreted and elongated in one direction parallel-columnar thinnest charoite fibers. The length of individual crystals reaches 3–4 cm with a width of 1–2 μm. When exposed to light at different angles, the "block" charoite changes its color from light lilac with a characteristic silky shine to dark purple. There are four areas in the sample (1a, 1b, 1c and 1d on Fig. 1), inside which the charoite fibers are oriented equally relative to each other, but at an angle relative to the charoite fibers in the adjacent area. The width of the area varies from 0.5 to 2.0 cm.

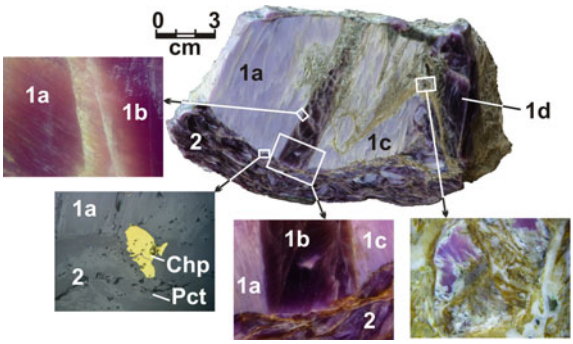

Fig. 1 The polished side of the sample with two generations of charoite: 1a, 1b, 1c, 1d—early "block" generation with different orientation of charoite crystal fibers in different blocks; 2—"schistose-goffered" generation of charoite. Cha—charoite, Chp—chalcopyrite

The second generation of charoite occupies about 15 vol% of the sample. It is assigned to the "schistose-goffered" morphological modification (according to Vorob'ev (2008)). The needle-fibrous crystals of charoite grow together tightly into numerous small aggregates, up to 0.5–1.0 cm long and up to 0.2 mm wide, which gives a slate-curved texture of this generation (2 on Fig. 1). The color of the "schistose-goffered" aggregates changes from light purple with a silky shine to dark violet. The small grains of pectolite in small quantities are associated with this charoite.

Copper and lead sulfides were found among charoite aggregates. Moreover, the intergrowth of galena and chalcopyrite was detected in the early generation ("block" charoite) (Fig. 1), whereas in the late generation ("schistose-goffered") charoite, chalcopyrite grains were found, sometimes in paragenesis with sphalerite. A part of the chalcopyrite grains was located on the border of various generations of charoite. The unpolished side of the sample was affected by secondary changes: here charoite was replaced by apophyllite. On the polished side of the sample, apophyllite filled the cracks.

Due to the fact that the sample has a decorative, artistic and commercial value, it cannot be destroyed. Therefore, a realization of analytical routines for the sample investigation was a difficult task. For the study of both generations, the minimum required amount of material was selected ($\sim$1–2 g). The samples were sequentially used for all types of analyses mentioned below.

The chemical composition was determined by the X-ray fluorescence method. Measurements were performed by a S4 Pioneer wavelength-dispersive X-ray fluorescence spectrometer (Bruker AXS, Germany). The powders were calcinated at 950 °C to determine the loss on ignition (LOI) values. Then a portion (500 mg) of calcinated sample was mixed with 7.5 g of lithium borate flux (33% of lithium metaborate and 67% of lithium tetraborate) with the addition of 7 drops of 4% LiBr solution) and fused in platinum crucibles in a TheOX (Claisse, Canada) electric furnace at 1050 °C. The calibration equation was constructed using the certified reference materials of igneous and sedimentary rocks.

Powder X-ray diffraction data were obtained using a D8 ADVANCE diffractometer (Bruker) equipped with a scintillation detector and a Göbel mirror. The radiation source was CuKα. The data were recorded in the step-scan mode in the range of 2θ diffraction angles from 3 to 80°. Experimental conditions were the following: 40 kV, 40 mA, time per step—1 s and step size—0.02° 2θ. The data processing was performed using the DIFFRACplus software package. The unit cell parameters were refined using TOPAS 4 software (Bruker 2008).

Infrared absorption spectra were obtained using an FT-801 FTIR spectrometer (Simex). Charoite was mixed with pre-dehydrated KBr and compressed into a tablet weighing 20 mg. The infrared spectra were acquired from 5300 to 450 cm^{-1}.

3 Results and Discussion

The results of the wavelength-dispersive X-ray fluorescence analysis of powder samples of two charoite generations under study are given in Table 1. The sum of the components is somewhat underestimated as compared, for example, with the data by Gladkochub (2016) (~93 wt% *vs* 95–96 wt%). However, they are consistent with the data by Rozhdestvenskaya (2010) (~93 wt% *vs* 92 wt%). Losses on ignition (LOI) are 6.51 and 6.55% for generations 1 and 2, respectively. In our samples, the Na_2O and K_2O content is lower relative to Rozhdestvenskaya et al. (2010) and Gladkochub (2016) (possibly included in the LOI).

Table 1 also presents the calculated parameters of the unit cell of the two polytype using the TOPAS software (Bruker 2008). The initial unit cell parameters and the atomic coordinates required for the calculations were taken from Rozhdestvenskaya et al. (2010) for "charoite-90" and Rozhdestvenskaya et al. (2011) for "charoite-96", respectively. According to Rozhdestvenskaya and Drits (2013), monophasic specimens of charoite are extremely rare. In addition to the two polytypes, after careful selection, impurity phases remain in the samples, complicating the powder diffraction pattern. Thus, apophyllite and pectolite have been diagnosed in the samples.

The normalized infrared absorption spectra of two charoite generations are given in Figs. 2 and 3. The group of peaks at 1116, 1100, 1084, 1056, 1015, 958, 935 cm^{-1} (Fig. 2) are assigned to asymmetric Si-O stretching modes of the SiO_4 tetrahedra, while the sharp peak in mid-frequency range from 703 to 610 cm^{-1} can

Table 1 Experimental crystal chemical data for the "block" and "schistose-goffered" generations of charoite, obtained by X-ray fluorescence and X-ray diffraction analyses

"Block generation" (1a, 1b, 1c and 1d on Fig. 1)				"Schistose-goffered generation" (2 on Fig. 1)			
Chemical composition according to XRF data (wt%)							
SiO_2	59.21	Al_2O_3	0.21	SiO_2	58.68	Al_2O_3	0.11
Na_2O	1.98	K_2O	7.51	Na_2O	1.80	K_2O	7.66
CaO	21.08	MnO	0.19	CaO	21.61	MnO	0.20
BaO	2.03	Sr	0.81	BaO	1.96	Sr	0.79
Zr	0.01	LOI	6.51	Zr	0.01	LOI	6.55
Total	99.54			Total	99.37		
Unit cell parameters for the polytypes (Å, °, $Å^3$), sp. gr. $P2_1/m$							
"charoite-90"							
a = 32.05(1); b = 19.67(1); c = 7.16(1); β = 90.07(2); V = 4514(2)				a = 32.08(2); b = 19.68(1); c = 7.16(1); β = 90.03(7); V = 4523(4)			
"charoite-96"							
a = 32.20(2); b = 19.67(1); c = 7.24(1); β = 94.87(4); V = 4570(3)				a = 32.19(3); b = 19.67(2); c = 7.25(1); β = 94.97(5); V = 4570(6)			
Ratio "charoite-90":"charoite-96" (%)							
75:25				70:30			

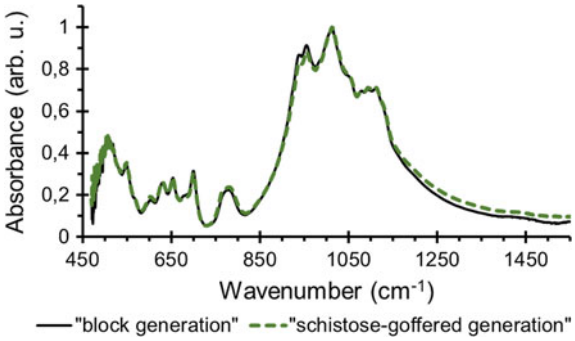

Fig. 2 Relative absorbance of the "block" and "schistose-goffered" generations of the studied charoite (450–1550 cm^{-1} range of absorption spectra)

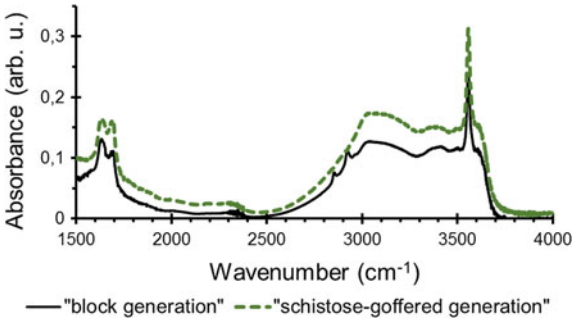

Fig. 3 Relative absorbance of "block" and "schistose-goffered" generations of the studied charoite in the water absorption region of spectra

be attributed to Si-O-Si bending mode as well as symmetric O-Si-O stretching vibrations (Infrared et al. 2001). Peaks at about 570 and 787 cm^{-1} can be assigned to symmetric Si-O and O-SiO vibrations, respectively (Gittins et al. 1976). The peak at about 553 cm^{-1} can correspond to the Ca-O stretching.

The band positions observed in the 1500–1400 cm^{-1} range and their assignment are given in Table 2. The table also contains the literature IR data for charoite. In charoite samples, strong wide bands in the 3000–3700 cm^{-1} spectral region correspond to symmetric and asymmetric stretching vibration of H_2O molecules (Fig. 3); they are bands peaked at 3111, 3429 and 3597 cm^{-1}. The sharp peak at 3556 cm^{-1} can correspond to stretching modes of OH-ions. Two bands in the region of 1631 and 1688 cm^{-1} are associated with the H_2O bending vibrations. Both samples contain similar amounts of SiO_2 and CaO. Therefore, a comparison of H_2O and OH amounts in the samples can be related to the OH and H_2O band

Table 2 Band position (cm^{-1}) of H_2O and OH in the IR spectra of the studied charoite samples and literature data

This study	Lacalamita (2018)	Rogova (1978)	Band assignment
1688, 1631	1667, 1595	1650, 1620, 1590	H_2O bending
3111, 3429, 3597	3453, 3385, 3285, 3150	3610, 3550, 3500, 3410	H_2O stretching
3556	3530		OH stretching

intensities with symmetric Si-O or Ca-O stretching modes. In general, the position and configuration of the bands in the frequency range of the H_2O and OH vibrations of both samples show a complete analogy, but there are slight differences in their intensities. The result indicates an increased content of H_2O and OH groups in the charoite sample, which belongs to the second, "schistose-goffered generation".

Figure 4 shows the thermal dehydroxylation curves of "schistose-goffered" generation of the charoite sample. There are bands measured at 3111, 3429, 3556, 3597, 1688 and 1631 cm^{-1} (Table 2). The figure shows the relative intensities of the hydroxyl and H_2O bands in the samples quenched over the temperature range from 25 to 750 °C at 50 °C intervals. The diagram clearly shows that there are three groups of lines. OH^- absorption (the band at 3556 cm^{-1}) disappears completely at 400 °C. For the bands at 3111 and 1688 cm^{-1}, assigned to the stretching and bending vibrations of H_2O, respectively, dehydroxylation mostly takes place at the 200 to 450–500 °C temperature range. The absorbance of another group of bands belonging to H_2O molecule vibrations (3429 cm^{-1}—stretching and 1631 cm^{-1}—bending) drops to zero at 650 °C. Finally, for the band at 3597 cm^{-1}, dehydroxylation completely disappears above 750 °C.

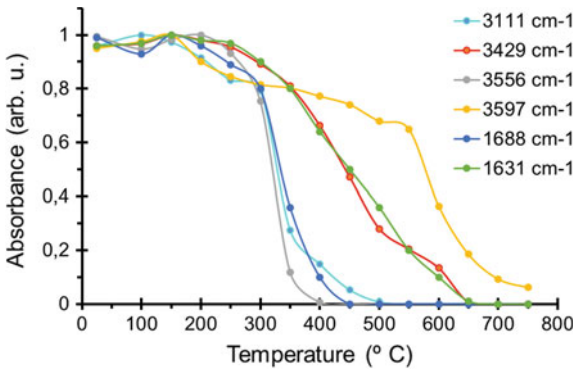

Fig. 4 Thermal dehydroxylation curves measured at 3111, 3429, 3556, 3597, 1688 and 1631 cm^{-1} for the "schistose-goffered generation" of the studied charoite sample

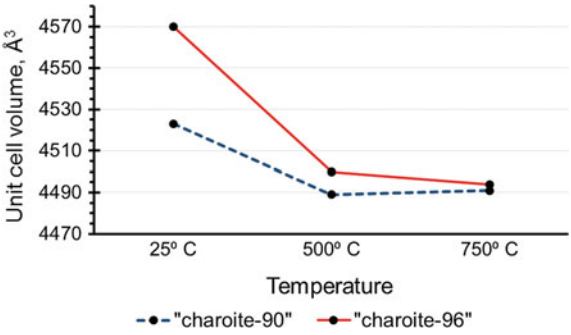

Fig. 5 The dependence of the change in the unit cell volume on temperature for "charoite-90" and "charoite-96" polytypes of the "schistose-goffered generation"

Thus, there are three water environments in the charoite structure with different removal temperatures. This fact confirms the results of the "charoite-90":"charoite-96" ratio calculation (Table 1) and verifies the prevalence of the "charoite-90" polytype in the sample. It contains three H_2O sites (Rozhdestvenskaya et al. 2010), while the "charoite-96" has only one H_2O site in the crystal structure model (Rozhdestvenskaya et al. 2011).

Investigating the process of dehydroxylation of the generation more enriched in water, it is necessary to pay attention to the changes in the unit cell parameters. Using the TOPAS software (Bruker 2008), the unit cell volumes of "charoite-90" and "charoite-96" polytypes in the "schistose-goffered" sample were calculated after heating at 500 and 750 °C. The dependence of the volume of the unit cell on temperature is shown in Fig. 5. It is clearly visible that the unit cell volume significantly decreases at 500 °C, corresponding to the H_2O and OH-group removal from the structure. Then, when heated to 750 °C, the unit cell volume ceases to change greatly. However, according to IR spectroscopy and XRD data, the second type of H_2O is removed from the crystal structure without any obvious effect on its unit cell parameters in the range from 500 to 750 °C (at about 650 °C, see Fig. 4).

The "charoite-90":"charoite-96" ratio does not change after heating. It means that one modification of charoite does not transfer into another.

4 Conclusions

According to the textural and structural features of the sample under study, two generations of charoite have been distinguished. They are similar in chemical composition and crystal structural features. However, as it follows from the obtained data, the processes of formation of the early generation ("block") occurred with a low rate of change in the temperature gradient. It led to the crystallization of

long parallel-columnar fibers forming block aggregates of charoite. The residual mineral-forming media seems to contain a greater amount of aqueous fluid and impurities. It led to the crystallization of the late generation "schistose-goffered" charoite.

Acknowledgements The study was performed using the equipment of the "Isotopic-geochemistry investigations centre" of Collective Use Center of A.P. Vinogradov Institute of Geochemistry SB RAS.
This work was supported by the grant of the President of the Russian Federation No. MK-936.2019.5.
The experiments on thermal dehydroxylation were supported by the grant of the Russian Science Foundation RSF 18-72-10085.

References

Bruker AXS. Topas V4: General profile and structure analysis software for powder diffraction data (User's Manual, Bruker AXS, Karlsruhe, Germany). 2008.

Gittins J, Bown MG, Sturman D. Agrellite, a new rock-forming mineral in regionally metamorphosed agpaitic alkali rocks. Can. Min. 1976; 14:120–126.

Lacalamita M. Micro-FTIR and EPMA characterisation of charoite from Murun massif (Russia). J. Spectroscopy. 2018. https://doi.org/10.1155/2018/9293637.

Marchuk MV, Medvedev VYa, Ivanova LA, Sokolova TS, Danilov BS, Gladkochub DP. Charoite. Experimental studies. Geodyn. Tectonoph. 2016;7(1):105–118. https://doi.org/10.5800/GT-2016-7-1-0199.

Rozhdestvenskaya IV, Drits VA. Peculiarities of the charoite X-ray powder diffraction pattern. Zap. Vseross. Mineral. Obsh. 2013;142(4):101–112.

Rozhdestvenskaya I, Mugnaioli E, Czank M, Depmeier W, Kolb U, Merlino S. Essential features of the polytypic charoite-96 structure compared to charoite-90. Min. Mag. 2011;75(6):2833–2846. https://doi.org/10.1180/minmag.2011.075.6.2833.

Rogova VP, Rogov YG, Drits VA, Kuznetsova NN. Charoite, a new mineral, and a new jewelry stone. Zap. Vses. Mineral. Obsh. 1978;107(1):94–100. (In Russ.).

Rozhdestvenskaya I, Mugnaioli E, Czank M, Depmeier W, Kolb U, Reinholdt A, Weirich T. The structure of charoite, $(K,Sr,Ba,Mn)_{15\text{-}16}(Ca,Na)_{32}[Si_{70}(O,OH_{180}](OH,F)_4{\cdot}nH_2O$, solved by conventional and automated electron diffraction. Min. Mag. 2010;74(1):159–177. https://doi.org/10.1180/minmag.2010.074.1.159.

Socrates G. Infrared and Raman characteristic group frequencies: tables and charts. John Wiley & Sons Ltd., 2001.

Vorob'ev EI. Charoite. Academy Publishing "Geo", Novosibirsk, 2008. (In Russ.).

Glauberite-Anhydrite Solid Solution from the Tenoritovaya Fumarole (Tolbachik Volkano, Kamchatka)

Dmitry A. Khanin and Valery M. Chubarov

Abstract

The fumarolic formations of GTFE (The Great Tolbachik Fissure Eruption of 1975–1976) slag cones are a great place to study the processes of mineral formation at high temperatures (500 °C) and atmospheric pressure. In fumaroles, along with simple halides of alkali metals (halite and sylvite), a variety of sulfates is also widespread. In fumaroles, they occur as primary sulfates, caused by gas jets, and secondary redeposited ones with the participation of meteoric waters. For the study, anhydrous sulfates were selected from sufficiently high-temperature areas of several fumaroles. The study of exsoluted glauberite-anhydrite solid solutions, as well as associated halite and sylvite was conducted.

Keywords

Fumaroles · Kamchatka · The Great Tolbachik Fissure Eruption · Glauberite-anhydrite solid solution · Exsolution structures

D. A. Khanin (✉)
Institute of Experimental Mineralogy RAS, 4 Akademika Osipyana str., 142432 Chernogolovka, Russia
e-mail: d_khanin@iem.ac.ru

D. A. Khanin · V. M. Chubarov
Institute of Volcanology and Seismology FEB RAS, 9 Piip Boulevard, 683006 Petropavlovsk-Kamchatsky, Russia

S. Votyakov et al. (eds.), *Minerals: Structure, Properties, Methods of Investigation*,
Springer Proceedings in Earth and Environmental Sciences,
https://doi.org/10.1007/978-3-030-49468-1_14

1 Introduction

The rich and diverse mineralogy of active fumaroles of the oxidative type of the Tolbachik Volcano (Kamchatka) has been studied for more than 50 years. The most widespread are the sulfates of alkali and alkaline earth metals. Among the primary anhydrous sulfates, anhydrite is the most widespread, but it also contains aphthitalite $K_2Na_2(SO_4)_2$, langbeinite $K_2Mg_2(SO_4)_3$, metathenardite and thenardite Na_2SO_4, glauberite $Na_2Ca(SO_4)_2$, bubnovaite $K_2Na_8Ca(SO_4)_6$, calciolangbeinite $K_2Ca_2(SO_4)_3$, vanthoffite $Na_6Mg(SO_4)_4$, arcanite K_2SO_4, and ivsite $Na_3H(SO_4)_3$. These minerals are most widely represented on the Arsenatnaya and Yadovitaya fumaroles and to a lesser extent on the Tenoritovaya fumarole. All of them are located on the Second Slag Cone of the Northern Breakthrough of the Great Tolbachik Fissure Eruption of 1975–1976 (GTFE). Sulfate mineralization is also common in fumaroles, which were formed during the eruption of 2012–2013. Most of these minerals are easily soluble in water and highly hygroscopic, and it is not always possible to accurately diagnose them and determine the nature of the relationship with other minerals.

2 Materials and Methods

The samples of salts (halite and sylvite) from the hottest part of the Tenoritovaya fumarole located on the Second slag cone of the Northern Breakthrough of the GTFE were studied by scanning electron microscopy (SEM). The photo and compositions of samples were investigated using a VEGA-3 scanning electron microscope with an XMax 80 (Oxford Instruments) energy dispersion spectrometer and an Aztec^{TM} software (Institute of Volcanology and Seismology, Russian Academy of Sciences, Petropavlovsk-Kamchatsky). The analytical conditions were as follows: accelerating voltage 20 kV, beam current 0.7 nA, counting live time 20 s. EDS data was processed using an Aztec^{TM} software. The samples were carbon-sputtered prior to analysis.

3 Results and Discussion

When studying the samples of halite and sylvite, the intergrowths of prismatic crystals up to 200 μm along the long axis were found in white dense halite crusts, which were composed of exsoluted glauberite-anhydrite solid solution (Fig. 1).

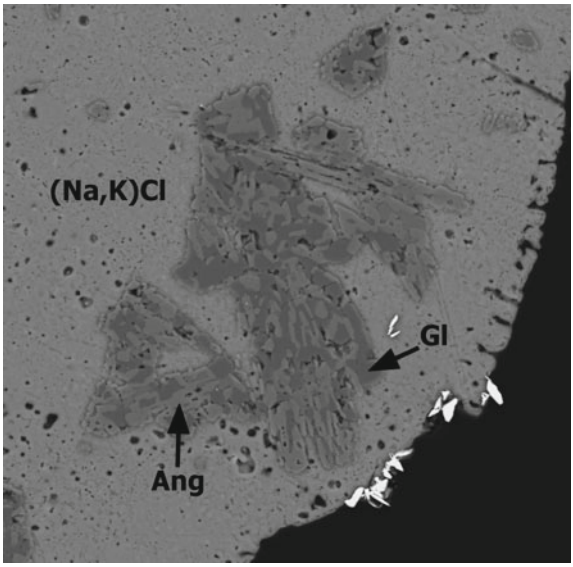

Fig. 1 The structure of the decomposition of a solid solution of glauberite (Gl) and anhydrite (Ang) in halite (Na, K) Cl. Back-scattered electron image. The width of field is 200 μ

Previously, Shchipalkina (2018) described the exsolution structures of various sulfates with aphtalite-like structure from the Arsenatnaya fumarole, which had a higher temperature regime.

It should be noted that in halite, from which the crusts are folded, has a constant admixture of K from 2 to 3.5 wt%, as well as Cs up to 0.2 wt%, which distinguishes it from the similar halite from the Arsenatnaya fumarole, where cesium is practically absent (Khanin and Chubarov 2018).

In the anhydrite precipitated from the solid solution, MgO impurities up to 0.1 wt%, SrO up to 0.2 wt%, SiO_2 up to 0.2 wt%, K_2O up to 0.8 wt% and Na_2O up to 1.5 wt% are observed. In glauberite, there is an admixture of MgO up to 0.1 wt%, SrO up to 0.2 wt% and K_2O up to 0.6 wt%.

In the fumarole, anhydrite is widely distributed at all temperature levels. In addition to the exsolution structures, glauberite was also observed in a single sample of halite from the fumarole's high-temperature part. Here, glauberite grows on bubnovaite and forms exsolution structures with it (Fig. 2). This glauberite is characterized by the presence of SrO up to 0.1 wt%, Cs_2O up to 0.2 wt% and BaO up to 0.2 wt%, but in the salt growing on them, cesium is not observed, as in the bubnovaite itself.

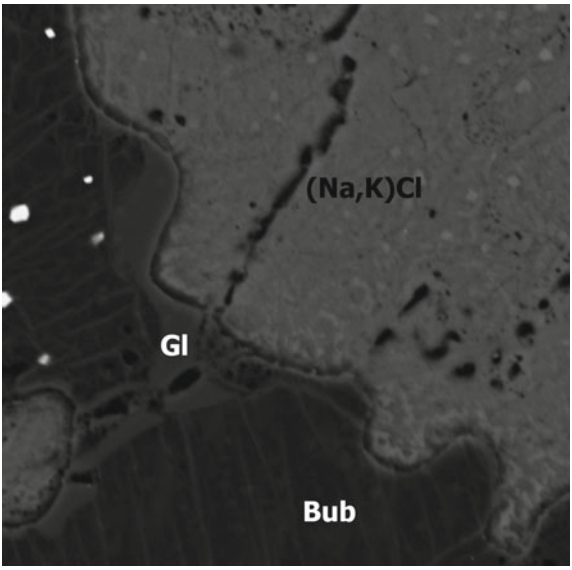

Fig. 2 Crust of glauberite (Gl) on bubnovaite (Bub) in halite (Na, K) Cl. Back-scattered electron image. The width of field is 100 μ

4 Conclusions

The crystallization of the primary solid solution from the gas phase occurred at a temperature of more than 800 °C. With a decrease in temperature (to about 350 °C), a stable metaphase disintegrated into more stable ones—anhydrite and glauberite, which were enriched in sodium and calcium, respectively. This process is in good agreement with the conditions proposed by Du (2000) for simpler binary systems.

Acknowledgements This study was supported by the Russian Foundation for Basic Research, grant no. 20-35-70008.

References

Du H. Thermodynamic Assessment of the K_2SO_4-Na_2SO_4-$MgSO_4$-$CaSO_4$ System. Journal of Phase Equilibria. 2000;21(1):1-18.

Khanin DA, Chubarov VM. About the Features of Exsolution Phenomena of NaCl-KCl Solid Solutions from Arsenatnaya Fumarole (Tolbachik Volcano, Kamchatka). Abstracts of the IX All-Russian Conference "Minerals: structure, properties, research methods". Institute of Geology and Geochemistry named after Academician A.N. Zavaritsky UB RAS, Ekaterinburg, 2018. P. 198–199.

Shchipalkina NV. Chemical Features and Disintegration Structures of Exhalation Aphtalitic-Like Sulfates from Arsenate Fumarole (Tolbachik Volcano, Kamchatka). Proceedings of the International Youth Scientific Forum LOMONOSOV-2018. MAX Press Moscow, 2018.

Concentrically-Zoned Mafic-Ultramafic Marinkin Massif, Middle Vitim Highland, Baikal Region, Russia: Inclusions in Chrome Spinel—Key to Mineral Formation Processes

Evgeniy V. Kislov, Vadim S. Kamenetsky, Alexey V. Malyshev, and Vladislav V. Vanteev

Abstract

The concentrically zoned Marinkin massif belongs to an island arc association. The massif was formed at the Neoproterozoic stage of mafic-ultramafic magmatism in the South-Eastern folded frame of the Siberian platform. Dunites and plagioclase dunites compose an ellipse-like core with an area of 2 km^2. The intrusion is related to the formation of the Baikal-Muya oceanic basin of the Paleoasian Ocean and the Kelyana island arc system. The features of the Marinkin massif composition, petrology and mineralogy demonstrate considerable thermal and fluid influence of recent granites. The ultramafic rocks were regenerated resulting in the alteration of mafic rocks. The disseminated sulfides of liquid origin had formed a veinlet nickel-copper sulfide mineralization as a result of dunite regeneration. Chromitite mineralization also occurred during the

E. V. Kislov (✉) · A. V. Malyshev · V. V. Vanteev
Geological Institute, Siberian Branch RAS, 6a Sakhyanovoy str., 670047 Ulan-Ude, Russia
e-mail: evg-kislov@ya.ru

V. V. Vanteev
Buryat State University, 24a Smolina str., 670000 Ulan-Ude, Russia

V. S. Kamenetsky
University of Tasmania, Hobart, Australia
e-mail: dima.kamenetsky@utas.edu.au

V. S. Kamenetsky
Institute of Experimental Mineralogy RAS, 4 AkademikaOsipyana str., 142432 Chernogolovka, Russia

S. Votyakov et al. (eds.), *Minerals: Structure, Properties, Methods of Investigation*,
Springer Proceedings in Earth and Environmental Sciences,
https://doi.org/10.1007/978-3-030-49468-1_15

regeneration of dunites. The lack of serpentine, the composition of non-magmatic inclusions in chrome spinels, olivines and sulfides, the inhomogeneity of chrome spinel grains, olivine lamellas, euhedral chlorite grains, and pure isometric magnetite grains without titanium indicate that phenomenon.

Keywords

Concentrically zoned massif · Nickel-copper sulfide mineralization · Chromitite · Dunite regeneration

1 Introduction

The Marinkin dunite-troctolite-gabbro massif is located around the Marinkin creek on the right bank of the Tuldun River (left tributary of the Vitim river) in the Baikal region. The massif was mapped by G.A. Kibanov in 1961–1963. V.S. Kosinov noted disseminated sulfides and chromitite in 1964 during geological mapping 1:50,000. E.L. Prudovsky studied the intrusion in detail, including the copper-nickel mineralization zones and asbestos in 1968. He named the massif after his daughter. The pluton's petrology was subsequently studied and reported in review monographs (Grudinin 1979; Balykin 1986; Tsygankov 2005) and conference proceedings (Prudovskiy and Grudinin 1972; Kislov et al. 2009; Kislov et al. 2009; Kislov et al. 2018a, b; Kislov et al. 2019). We have studied the nickel-copper sulfide and chromitite mineralization genesis.

2 Materials and Methods

Trace element analyses were made at the Center for collective use of scientific equipment for multi-element and isotope research, Siberian Branch, Russian Academy of Sciences (Novosibirsk) by the inductively coupled plasma mass-spectrometry (ICP-MS) with $LiBO_2$ fusion.

Sulfur isotope analyses were conducted at the Laboratory of stable isotopes, Analytical Center, Far Eastern Branch of Russian Academy of Sciences (Vladivostok) on a Finnigan MAT 253 double focusing isotope mass spectrometer.

Samples of dunites with disseminated chrome spinels were mounted in epoxy resin and dry polished with 800 μm grit paper to 1 μm oil-based diamond compound and cleaned with petroleum-based solvent (shellite). All grinding and polishing procedures were carried out using kerosene as a lubricant to avoid any damage to the soluble contents of the samples. Coarse-grained polishing paper was also avoided as the contrast in hardness between silicates and carbonates in the

samples can result in the loss of the softer carbonates. Samples were analyzed with a Hitachi SU-70 field emission scanning electron microscope (SEM) at the University of Tasmania (Hobart, Australia).

The standard polished sections mounted in epoxy resin were analyzed at the Analytical Center of mineralogical, geochemical and isotope studies of the Geological Institute, Siberian Branch of Russian Academy of Sciences (Ulan-Ude) on a Carl Zeiss LEO 1430VP scanning electron microscope with an Oxford Instruments INCA Energy 350 X-Ray energy dispersive spectrometer.

3 Results and Discussion

3.1 The Marinkin Massif

The age of intrusion is 825 ± 12 million years as estimated by the Sm–Nd method (Izokh et al. 1998). The host granites are similar to the plagiogranites of the Krivoy creek with an age of 815 million years (Rytsk et al. 2001), earlier associated with the Muya gabbro-diorite-plagiogranite complex.

Pluton is traced for 5.5 km along the long axis in the northwest direction (320–330°). The maximum width in the northwest part is 4 km, an average width is 2 km, the area is 11 km^2. The massif is penetrated by the Marinkin creek down the cutting about 700 m in the vertical direction. The basic metamorphized effusives are exposed in the creek channel at the intrusion bottom.

The massif is concentrically zoned. Dunites and plagioclase dunites compose an ellipse-like core with an area of 2 km^2. Serpentinites and serpentine-actinolite rocks are developed over the dunites. Gabbros and troctolites are replaced by zoisite and zoisite-saussurite-actinolite rocks almost everywhere. The small blocks of fresh mafic rocks are observed near ultramafic core. Ultramafic and mafic rocks are connected by mutual transitions and are considered as intrachamber differentiates.

Minerals are fairly constant in their composition. Olivine is represented by its chrysolite variety (f = 9–16.3%), plagioclase by bytownite, less often by ($An_{70–94}$) anorthite, clinopyroxene by subcalcic low-aluminous high-magnesian augite (f = 13–23%), orthopyroxene by alumobronzite (f = 16.2%), and amphibole by low-titanium hornblende (f = 19%); Cr_2O_3 content in chrome spinel is 19–32% (Balykin et al. 1986). Na_2O concentration in the rocks varies from 0.01 to 1.25%, K_2O reaches 0.11%.

The Marinkin massif belongs to an island arc association (Tsygankov 2005). REE distribution patterns of the Marinkin massif are similar to those of other island arc massifs, such as Akkermanovsky, Kirpichninsky, Galmoenan, Lukindinsky, Munilkan, Nurali, and the Ural platinum belt. The massif was formed at the Neoproterozoic stage of mafic-ultramafic magmatism in the South-Eastern folded frame of the Siberian platform. The intrusion is related to the formation of the Baykal-Muya oceanic basin of the Paleoasian Ocean and the Kelyana island arc system.

3.2 Sulfide Mineralization

Nickel-copper sulfide mineralization is localized in the ultramafic core. Both areal disseminated sulfides and linear zones of nest-like and veinlet mineralization are observed. The disseminated mineralization is presented mainly and is typical for all rocks. The amount of sulfides usually does not exceed 0.5–1% of the rock. Fine grains of pentlandite and troilite are characteristic of such mineralization. Monomineral grains are rare. Small drop-like inclusions of sulfides are observed in olivine.

Two zones of nest-like and veinlet mineralization of 100 × 500 and 100 × 750 m in size striking to the North-West are discovered (Prudovskiy and Grudinin 1972). Maximum contents are: Ni—up to 0.6%, Co—0.08%, Cu—0.15%. The content of sulfides exceeds 10% in breccia rocks. Their branchy veinlets up to 10–15 cm long and 0.1–0.2 cm wide are found. Sulfide lenses up to 1.0–1.5 cm long and sulfide grains up 0.5–2.0 mm, rarely 2–4 mm in size are observed. Pyrrhotite and pentlandite prevail, chalcopyrite is found less often. Chrome spinel and magnetite are frequent, while chalcocite and violarite are the minor minerals.

We have analyzed the sulfur isotope composition of pyrite from the bottom amphibolite sampled on the Marinkin creek bank in the central part of the intrusion, and pentlandite and troilite from dunite in the central part of ultramafic core (Table 1).

The sulfur isotope ratios in sulfides of intrusive and host rocks vary within very narrow limits, which demonstrates the sulfur source uniformity. The ratios are insignificantly heavier than the meteoric standard, which corresponds to its mantle origin. Sulfur could be introduced to the host rocks from magma. It is also impossible to exclude the assimilation of sulfur by magma from the host rocks, but the effusive origin of amphibolite contradicts this version.

3.3 Chrome Spinels and Chromitites

The ultramafic rocks of the Marinkin massif contain the grains of accessory chrome spinel from 2 to 10%. Chrome spinel is disseminated in dunite irregularly and forms isometric grains and octahedrons from 0.0n to 0.6 mm in size. Small crystals form

Table 1 Sulfur isotope composition of sulfides from the intrusive and host rocks of the Marinkin massif

Sample No.	Mineral	Rock	$\delta^{34}S$, ‰ (CDT)
M-13/1-08	Pyrite	Amphibolite	2.2
M-13/2-08	Pyrite	Amphibolite	1.4
M-8/1-08, M-8/2-08	Pentlandite, troilite	Dunite	1.6

The analyses were conducted at the Laboratory of stable isotopes of the Analytical Center, FEB RAS (Vladivostok) on a Finnigan MAT 253 double focusing isotope mass spectrometer. Analyst T.A. Velivetskaya

inclusions in olivine. Larger crystals, being close, are localized in joints of olivine grains. Chrome spinel contains inclusions. The chrome spinel in troctolites forms small (up to 0.5 mm) evenly scattered octahedrons with frequent inclusions, which are found both in the interstices and in plagioclase, and more rarely - in olivine. The Cr_2O_3 concentration in dunites reaches 1.5%.

Massive and nest-like chromitites in the dunite core were described by Kosinov and Prudovsky (1972). The chromitites compose a linear zone about 300 m long and about 1 m thick, traced by fragments and blocks in talus. Chromitite fragments are also noted elsewhere in the dunite core. Chromitites represent medium-grained black rocks with roundish grains of brown olivine. The olivine concentration increases to 30–50% in the contact parts of the ore zone, the chromitite grains have a spotty outlook.

Chrome spinel forms crystals with the prevailing octahedron form and xenomorphic grains up to 3–4 mm in size. Their content is up to 90% in massive chromitites. Chrome spinel often contains mineral inclusions. Chromitites contain olivine grains and clusters of crystals. These olivine peripheral parts contain up to 20–30% of small chrome spinel inclusions on the border with chrome spinel. The central part of olivine grains is free from them. Chrome spinel is sometimes surrounded by magnetite rims on the peripheral or contains magnetite plates. Olivines, carbonates and pentlandites are observed in the interstices. Pentlandite forms worm-shaped grains in chrome spinel in contact with olivine. Cr_2O_3 concentration in chromitites reaches 18.87%.

We have studied dunites with high concentration of disseminated chrome spinel. Isometric shapes and weathered black crusts are characteristic of dunites with a high concentration of disseminated chrome spinel in the outcrops. These are massive panidiomorphic rocks. Olivine forms grains from 0.n up to 10 mm in size. The size of olivine grains is extremely irregular. The olivine fine grains sometimes form inclusions in large grains. Some olivine grains have undulose extinction and distinguishable lamellas. Inclusions of magnetite (sometimes as lamellas), chlorite, dolomite, halite, brucite, diopside, amphibole, aspidolite are observed in olivine. Chlorite and dolomite form aggregates in joints of olivine grains. Fanlike aggregates of crystals are characteristic of chlorite. Chlorite crystals sometimes penetrate the edges of olivine grains because olivine grains have irregular contours of their boundaries.

Olivine grains are intersected by cracks filled with dolomite, and sometimes with films of iron hydroxides. Magnesite, siderite, calcite (0.46–6.96% MgO, up to 7.72% FeO, 5 analyses), and ankerite are less commonly found. Brucite and dolomite often contain iron, and dolomite contains strontium. Calcite sometimes contains multiple inclusions of magnesite.

Chrome spinel is present in the form of euhedral grains up to 1.5 mm in size, evenly distributed through the rock. Octahedrons of smaller size form inclusions in olivine. Single-grain chrome spinel can contain various constituents including pure chromite. Chrome spinel replacement by ferrochromite is observed on the

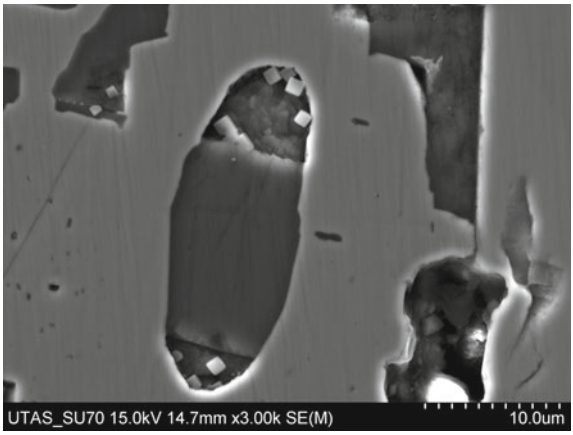

Fig. 1 Inclusions in chrome spinel in sample 27-15: dolomite (in the center with high relief), chlorite (top and bottom parts of inclusion in the center, an inclusion at the left above), halite (small light cubes)

peripheral and in cracks in some grains. The inclusions of olivine, chlorite, halite, dolomite, amphibole, phlogopite, aspidolite, chlorapatite, pentlandite, brucite, magnetite, diopside, ankerite, magnesite, probable chlorides of calcium, magnesium, potassium, iron, and rare serpentine are observed in the majority of chrome spinel grains (Fig. 1). Galena-pentlandite stringers are observed in cracks of chrome spinel grains. Chrome spinel is often surrounded by chlorite and dolomite aggregates, more rarely it is corroded and replaced by them. Chlorite, dolomite, brucite, chalcopyrite, pentlandite and phlogopite are also observed around chrome spinel grains.

Amphibole more often forms inclusions in chrome spinels, but it also forms individual grains in the aggregate of chlorite and dolomite. Amphibole contains up to 5% of chlorine and sometimes ilmenite inclusions.

Spinel is observed in the form of single euhedral grains in interstices of olivine grains. In addition, spinel forms inclusions in olivine grains. It is colorless without polarizer. Al_2O_3 concentrations in spinel are 53–55%.

Sulfides are rare, up to 0.5 mm in size, distributed unevenly. Combined grains are noted: pyrrhotite + chalcopyrite + magnetite, pentlandite + chrome spinel + pyrrhotite, magnetite + pyrrhotite + pentlandite, pyrrhotite + chalcopyrite + chlorapatite + amphibole, chalcopyrite grains with pentlandite exsolution and dolomite inclusions, inclusions of barite in chalcopyrite and serpentine in pyrrhotite.

Sphalerite occurs in associations with chlorite, amphibole, and olivine, while pentlandite occurs in chrome spinel inclusions. Cubanite is found among olivine.

Magnetite forms both euhedral grains in sulfides, and stringers on cracks, independent fine isometric grains among olivine and dolomite. Magnetite is chemically pure. Greenockite grains with isomorphic iron, copper and zinc are noted in magnetite.

4 Conclusion

The features of the Marinkin massif composition, petrology and mineralogy demonstrate considerable thermal and fluid influence of late granites. The ultramafic rocks were regenerated, and as a result the mafic rocks were changed.

Sulfide nickel-copper and chromitite mineralization occurred at the upper part of the mountain, unusual for such mineralization, which is more typical for the lower part of intrusions.

The sulfur was of mantle origin. Its quantity was not enough for mineralization because of low sulfur solubility in ultramafic-mafic magmas. The disseminated sulfides of liquid origin formed a veinlet nickel-copper sulfide mineralization as a result of dunite regeneration.

Chromitite mineralization also occurred during the regeneration of dunites, which is proven by the lack of serpentine. The composition of non-magmatic inclusions in chrome-sspinels, olivines and sulfides, as well as the inhomogeneity of chrome spinel grains and olivine lamellas, euhedral chlorite and isometric magnetite grains of pure composition without titanium indicate that phenomenon.

Acknowledgements The reported study was carried out as a part of the IX.130.3.3. project of the Geological Institute SB RAS, state registration No. AAAA-A17-117011650012-7 and funded by RFBR according to the research project № 19-05-00337. The study was conducted using facilities of the Analytical Center of mineralogical, geochemical and isotope studies at the Geological Institute, SB RAS Ulan-Ude, Russia.

References

Balykin PA, Polyakov GV, Bognibov VI, Petrova TE. Proterozoyskie ul'trabazit-bazitovye formatsii Baikalo-Stanovoy oblasti. Novosibirsk: Nauka, 1986. [Balykin PA, Polyakov GV, Bognibov VI, Petrova TE. Proterozoic ultrabasite-basite formations of the Baikal-Stanovoy area. Novosibirsk: Nauka, 1986. (In Russ.)].

Grudinin MI. Bazit-giperbazitovyi magmatism Baikalskoy gornoy oblasti. Novosibirsk: Nauka, 1979. [Grudinin MI. Basite-hyperbasite magmatism of the Baikal mountain region. Novosibirsk: Nauka, 1979. (In Russ.)].

Izokh AE, Gibsher AS, Zhuravlev DZ, Balykin PA. Sm-Nd dannye o vozraste ultrabasit-basitovykh massivov vostochnoy vetvi Baikalo-Muyiskogo ofiolitovogo poyasa. Doklady akademii nauk. 1998;360:88–92 [Izokh AE, Gibsher AS, Zhuravlev DZ, Balykin PA. Sm-Nd age of ultrabasite-basite massifs from Eastern part of the Baikal-Muya ophiolite belt. Doklady Earth Sciences. 1998;360:88–92 (In Russ.)].

Kislov EV, Malyshev AV, Orsoyev DA, Balykin PA. Marinkin massiv – platinometal'no-medno-nikelevoe rudoproyavlenie v Sredne-Vitimskoy gornoy strane. Ultrabazit-bazitovye komplexy skladchatykh oblastey I svyazannye s nimi mestorozhdeniya. 2009, Ekaterinburg, IGG URO RAN. T. 1. S. 222-225. [Kislov EV, Malyshev AV, Orsoyev DA, Balykin PA. Marinkin massif – platinum group elements-copper-nickel ore occurrence in the Middle Vitim highland. Ultrabasite-basite complexes of folded areas and the related deposits. 2009, Ekaterinburg, IGG UrB RAS. V. 1. P. 222-225. (In Russ.)].

Kislov EV, Malyshev AV, Orsoev DA. Marinkin massif – platinum metals-nickel-copper locality at the Middle Vitim mountain region, East Siberia. Northwestern Geology. 2009;42:185–188.

Kislov EV, Malyshev AV, Vanteev VV. Marinkin ultramafit-mafitovyi massiv – geodinamika, sostav, rudoobrazovanie. Geodinamika I minerageniya Severnoy I Tsentral'noy Azii: materialy V Vserossiyskoy nauchno-prakticheskoy konferentsii, posvyashennoy 45-letiyu Geologicheskogo instituta SO RAN. 2018a, Ulan-Ude: Izdatel'stvo Buryatsogo gosuniversiteta. S. 215-217 [Kislov EV, Malyshev AV, Vanteev VV. Marinkin mafic-ultramafic massif – geodynamics, composition, ore genesis. Geodynamics and Metallogeny of North and Central Asia: Proceedings of the 5th All-Russian scientific-practical conference dedicated to the 45th anniversary of the Geological Institute, SB RAS. 2018, Ulan-Ude, Buryat State University Publishing Department. P. 215-217. (In Russ.)].

Kislov EV, Malyshev AV, Vanteev VV. Marinkin ultramafit-mafitovyi massiv, Sredne-Vitimskaya gornaya strana – geodinamika I sostav rudoobrazuyushego komplexa. Voprosy geologii I komplexnogo osvoeniya pripodnykh resursov Vostochnoy Azii: Pyataya Vserossiyskaya nauchnaya konferentsiya s mezhdunarodnym uchastiem. 2018b, Blagoveshchensk, IGiP DVO RAN. V. 1. S. 33-36 [Kislov EV, Malyshev AV, Vanteev VV. Marinkin ultramafic-mafic massif, Middle Vitim highland – geodynamics and ore-forming complex composition. Questions of geology and complex exploitation of natural resources of East Asia: Fifth All-Russian Scientific conference with international participation. 2018, Blagoveshchensk, IGIP FEB RAS, V. 1. P. 33-36. (In Russ.)].

Kislov EV, Kamenetsky VS, Malyshev AV, Vanteev VV. Marinkin ultramafit-mafitovyi massiv (Sredne-Vitimskaya gornaya strana): spetsifika obrazovaniya orudeneniya. Metallogeniya drevnikh i sovremennykh okeanov–2019. Chetvert' veka v izuchenii submarinnykh mestorozhdeniy. 2019, Miass, Ekaterinburg, OOO Fort-Dialog-Iset, S. 79-83. [Kislov EV, Kamenetsky VS, Malyshev AV, Vanteev VV. Marinkin ultramafic-mafic massif (Middle Vitim highland): mineralization origin specifics. Metallogeny of ancient and modern oceans–2019. Twenty five years of advances in study of submarine deposits. 2019, Miass, Ekaterinburg, OOO Fort-Dialog-Iset. P. 79-83. (In Russ.)].

Prudovskiy EL, Grudinin MI. Osobennosti geologicheskogo stroeniya i veshestvennogo sostava dunit-troktolitovogo massiva Marinkin (Sredne-Vitimskaya gornaya strana). Geologicheskie formatsii Pribaikalya i Zabaikalya. 1972, Chita, S. 13-14. [Prudovskiy EL, Grudinin MI. Features of geological structure and material composition of Marinkin dunite-troktolite massif (Middle Vitim highland). Geological formations of the Baikal region and Transbaikalia. 1972, Chita, P. 13-14. (In Russ.)].

Rytsk EY, Amelin YV, Rizvanova NG, Krimsky RS, Mitrofanov GL, Mitrofanova NN et al. Age of rocks in the Baikal-Muya fold belt. Stratigraphy and Geological Correlation. 2001;9:315-326.

Tsygankov AA. Magmaticheskaya evolutsiya Baikalo-Muyskogo vulkano-plutonicheskogo poyasa v pozdnem dokembrii. Novosibirsk: SO RAN, 2005. [Tsygankov AA. Magmatic evolution of the Baikal-Muya volcano-plutonic belt in the late Precambrian. Novosibirsk: SB RAS, 2005. (In Russ.)].

Preliminary Study of Composition and Mechanical Properties of the NWA 12370 Meteorite

Andrey Kocherov, Sergey Voropaev, Alexander Korochantsev, and Ilmir Nugmanov

Abstract

In this paper, new NWA 12370 meteorite is described using the geochemical methods including its compositional and structural features. The possible type and structure of the parent asteroid is also assessed in comparison with other groups of chondrites.

Keywords

NWA 12370 · Meteorite · Method · Chondrite · HED · Properties · Structure

1 Introduction

Since the mid-nineties of the last century, a large flow of extraterrestrial finds from the Sahara desert has significantly enriched museums, research centers and private collections with meteorites of various types, including the rarest ones form the Vestoids (HED-meteorites), as well as lunar and martian meteorites. All these meteorites received the designation of NWA (North-West Africa), and current-lythere are more than 12 000 registered samples of this "family" on the website of

A. Kocherov (✉)
South Ural State University, 76 Lenina prospekt, 454080 Chelyabinsk, Russia
e-mail: kocherov.andrey@gmail.com

S. Voropaev · A. Korochantsev
Vernadsky Institute of Geochemistry and Analytical Chemistry of Russian Academy of Sciences, 19 Kosygina street, 119334 Moscow, Russia

I. Nugmanov
Kazan Federal University, 18 Kremlyovskaya street, 420008 Kazan, Russia

S. Votyakov et al. (eds.), *Minerals: Structure, Properties, Methods of Investigation*, Springer Proceedings in Earth and Environmental Sciences,
https://doi.org/10.1007/978-3-030-49468-1_16

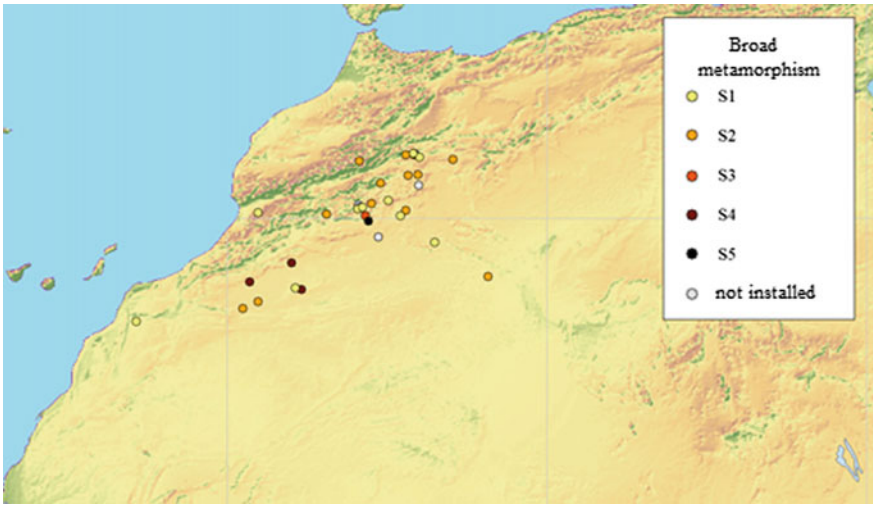

Fig. 1 Locations of H chondrites in the Sahara desert, which have exact coordinates

the Meteoritical Society Bulletin (http://www.lpi.ursa.edu/meteor/). However, only a small part of their entire amount (about 2%) has an adequate description, indicating the location of the find and its petrochemical features.

Sahara, along with Antarctica, is a unique natural place for the accumulation of meteorites (Fig. 1). This is due to its geological history and climate. According to modern concepts, the formation of the Sahara desert occurred about 2–3 million years ago, but the results of simulations suggest the establishment of an arid climate from the end of the Tortonian stage (about 7 million years).

In dry conditions, the rate of rock weathering is much lower than in more humid conditions, and therefore the meteorites that have fallen in this area over the past few million years, on average, have a rather low stage of weathering. A similar state of preservation is observed only in meteorites found in Arctic ice, the formation of which began approximately in the late Eocene ($\sim$40 mln years).

2 Materials and Methods

The study of the composition of the meteorites of the NWA group makes it possible to clarify important features of the history of small bodies and bodies of the terrestrial group. Thus, as it was stated by (Friedrich et al. 2014), the structure of the NWA 7298 meteorite reflects numerous impacts on the surface of the parent body of H chondrite and itself is probably an impact fragment. Based on the petrostructures and stages of shock metamorphism, which are present in three different lithological variations of the meteorite under study, the sequence of impact on the

originally porous parent asteroid was outlined. The simplest version of events is a double strike scenario in which the impact material with a different degree of change is first mixed and then subjected to shock metamorphism again.

Another example is the study of the NWA 3136 meteorite, which is a granulite mafic breccia with micro-sized baddeleyite grains. Using the methods of microstructural analysis and nanoscale geochronology using the U-Th-Pb system, it was possible to determine the melt crystallization age of the original protolith, which amounted to ~4.3 billion years (White et al. 2019). This age refers to the period of freezing of the magmatic ocean and the end of the formation of the crust and mantle of the Moon, therefore the study of this meteorite made a significant contribution to understanding the process and conditions of formation of the primary crust of the Moon.

In the course of petrographic and mineralogical studies of the NWA 8009 meteorite (Liao and Hsu 2017), it was found that it was a melted impact breccia of the eucrite type. It was formed by the deformation and in situ melting of the previously existing non-cumulative eucrite during an intense shock event. The investigated meteorite is one of the most intensely transformed samples of the HED group (Vestoids) as a result of the shock metamorphism currently known. The U-Pb isotope system in apatite within the bulk of the fragments of plagioclase was completely zeroed. An impact event was recorded that caused this zeroing (4143 ± 61 mln years), associated with the formation of a shock melt breccia. This discovery made it possible to discover a new stable age of a single significant shock event on Vesta.

3 Results and Discussion

In this work, the geochemical methods was used to describe new NWA 12370 meteorite, its composition and structural features, and the possible type and structure of the parent asteroid was also assessed in comparison with other groups of chondrites.

Table 1 shows the chemical composition of the meteorite according to the results of X-ray fluorescent analysis. Note that for comparative analysis, the values in columns 3–4 (marked with asterisk) are taken from the work of Jarosewich (1990), and the value ** is calculated based on Fe_{all}, sulfide Fe and Fe_{met}.

Usually, pre-entry 10–100 m scale interplanetary meteoroids are typically highly fractured and can break up under tensile stresses of 0.03 + 1 MPa (Popova et al. 2011). The exception is the fall (September 15, 2007) of the Carancas stony meteorite in Peru that caused the formation of a 13 m wide impact crater. It was classified as an ordinary H4-5 W0 S3 chondrite with an estimated initial size ~0.9 + 1.7 m, a compressive strength ~20 + 40 MPa and a tensile strength

Table 1 The chemical composition of the NWA 12370 meteorite according to the results of X-ray fluorescence analysis

Component	NWA 12370	H chondrite*	L chondrite*	LL chondrite*
SiO_2	40.319	36.60	39.72	40.60
TiO_2	0.106	0.12	0.12	0.13
Al_2O_3	3.421	2.14	2.25	2.24
Cr_2O_3	0.346	0.52	0.53	0.54
FeO	10.435**	10.30	14.46	17.39
MnO	0.310	0.31	0.34	0.35
MgO	21.956	23.26	24.73	25.22
CaO	1.884	1.74	1.85	1.92
Na_2O	1.589	0.86	0.95	0.95
K_2O	0.131	0.09	0.11	0.10
P_2O_5	0.553	0.27	0.22	0.22
Fe_{met}	13.32	15.98	7.03	2.44
Ni	0.987	1.74	1.24	1.07
Co	0.046	0.08	0.06	0.05
FeS	5.469	5.43	5.76	5.79
C	0.1	0.11	0.12	0.22
Total wt%	99.9	99.9	99.9	99.9
Fe (total)	27.703	27.45	21.93	19.63

Table 2 Mineral compositions of the Carancas and NWA 12370 meteorites

Meteorite, name	Classification	Ferrosilite (mol %)	Fayalite (mol %)	Wollastonite (mol %)	Oxygen isostopes (‰)
Carancas	H4-5 W0 S3	16.1 ± 0.2	18.4 ± 0.5	No data	$\Delta^{17}O = 3.017$; $\delta^{18}O = 4.519$; $\Delta^{17}O = 0.667$
NWA 12370	H5 W1 S2	16.1 ± 0.3	19.3 ± 0.6	1.5 ± 0.9	No data

~1.2 + 2.4 MPa, depending of the trajectory (Connolly et al. 2007). So the Carancas meteorite is a rare example of a monolithic meteoroid that was almost free of internal cracks. Such meteorites are the most dangerous to the Earth and we have tried to study their mechanical properties more fully with the help of the most appropriate analogue. The very similar meteorite, Norhtwest Africa 12370, was purchased at the mineralogical exhibition (Mineralientage München, Germany) in October 25, 2018 from the Mr. Ait Ha Lahcen from Erfoud, Morocco. It was classified by Lorenz C.A., Vernadsky Institute, as H5 W1 S2 (Lorenz et al. 2019) (Table 2).

The study of mechanical properties of the meteorite sample was performed in accordance with the following regulatory documents: ASTM D2845-08 Standard Test Method for Laboratory Determination of Pulse Velocities and Ultrasonic Elastic Constants of Rock. The testing was carried out at the Institute of Geology and Petroleum Technologies, Kazan Federal University. Measurement of the velocity of the longitudinal and transverse ultrasonic wave is performed at the PEAK-ULTRASONIC-EP installation. The system consists of two ultrasonic sensors, a signal source, an oscilloscope, an RLC and a relay systems. The source generates a signal with a frequency of 1 MHz. The signal is received by one of the sensors, which excites the pulses of S and P waves. The waves pass through the sample installed in the core holder and are detected by a second ultrasonic measurement sensor.

The calculation of the dynamic elastic moduli (Young's and Poisson's ratio) were carried out according to the formula (1):

$$R = V_p/V_s = \sqrt{2(1 - \mu)/(1 - 2\mu)},\ E = \left(V_p\right)^2 \rho(1 + \mu)(1 - 2\mu)/(1 - \mu) \quad (1)$$

where

R—ratio of longitudinal and transverse waves,
V_p—velocity of longitudinal waves,
V_s—velocity of transverse waves,
μ—dynamic Poisson's ratio,
E—dynamic Young's modulus,
ρ—density of rocks.

Cylindrical sample of NWA 12370 with length 41.74 mm and diameter 29.55 mm had a density ρ = 3.518 g/cm^3 (Table 3).

Dynamic parameters and values obtained by static load of meteorites (Voropaev et al. 2017) may differ significantly.

Table 3 Results of determining the velocity and dynamic elastic parameters of NWA 12370

Pressure, MPa	V_s, km/s	V_p, km/s	E (dyn), GPa	Poissonratio, (dyn)
1	3.413	5.471	95.97	0.1814
10	3.441	5.773	101.12	0.2245
30	3.528	5.773	104.35	0.2019

4 Conclusions

Generally, the distribution of metals in ordinary chondrites is rather complicated and depends on the variety of components of the gas-dust cloud in which they were formed. However, a systematic decrease in the ratio of the refractory siderophilic

element/Si in a series of meteorites of the groups H > L > LL is evident with an increase in the ratio of chalcophilic element/Si, where Zn, Cu, Ga, etc., are indicated as such an element for the CM and EH groups. Comparing the Zn/Cu ratios of the NWA 12370 samples, ordinary chondrites and EH, we assume that the nucleus of their parent asteroids was formed in areas with a similar heliocentric distance. But their growth subsequently occurred in various reducing environments with very different composition and concentration of sulfur and hydrogen compounds.

Recent studies on the migration of cosmic dust in the early Solar System have shown that the contribution of volatiles due to the "snow" line (>3.5 AU) to the formation of the early planets of the Earth group was very significant. The results of numerical calculations (Marov and Ipatov 2018) showed that during the formation of the solar system, the mass of water delivered to the Earth from the orbit of Jupiter could be comparable with the mass of the Earth's oceans. In the same place, in the cold zone, a significant amount of condensed volatile compounds Zn, Cu, etc. could be adsorbed on the dust grains. Subsequent mixing of dust and chondrules at the outer boundary of the asteroid belt could contribute to the enrichment of some representatives of H-L-LL groups and most of EH group with chalcophilic elements.

Acknowledgements This work was supported by the Russian Science Foundation (RSF) grant, project No. 17-17-01279.

References

Connolly HC et al. The Meteoritical Bulletin. Meteoritics and Planetary Science 2007;43:571-632.

Friedrich JM, WeisbergMK, Rivers ML. Multiple impact events recorded in the NWA 7298 H chondrite breccia and the dynamical evolution of an ordinary chondrite asteroid. Earth and Planetary Science Letters.2014;394:13–19.

Jarosewich E. Chemical analyses of meteorites: A compilation of stony and iron meteorite analyses. Meteoritics & Planetary Science.1990;25:323-337.

Lorenz CA et al. The Meteoritical Bulletin. 2019;108 (in preparation).

Marov M.Ya., Ipatov S.I. Delivery of water and volatiles to the planets of the chem group and to the moon. Astronomical Bulletin.2018;52(5):402-410.

Popova O et al. Very low strengths of interplanetary meteoroids and small asteroids. Meteoritics and Planetary Science.2011;46:1525-1550.

Shiyong Liao, Weibiao Hsu. The petrology and chronology of NWA 8009 impact melt breccia: Implication for early thermal and impact histories of Vesta. Geochimica et Cosmochimica Acta.2017;204:159–178.

Voropaev S, Nugmanov I, Dushenko N. et al. Features in constructing a certificate of strength of extraterrestrial material by the example of the Chelyabinsk meteorite. Doklady Astronomy&Physics. 2017;62:486-489.

White LF, Moser DE, Tait KT, Langelier B, Barker I, Darling JR. Crystallization and impact history of a meteoritic sample of early lunar crust (NWA 3163) refined by atom probe geochronology. Geoscience Frontiers (in press). https://doi.org/10.1016/j.gsf.2018.11.005.

Study of Calcites of the Crimean Emine-Bayir-Khosar Cave and Its Surroundings

Gleb S. Maksimov, Igor A. Nauhatsky, Elena M. Maksimova, and Elizaveta I. Timohina

Abstract

X-ray diffraction and spectroscopic study of the structural and elemental composition of calcites from water-chemogenic deposits of the Emine-Bayir-Khosar cave and its surroundings was carried out. The composition of the surface calcites was found to be close to the classical one. Different colors of these samples are due to different elemental impurities. Calcites from the Emine-Bayir-Khosar cave are characterized by an increased (as compared to surface calcites) content of Fe, Mn and Si. Pebbles are composed of several minerals.

Keywords

Calcites · Mineral composition · X-ray diffraction · X-ray fluorescence analysis

1 Introduction

Calcite ($CaCO_3$) is one of the most widespread minerals in Crimea, it serves as a rock-forming basis for limestone and marl. It is found in the form of veins and nests in limestone and igneous rocks, as well as in sand, shale and in conglomerates. Calcite is the basis of karst deposits in caves; it forms porous tuff masses at the spring exits to the surface, and fills cavities and cracks (Polkanov 1989).

G. S. Maksimov · I. A. Nauhatsky · E. M. Maksimova (✉) · E. I. Timohina
V.I. Vernadsky Crimean Federal University, 4 Vernadsky ave., 295033 Simferopol, Russia
e-mail: maksimovaem@cfuv.ru

S. Votyakov et al. (eds.), *Minerals: Structure, Properties, Methods of Investigation*,
Springer Proceedings in Earth and Environmental Sciences,
https://doi.org/10.1007/978-3-030-49468-1_17

Along with the thinnest veins, calcite sometimes forms powerful, up to several meters, veins that serve as indicators of the paleohydrogeological conditions of the Mountain Crimea (Dublyanskiy 1988). The veins are located in the limestones of the Qarabiy-Yayla, Chatyr-Dah, Ai-Petri and other mountain chains. There are also drip, nesting and other forms of calcium carbonate. Transparent calcite—Icelandic spar—is found in the central parts of the veins. Less common are different tones of yellow, green, pink, brown, and rarely black. Other carbonates (mainly siderite and dolomite) and a clayey substance are present in a mixture with calcite (Polkanov 1989).

2 Materials and Methods

Five samples of calcites were investigated, three of which were found in calcite veins in the surroundings of the Emine-Bayir-Khosar cave, Fig. 1 and two in the cave itself, Fig. 2.

Emine-Bayir-Khosar is one of the most beautiful caves in Crimea, located on the Chatyr-Dah mountain, which is part of the Main Ridge of the Crimean Mountains and occupies a central position. Chatyr-Dah is a territory, in which there is almost all

a) Sample No. 1 b) Sample No. 2 c) Sample No. 3

Fig. 1 The calcites from veins in the surroundings of the Emine-Bayir-Khosar cave: **a** crystals of rhombohedral calcite, color from translucent to transparent; **b** honey color calcite crystals; **c** crystals of small-crystalline rhombohedral calcite of white color

a) Sample No. 4 b) Sample No. 5

Fig. 2 The calcites from the Emine-Bayir-Khosar cave: **a** chemogenic formations of dark color (calcite "flowers") on the wall of the Idol Hall; **b** dark brown-black pebbles, washed out in clay from the bottom of the Idol Hall (on the way to the tunnel)

the variety of karst forms, both surface and subsurface, with more than 140 caverns of genetic classes of corrosion and erosion-corrosion (Maksimov et al. 2018).

The study of the mineral composition of its water-chemogenic deposits was carried out by us earlier (Maksimov et al. 2018).

The study of the elemental composition of the samples was carried out by X-ray fluorescence analysis using a Rigaku Supermini200 high-power benchtop sequential wavelength dispersive X-ray fluorescence spectrometer.

Structural studies were performed on a Bruker X-ray diffractometer with cobalt monochromatic radiation. The registration of sample diffraction spectra was carried out in an angular 2θ region from 10 to 100°.

Table 1 Elemental composition (wt%) of the samples

Sample	Ca	Si	Fe	Mn	P	Cl	K	Ti	S
№ 1	97.6	0.998	0.919	–	0.120	0.060	0.239	–	0.027
№ 2	97.6	0.309	1.760	0.215	0.071	–	0.065	–	0.008
№ 3	98.100	0.726	0.493	–	0.124	0.093	0.132	–	0.056
№ 4	84.600	2.240	4.860	6.380	0.144	0.017	0.690	0.716	0.017
№ 5	7.260	7.290	73.400	8.630	2.030	0.058	0.554	0.120	0.009

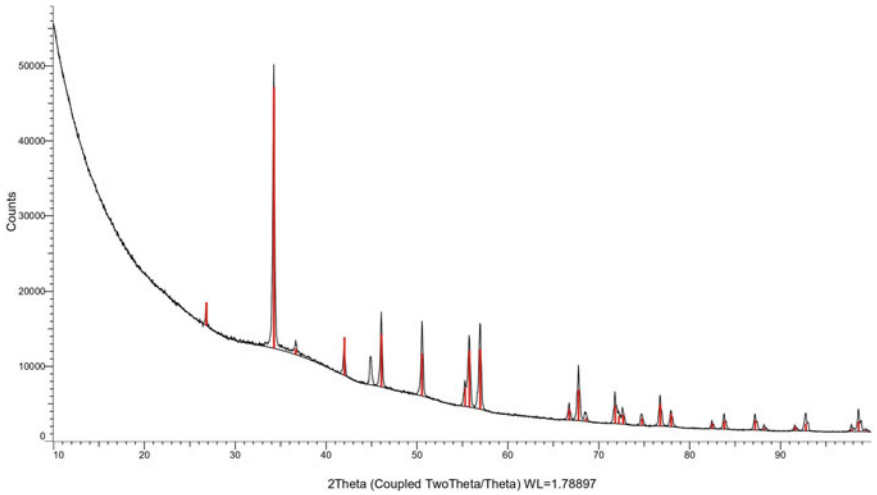

Fig. 3 The diffraction pattern of sample № 1—translucent calcite from veins in the surroundings of the Emine-Bayir-Khosar cave. Calcite peaks are marked by red

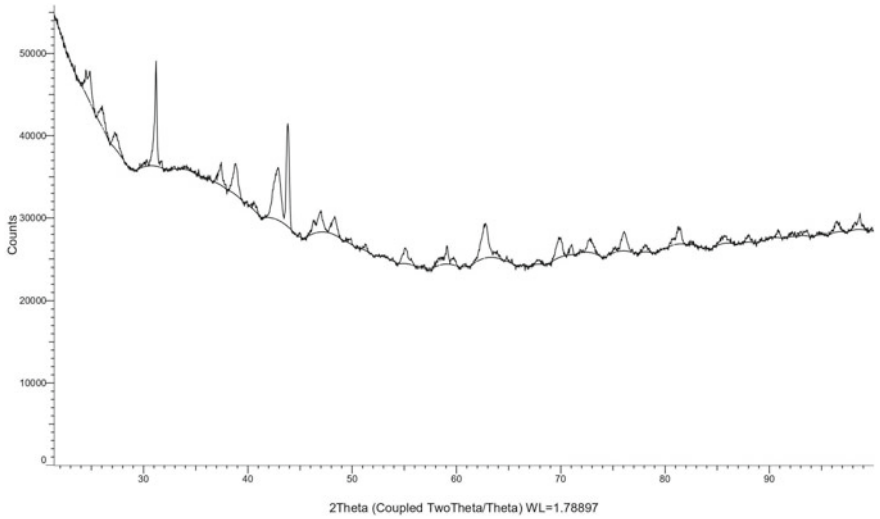

Fig. 4 The diffraction pattern of sample № 4—calcite "flowers" from the Emine-Bayir-Khosar cave. Calcite peaks are marked by red

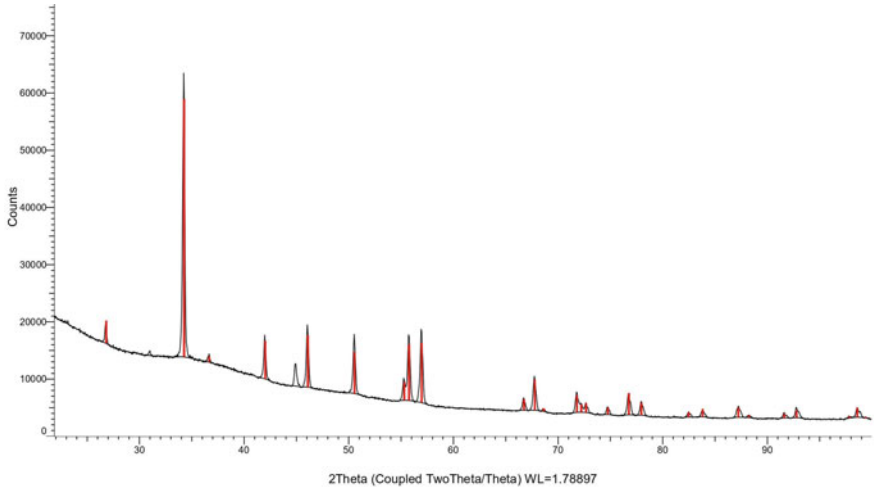

Fig. 5 The diffraction pattern of sample № 5—a pebble from the Emine-Bayir-Khosar cave

3 Results and Discussion

The elemental composition of the studied samples is shown in Table 1.

The results of X-ray phase analysis are shown in Figs. 3, 4 and 5.

The diffraction patterns of calcites from veins in the surroundings of the Emine-Bayir-Khosar cave have the form similar to the diffraction pattern from Fig. 3. A diffraction pattern of calcite "flowers" from cave formations has a similar appearance, Fig. 4.

Sample № 5 of dark brown-black pebbles, washed out in clay from the bottom of the Idol Hall of the Emine-Bayir-Khosar cave, is a multi-phase formation, Fig. 5.

This sample consists of calcite, FeO(OH) goethite and SiO_2 quartz.

4 Conclusion

The chemical composition of veined calcites (samples № 1–3) has been found to be close to the classical one. Different colors of these samples are due to different elemental impurities. For example, manganese is present in the composition of "honey" calcite, as distinct from the other two calcites (white and transparent); it also has a higher iron content, and no chlorine.

Calcites from the Emine-Bayir-Khosar cave are characterized by an increased (as compared to surface calcites) content of Fe, Mn and Si. Samples of pebbles and calcites from the chemogenic deposits of the Idol Hall contain: pebbles—Mg (0.247 wt%), Zn (0.101 wt%), and traces of Cu, Ni, Sr, Pb, Y; calcite "flowers" contain Mg (0.105 wt%), Zn (0.129 wt%) and traces of Cu.

It is worth noting that calcites from the surroundings of the Emine-Bayir-Khosar cave, for example, have no titanium, in contrast to the samples of cave deposits, which include it. This may be due to the Ti content in the groundwater feeding the investigated karst.

References

Dublyanskiy VN, Dublyanskiy YV. Kal'tsitovyye zhily Gornogo Kryma kak indikatory yego paleogidrogeologicheskikh usloviy. Geologicheskiy zhurnal. 1988;3:81–85. [Dublyansky VN, Dublyansky YV. Calcite veins of the Mountain Crimea as indicators of its paleo-hydrogeological conditions. Geological Journal. 1988;3:81–85. (In Russ.)].

Maksimov GS, Naukhatskiy IA, Timokhina EI, Maksimova EM. Issledovaniye mineral'nogo sostava stalaktita iz Krymskoy peshchery Emine-Bair-Khosar. Mineraly: stroyeniye, svoystva, metody issledovaniya. 2018, 9. ss. 121-122. [Maksimov GS, Naukhatsky IA, Timokhina EI, Maksimova EM. Study of the mineral composition of stalactite from the Crimean Emine-Bayir-Khosar cave. Minerals: structure, properties, methods of investigation. 2018; 9, pp. 121-122. (In Russ.)].

Maksimov GS, Timokhina EI, Naukhatskiy IA, Maksimova EM. Issledovaniye mineral'nogo sostava karstov krymskikh peshcher. Sovremennyye issledovaniya v geologii Sbornik tezisov dokladov Molodezhnoy nauchno-prakticheskoy konferentsii i XVI konferentsii studencheskogo nauchnogo obshchestva. Sankt-Peterburgskiy gosudarstvennyy universitet, Institut nauk o Zemle. 2018; ss. 120-122. [Maksimov GS, Timokhina EI, Naukhatsky IA, Maksimova EM. Study of the mineral composition of the karsts of the Crimean caves. Modern research in geology. Collection of reports theses of the Youth Scientific and Practical Conference and the XVI Conference of the Student Scientific Society. St. Petersburg State University, Institute of Earth Sciences. 2018; pp. 120-122. (In Russ.)].

Polkanov YA. Mineraly Kryma. Simferopol': Tavriya, 1989. [Polkanov YA. Minerals of the Crimea. Simferopol: Tavria, 1989. (In Russ.)].

Gallstones: Chemical and Amino Acid Composition

Ekaterina V. Mashina, Olga E. Amosova, and Svetlana N. Shanina

Abstract

The chemical and amino acid composition of gallstones of cholesterol, mixed (cholesterol + mineral component (calcium carbonate, calcium phosphate)), and pigment types was studied. The Mann-Whitney test revealed statistically significant differences in the levels of chemical elements and amino acids in the three types of gallstones studied. All types of gallstones in pairs were found to differ only in the content of the Ala, Ile, Leu, Pro, Phe, Asp and Glu amino acids. When comparing the pairs of gallstone types separately, it was revealed that cholesterol gallstones were statistically significantly different ($p < 0.05$) from cholesterol gallstones with a mineral component (phosphate, carbonate) in the content of Ca, Mg, Mn, Zr, and Ala, Val, Gly, Ile, Leu, Pro, Asp, Phe, and Glu amino acids. In pigment gallstones, the content of Na, Cu, Fe, Tl, Zn and Mo was statistically significantly different from both types of cholesterol gallstones. The revealed differences in the chemical and amino acid compositions indicate different conditions for the formation of cholesterol, mixed, and pigment types of gallstones.

Keywords

Gallstones · Biominerals · Amino acids · Metals · Non-parametric Mann-Whitney test

E. V. Mashina (✉) · O. E. Amosova · S. N. Shanina
Institute of Geology of Komi Science Centre of the Ural Branch of the Russian Academy of Sciences, 54 Pervomayskaya str., 167982 Syktyvkar, Russia
e-mail: borovkova@geo.komisc.ru

S. Votyakov et al. (eds.), *Minerals: Structure, Properties, Methods of Investigation*, Springer Proceedings in Earth and Environmental Sciences,
https://doi.org/10.1007/978-3-030-49468-1_18

1 Introduction

The study of the mechanisms of pathogenic mineral formation in the human body is one of the urgent tasks of biomineralogy. Gallstones are one of the types of pathogenic mineral formations, the development of which is associated, as a rule, with the supersaturation of bile with cholesterol or bilirubin. However, there are other, less studied, factors affecting the mechanism of gallstone formation. Some researchers have noted that gallstones can form against the background of increasing concentrations of certain chemical elements and protein content in bile (Galeev 1997; Keulemans et al. 1998; Chandran et al. 2007; Zaprudnov et al. 2010). It is considered that the metabolism of Fe, Cu, Mn and Zn elements is disturbed in cholelithiasis (Galeev 1997). These microelements are known to be present in the body in a bound state, being structural components of many enzymes involved in the antioxidant and immune system activity (Avtsyn et al. 1991). For example, during cholelithiasis, the level of alkaline phosphatase, transferrin and ceruloplasmin may increase. The composition of these enzymes includes Zn, Mg, Fe and Cu. It is assumed that the formation of Fe an Cu minerals and some others in the human body occurs as a result of the breakdown of protein metal-binding molecules (enzymes, transport proteins, etc.) under the influence of endogenous and/or exogenous factors (Lamanova 2008; Lamanova and Alyab'ev 2010). It has been found that pigment gallstones, in contrast to cholesterol gallstones, are characterized by high contents of Na, K, Mg, Ca (Chandran et al. 2007), Cu, Zn and Fe (Zaprudnov et al. 2010; Aslanov et al. 2015; Verma et al. 2002; Omer 2011). Recent studies (Parviainena et al. 2017) have shown that the variation in the contents of elements in gallstones is due to their phase composition. The concentration of Ca has been found to increase in samples containing calcium carbonate, calcium phosphate and pigment stones. In addition to Ca, calcium carbonate and phosphate containing gallstones have increased concentrations of Mg and Mn, while pigment stones have elevated concentrations of Cu, Fe, Ni, and Mg. According to (Miquel et al. 1998), the main factor affecting the crystallization of cholesterol is the supersaturation of bile with cholesterol, while soluble proteins do not affect this process. Pigment stones have high concentrations of soluble proteins as compared to cholesterol stones (Chandran et al. 2007). According to (Keulemans et al. 1998), the content of certain proteins in bile with cholelithiasis can be increased due to inflammatory processes in the gallbladder. An increase in the content of α, γ-globulin proteins is stimulated by infectious processes (Korkin 2009). Thus, despite numerous studies of the chemical and protein composition of gallstones, the role of protein and trace elements in the formation of gallstones has not been fully clarified and requires further study.

2 Materials and Methods

The purpose of this study was to study the elemental and amino acid composition of cholelites of three types: 1—cholesterol (5 samples), 2—mixed (cholesterol + mineral component (calcium carbonate, calcium phosphate)) (6 samples), and 3—pigment (4 samples), identifying differences between them (their compositions). Inductively coupled plasma mass-spectrometry (Elan-6100) and atomic emission spectrometry (Optima-4300 DV) were used as research methods. Identification and determination of the content of amino acids was performed using a GC-17A (Shimadzu) gas chromatograph. The content of 12 amino acids was determined (alanine—Ala, valine—Val, glycine—Gly, isoleucine—Ile, leucine—Leu, proline—Pro, serine—Ser, phenylalanine—Phe, tyrosine—Tyr, lysine—Lys, glutamic acid—Glu, aspartic acid—Asp). Data processing was carried out by statistical analysis methods. The non-parametric Mann-Whitney test was used to identify the differences in amino acid and chemical composition of different types of gallstones. The statistical evaluation was carried out for the significance level $p = 0.05$. The statistical analysis was performed using STATISTICA 6.0 software.

3 Results and Discussion

It has been found that the main elements present in gallstones are Ca, Na, K, Mg, Fe, Mn, Cu, Ti, Zn, Sr, Pb, Co, their content in the samples is more than 10^{-4} wt%. The Mann-Whitney test has revealed differences in samples of gallstones of three types according to the content of chemical elements and amino acids. In cholesterol gallstones (type 1), the contents of Ca, Mg, and Mn are statistically significantly lower as compared to type 2 and 3 gallstones (Tables 1, 2). This is consistent with the data (Parviainena et al. 2017). In our opinion, an increase in the Ca content in type 2 samples is explained by the presence of calcium-containing minerals (calcium carbonate, calcium phosphate), and Mg and Mn can be incorporated in their structure. An increased Ca content is probably due to its entry into the structure of bilirubin, which is the main component of pigment gallstones. Also, cholesterol gallstones are characterized by a higher, statistically significant Zr content than in type 2 gallstones. Pigment gallstones (type 3) are statistically significantly different from cholesterol gallstones (types 1 and 2) in the Fe, Tl and Mo content. High concentrations of Na in pigment gallstones as compared to cholesterol gallstones have also been noted by other researchers (Chandran et al. 2007; Channa et al. 2008). One of the reasons for the accumulation of Na can be functional disorders of the gallbladder when absorption functions are disturbed, since normally the process of transporting chemical elements is performed through its shell (Channa et al. 2008). It has been shown (Mashina 2018) that Na in gallstones occurs as halite and albite. The increased Cu content is associated with its entry into the structure of bilirubin and into the composition of various minerals. It has been shown that Cu and Fe in gallstones are present in the form of oxides, sulfates, sulfides and in the

form of native metal phases (Mashina and Filippov 2018). High contents of Cu and Fe in pigment gallstones have also been noted in (Zaprudnov et al. 2010; Aslanov et al. 2015; Verma et al. 2002; Omer 2011). An increase in the Cu and Zn content is due to a violation of the exchange of metal-containing proteins in hepatocytes, and an increase in the Fe content is due to its hematogenous origin (Aslanov et al. 2015). Pigmented cholelithiasis most often occurs against the background of accelerated hemolysis of red blood cells. This phenomenon can be caused by different factors including an increase in the content of heavy metals in the body. Heavy metals inhibit heme biosynthesis and contribute to the accumulation of free Cu, Fe, and bilirubin ions (Avtsyn et al. 1991). Tl trace element is not a vital element for humans, its concentrations increase with impaired metabolism of Na and K. Increased Mo inhibits the activity of copper-containing protein—ceruloplasmin—in hepatocytes, which can also contribute to the accumulation of Cu ions in bile (Avtsyn et al. 1991). Thus, there is a reason to believe that pigmented cholelithiasis is formed in the presence of an imbalance of chemical elements in the body. Concentrations of Co, Ni, Ga, La, Ti, Y, Ce, Sn, Sr, Ba, Pb and Cr do not differ statistically significantly ($p = 0.05$) for different types of gallstones. A pairwise joint comparison of all three types of gallstones (cholesterol with mixed, cholesterol with pigment, mixed with pigment) using the Mann-Whitney test (corrected critical significance level $p = 0.017$ was used for statistical evaluation) has shown that they do not have significant differences by one chemical element.

As a result of the pairwise joint comparison of all three types of gallstones in amino acid composition, it has been found that they have statistically significant differences in the content of Ala, Ile, Leu, Pro, Phe, Asp and Glu (Table 1). The lowest content of the listed amino acids is defined in cholesterol gallstones, the highest - in pigment gallstones (Table 2). Type 1 gallstones have a lower (statistically significant) Gly content as compared with types 2 and 3. Type 3 gallstones are characterized by a higher (statistically significant) Tyr content as compared with other types. According to Val, only types 1 and 2 are statistically significantly different. The ranges of change in the content of Val for these types do not overlap and constitute (0.034; 0.136) and (0.21; 0.50), respectively. For the samples of pigment gallstones, the range of variation in the Val content is rather wide, from 0.0 to 1.47 mg/g, and has ranges of variation in types 1 and 2. For Ser, only pigment and cholesterol (type 1) gallstones differ statistically significantly. Pigment gallstones are characterized by a higher content of Ser. Lys is the only amino acid, in which statistically significantly different types of gallstones do not differ. Based on the foregoing, it can be stated that pigment stones (type 3) are characterized by the highest content of most of specific amino acids, while cholesterol-type gallstones, on the contrary, are characterized by their lowest content. Thus, in the studied samples, the intertype difference is observed for amino acids belonging to aliphatic, acidic and aromatic groups.

Table 1 Results of Mann-Whitney test calculation

Chemical elements and amino acids	Compared types of gallstones								
	Type 1 (n_1 = 5) and Type 2 (n_2 = 6)			Type 1 (n_1 = 5) and Type 3 (n_2 = 4)			Type 2 (n_1 = 6) and Type 3 (n_2 = 4)		
	U	Z	p	U	Z	p	U	Z	p
Ca	0.0	−2.739	0.006	0.0	−2.449	0.014	10.0	−0.426	0.670
Na	13.0	−0.365	0.715	0.0	−2.449	0.014	0.0	−2.558	0.010
K	7.5	1.369	0.171	2.5	−1.837	0.066	0.5	−2.452	0.014
Mg	3.0	−2.191	0.028	1.0	−2.204	0.027	6.0	−1.279	0.201
Co	8.0	1.278	0.201	8.5	−0.367	0.713	4.0	−1.706	0.088
Ni	11.0	0.730	0.465	9.0	−0.245	0.806	7.0	−1.066	0.286
Zn	12.0	0.548	0.584	1.0	−2.204	0.027	2.0	−2.132	0.033
Rb	6.0	1.643	0.100	5.0	−1.225	0.221	1.0	−2.345	0.019
Sr	14.0	−0.182	0.855	10.0	0.000	1.000	12.0	0.000	1.000
Ba	8.0	1.278	0.201	9.0	−0.245	0.806	8.0	−0.853	0.394
La	6.0	1.643	0.100	6.0	0.980	0.327	6.0	−1.279	0.201
Pb	13.0	−0.365	0.715	4.0	−1.470	0.142	5.0	−1.492	0.135
Cu	5.5	−1.734	0.083	0.0	−2.449	0.014	0.0	−2.558	0.010
Fe	14.5	−0.091	0.927	0.0	−2.449	0.014	1.0	−2.345	0.019
Mn	2.0	−2.373	0.018	1.0	−2.204	0.027	7.0	−1.066	0.286
Ti	6.0	1.643	0.100	4.0	−1.470	0.142	4.0	−1.706	0.088
Cr	13.0	0.365	0.715	7.0	0.735	0.462	8.0	0.853	0.394
Y	6.0	1.643	0.100	9.0	0.245	0.806	5.0	−1.492	0.135
Ce	6.0	1.643	0.100	4.5	1.347	0.178	11.0	0.213	0.831
Zr	4.0	2.008	0.045	4.0	−1.470	0.142	1.0	−2.345	0.019
Sn	6.5	1.552	0.121	7.0	−0.735	0.462	4.0	−1.706	0.088
Tl	10.0	0.913	0.361	0.0	−2.449	0.014	0.0	−2.558	0.010
Ga	7.0	1.460	0.144	6.0	0.980	0.327	11.0	−0.213	0.831
Mo	6.0	1.643	0.100	0.0	−2.449	0.014	0.0	−2.558	0.010
Ala	0.0	−2.739	0.006	0.0	−2.449	0.014	0.0	−2.558	0.010
Gly	1.0	−2.556	0.010	0.0	−2.449	0.014	9.0	−0.640	0.522
Val	0.0	−2.739	0.006	5.0	−1.225	0.221	6.0	−1.279	0.201
Ile	4.0	−2.008	0.045	0.0	−2.449	0.014	0.0	−2.558	0.010
Leu	0.0	−2.739	0.006	0.0	−2.449	0.014	0.0	−2.558	0.010
Ser	5.0	−1.826	0.068	0.0	−2.449	0.014	4.0	−1.706	0.088
Asp	0.0	−2.739	0.006	0.0	−2.449	0.014	0.0	−2.558	0.010
Glu	1.0	−2.556	0.010	0.0	−2.449	0.014	0.0	−2.558	0.010
Pro	0.0	−2.739	0.006	0.0	−2.449	0.014	1.0	−2.345	0.019
Phe	0.0	−2.739	0.006	0.0	−2.449	0.014	0.0	−2.558	0.010
Tyr	9.0	−1.095	0.273	0.0	−2.449	0.014	1.0	−2.345	0.019
Lys	10.0	−0.913	0.361	3.0	−1.715	0.086	4.0	−1.706	0.088
$\sum$ AA	0.0	−2.739	0.006	0.0	−2.449	0.014	0.0	−2.558	0.010

Note. n_1, n_2—numbers of each gallstone type; U—the value of the Mann-Whitney test; p—achieved significance level; Type 1—cholesterol gallstones; Type 2—mixed gallstones; Type 3—pigment gallstones; $\sum$ AA—amount of amino acids

Table 2 Results of statistical data processing for gallstones of three types

Chemical elements and amino acids	Compared types of gallstones		
	Type 1 ($n_1 = 5$)	Type 2 ($n_1 = 6$)	Type 3 ($n_2 = 4$)
	Me Min – Max	Me Min – Max	Me Min – Max
Ca	3000.00 630.000 – 4500.000	13755.00 6735.000 – 26205.00	18570.00 7000.00 – 99000.00
Na	430.000 120.000 – 670.000	406.00 222.000 – 1400.00	6900.00 1594.000 – 19000.00
K	100.000 36.000 – 190.000	36.00 20.000 – 110.00	633.50 110.000 – 1600.00
Mg	76.000 44.000 – 210.000	232.00 82.000 – 402.00	1035.00 200.000 – 4100.00
Co	0.130 0.000 – 0.260	0.01 0.001 – 0.20	0.17 0.009 – 0.36
Ni	1.100 0.100 – 4.000	0.69 0.100 – 1.30	1.18 0.405 – 1.80
Zn	13.000 1.130 – 18.000	9.60 2.440 – 42.00	62.00 16.000 – 230.00
Rb	0.140 0.080 – 1.100	0.07 0.050 – 0.28	0.63 0.254 – 1.50
Sr	2.600 0.560 – 15.000	4.91 0.420 – 11.67	4.64 0.421 – 16.00
Ba	2.900 0.400 – 6.500	1.05 0.200 – 5.40	3.40 0.549 – 4.70
La	0.340 0.002 – 1.300	0.00 0.001 – 0.44	0.18 0.003 – 0.33
Pb	0.470 0.100 – 3.600	1.03 0.200 – 4.11	19.10 0.254 – 38.00
Cu	9.800 4.600 – 27.000	18.50 12.000 – 66.00	947.50 380.00 – 2400.0
Fe	100.000 32.000 – 140.000	92.50 43.000 – 148.00	440.00 145.000 – 660.00
Mn	8.000 2.100 – 33.000	49.50 12.000 – 185.00	131.50 32.000 – 1300.0
Ti	2.600 0.300 – 13.000	1.15 0.100 – 2.40	31.00 0.940 – 76.00
Cr	0.600 0.100 – 2.200	0.40 0.100 – 1.80	0.19 0.000 – 2.70
Y	0.270 0.001 – 0.650	0.00 0.001 – 0.22	0.08 0.003 – 0.42
Ce	0.370 0.002 – 0.590	0.01 0.001 – 0.35	0.07 0.000 – 0.18
Zr	0.370 0.050 – 0.990	0.04 0.012 – 0.19	2.85 0.065 – 5.20
Sn	0.780 0.020 – 2.600	0.06 0.012 – 0.79	0.88 0.050 – 1.10
Tl	0.008 0.001 – 0.061	0.00 0.001 – 0.02	0.47 0.169 – 0.57
Ga	0.067 0.005 – 0.180	0.02 0.007 – 0.06	0.03 0.004 – 0.12
Mo	0.040 0.006 – 0.090	0.01 0.004 – 0.04	0.82 0.170 – 4.80
Ala	0.140 0.080 –0.188	0.46 0.301 – 0.71	1.77 1.259 – 6.09
Gly	0.799 0.367 – 1.149	2.83 1.101 – 4.16	6.74 1.216 – 23.60
Val	0.078 0.033 – 0.136	0.40 0.210 – 0.50	1.18 0.000 – 1.47
Ile	0.030 0.000 – 0.056	0.14 0.000 – 0.22	0.81 0.684 – 2.69
Leu	0.128 0.058 – 0.207	0.74 0.315 – 0.94	1.97 1.662 – 7.93
Ser	0.341 0.075 – 0.389	0.44 0.316 – 0.53	1.42 0.397 – 3.52
Asp	0.051 0.000 – 0.189	0.47 0.326 – 0.67	2.42 1.636 – 7.14
Glu	0.139 0.035 – 0.298	0.54 0.228 – 0.67	2.68 2.373 – 13.58
Pro	0.039 0.000 – 0.115	0.33 0.269 – 0.55	1.06 0.476 – 4.16
Phe	0.081 0.024 – 0.141	0.30 0.255 – 0.41	1.16 0.913 – 1.70

(continued)

Table 2 (continued)

Chemical elements and amino acids	Compared types of gallstones		
	Type 1 ($n_1 = 5$)	Type 2 ($n_1 = 6$)	Type 3 ($n_2 = 4$)
	$\frac{\text{Me}}{\text{Min} - \text{Max}}$	$\frac{\text{Me}}{\text{Min} - \text{Max}}$	$\frac{\text{Me}}{\text{Min} - \text{Max}}$
Tyr	$\frac{0.025}{0.000 - 0.089}$	$\frac{0.08}{0.000 - 0.25}$	$\frac{0.78}{0.182 - 1.54}$
Lys	$\frac{0.067}{0.000 - 0.112}$	$\frac{0.09}{0.031 - 0.35}$	$\frac{0.94}{0.051 - 3.57}$
$\sum$ AA	$\frac{2.129}{1.021 - 2.707}$	$\frac{7.17}{4.437 - 7.95}$	$\frac{23.09}{12.574 - 75.00}$

Note. n_1, n_2—numbers of each gallstone type; Me—median value; Min, Max—minimum and maximum values; Type 1—cholesterol gallstones; Type 2—mixed gallstones; Type 3—pigment gallstones; $\sum$ AA—amount of amino acids

4 Conclusions

We have found significant differences in the composition of chemical elements and amino acids in the three studied types of gallstones. The Mann-Whitney test has found that all three types of gallstones differ in pairs according to the content of Ala, Ile, Leu, Pro, Phe, Asp and Glu. It has been shown that all three types of gallstones in pairs do not differ in chemical elements. When comparing the pairs of gallstone types, it has been found that cholesterol gallstones are statistically significantly ($p < 0.05$) different from cholesterol gallstones with a mineral component (phosphate, carbonate) in the content of Ca, Mg, Mn, Zr, and Ala, Val, Gly, Ile, Leu, Pro, Asp, Phe, and Glu amino acids. The pigment gallstones are statistically significantly different from both types of cholesterol stones in terms of the Na, Cu, Fe, Tl, Zn and Mo content, which suggests that the pigment cholelithiasis is formed under the conditions of an imbalance of chemical elements in the body. Cholesterol type gallstones are characterized by a lower content of almost all certain chemical elements and amino acids, on the contrary, pigment type gallstones have their highest content. The revealed statistically significant differences in the chemical and amino acid compositions indicate different conditions for the formation of cholesterol, mixed and pigment gallstones.

References

Aslanov AM, Yalovega GEH, Kolmakova TS, Brzhezinskaya MM. Mikroehlementnyi sostav i ul'trastruktura zhelchnykh kamnei raznogo tipa. Sovremennye problemy nauki i obrazovaniya. 2015; 3: 132-138. [Aslanov AM, Yalovega GE, Kolmakova TS, Brzezinska MM. Microelement composition and ultrastructure of gallstones of different types. Journal of Modern problems of science and education. 2015; 3: 132-138. (In Russ.)].

Avtsyn AP, Zhavoronkov AA, Rish MA, Strochkova LS. Mikroehlementozy cheloveka: ehtiologiya, klassifikatsiya, organopatologiya. Moskva.: Meditsina, 1991. 496 s. [Avtsyn AP, Zhavoronkov AA, Rish MA, Strochkova LS. Human microelementoses: etiology, classification, organopathology. Moscow: Meditsina, 1991. 496 p. (In Russ.)].

Channa NA, Ghanghro AB, Soomro AM, Khand F, Mahessar H. Comparative study of sodium and potassium in different types of gallstones and in serum of subjects with gallstones and controls. J. Anal. Environ. Chem. 2008; 9 (1): 38-42.

Chandran P, Kuchhal K, Garg P, Pundir S. An extended chemical analysis of gallstone. Indian J. Clin Biochem. 2007; 22(2): 145-150. https://doi.org/10.1007/BF02913334.

Galeev MA, Timerbulatov VM. Zhelchnokamennaya bolezn' i kholetsistit. UfA: BGMU, 1997. 219 s. [Galeev MA, Timerbulatov VM. Gallstone disease and cholecystitis. - Ufa: BSMU, 1997. 219 p. (In Russ.)].

Keulemans YC, Mok KS, Wit LT, Gouma DJ, Groen AK. Hepatic bile versus gallbladder bile: a comparison of protein and lipid concentration and composition in cholesterol gallstone patients. Journal of Hepatology. 1998; 28: 11-6. https://doi.org/10.1002/hep.510280103.

Korkin AL. Obshchie zakonomernostI, osobennosti razvitiya i techeniya zhelchnokamennoi bolezni na fone opistorkhoza: avtoref. dis. … dokt. med. nauk. Tyumen, 2009. 44 s. [Korkin AL. General patterns, peculiarities of the development and course of gallstone disease against the background of opisthorchiasis: Abstract. dis. … Dr. Med. sciences. Tyumen, 2009. 44 p. (In Russ.)].

Lamanova LM. Sul'fidnye mineraly v kholelitakh. Struktura i raznoobrazie mineral'nogo mira: Materialy Mezhdunarodnogo mineralogicheskogo seminara. Syktyvkar, 2008, ss. 344–346. [Lamanova LM. Sulfide minerals in gallstones. Structure and diversity of the mineral world: Materials of the International Mineralogical Seminar. Syktyvkar, 2008, pp. 344-346. (In Russ.)].

Lamanova LM, Alyab'ev FV. Metody obnaruzheniya vnekletochnykh mineral'nykh zeren v tkanyakh serdechno-sosudistoi sistemy. Sibirskii meditsinskii zhurnal. 2010;25(1):78-83. [Lamanova LM, Alyabyev FV. Methods for the detection of extracellular mineral grains in the tissues of the cardiovascular system. Siberian Medical Journal. 2010;25(1):78-83. (In Russ.)].

Mashina EV. Kholelity u zhitelei Respubliki KomI: rasprostranennost', sostav, struktura, faktory obrazovaniya.Vestnik Kol'skogo nauchnogo tsentra RAN. 2018;4:33-40. [Mashina EV. Gallstones in the inhabitants of the Komi Republic: prevalence, composition, structure, factors of formation. Vestnik of the Kola Scientific Center of the Russian Academy of Sciences. 2018;4:33-40. (In Russ.)].

Mashina EV, Filippov VN. Mikromineraly i vklyucheniya v kholelitakh. Materialy IX Vserossiiskoi nauchnoi konferentsii MINERALY: STROENIE, SVOISTVA, METODY ISSLEDOVANIYA. Ekaterinburg, 5-8 fevralya, 2018, ss. 126-127. [Mashina EV, Filippov VN. Microminerals and inclusions in gallstones. Proceedings of the IX Russian scientific conference "MINERALS: STRUCTURE, PROPERTIES, RESEARCH METHODS", Ekaterinburg, 5-8 February, 2018, pp. 126-127. (In Russ.)].

Miquel J, Núñez L, Amigo L, González S, Raddatz A, Rigotti A, Nervi F. Cholesterol saturation, not proteins or cholecystitis, is critical for crystal formation in human gallbladder bile. J. Gastroenterology. 1998; 114(5): 1016-23. https://doi.org/10.1016/S0016-5085(98)70322-1.

Omer LS. Quantitative analysis in (33) traces metals in human gallstones by ICP-AES. International Journal of Chemistry. 2011; 3 (2): 105-110. https://doi.org/10.5539/ijc.v3n2p105.

Parviainena A, Roman-Alpiste M, Marchesi C, Suárez-Grauc J, Pérez-López R. New insights into the metal partitioning in different microphases of human gallstones. J. Trace Elements in Medicine and Biology. 2017; 44: 339-348. https://doi.org/10.1016/j.jtemb.2017.09.013.

Verma GR, Pandey AK, Bose SM, Prasad R. Study of serum calcium and trace elements in chronic cholelithiasis. J. Surgery. 2002; 72(8): 596-599. https://doi.org/10.1046/j.1445-2197.2002.02485.x.

Zaprudnov AM, Tsar'kova ON, Kharitonova LA. Kliniko-patogenetichnskoe znachenie biliarnogo sladzha kak nachal'noi stadii zhelchnokamennoi bolezni v detskom vozraste. Pediatriya. 2010; 89 (2): 40-45. [Zaprudnov AM, Tsarkova ON, Kharitonova LA. Clinical and pathogenetic significance of biliary sludge as the initial stage of gallstone disease in childhood. Journal of Pediatrics. 2010; 89 (2): 40-45. (In Russ.)].

The Nature of Beryl Color from the Sherlovaya Gora Deposit

Angelina D. Mikheeva, Anatoliy G. Nikolaev, Georgiy A. Yurgenson, and Alena A. Borzenko

Abstract

In this work, the studies of the crystal chemical characteristics and nature of the color of beryl from the Sherlovaya Gora deposit (Transbaikalia) were carried out. The color of beryl is associated with Fe^{2+} and Fe^{3+} ions which are isomorphically replaced by Al^{3+} ions in the mineral structure. It has been found that in the color of yellow, green and blue beryl, the absorption bands at a wavelength of 810 nm associated with Fe^{2+} ions have the same intensity. And the intensity of the absorption band associated with Fe^{3+} ions increases from blue to yellow beryl. The research results have shown that the color of beryl is associated with the redox state of mineral formation. The calculation of chromaticity coordinates was carried out using the International Commission on Illumination CIE—1931.

Keywords

Beryl · Optical spectroscopy · Mineral color · Gemology

A. D. Mikheeva (✉) · A. G. Nikolaev
Kazan (Volga Region) Federal University, 18 Kremlyovskaya str., Kazan, Russia
e-mail: miheevaangelina@yandex.ru

G. A. Yurgenson · A. A. Borzenko
Institute of Natural Resources, Ecology and Cryology, Siberian Branch of the Russian Academy of Sciences, 16a Nedorezova str., Chita, Russia
e-mail: yurgga@mail.ru

S. Votyakov et al. (eds.), *Minerals: Structure, Properties, Methods of Investigation*, Springer Proceedings in Earth and Environmental Sciences,
https://doi.org/10.1007/978-3-030-49468-1_19

1 Introduction

Beryl is considered the main mineral for obtaining the beryllium chemical element. In addition, the colored varieties of this mineral are valuable jewels. The purpose of the proposed work was to study beryl crystals from the Sherlovaya Gora deposit by optical absorption spectroscopy, as well as to study their crystal-chemical features and the nature of their color.

From the second quarter of the 18th century, Sherlovaya Gora is known in Russia and abroad as a unique natural reserve of jewelry and collection stones, many of which are the pride of many museums around the world. Since 1930, it has entered the list of large deposits of tin, lead, zinc, indium and cadmium. The Sherlovogorsk ore-magmatic system in the 1950–1970s was the object of close attention of geologists, miners, petrologists, geochemists, and mineralogists. Another attraction of the Sherlovaya Gora is the zone of modern mineral formation, caused by the removal of temporary water streams of a number of components from the dumps of overburden and near-ore rocks, poor ore stockpiles, and from the pit walls. The geological position of the field is described in (Yurgenson and Kononov 2014).

2 Materials and Methods

The main research method in this paper is optical absorption spectroscopy. Optical absorption spectra were recorded on a specialized SHIMADZU UV—3600 spectrophotometer in the wavelength range of 185–3300 nm. Additionally, the optical spectra were recorded on a standardized MSFU-K spectrophotometer. The registration of optical absorption spectra was performed in the wavelength range of 400–800 nm, with a step of 1 nm. For an objective measurement and description of the beryl color, the method of calculating the chromaticity coordinates for the international colorimetric system XYZ was used. All colorimetric results on the interpretation of the optical absorption spectra of minerals were placed on the standard color triangle of the International Commission on Illumination (CIE—1931). The colorimetric parameters of the studied minerals (x, y, z are the chromaticity coefficients; λ is the wavelength, p is the density, L is the brightness of the basic color tone) were calculated using the specialized Spectrum software. Optical absorption spectra were recorded from crystal fragments and from plane-parallel preparations; the color of beryl samples was pale yellow, bright yellow, bluish-green, light green, and saturated blue. All experimental studies were performed at room temperature.

Beryl is an annular silicate of beryllium and aluminum $Be_3Al_2[Si_6O_{18}]$, its structure consists of $[Si_6O_{18}]^{12-}$ rings connected via Be and Al atoms. The rings form columns elongated along the sixth-order axis, connected by beryllium-oxygen tetrahedron and aluminum-oxygen octahedron (Kornilov et al. 1987).

A characteristic feature of the mineral structure is the presence of sufficiently capacious cavities—channels—that explain the possibility of a wide manifestation of heterovalent isomorphism with the occurrence of ion-compensators. The channels are large enough to contain water molecules, large alkaline and alkaline earth cations. The structure of beryl is characterized by partial replacement of Be^{2+} atoms with Li^{+} and Mg^{2+}. Al^{3+} ions in octahedral positions of the structure are also subject to isomorphism, which can be replaced by three- and divalent cations: $Al^{3+} \rightarrow Fe^{3+}$, Cr^{3+}, Mg^{2+}, Ni^{2+}, Fe^{2+}, Si^{4+}.

As ions-compensators, the channels of the structure include large alkali metal cations (Na^{+}, Cs^{+}), as well as $(OH)^{-}$ groups, H_2O molecules, F^{-} ions, and others (Egorov-Tismenko 2005). In addition to iron, in the crystals of Sherlovaya Gora beryl V, Cr, Sc, and Zr were found as impurities, the influence of which on the characteristics of their color remains to be revealed.

3 Results and Discussion

A common feature of the optical absorption spectra of beryl crystals from Sherlovaya Gora is the presence of one broad intense band in the near infrared region with a maximum of 810 nm due to the spin-allowed electronic transition $^{5}T_2$ (^{5}D) $\rightarrow$ ^{5}E (^{5}D) in ferrous ions, isomorphically replacing aluminum in octahedral positions of the structure (Fig. 1) (Bakhtin 1985). In the ultraviolet region there is an absorption band, the long-wavelength shoulder of which can be observed in the visible region of the spectrum and is associated with the charge transfer mechanism $O^{2-} \rightarrow Fe^{3+}$. Narrow absorption bands at a wavelength of 1400 and 1896 nm are associated with vibrations of water molecules in the channels of the beryl structure, namely, the line at 1896 nm corresponds to the vibrations of the first overtone, and the line at 1400 nm corresponds to the second overtone of the H_2O molecule. From the configuration of the narrow absorption band in the region of 1896 nm, we can say that molecular water of type I and type II is present in beryls (Nassau 1976; Wood and Nassau 1968).

The interpretation of the optical absorption spectra of beryl crystals from the Sherlovaya Gora deposit showed the following results. The intensity of the absorption bands associated with Fe^{2+} ions at a wavelength of 810 nm for all crystals is almost the same; there is no direct dependence on the peak height and color of beryl. With an increase in the $O^{2-} \rightarrow Fe^{3+}$ absorption band, only an enhancement of green hues and a transition from green beryl to yellow heliodor occurs. This dependence of the color of beryl crystals on the fraction of ferric iron is shown in Fig. 2 (Yurgenson et al. 2010).

According to the results of the interpretation of optical absorption spectra of beryl crystals, the chromaticity coordinates were calculated using the CIE 1931 international colorimetric system. The dominant wavelength of the main color tone

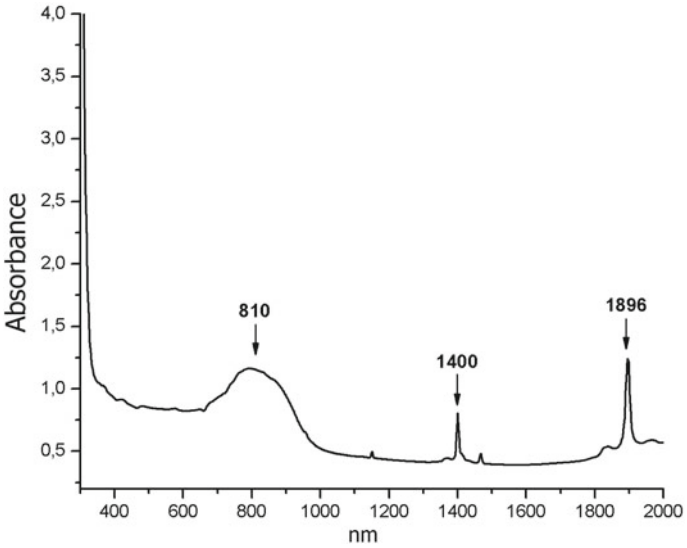

Fig. 1 Optical absorption spectrum of the beryl from the Sherlovaya Gora deposit

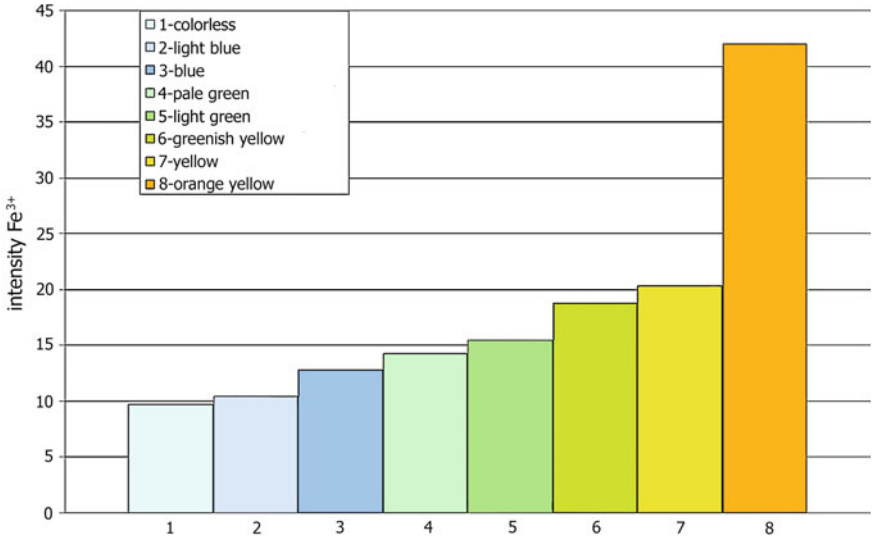

Fig. 2 An increase in the content of ferric iron in the octahedral positions of beryl crystals of various colors (The vertical axis gives the intensity of the positions of ferric iron in the EPR spectra (Yurgenson et al. 2010))

was λ = 495.2–573.4 nm, and the saturation value of the main color tone varied within 2.05–33.17%. These parameters are well correlated with the color characteristics of beryl crystals from the Sherlovaya Gora deposit.

4 Conclusions

The performed study of the coloration of jewelry varieties of beryl from Sherlovaya Gora has revealed that iron ions are the main chromophore in beryl coloration. Depending on the oxidative or reducing conditions of the formation of beryl, it develops a yellow, green or blue color.

Acknowledgements This work was carried out as part of the state assignment for project No. 0386-2019-0004 (IX.137.1.2.).

References

Bakhtin AI. Porodoobrazuyushhie silikaty: opticheskie spektry, kristallokhimiya, zakonomernosti okraski, tipomorfizm. Kazan: Kazan University; 1985. [Bakhtin AI. Rock-forming silicates: optical spectra, crystal chemistry, color patterns, typomorphism. Kazan: Kazan University; 1985. (In Russ.)]

Egorov-Tismenko YK. Kristallografiya i kristallokhimiya. M.: Publishing House "Book House University"; 2005. [Egorov-Tismenko YK. Crystallography and crystal chemistry. M.: Publishing House "Book House University"; 2005. (In Russ.)]

Kornilov NI, Solodova YP. Yuvelirnyye kamni. M.: Nedra; 1987. [Kornilov NI, Solodova YP. Jewelry stones. M .: Nedra; 1987. (In Russ.)]

Nassau K. Synthetic emerald. The Journal of Crystal Growth. 1976;35(2):211-222.

Wood DL, Nassau K. The characterization of the beryl and emerald visible and infrared absorption spectroscopy. American Mineralogist. 1968;53(5-6):777-800.

Yurgenson GA, Afanasieva AS, Kononov OV, Prokofiev VY. Typomorphic peculiarities of noble beryl varieties from Sherlovaya Montain. Geology and Resources. 2010;19(1):28-30.

Yurgenson GA, Kononov OV. Sherlova Gora: a Deposit for Gemstones and Rare Metals. Mineralogical Almanac. 2014;19(2):12-93

Historical List of Harmful Meteorites

Lev A. Muravyev and Viktor I. Grokhovsky

Abstract

As is known, the possibility of stones falling from the sky was completely confirmed by scientists only in the early 19th century. The problem of the asteroid-comet hazard is now being actively discussed, because the consequences of the fall of large cosmic bodies on the Earth can be catastrophic and affect the survival of humanity and all living beings. Fragments of smaller celestial bodies, e.g. meteorites, fall to the earth much more often, and they can also create a certain danger. In several papers that were published about 20 years ago, attempts were made to compile a list of events related to the damage caused by meteorites falling from the sky. In this work, we systematized, analyzed and critically revised information previously published in many sources about cases of damage to the property or human health as a result of fallen meteorites until May 2019. The key criteria were the data of meteoritic bulletins and catalogs, proving the existence of extraterrestrial material collected on the site, and studied later. The created list will allow us to evaluate how significant this threat is for humanity.

Keywords

Asteroid-comet hazard · Estimates of encounter probability · Damage · Injury · Chelyabinsk meteorite

L. A. Muravyev (✉) · V. I. Grokhovsky
Ural Federal University, 19 Mira str., 620002 Ekaterinburg, Russia
e-mail: mlev@igeoph.net

V. I. Grokhovsky
e-mail: grokh47@mail.ru

L. A. Muravyev
Institute of Geophysics, Ural Branch of RAS, 100 Amundsena str., 620016 Ekaterinburg, Russia

S. Votyakov et al. (eds.), *Minerals: Structure, Properties, Methods of Investigation*,
Springer Proceedings in Earth and Environmental Sciences,
https://doi.org/10.1007/978-3-030-49468-1_20

1 Introduction

Each planet of the solar system from the moment of formation is constantly exposed to interplanetary matter. The solid surfaces of the planets, their satellites and asteroids are dotted with impact craters of various sizes, arising as a result of long-term bombardment by meteorites and smaller asteroids. A soil, vegetation and erosion as a result of geodynamic processes have led to the fact that most of the craters are not visible on the earth's surface, and their presence can be visualized only by remote sensing and analysis of geophysical fields (Muravyev 2019).

Of course, such dramatic events as the collision of the Earth with a huge meteorite or comet can affect the climatic conditions on the planet, but these events rarely occur. Presumably, a similar phenomenon led to the extinction of the dinosaur and a sharp cooling of the climate. Relatively small meteorites fall more often. Therefore, the probability of a meteorite falling into the environment of a human being is not equal to zero, despite the fact that most of the falling meteorites fall into the ocean, seas, deserts, dense forests and other sparsely populated areas.

2 Initial Data

We systematized information about cases of damage as a result of fallen meteorites, that was published in many sources until present time (May 2019). The first study aimed at the same goal was carried out in 1996 by Lewis (1996), who compiled a table of cases of damage caused by meteorites, based on the preprint of Yao et al. (1993) and media information. A similar table was compiled in Russia (Boyarchuk 1999). In it, the reports of a significant number of victims cited by Lewis were critically reviewed, and the information about similar cases in Russia/USSR from sources (Fedynskii 1950; Astapovich 1941) was added. A brief report on this work was published in (Muravyev and Grokhovsky 2019).

The first record of the harm from a meteorite (Schulz 1956) is in the meteorite catalog of the British Museum (Hey 1966) – about Franciscan monk killed by a meteorite in 1654.

The mentioned catalog was the basis for verifying information about the fall of harmful meteorites before 1966. Incidents after this year has been found and checked in regular online meteorite bulletins (The Meteoritical Bulletin 2019).

Information on direct damage to buildings (broken roof or house structure) or property (usually a car) or damage to people or animals was included in the general list. In compiling our table, we critically analyzed the previous data mentioned above, and in other sources (Siber; Spratt 1991). Also, in the table we did not include many cases when a meteorite fell right next to a person (up to 1 m, such as the Tika meteorite in Kenya, 2011), since this fall did not cause any harm, it only allowed to immediately find a meteorite. The messages about falls of meteorites on agricultural fields, roads' edges, football fields, etc. were not included as well.

The well-known Tunguska space phenomenon was also not included in the table because meteorite matter was not found.

3 Results and Discussion

The verified information on evil meteorites summarized in the table was published by us in Russian in 2008 (Grokhovskii and Murav'ev 2009). By that time, for the entire time that meteorite falls had been recorded, there were only a few dozen cases when of extraterrestrial substances entering the human environment. Also, several cases of meteorite falling into a person were considered (according to unreliable information). Most often, meteorites caused local damage to various buildings, falling on the roofs of houses. Thereat, we could conclude that there was practically no danger from falling meteorites. This would further doubt the reports cited in the work by Yao et al. (1993) of the numerous destructions and the thousands of victims of meteorites, according to the chronicles in ancient China.

The picture that was then formed was turned upside down as a result of the Chelyabinsk meteorite's fall (Popova et al. 2013). The shock wave led to unprecedented destruction. In the regional center of Chelyabinsk and nearby, many windows were broken. Glass shards injured people. 1,613 people turned to hospitals in the Chelyabinsk region with wounds and 69 of which were hospitalized (according to media reports).

In Chelyabinsk, the zinc factory suffered: the roof was damaged and the brickwork of the wall was destroyed. The indicated damage was associated with the impact of a meteorite shock wave – i.e. with its flight in the atmosphere. Therefore, the Chelyabinsk meteorite added to the list of bad meteorites, and this event showed the importance of working to continue compiling this list.

Now we can present a table containing information about such cases until May 2019. The information presented earlier has been again critically revised and re-checked. Due to their historical value, we have kept several records officially (in the bulletin) recognized as doubtful. The main criterion for inclusion in the table was the substance collected at the site of the fall, which was subsequently investigated and registered. This confirms the indication of the meteorite type for each record. For each entry, the source from the list of references or the number of the Meteoritical Bulletin (abbreviation MB with its number) has been indicated. "Doubtful" in the Type column means dubious meteorite nature. "Doubtful" in the Description column means doubting the reliability of the given report about the circumstances of the find.

The list of bad meteorites is given in Table 1.

Table 1 The chrono list of bad meteorites

Date	Name	Place	Type	Description	Source
04.09.1511	Crema	Lombardia, Italy	*Doubtful meteorite*	Killed birds, sheep, and a man	(Boyarchuk 1999; Hey 1966)
04.09.1654	Milan	Italy	*Doubtful meteorite*	Killed a monk	(Boyarchuk 1999; Hey 1966)
24.07.1790	Barbotan	Aquitaine, France	H5	Crushed a cottage, killed a farmer and cattle *(doubtful)*	(Lewis 1996; Siber)
19.12.1798	Benares (a)	Uttar Pradesh, India	LL4	Struck a building	(Hey 1966; Siber; Spratt 1991)
13.12.1803	Mässing	Bayern, Germany	Howardite	struck a building	(Lewis 1996; Spratt 1991)
05.09.1812	Borodino	Moscow, Russia	H5	Observed by a soldier on guard	(Hey 1966)
16.01.1825	Oriang	Rajasthan, India	*Doubtful meteorite*	Killed a man and injured a woman	(Boyarchuk 1999; Hey 1966)
16.02.1827	Mhow	Uttar Pradesh, India	L6	Wounded a man *(doubtful)*	(Boyarchuk 1999; Hey 1966; Siber; Spratt 1991)
11.11.1836	Macau	Rio Grande do Norte, Brazil	H5	Killed several cattle *(doubtful)*	(Hey 1966; Siber; Spratt 1991)
14.07.1847	Braunau	Královéhradecký, Czech Republic	IIAB	Struck the roof of a house	(Lewis 1996; Spratt 1991)
09.12.1858	Ausson	Midi-Pyrenees, France	L5	Hit a building	(Lewis 1996; Spratt 1991)
01.05.1860	New Concord	Ohio, United States	L6	Killed a colt	(Hey 1966; Siber; Spratt 1991)
08.08.1868	Pillistfer	Estonia	EL6	Struck a building	(Lewis 1996; Siber)
23.01.1870	Nedagolla	Andhra Pradesh, India	Iron, ungrouped	Stunned a man	(Lewis 1996; Boyarchuk 1999)
16.02.1876	Judesegeri	Karnataka, India	H6	Fell in the bed of a tank	(Hey 1966; Spratt 1991)

(continued)

Table 1 (continued)

Date	Name	Place	Type	Description	Source
19.11.1881	Grossliebenthal	Odessa, Ukraine	L6	Injured a man *(doubtful)*	(Lewis 1996; Boyarchuk 1999)
22.09.1893	Zabrodje	Vitebsk, Belarus	L6	Struck the roof of a house	(Hey 1966; Siber)
05.08.1898	Andover	Maine, United States	L6	Struck a brick wall	(Siber; Spratt 1991)
04.11.1906	Diep River	Western Cape, South Africa	L6	Roof of a house *(probably)*	(Hey 1966; Spratt 1991)
16.06.1911	Kilbourn	Wisconsin, United States	H5	Struck the roof of a barn	(Hey 1966; Siber; Spratt 1991)
28.06.1911	Nakhla	Al Buhayrah, Egypt	Martian (nakhlite)	Killed a dog	(Hey 1966; Siber; Spratt 1991)
19.07.1912	Holbrook	Arizona, United States	L/LL6	Struck a building	(Lewis 1996; Spratt 1991)
18.01.1916	Baxter	Missouri, United States	L6	Struck a house roof	(Hey 1966; Siber; Spratt 1991)
03.12.1917	Strathmore	Scotland, United Kingdom	L6	Struck a building	(Lewis 1996; Spratt 1991)
30.06.1918	Richardton	North Dakota, United States	H5	Struck a building	(Lewis 1996; Spratt 1991)
31.12.1921	Beyrout	Beirut, Lebanon	LL3.8	Struck a hut roof	(Hey 1966; Siber; Spratt 1991)
02.04.1936	Yurtuk	Zaporozh'ye, Ukraine	Howardite	Struck a house roof	(Hey 1966; Siber; Spratt 1991)
31.03.1938	Kasamatsu	Chubu, Japan	H	Struck a house roof	(Hey 1966; Siber; Spratt 1991)
16.06.1938	Pantar	Mindanao, Philippines	H5	Struck many roofs	(Hey 1966; Spratt 1991)
24.06.1938	Chicora	Pennsylvania, United States	LL6	Injured a cow	(Hey 1966; Siber)

(continued)

Table 1 (continued)

Date	Name	Place	Type	Description	Source
29.09.1938	Benld	Illinois, United States	H6	Struck a garage roof	(Hey 1966; Siber; Spratt 1991)
11.06.1949	Kunashak	Chelyabinsk region, Russia	L6	Struck a grain dryer roof	(Boyarchuk 1999)
21.09.1949	Beddgelert	Wales, United Kingdom	H5	Struck a hotel roof	(Hey 1966; Siber; Spratt 1991)
20.11.1949	Kochi	Shikoku, Japan	Doubtful meteorite	Struck a window	(Hey 1966; Siber)
23.05.1950	Madhipura	Bihar, India	L	Struck a shed roof	(Hey 1966; Spratt 1991)
20.09.1950	Murray	Kentucky, United States	CM2	Struck several buildings	(Lewis 1996; Spratt 1991)
10.12.1950	St. Louis	Missouri, United States	H4	Struck a car	(Lewis 1996)
01.11.1954	Sylacauga	Alabama, United States	H4	Through the roof, hit a women	(Boyarchuk 1999; Hey 1966; Siber; Spratt 1991)
19.02.1956	Sinnai	Sardinia, Italy	H6	Struck roof and floor of the house	MB10
29.02.1956	Centerville	South Dakota, United States	H5	Struck a roof and a corn planter	(Hey 1966; Spratt 1991)
13.10.1959	Hamlet	Indiana, United States	LL4	Struck a house	(Hey 1966; Spratt 1991)
23.02.1961	Ras Tanura	Ash Sharqiyah, Saudi Arabia	H6	Struck a loading dock	(Lewis 1996; Spratt 1991)
09.09.1961	Bells	Texas, United States	C2-ung	Struck the roof of a house	(Spratt 1991)
26.04.1962	Kiel	Schleswig-Holstein, Germany	L6	Made a hole in the roof of a house	(Hey 1966; Siber; Spratt 1991)
24.12.1965	Barwell	England, United Kingdom	L5	Two buildings and a car	(Lewis 1996; Spratt 1991)
17.07.1967	Denver	Colorado, United States	L6	Struck a warehouse roof	(Siber; Spratt 1991), MB44

(continued)

Table 1 (continued)

Date	Name	Place	Type	Description	Source
14.08.1967	Buritizal	Sao Paulo, Brazil	LL3.2	Found in the stable	MB105
12.04.1968	Schenectady	New York, United States	H5	Struck a building's roof	(Siber; Spratt 1991), MB44
10.08.1968	Piancaldoli	Emilia-Romagna, Italy	L3.4	Struck the roof of a house	MB51
25.04.1969	Bovedy (Belfast)	North Ireland, United Kingdom	L3	Struck a building	(Spratt 1991)
07.08.1969	Andreevka	Ukraine, USSR	L3	Struck the slate roof of a house	(Spratt 1991), MB54
16.09.1969	Suchy Dul	Královéhradecký, Czech Republic	L6	Struck the roof of a house	(Spratt 1991), MB48
28.09.1969	Murchison	Victoria, Australia	CM2	Struck the roofs of several buildings	(Siber; Spratt 1991), MB48
1945 – 1970?	Wernigerode	Sachsen-Anhalt, Germany	H5	Was found in the attic of a house	MB86
February 1971?	Tintigny	Luxembourg, Belgium	Eucrite, polymict	Struck the roof of a barn	MB107
08.04.1971	Wethersfield (1971)	Connecticut, United States	L6	Fell through the roof of the house	(Siber; Spratt 1991), MB50
02.08.1971	Havero	Turku Ja Pori, Finland	Ureilite	Struck the roof of a storehouse	(Spratt 1991), MB51
15.10.1972	Valera	Trujillo, Venezuela	L5	Killed a cow	MB85
15.03.1973	San Juan Capistrano	California, United States	H6	Struck the aluminum roof of a carport	(Siber; Spratt 1991), MB53
27.10.1973	Canon City	Colorado, United States	H6	Fell through the roof of a garage	(Siber; Spratt 1991), MB52
18.08.1974	Naragh	Esfahan, Iran	H6	Fell through the roof of a school	(Spratt 1991), MB53
31.01.1977	Louisville	Kentucky, United States	L6	Damaged buildings	(Spratt 1991), MB50
Found 10.1978	Walnut Hill	Maine, United States	OC	Struck a shed roof	MB75

(continued)

Table 1 (continued)

Date	Name	Place	Type	Description	Source
13.05.1981	Salem	Oregon, United States	L6	Fell onto the roof of a house	(Spratt 1991), MB60
12.10.1982	Wethersfield (1982)	Connecticut, United States	L6	Struck the roof of a house	(Siber; Spratt 1991), MB62
30.06.1984	Aomori	Tohoku, Japan	L6	Struck the zinc roof of a printing shop	(Spratt 1991), MB63
22.08.1984	Tomiya	Tohoku, Japan	H4/5	On the veranda of a house	(Spratt 1991), MB63
10.12.1984	Claxton	Georgia, United States	L6	Hit a metal mail box	(Spratt 1991), MB63
06.01.1985	La Criolla	Entre Rios, Argentina	L6	Farmhouse roof, and the door	(Lewis 1996; Spratt 1991)
29.04.1986	Sayama	Kanto, Japan	CM2	The porch of the house	MB85
29.07.1986	Kokubunji	Shikoku, Japan	L6	Hit several buildings	(Lewis 1996; Spratt 1991), MB67
01.03.1988	Trebbin	Brandenburg, Germany	LL6	Struck a greenhouse	(Lewis 1996; Spratt 1991), MB67
18.05.1988	Torino	Piemonte, Italy	H6	Struck a building	(Lewis 1996; Spratt 1991)
15.08.1989	Sixiangkou	Jiangsu, China	L5	Hit the roof of a house	(Spratt 1991), MB69
07.04.1990	Glanerburg	Netherlands	L/LL5	Fell on the roof of a house	MB70
04.09.1990	Burnwell	Kentucky, United States	H4-an	Fell through the porch	MB82
14.08.1992	Mbale	Eastern, Uganda	L5/6	Struck several buildings, a boy on the head	(Siber), MB75
09.10.1992	Peekskill	New York, United States	H6	Struck a car	(Siber), MB75
10.12.1992	Mihonoseki	Chugoku, Japan	L6	Struck the roof and floor	MB75
20.10.1994	Coleman	Michigan, United States	L6	Penetrated the roof of a house	MB80
18.02.1995	Neagari	Chubu, Japan	L6	hit a car trunk	MB78
07.01.1996	Tsukuba	Kanto, Japan	H5-6	Penetrated a roof	MB80

(continued)

Table 1 (continued)

Date	Name	Place	Type	Description	Source
21.10.1996	Turtle Lake	Wisconsin, United States	L5	Struck a car	MB93
15.02.1997	Juancheng	Shandong, China	H5	Penetrated a roof and landed in a pot on a stove	MB82
01.09.1997	Worden	Michigan, United States	L5	Struck a garage	MB85
31.12.1997	Vissannapeta	Andhra Pradesh, India	Eucrite-cm	Fell with a loud thud on the roof	MB84
13.06.1998	Portales Valley	New Mexico, United States	H6	Hit a barn roof and wall	MB83
26.09.1999	Kobe	Kinki, Japan	CK4	Fell through the roof of a house on a bed	MB84
14.12.1999	Dunbogan	New South Wales, Australia	L6	Struck the roof and the ceiling of a living room	MB85
02.2002	Alby sur Chéran	Haute Savoie, France	Eucrite-mmict	Struck the roof of a building	MB88
20.02.2002	San Michele	Marche, Italy	L6	Struck a building roof	MB89
07.2002	Dongyang	Zhejiang, China	H5	Found under the leaking roof	MB102
01.02.2003	Hiroshima	Chugoku, Japan	H5	Found on the leaking roof	MB87
23.09.2003	New Orleans	Louisiana, United States	H5	Crashed through the house	MB88
14.07.2006	Moss	Østfold, Norway	CO3.6	Landed on an aluminum sheet	MB91
31.07.2006	Jodiya	Gujarat, India	L5	Struck many roofs	MB94
21.02.2007	Mahadevpur	Arunachal Pradesh, India	H4/5	Fell through the roof of a house	MB94
06.07.2007	Cali	Valle del Cauca, Colombia	H/L4	Struck many roofs	MB93

(continued)

Table 1 (continued)

Date	Name	Place	Type	Description	Source
22.09.2007	San Juan de Ocotán	Jalisco, Mexico	L5	Struck a building	MB104
10.01.2008	Sokoto	Sokoto, Nigeria	IIIAB	Destroyed the roof of the house	MB107
12.04.2008	Xinglongquan	Hebei, China	L3	Penetrated the roof of a house	MB104
01.03.2009	Cartersville	Georgia, United States	L5	Struck the roof, joist, ceiling, door of a house	MB104
26.09.2009	Grimsby	Southern Ontario, Canada	H5	Struck a car	MB97
18.01.2010	Lorton	Virginia, United States	L6	Fell through the roof and ceiling	MB99
14.04.2010	Mifflin	Wisconsin, United States	L5	Hit the metal roof of a shed	MB99
30.04.2011	Sołtmany	Warmińsko-mazurskie, Poland	L6	Struck a roof and a concrete step at a farm	MB100
13.06.2011	Draveil	Ile-del-France, France	H5	Several roofs were damaged	MB102
16.07.2011	Thika	Kiambu County, Kenya	L6	Struck a building and greenhouses	MB100
17.10.2012	Novato	California, United States	L6	A building and a garage	MB103
15.02.2013	Chelyabinsk	Chelyabinsk region, Russia	LL5	Buildings, people wounded by glass	MB102
19.04.2013	Wolcott	Connecticut, United States	L5	Building roof and a pipe	MB103
23.04.2013	Braunschweig	Niedersachsen, Germany	L6	Damaged concrete pavement	MB102
09.12.2013	Parauapebas	Para, Brazil	H4-5	Struck a building's roof and (doubtfully) a woman	MB107

(continued)

Table 1 (continued)

Date	Name	Place	Type	Description	Source
09.05.2014	Jinju	Gyeongsangnam-do, South Korea	H5	Struck the roof of a greenhouse	MB103
27.06.2015	Famenin	Hamadan, Iran	H/L3	Damaged a roof	MB104
02.09.2015	Sariçiçek	Bingol, Turkey	Howardite	Fell down on houses	MB105
06.02.2016	Ejby	Hovedstaden, Denmark	H5/6	Damaged tiles in front of a house	MB105
11.01.2017	Broek in Waterland	Noord-Holland, Netherlands	L6	Struck the roof of a garden shed	MB106
Found 17.07.2017	Dueodde	Denmark	H5	Struck the roof of the annex of a summer house	MB107
01.06.2018	Mangui	Yunnan, China	L6	Broke through a farmer's silt-roofed house	MB107
26.09.2018	Komaki	Chubu, Japan	L6	Hit several buildings	MB108
23.04.2019	Aguas Zarcas	Alajuela, Costa Rica	CM2	Hit a house and a dog-house	MB108

4 Conclusions

Currently (May 2019) meteorite catalogs and bulletins contain information about 122 harmful meteorites; 9 of them are doubtful records, which we have left in the table as having historical value. In six cases, meteorites were reported to have killed animals (2 of them are doubtful). There is a certain case of a meteorite hitting a human being (Sylacauga, not fatal) and another one of a man stunned by meteorite (Nedagolla, 1870). As a result of the shock wave caused by the Chelyabinsk meteorite, many people were injured by fragments of broken windows. There is also a report that a fragment of the Mbalé meteorite hit a person. Six meteorites damaged cars. The distribution of bad meteorites by the damaged object, type and fall region is shown in Fig. 1.

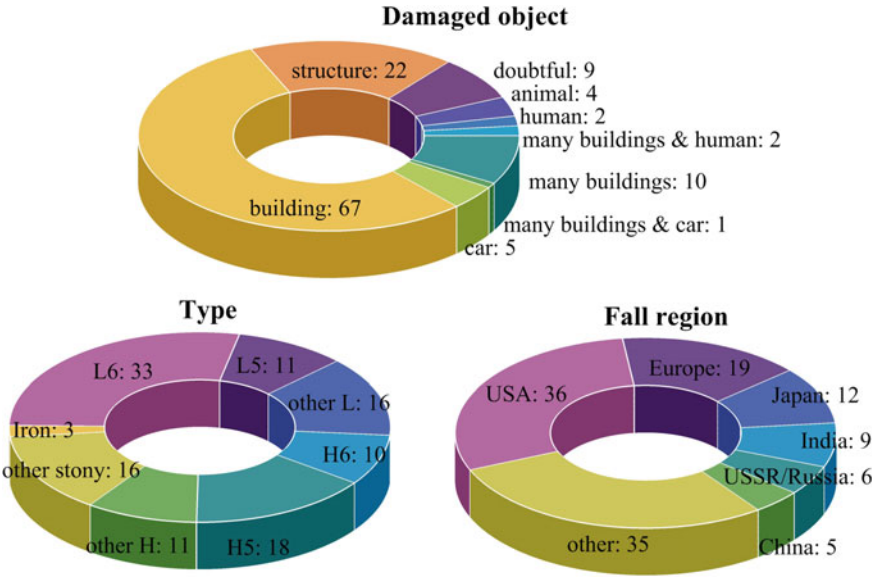

Fig. 1 Distribution of bad meteorites by damaged object, type and fall region

The number of bad meteorites that hit individual residential buildings: 66; several buildings in one fall: 14; structures (non-residential buildings, garages, barns, stables, greenhouses, etc.)—22 cases. Of course, we cannot exclude that other events indicated in the Lewis (1996) and Yau (1993) lists also took place, but the absence of extraterrestrial matter does not make them definitively convincing.

So, for every tenth fall of a meteorite (out of a total of 1,300 falls, counting by (The Meteoritical Bulletin 2019), not including the finds), meteorite material directly invades the human environment (directly people, their property and animals).

References

Astapovich IS. Komety, meteory, zatmeniya. M.: Mosk. planetarii, 1941. [Astapovich IS. Comets, meteors, eclipses. Moscow: Moscow Planetarium; 1941. (In Russ.)]

Boyarchuk AA. Ugroza s neba: rok ili sluchainost'? Opasnost' stolknoveniya Zemli s asteroidami, kometami i meteoroidami. M.: Kosmosinform, 1999. [Boyarchuk AA. Threat from the sky: rock or accident? The danger of a collision of the Earth with asteroids, comets and meteoroids. Moscow: Cosmosinform, 1999. (In Russ.)]

Fedynskii V. Nebesnye kamni-meteority i meteory. M.: Pravda; 1950. [Fedynsky V. Heavenly rocks-meteorites and meteors. Moscow: Pravda; 1950. (In Russ.)]

Grokhovskii VI, Murav'ev LA. Khronolist "zlykh" meteoritov. Geologicheskie opasnosti. Arkhangel'sk, IEPS ANTs UrO RAN; 2009. ss.315-319 [Grokhovsky VI, Muravyev LA. Chrono list of "evil" meteorites. Geological Hazards. Arkhangelsk: IEPA ANC UB RAS; 2009. pp.315-319. (In Russ.)]

Hey MH. Catalogue of meteorites. 3rd ed. London: British Museum; 1966.

Lewis JS. Rain of iron and ice. Addison-Wesley Pub. Co. 1996 IBSN 0201489503

Muravyev LA. Global datasets of the geophysical fields as an instrument for impact structures discovery. Meteoritics & Planetary Science, 54(S2); 2019 p. 6462.

Muravyev LA, Grokhovsky VI. The chrono list of bad meteorites. Meteoritics & Planetary Science, 54(S2); 2019. p. 6454.

Popova OP et al. Chelyabinsk airburst, damage assessment, meteorite recovery, and characterization. Science 342(6162); 2013 pp.1069-1073.

Spratt CE. Possible hazards of meteorite falls. J Roy. Astron. Soc. Can., V.85, N.5, 1991

Schulz B. Steine, die vom Himmel fallen. Wittenberg, Zienisen Verlag; 1956.

The Meteoritical Bulletin. https://www.lpi.usra.edu/meteor/. Accessed 21 May 2019.

Siber HJ. Meteorite & Megakatastrophen. Sonderdchau des Sauriermuseum Aathal.

Yau K, Wiessman P, Yeomans D. Prepring of the Jet Propulsion Laboratory (California Institute of Technology); 1993.

Use of Modern Spectroscopy Methods in Applied Gemology

Anatoliy G. Nikolaev

Abstract

This paper provides the information on the use of spectroscopy methods in gemological practice of studying gems. The possibilities of optical absorption and luminescence spectroscopy, Raman spectroscopy and infrared vibrational spectroscopy for the diagnosis of synthetic analogues of natural gemstones and the traces of their enhancement are described. This review shows the results of studies of rubies, sapphires, emeralds, diamonds and other gemstones.

Keywords

Spectroscopy · Gemstones · Gemology · Diamonds · Rubies · Sapphires · Emeralds

1 Introduction

Gemology is the field of science studying precious stones. At the early stages of its development it was intended to support jewelry trade. Gemology was separated from mineralogy into an independent scientific discipline at the beginning of the 20th century. Conventionally, the beginning of gemology development can be considered 1902, when the French chemist August Verneuil first obtained and began to supply the world market with synthetic rubies and later with synthetic sapphires and spinel. The appearance of a large number of synthetic stones increased the value and cost of natural gemstones. According to literature

A. G. Nikolaev (✉)
Kazan (Volga Region) Federal University, 18 Kremlyovskaya str., Kazan, Russia
e-mail: anatolij-nikolaev@yandex.ru

S. Votyakov et al. (eds.), *Minerals: Structure, Properties, Methods of Investigation*,
Springer Proceedings in Earth and Environmental Sciences,
https://doi.org/10.1007/978-3-030-49468-1_21

(Gadiyatov et al. 2007), over the past twenty years, the cost of jewelry diamonds has increased almost four times, and the prices for natural emeralds and rubies often exceed the prices of diamonds. In this regard, the technologies and methods for the production of synthetic analogues of natural stones and enhancement methods for various jewelry materials began to develop actively. In this context, difficulties began to arise in the diagnosis and identification of synthetic and enhanced gemstones, since standard gemological tests were no longer suitable for this purpose.

In recent years, gemology as an independent science has been developing particularly intensively, since new, modern research methods help gemologists, such as luminescence spectroscopy, Raman spectroscopy, IR Fourier spectroscopy, absorption optical spectroscopy, and luminescence spectroscopy. These methods of spectroscopic analysis are effective for identifying all sorts of fakes and well identify synthetic gems.

2 Methods

2.1 Raman Spectroscopy

This method is appropriate for identifying mineral species when it is impossible to use standard gemological tests. Raman spectroscopy can identify various inclusions in precious stones, such as mineral solid inclusions and gas-liquid inclusions in order to determine the genesis of a gemstone and possible traces of its enhancement. Solid inclusions can give information about the formation conditions. They can be typomorphic for a particular deposit, and sometimes can be used for the assessment of PT parameters of mineral formation. Unambiguous diagnostics of typomorphic inclusions allows the country of the gem origin to be determined.

Using Raman spectroscopy, synthetic analogs of natural stones can be diagnosed by the inclusions of lead molybdate, lithium tungstate, and vanadium pentoxide, etc. (Elwell 1986).

Determination of Aggregates in Gemstones using Raman Spectroscopy. Minerals are often filled with various organic compounds. The most commonly used are synthetic resins, oils, and various organic fillers. Emeralds are a good example of enhancement by crack filling. Organic substances used for filling significantly reduce the visibility of cracks on the mineral surface. It is possible to identify a specific aggregate—resin, oil, Canadian balm, or their mixture—having obtained the Raman spectrum of a substance.

Various aggregates are often present in gemstones, such as turquoise, jade, etc. Their presence can be identified in a similar way using Raman spectroscopy.

Diagnostics of Natural GE POL Enhanced Diamonds. Type IIa low-grade brown diamonds are subjected to HPHT (high-pressure high-temperature) enhancement in order to remove the brown component from their color and to obtain colorless gems. According to the diamond FWHM (the full width of the Raman peak at its

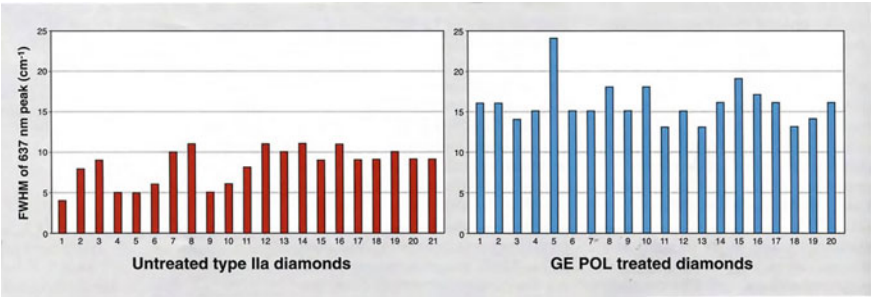

Fig. 1 The FWHM of the 637 nm luminescence peak measured at liquid nitrogen temperature is 13 cm^{-1} in GE POL diamonds or higher, while that of untreated IIa type diamonds (both colorless and brown) is 11 cm^{-1} or lower

half maximum), one can determine whether the diamond is natural, synthetic, or enhanced (Fig. 1). For natural gemstones, this value is less than 2.5 cm^{-1}, for Ib synthetic diamond it is 3.2 cm^{-1} or higher (Gems & Gemology in Review 2008).

2.2 IR Spectroscopy

Natural and synthetic gemstones have the same chemical and physical properties, but differ in trace elements, structural and crystal chemical defects, in particular, and the presence or absence of the OH-groups in their structure. This results in specific features, which are used by specialists for the diagnostics of natural stones and their synthetic analogues by the infrared spectra.

Synthetic solution-melt emeralds are characterized by the absence of crystallization water in their structure, while in natural emeralds the water content can reach up to 2–4%. This difference is easily determined by the infrared spectra and serves as an unambiguous criterion for diagnosing such stones. The same criterion is used to distinguish synthetic solution-melt and natural alexandrites. Emeralds obtained by hydrothermal synthesis contain only type I H_2O molecules in their structure, which can be used to diagnose such stones. Chlorine is not included in the structure of natural emeralds, but forms salt compounds in gas-liquid inclusions, therefore the presence of chlorine absorption lines in the infrared spectrum is a sign of synthetic hydrothermal emeralds.

Synthetic analogues of sapphires and rubies also have their own distinctive features in the infrared spectra, this applies to various bands of OH-groups. IR Fourier spectroscopy allows most synthetic corundum to be diagnosed.

IR spectroscopy allows the express diagnostics of natural quartz and its synthetic analogs to be performed. By the presence of a water absorption band (3000–3800 cm^{-1}) in the quartz spectra, natural stones can be distinguished from synthetic hydrothermal ones.

The method of IR spectroscopy is basic in determining the nature of the diamond origin by nitrogen structural defects. In some cases, the type of infrared spectrum can directly indicate the nature of the diamond, and further testing by instrument methods is not required (Gems & Gemology in Review 2005).

It is possible to determine any imitation of a precious stone or identify its mineral species with the help of IR-spectroscopy. If the diagnostics concerns translucent minerals (turquoise), mineral aggregates (jadeite, jade), amber, etc., such samples are often difficult to identify. In these cases, you can use the methods of infrared Fourier spectroscopy and Raman spectroscopy together.

Using IR Fourier spectroscopy, it is possible to diagnose amber and copal and their various simulations, while the IR spectrum characteristics can distinguish natural Baltic amber from the amber of other deposits.

In order to improve the appearance of fractured stones, they are filled with various types of fillers. Emeralds, rubies and sapphires are most often filled of all gemstones. Diagnostics of their filling is carried out mainly with the help of infrared spectroscopy (Fig. 2).

Cracks in natural corundum are often filled with borax and lead glass. The presence of the latter in the gem can be diagnosed by the characteristic absorption bands in the infrared spectrum. Various ornamental opaque jewelry materials (jadeite, turquoise) are also impregnated, which is recorded in typical C-H bands in the infrared spectrum.

Infrared spectroscopy is one of the main methods for identifying traces of gem enhancement, such as heat treatment and irradiation. To identify the color nature of colored and colorless diamonds, it is necessary to determine the physical type of diamond, according to IR spectroscopy, and, based on this, choose the method of its research, depending on the types of nitrogen centers in it.

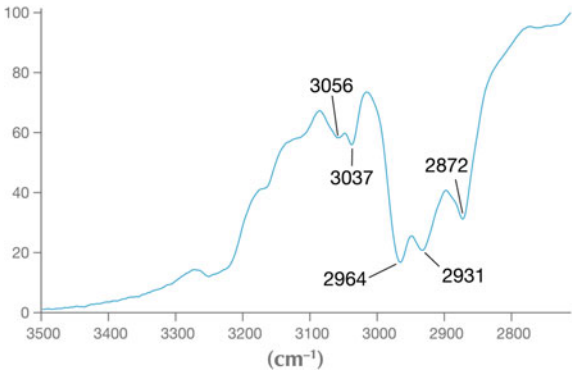

Fig. 2 FTIR spectroscopy showing epoxy resin peaks at 3056, 3037, 2964, 2931, and 2872 cm^{-1}

2.3 Optical Absorption and Luminescent Spectroscopy

Optical absorption spectroscopy studies the nature of the color of a gemstone. Color is the main criterion for the formation of its final cost. The main chromophores in colored stones are elements of the iron group (Platonov et al. 1984). Nitrogen centers and various color centers associated with structural defects in the form of plastic deformations are responsible for the color in diamonds (Solodova et al. 2008; Gems & Gemology in Review 2006).

The main application of optical spectroscopy methods is to diagnose natural diamonds and their synthetic analogues, as well as to identify the traces of their enhancement (Figs. 3 and 4).

Currently, diamonds are irradiated in cyclotrons and nuclear reactors. Diamonds of Ia type are colorless before irradiation, colored in various shades of blue and green. Their absorption spectrum is determined by the GR1 band at wavelength of 470 nm with an additional absorption in the range of 430–550 nm, which gives the diamond color a greenish tint. Depending on the concentration of A and B1 defects, the position of the absorption edge varies from 240 to 300 nm. The position of the absorption edge also affects the predominance of the blue or green component in the final color of the irradiated diamond.

During the HPHT process, with the onset of plastic deformation, the impurity atoms associated with the dislocations are released, and a huge amount of free defects, i.e. vacancies, intrinsic and impurity interstitial atoms appear in the crystal structure. The number of relatively stable atoms includes H3, H4, H2, N3, A and B1. The detection of the H3 and H4 defects in the absorption spectra at the same time is one of the signs of the HPHT treatment, since in natural non-enhanced

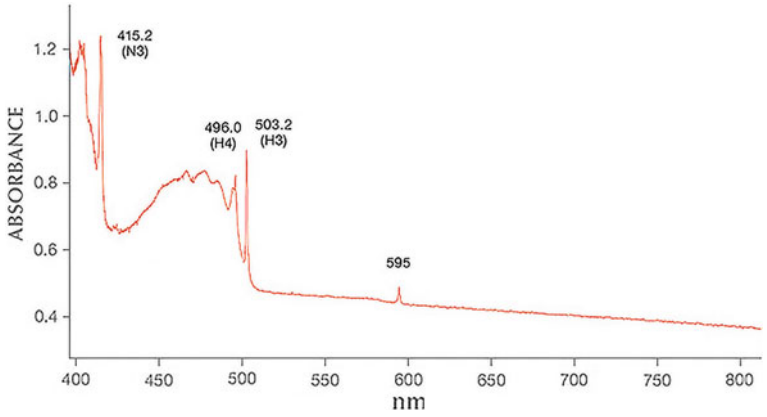

Fig. 3 Vis-NIR absorption spectrum of irradiated yellow diamond recorded at liquid-nitrogen temperature, showing strong absorption due to H3 and H4 defects artificially introduced to enhance the yellow color

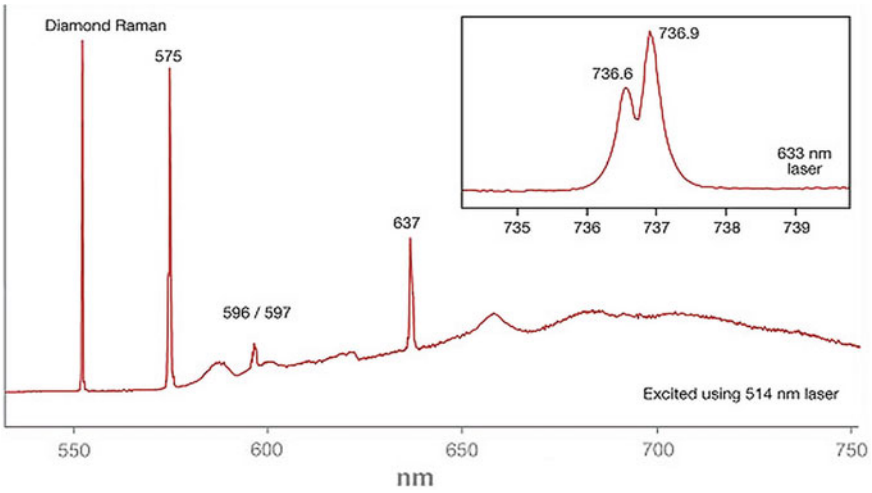

Fig. 4 The 2.16 ct synthetic diamond showed typical photoluminescence features of CVD growth, including strong emissions from N-V centers at 575 and 637 nm, moderate CVD-specific emissions at 596/597 nm, and 736.6 and 736.9 nm emissions from the $[Si\text{-}V]^-$ center

diamonds these two defects have not been simultaneously encountered (Gems & Gemology in Review 2008).

A combined treatment is also possible: after high pressure annealing, diamonds are irradiated with an electron beam and then subjected to high temperature annealing without pressure (HPHT + βHT). After annealing, most Ia type diamonds acquire a yellow-green color, while other types become red of varying intensity. The red color of the crystals is due to the absorption at 637 nm, associated with the appearance of $(N\text{-}V)^-$ defects. A βHT treatment leads to a decrease in the intensity of the brown color of diamonds. Crystals with an initial light brown color turn yellow-green and have no brown tint in the color.

When conducting βHT processing, the following changes in the color of diamonds can occur: crystals containing B2 defects are of yellow-green color; crystals containing an A-defect and no B2 or C defects are of red color; the intensity of the brown color in IIa type diamonds decreases by reducing the concentration of dislocations.

3 Conclusions

This paper presents an overview of the use of spectroscopy methods in the study of gems and their synthetic analogs, as well as methods of their refining. The use of modern instrumental physical methods in combination with traditional gemological studies allows a number of problems in gemology to be solved.

Acknowledgements This study was performed in the context of the Russian Government Program of Competitive Growth of Kazan Federal University.

References

Elwell D. Iskusstvennyye dragotsennyye kamni. M.: Mir; 1986. [Elwell D. Artificial gems stones. M.: Mir; 1986. (in Russ.)].

Gadiyatov VG, Gadiyatova MV, Goncharova II. Kommercheskaya gemmologiya. Voronezh: Ed.-printing center of the Voronezh State. un-ta; 2007. [Gadiyatov VG, Gadiyatova MV, Goncharova II. Commercial gemology. Voronezh: Ed.-printing center of the Voronezh State. un-ta; 2007. (in Russ.)].

Gems & Gemology in Review. Synthetic Diamonds. Carlsbad: GIA; 2005.

Gems & Gemology in Review. Colored Diamonds. Carlsbad: GIA; 2006.

Gems & Gemology in Review. Treated Diamonds. Carlsbad: GIA; 2008.

Platonov AN, Taran MN, Balitsky VS. Priroda okraski mineralov. M.: Nedra; 1984. [Platonov AN, Taran MN, Balitsky VS. The nature of coloring minerals. M.: Nedra; 1984. (in Russ.)].

Solodova YP, Nikolaev MV, Kurbatov KK et al. Gemmologiya almaza. M.: Agat; 2008. [Solodova YP, Nikolaev MV, Kurbatov KK et al. Gemology of a diamond. M.: Agat; 2008. (in Russ.)].

Formation Conditions of Volga-Ural Domanikites and Their Prospective Assessment

Aigul V. Nizamova, Vladimir P. Morozov, and Alexey A. Eskin

Abstract

In Russia, due to the depletion of traditional and relatively easily recoverable hydrocarbon resources, a great deal of attention is currently being paid to finding and evaluating a relatively new source of raw materials—hydrocarbons of oil source rocks. The latter relate to non-traditional resources and their commissioning predetermines a high degree of their mineralogical, lithological and geochemical study.

Keywords

Volga-Ural region · Domanik · Simultaneous thermal analysis · Gas-liquid inclusions

1 Introduction

Domanikian deposits in the Volga-Ural region stretch from the Pechora Sea in the north to the Caspian Depression in the south along the western slope of the Ural Mountains. The deposits are cyclical in nature and are characterized by the alternation of carbonate and carbonate-siliceous layers enriched by organic matter of the sapropel type (Poludetkina et al. 2017). The depth of the deposit occurrence is 1500–1800 m. Beginning with the work of A.D. Arkhangelsky (1929), these rocks are considered an oil source for oil fields in the eastern part of the East European Platform (Galimov and Kamaleeva 2015).

A. V. Nizamova (✉) · V. P. Morozov · A. A. Eskin
Kazan (Volga Region) Federal University, 18 Kremlyovskaya str., Kazan, Russia
e-mail: aigulv96@mail.ru

S. Votyakov et al. (eds.), *Minerals: Structure, Properties, Methods of Investigation*,
Springer Proceedings in Earth and Environmental Sciences,
https://doi.org/10.1007/978-3-030-49468-1_22

Based on the study of various groups of faunas, the sea basin of sedimentation during the Domanik was characterized by normal salinity, normal oxygen regime and the prevailing depth of about 100 m (Maksimova 1970). The literature also mentions the influence of endogenous fluids on the formation of sediments, in which the proportion of the sapropel component is large (Tsekhovsky et al. 2018).

2 Materials and Methods

The core material was used for the study. A total of 5 wells were studied, characterized by core material selected within Tatarstan. The core recovery in all of them was 100%.

The research methods used were optical microscopic analysis of thin sections, X-ray diffraction analysis, electron microscopic analysis, X-ray fluorescence analysis, and simultaneous thermal analysis.

A macroscopic description of the pre-sawn core was carried out to identify the lithological heterogeneity of the core material and to identify the sequence of bedding of certain lithotypes.

An optical microscopic analysis of thin sections was performed using an Axio Imager (Carl Zeiss, Germany) optical polarization microscope of the research class in the transmitted light. The microscope is equipped with a digital camera.

An X-ray phase analysis was performed using a D2 Phaser diffractometer (Bruker, Germany) used for measuring powdered samples in the Bragg-Brentano geometry, with monochromatic CuKα-radiation (λ = 1.54178 Å) in the step-scan mode. Measuring and recording parameters: X-ray tube voltage 30 kV, current 30 mA, scanning step 0.02°, speed 1°/min. The range of scanning angles in the Bragg-Brentano geometry was 3–40°. Powdered samples were analyzed.

The thermal analysis was performed on an STA 449 Jupiter F3 (Netzsch, Germany) to determine the calorific values and phase transitions of the combustible structural components of shale. The heating ranged from 30 to 1000 °C, the heating step was 10°/min in a constant air medium.

3 Results and Discussion

Domanikites macroscopically have a dark gray and black color. In the studied sections they alternate with light limestone. They have a coarse-grained structure and dense texture. According to the data of optical microscopic studies, the structure of domanikites is micro-fine-grained, the texture is homogeneous (Fig. 1). They are composed mainly of individual grains or aggregates of calcite and chalcedony, whose content is estimated as 10–20%. Organic matter is distributed evenly, although sometimes it is concentrated in clumps of lenticular isolations ~0.05 mm thick. Organic residues, represented by radiolarian shells, ostracods, tentakulita, and algal detritus are rarely found in thin sections. Very thin

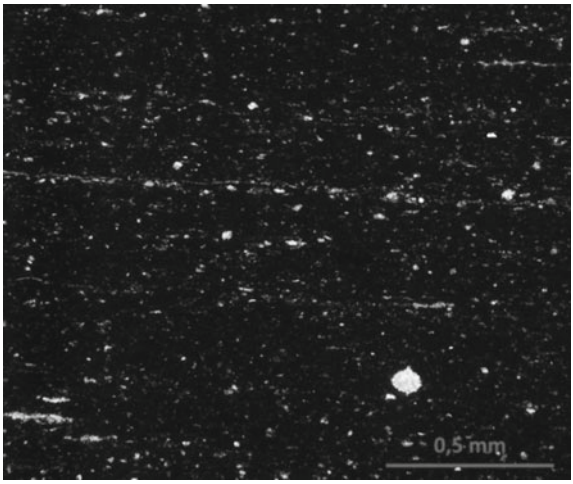

Fig. 1 Photo of thin rock section in crossed polarizers. Eastern part of the East European platform. Volga-Ural oil and gas province. Well 9916b. Depth 1707.8 m

light-brown grains of volcanic glass up to 0.1 mm in size are sometimes found in thin sections. Volcanic glass fragments are characterized by an isometric and elongated shape. Pyrite grains are also rarely found. Under the microscope, rocks are dense, porosity is not detected.

The results of X-ray diffraction (Table 1) indicate that quartz (chalcedony) is the main mineral. Feldspars, mica, carbonates, and pyrite are less abundant (Fig. 2).

A simultaneous thermal analysis was performed in order to determine the amount of organic matter present in the samples under study, as well as to identify its types. Graphically, the results of the analysis are shown in Fig. 3. The results of a simultaneous thermal analysis have shown that the content of the light fraction of hydrocarbons is on average about 4.5%, and the heavy fraction of hydrocarbons is 11.55%. Kerogen has not been detected in the studied samples.

Another important fact, in our opinion, is the anomalous thermal behavior of quartz (chalcedony). The endothermic effect of quartz at 573 °C, which indicates that quartz has a detrital genesis, has not been detected on the DSC curve of the studied samples. It can be assumed that the source of the substance for the deposition of silica minerals of the studied oil-bearing rocks was deep fluids.

Coarse-grained secondary calcites from veinlets cross-cutting carbonate-siliceous or carbonate rocks were used to determine the homogenization temperature of gas-liquid inclusions (Fig. 4). As a result, the average homogenization temperature of gas-liquid inclusions in secondary calcites was 117 °C, the minimum temperature was 97 °C, and the maximum temperature was 137 °C. The data obtained indicate that the calcite from the veinlets was formed at temperatures higher than the homogenization temperature.

Table 1 The mineral composition of a typical domanikite samples

Mineral	Quartz	K-feldspar	Mica	Calcite	Dolomite	Pyrite
Mineral composition, %	72.70	6.39	6.06	10.40	4.27	0.23

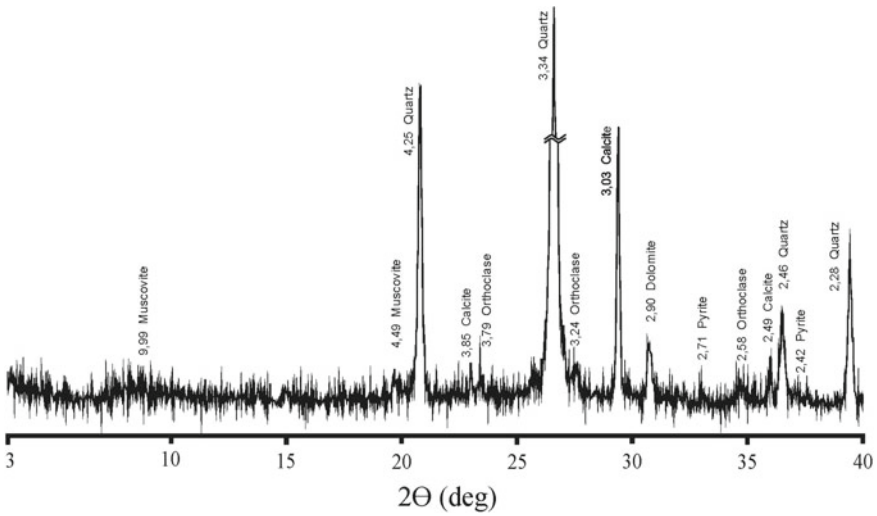

Fig. 2 Domanikite diffraction pattern. Eastern part of the East European platform. Volga-Ural oil and gas province. Well 22098. Depth 1506.3 m

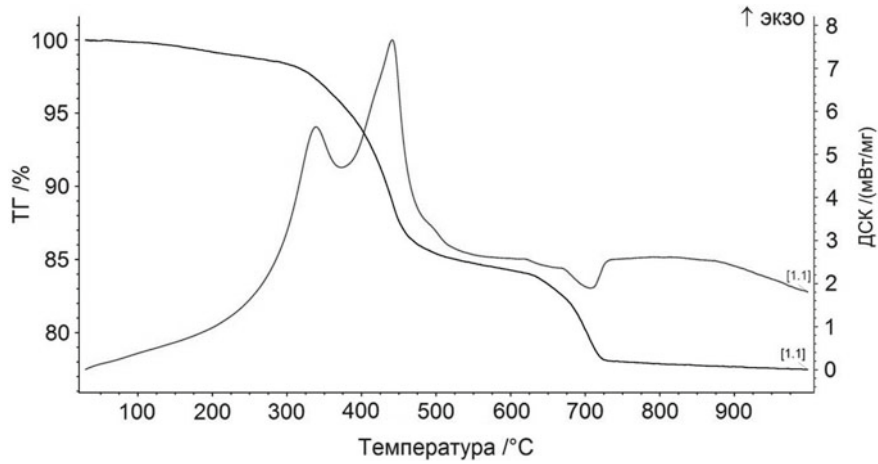

Fig. 3 Thermal analysis. Eastern part of the East European platform. Volga-Ural oil and gas province. Well 630s. Depth 1648 m

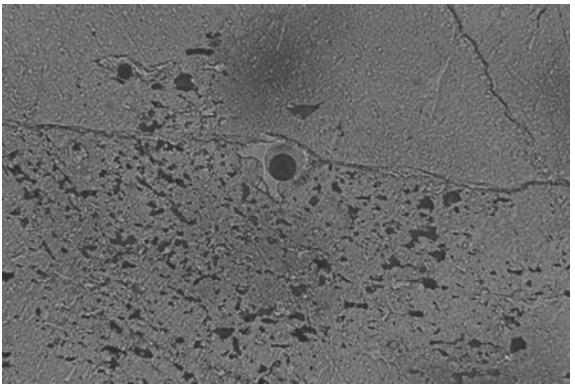

Fig. 4 Photo of gas-liquid inclusions (scale 1:50). Eastern part of the East European platform. Volga-Ural oil and gas province. Well 630 s. Depth 1,652.4 m

4 Conclusions

As a result of the work done, it is possible to draw the following conclusions:

1. The source of substance for the formation of anomalous by its thermophysical properties quartz was deep fluids.
2. The paleotemperature of the oil reservoir was found to be above 100 °C.

Acknowledgements This study was performed in the context of the Russian Government Program of Competitive Growth of Kazan Federal University.

References

Galimov EM, Kamaleeva AI. Source of hydrocarbons from the supergiant oil field Romashkino (Tatarstan) - inflow from the crystalline basement or oil source sediments? Geochemistry. 2015;2:103-122.

Maksimova SV. Ekologo-fatsial'nye osobennosti i usloviya obra-zovaniya domanika. M.: Nauka, 1970. p 101. [Maksimova SV. Ecological and facial features and conditions for the formation of Domanik. M.: Nauka, 1970. p 101. (in Russ.)].

Poludetkina EN, Smirnov MB, Fadeeva NP, Kozlova EV. Proof of the formation of organic matter in carbonate and carbonate-siliceous deposits of the Upper Devonian of the South Tatar Arch under conditions of constant anoxia in the photic layer. Geochemistry. 2017;8:730-740.

Tsekhovsky YuG, Baluev AS, Stukalova IE, Korneva RG. Sedimentogenez v mezozoiskikh i kainozoiskikh riftovykh vpadinakh Tsentral'noi Azii. M.: GEOS. 2018. p 168. [Tsekhovsky YuG, Baluev AS, Stukalova IE, Korneva RG. Sedimentogenesis in Mesozoic and Cenozoic rift depressions of Central Asia. M.: GEOS. 2018. p 168. (in Russ.)].

The Study of Fluid Inclusion Salinity in Minerals by Raman Spectroscopy Revisited

Elizaveta A. Pankrushina, Mikhail T. Krupenin, Yuliya V. Shchapova, Aleksander S. Kobuzov, Asya A. Garaeva, and Sergei L. Votyakov

Abstract

Raman spectroscopy is an efficient non-contact and non-destructive method and has been widely employed in many research fields, including fluid inclusion studies. The Raman spectra of OH vibrations can be used to determine the salinity of solutions and consequently the salinity of natural fluid inclusions in minerals. However, when analyzing a poorly resolved spectrum with a low signal-to-noise ratio, the problem of the ambiguity of its conventional deconvolution using peak fitting and the determination of weak changes in the parameters of its elementary components arises. The aim of the study was to develop and test the central moment (kurtosis) method for processing Raman spectra by the example of a series of quartz samples with fluid inclusions and to determine their salinity using the H_2O vibrational modes avoiding the conventional peak fitting. The calibration curves for salinity determination were constructed using 26 model solutions of chemically pure NaCl with a mass fraction of 1 to 26%. To simulate the birefringence effect, a quartz plate was used to cover the cuvettes with solutions. A quantitative assessment of spectral shape variations was performed according to the values of their integral parameters (skewness and kurtosis). The regression coefficient for linear approximation of skewness and kurtosis based calibration curves was 0.97 and 0.98, respectively. The convergence with the microthermometric data for the two-phase fluid inclusions in quartz from a number of magnesite deposits of the Southern Ural was satisfactory.

E. A. Pankrushina (✉) · M. T. Krupenin · Y. V. Shchapova · A. S. Kobuzov · A. A. Garaeva · S. L. Votyakov
A.N. Zavaritsky Institute of Geology and Geochemistry, UB RAS, 15 Vonsovskogo Street, 620016 Ekaterinburg, Russia
e-mail: lizaveta.94@list.ru

S. Votyakov et al. (eds.), *Minerals: Structure, Properties, Methods of Investigation*, Springer Proceedings in Earth and Environmental Sciences,
https://doi.org/10.1007/978-3-030-49468-1_23

Keywords

Fluid inclusions · Salinity · Raman spectroscopy · Microthermometry · Kurtosis · Skewness

1 Introduction

The degree of mineralization (salinity) of fluids responsible for mineral formation in a wide range of conditions of the Earth's crust is an important characteristic of the fluid source that helps clarify their nature (from the diagenesis of sedimentary rocks to the crystallization of igneous rocks) (Redder 1987). An important role in the composition of fluids, primarily ore-bearing ones, the carriers of most metals, including rare and noble ones, are natural brines both buried evaporitic ones and formed during the dissolution of natural salt deposits. Given the high solubility of chlorides in water and the high crustal clarke of Cl, a measure of natural fluid mineralization can be their chloride salinity. The latter can be assessed by the composition of fluid inclusions in minerals as part of the microthermometric approach (Borisenko 1977; Bodnar 1993) or using the method of aqueous extracts from powdered mineral samples by ion chromatography (Bottrell et al. 1988). However, taking into account the difficulties of observing small fluid inclusions under a microscope, the effects of birefringence inside a host mineral, the presence of hydrocarbon gases (clathrates), which distort the data on the ice melting temperature, it is imperative to use modern non-destructive local physical and chemical methods to carry out such studies. Raman spectroscopy is an effective non-destructive method with high (up to a few microns) spatial resolution to study the structural features and content of various molecular groups both in a solid and in a solution (gas).

The dissolution of salts is known to result in the interaction of the respective cations and anions in a solution with H_2O molecules, which is detected by a change in the shape of the Raman spectrum of the characteristic mode associated with the O-H bond variation of H_2O molecules (see, for example, (Sun et al. 2010). The latter is used to assess the salinity of fluid inclusions in minerals. Some papers (Georgiev et al. 1984; Mernagh and Wilde 1989) give the analysis of changes in the spectral shape of the H_2O molecule bands with increasing salinity of the solution. It has been shown that the spectral skewness parameter, estimated by the area of its two fragments in the range of 2800–3300 and 3300–3800 cm^{-1}, varies linearly with increasing salinity of the aqueous solution up to its saturation. Dubessy et al. (2002) proposed to use the difference in the areas of the Raman spectra corresponding to pure water and a solution of a certain composition to quantify salinity. Calibration curves were obtained by the authors before the solutions were saturated with Li, Na, K, Mg, and Ca chlorides.

In general, it can be stated that in most publications on this issue, the traditional methods of processing a complex superimposed spectrum of fluid inclusion in the water region are used, i.e. a conventional procedure for its deconvolution into elementary components (peak fitting). The subsequent analysis of the experimental data is based on a comparison of the individual mode parameters, in most cases their intensities and the positions of the centers depending on the solution salinity. However, when analyzing a poorly resolved spectrum of a solution with a low signal-to-noise ratio, the problem of the ambiguity of its deconvolution and determination of weak changes in the parameters of its elementary components arises. In such cases, it is promising to use statistical methods for analyzing the variations of the full spectral profile without decomposing it into components, which makes it possible to quickly and objectively diagnose changes in the spectrum shape, in particular, depending on the solution salinity variations. There are various statistical techniques applied in spectroscopy to study the correlation of multidimensional data (see, for example, (Salje et.al. 2000; Robben 2017; Kollias et al. 2011)).

The aim of the study is to develop and test the central moment method (namely kurtosis) for processing Raman spectra by the example of a series of quartz samples with fluid inclusions and to determine their salinity using the H_2O vibrational modes.

2 Materials and Methods

The Raman spectra characterizing OH bond variations in an H_2O molecule in the range of 2800–3800 cm^{-1} were obtained using a Horiba LabRam HR800 Evolution spectrometer equipped with an Olympus BX-FM confocal microscope, an Ar laser (radiation wavelength of 488 nm) with Olympus 100x lens (NA = 0.9), with a diffraction grating of 600 gr/mm. The spectrometer was calibrated using the Rayleigh line and the emission lines of a neon lamp. The spectral resolution was about 2 cm^{-1}, the spatial lateral resolution was about 2 μm and the depth of about 5 μm. Before calculations, the initial Raman spectra were processed by Labspec 6.0, and the background, which was approximated by a linear function, was subtracted and normalized to the maximum value.

Two-phase fluid inclusions of various sizes (from 5 to 40 μm) in 08-3-5, K-11-4, K-11-3, 33604 20512, and 672 quartz samples representing the Satka, Ismakaevo, Abolovo, and Otnurok magnesite deposits of the Southern Ural province were studied. The independent estimates of NaCl mass fraction in the fluid inclusions of the listed quartz samples were carried out by the microthermometric (MTM) analysis on a Linkam TSH600 heating/freezing stage using the diagrams of fluid ice melting temperatures according to (Borisenko 1982). The salinity of the samples was approximately equal to the mass fraction of NaCl in solution.

To construct the calibration curves, the Raman spectra were studied for 26 model solutions of chemically pure NaCl with a mass fraction of 1 to 26% (according to (Memagh and Wilde 1989). The salinity of chloride solutions can be estimated by the calibration curve, and this procedure does not require the detailed information on the cationic composition of the fluid. The results of measuring the Raman spectra of distilled water were used as a "blank experiment". To simulate the birefringence inherent in the quartz matrix, the calibration data for solutions with a volume of 65 μl in plexiglass cuvettes were obtained when measuring their Raman spectrum through a plane-parallel quartz plate with a thickness of about 70 μm.

3 Results and Discussion

Figure 1 shows the Raman spectra of fluid inclusions in quartz samples in comparison with those in model solutions with different mass fractions of NaCl. Using the MTM data, the samples are found to be characterized by a wide range of salinity: it varies in the intervals of 0 ÷ 7, 10 ÷ 15, 10 ÷ 15, 24 ÷ 26, 23 ÷ 24, 11 ÷ 17 and 7 ÷ 13% in 20512, 672 08-3-5, K-11-2-3, K-11-2-4, and 33604 samples, respectively. It can be seen in Fig. 1 that the Raman spectra of inclusions in both quartz and model solutions vary significantly due to variations in salinity: some changes in the relative intensities and positions of various vibrational modes in the water region of the spectrum are recorded. It should be noted that the spectral bands

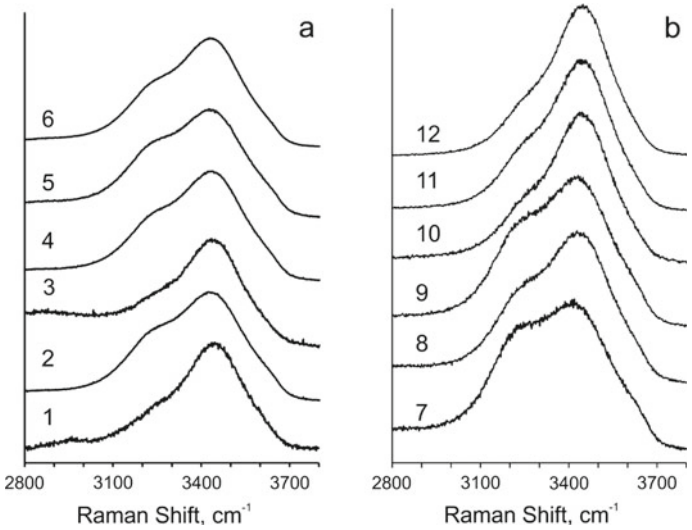

Fig. 1 The Raman spectra of fluid inclusions in quartz **a** and model solutions with various NaCl mass fractions **b**. 1–6—inclusions in 08-3-5, K-11-4, K-11-3, 33604, 20512, and 672 samples; 7–12—solutions containing 0, 5, 10, 15, 20 and 26% of NaCl, respectively

are quite wide, overlapping each other, as a result of which the deconvolution of the superimposed spectrum and the identification of its components by peak fitting are rather ambiguous.

Figures 2a, d show two calibration curves constructed following the cited papers using the peak fitting procedure for the I_1/I_2 intensity ratio of H_2O vibrational modes at 3210 and 3430 cm^{-1} and the $(\nu_n–\nu_0)$ shift of the mode center at 3210 cm^{-1} in the solution as a function of the NaCl content (here ν_n and ν_0 are the positions of the mode centers in the solution and in distilled water, respectively). In this case, the error in the I_1/I_2 ratio is experimentally estimated as a confidence interval using four measurements, the error of the NaCl molar fraction in solution as the error in indirect measurements, including the errors of measuring instruments, and the error $(\nu_n–\nu_0)$ as the error in indirect measurements, including errors in determining the vibrational mode positions in the spectrum (their position is monitored by Ne emission lines). The calibration curves I_1/I_2 *vs* ω_{NaCl} and $(\nu_n–\nu_0)$ *vs* ω_{NaCl} are characterized by a significant scatter: when they are linearly approximated, the regression coefficients are 0.70 and 0.93, respectively. The use of the

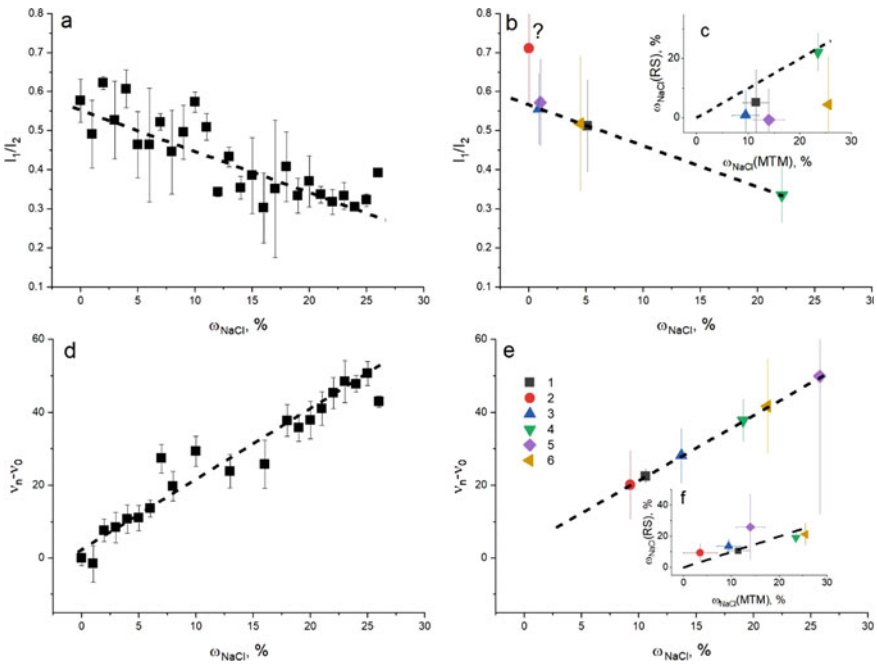

Fig. 2 The dependences of the I_1/I_2 intensity ratio of the H_2O vibrational modes at 3210 and 3430 cm^{-1} **a** and the $(\nu_n–\nu_0)$ shift of the mode center at 3210 cm^{-1} in solution **d** on the NaCl content (ω_{NaCl}, %); the results of assessing the salinity of fluid inclusions in quartz performed using I_1/I_2 ratio (b) and $(\nu_n–\nu_0)$ center shift **e** of vibrational modes in the Raman spectra and their comparison **c**, **f** with those obtained by the MTM method. Here and in Fig. 3: 1—sample 672; 2-20512; 3-33604; 4—K-11-3; 5—K-11-4; 6—08-3-5

obtained calibration curves based on the conventional peak fitting procedure to estimate the NaCl mass fraction in fluid inclusions of the quartz test samples indicates their low reliability, i.e. the estimates are characterized by a significant error (Fig. 2b, e); the convergence with the MTM data is unsatisfactory (Fig. 2c, f).

In the papers (Georgiev et al. 1984; Mernagh and Wilde 1989), a fundamentally different approach was used for constructing calibration curves based on the analysis of variations in the full profile of the Raman spectrum without its deconvolution into components. Following the above cited papers, the profile of O-H bond vibrations can be expressed in terms of the symmetric and asymmetric components, and the change in the shape of water spectrum with increasing NaCl in solution can be estimated according to the formula:

$$D = \frac{\sum_{n>0}\{[I(n) - I(-n)]/2\}}{\sum_{n>0}\{[I(n) + I(-n)]/2\}},$$

Where D is the skewness coefficient, n is Raman shift (n = 0 corresponds to 3300 cm^{-1}), I is intensity.

Following this approach, Fig. 3a shows the calibration curve constructed for the skewness parameter of the Raman spectrum of the H_2O molecule as a salinity function of the ω_{NaCl} solution. The skewness parameter is determined by the ratio of the areas of two spectral fragments in the ranges of 2800 ÷ 3300 and 3300 ÷ 3800 cm^{-1}; its error is estimated as a confidence interval in three dimensions. Note that the vibrational modes in the H_2O spectrum overlap each other; the intersection point of the contours of 3210 and 3430 cm^{-1} modes is about 3300 cm^{-1}; as a result, the superimposed vibrational profile of O-H bonds is divided into two ranges indicated above. The analysis of the obtained data indicates that the use of the calibration based on the spectral skewness parameter is more promising than those based on peak fitting data: the linear regression coefficient for this calibration curve is higher and reaches 0.97; a satisfactory (within the method error) convergence with the MTM data is observed (Fig. 3c). Nevertheless, it seems relevant to continue the studies on the use of the central moment approach for processing spectroscopy data of Raman fluid inclusions, particularly, the kurtosis coefficient (Press et al. 1993). Note that earlier (Pankrushina et al. 2020) this coefficient was successfully used to analyze critical temperature zones by the Raman spectra of minerals obtained in the range of 80–800 K.

By definition, kurtosis is the normalized fourth central moment, an integral characteristic of the spectral shape, the measure of the distribution tail heaviness, which is calculated as:

$$Kurt = \frac{1}{N}\sum_{i=1}^{N}\left[\frac{\alpha_i - \bar{\alpha}}{Sd}\right]^4 - 3$$

where N is the number of spectral points, α_i is the intensity, and α is the mathematical expectation of spectral intensity (Press et al. 1993).

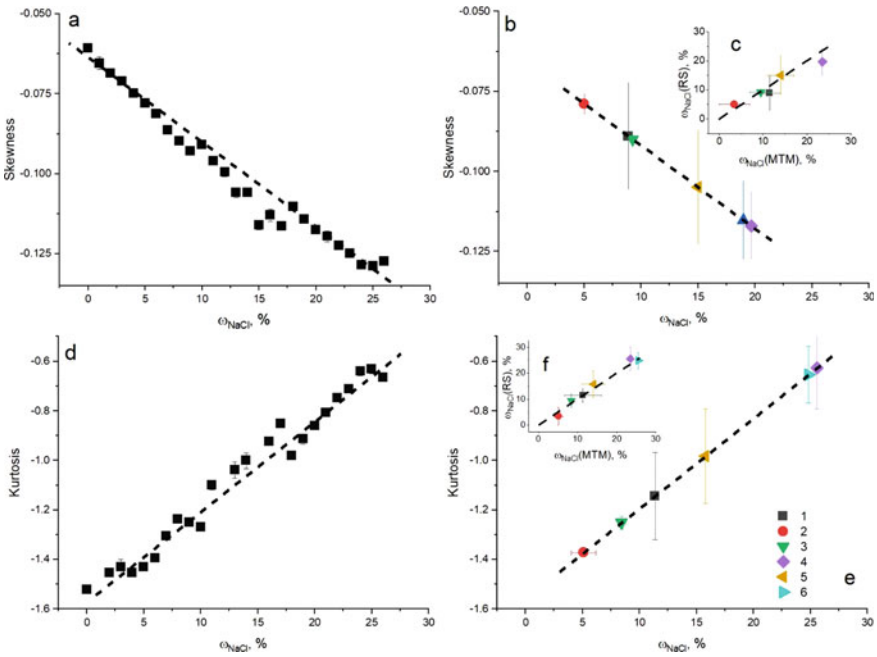

Fig. 3 The dependences of the skewness **a** and the kurtosis coefficient **d** of the Raman spectrum of the H_2O molecule in solution on the ω_{NaCl} content; the results of estimating the salinity of inclusions in quartz performed using the skewness parameter **b** and the kurtosis coefficient **e** of the Raman spectrum and their comparison **c**, **f** with those obtained by the MTM method

All mathematical calculations are performed using the Mathcad 15 software package. The algorithm description is given in (Pankrushina et al. 2020). It should be noted that the kurtosis coefficient can be calculated for any spectral shape, in contrast to the skewness parameter, which can be calculated by selecting the axis of the spectral symmetry. However, a necessary condition for calculating both parameters, based on their definition, is the coincidence of the number of spectral points of reference and analyzed samples.

Figure 3d–f shows the calibration curve for the kurtosis coefficient of the Raman spectrum as a function of ω_{NaCl} salinity, as well as the results of salinity assessment of the inclusions in quartz using this coefficient value, and their comparison with MTM data (the error of kurtosis coefficient determination is calculated as a confidence interval in three dimensions). The regression coefficient for linear approximation of calibration curve is 0.98; the convergence with MTM data is satisfactory.

4 Conclusions

Thus, the approach based on the use of the kurtosis method to estimate the salinity of inclusions in quartz according to the Raman spectroscopy data is more promising than using the conventional procedure of spectrum deconvolution into elementary components and their analysis. As a part of the kurtosis method, a quantitative assessment of variations in the spectral shape is performed according to the values of their integral parameters—skewness and kurtosis. The spectra of reference solutions obtained under the same experimental conditions as the inclusion spectra in mineral samples should be used for the construction of the respective calibration curves. To simulate the birefringence effect, which significantly affects the shape of the H_2O spectrum, it is necessary to introduce a plate made of the host mineral of fluid inclusions into the optical system of the Raman excitation-registration.

Acknowledgements The authors are grateful to N.V. Cherednichenko for helping prepare reference solutions and V.A. Volosatov for his help with technical preparation.
The reported study was carried out at the UB RAS "Geoanalitik" Center for Collective Use. Raman spectroscopy measurements were funded by RSF grant No. 16-17-10283; the statistical analysis was funded by RFBR, grant No. 19-35-90020; the microthermometric analysis was performed as part of topic No. AAAA-A18-118052590027-2 of the IGG UB RAS state assignment.

References

Bodnar RJ. Revised equation and table for determining the freezing point depression of H_2O-NaCl solutions. Geochim. et Cosmochim. Acta. 1993;57:683–684. 10.1016/0016-7037(93)90378-A.

Borisenko AS. Analiz solevogo sostava rastvorov gazovo-zhidkih vklyucheniy v mineralah metodom kriometrii. Ispolzovanie metodov termobarogeohimii pri poiskah i izuchenii rudnyih mestorozhdeniy. M. 1982: 37-47. [Borisenko AS. The analysis of the salt composition of solutions of gas-liquid inclusions in minerals by the cryometry method. The use thermobarogeochemistry methods in the search and study of ore deposits. M. 1982: 37–47 (In Russ)].

Borisenko AS. Izuchenie solevogo sostava rastvorov gazovo-zhidkih vklyucheniy v mineralah metodom kriometrii. Geologiya i geofizika. 1977;8:16-27 [Borisenko AS. The study of the salt composition of solutions of gas-liquid inclusions in minerals by cryometry. Geology and Geophysics. 1977;8:16–27 (In Russ)].

Bottrell SH, Yardley BWD, Buckley F. A modified crush-leach method for the analysis of fluid inclusion electrolytes. Bulletin Minéralogie. 1988;111:279–290. https://doi.org/10.3406/bulmi.1988.8048.

Dubessy J, Lhomme T, Boiron MC, Rull F. Determination of chlorinity in aqueous fluids using Raman spectroscopy of the stretching band of water at room temperature: application to fluid inclusions. Appl. Spectrosc. 2002;56:99–106.

Georgiev GM, Kalkanjiev TK, Petrov VP, Nickolov ZH. Determination of salts in water solutions by a skewing parameter of the water Raman band. Appl. Spectrosc. 1984;38:593–595. https://doi.org/10.1366/0003702844555106.

Kollias P, Rémillard J, Luke E, Szyrmer W. Cloud radar Doppler spectra in drizzling stratiform clouds: 1. Forward modeling and remote sensing application. J. Geophys. Res.. 2011;116:D13201. https://doi.org/10.1029/2010jd015237.

Mernagh TP, Wilde AR. The use of laser Raman microprobe for the determination of salinity in fluid inclusions. Geochim. Cosmochim. Acta. 1989;53:765–771. https://doi.org/10.1016/0016-7037(89)90022-7.

Pankrushina EA, Kobuzov AS, Shchapova YV, Votyakov SL. Analysis of temperature-dependent Raman spectra of minerals: Statistical approaches. J. Raman Spectrosc. 2020:1–14. https://doi.org/10.1002/jrs.5825.

Press JWH, Teukolsky SA, Vetterling WT, Flannery BP. Numerical Recipes in FORTRAN: The Art of Scientific Computing. Cambridge Univ. Press, Cambridge 1993:49.

Redder E. Fluid inclusions in minerals. M.: Mir. 1987;I:557.

Robben L. On the autocorrelation method of external parameter depending data-sets. Crystal. Mater. 2017;232 (4):267–277. 10.1515/zkri-2016-2000.

Salje EKH, Carpenter MA, Malcherek T, Boffa Ballaran T. Autocorrelation analysis of infrared spectra from minerals. Eur. J. Mineral. 2000;12 (3):503–519. https://doi.org/10.1127/0935-1221/2000/0012-0503.

Sun Q, Zhao L, Li N, Liu J. Raman spectroscopic study for the determination of Cl-concentration (molarity scale) in aqueous solutions: Application to fluid inclusions. Chemical Geology. 2010;4:55–61. https://doi.org/10.1016/j.chemgeo.2010.02.004.

The First Russian-Mongolian Meteorite Expedition to the Gobi Desert

Aleksander Yu. Pastukhovich, S. Demberel, Viktor I. Grokhovsky, Viktor V. Sharygin, Stepan V. Berzin, Kseniya A. Dugushkina, Mikhail Yu. Larionov, Lev A. Muravyev, T. Nasan-Ochir, Evgeniya V. Petrova, and Grigoriy A. Yakovlev

Abstract

The article describes the results of the work of the Russian-Mongolian meteorite expedition in the Gobi Desert during 08-09.2018. The coordinates of the areas of the search works, the search method and description of the meteorite substance are given. Two Mongolian meteorites were classified and their mineralogy and composition were studied in detail. Noyon and Shinejinst meteorites are ordinary chondrites of LL (L)3 S2 W2-3 and H4 S3-4 W2 classes, respectively.

A. Yu. Pastukhovich · V. I. Grokhovsky (✉) · V. V. Sharygin · M. Yu. Larionov · L. A. Muravyev · E. V. Petrova · G. A. Yakovlev
Ural Federal University, 19 Mira str., 620002 Ekaterinburg, Russia
e-mail: grokh47@mail.ru

S. Demberel · T. Nasan-Ochir
Institute of Astronomy and Geophysics of MAS, Ulaanbaatar, Mongolia

V. V. Sharygin
The Sobolev Institute of Geology and Mineralogy SB RAS, 3 Akademika Koptyuga ave., 630090 Novosibirsk, Russia

V. V. Sharygin
Novosibirsk State University, 1 Pirogova str., 630090 Novosibirsk, Russia

S. V. Berzin · K. A. Dugushkina
The Zavaritsky Institute of Geology and Geochemistry UB RAS, 15 Academika Vonsovskogo str., 620016 Ekaterinburg, Russia

L. A. Muravyev
Institute of Geophysics, Ural Branch of RAS, 100 Amundsena str., 620016 Ekaterinburg, Russia

S. Votyakov et al. (eds.), *Minerals: Structure, Properties, Methods of Investigation*, Springer Proceedings in Earth and Environmental Sciences,
https://doi.org/10.1007/978-3-030-49468-1_24

Keywords

Meteorites · Chondrites · Scanning electron microscopy · Gobi Desert · Mongolia

1 Introduction

The arid hot desert climate creates ideal conditions for the accumulation and preservation of extraterrestrial matter. Numerous zones of accumulation of meteorite fragments were found in the deserts of Oman, North-West Africa, and Chile. The Gobi Desert in Mongolia is the third largest hot desert, however, the Meteoritical Bulletin Database currently contains only 10 records of meteorites found in Mongolia. In addition, no dense collection areas (DCA) has been found in the Gobi Desert.

In 2018, the first Russian-Mongolian expedition to the Gobi Desert was undertaken with the purpose of searching for meteorites and studying the mechanisms of their accumulation (Pastukhovich et al. 2019). To the best of our knowledge, the only large-scale targeted expedition to search for meteorites and study the Tabun-Khara-Obo crater was organized in 1993 by Bishoff et al. (1996). When we planned this expedition, we also relied on our own experience in organizing prospecting in hot (Muravyev and Grokhovsky 2018; Pastukhovich et al. 2017; Pastukhovich et al. 2018) and cold (Larionov et al. 2016) deserts. Field work was carried out from August 23 to September 6, 2018. The total length of the expedition route was about 3000 km (Fig. 1).

Fig. 1 The expedition route (red line)

2 Materials and Methods

The technique of exploration is described in detail earlier in Pastukhovich et al. (2019). A visual search was carried out both on foot and using vehicles. The key criteria for identifying fragments of meteorites were color, the presence of a melting crust, magnetic properties, and the specific gravity of the samples. Heavy rains in the first half of August made search work difficult, due to the large amount of green vegetation.

Polished samples and thin sections of meteorites from the Gobi Desert were examined using an Olympus BX51 optical microscope at the UB RAS Geonalitik Common Use Center (Ekaterinburg), and TESCAN MIRA 3MLU SEM with EDS/WDS system and JEOL JXA-8100 (WDS electron microprobe) in the analytical laboratory of the Sobolev Institute of Geology and Mineralogy SB RAS (Novosibirsk).

3 Results and Discussion

The expedition has discovered 5 meteorite samples with a total weight of about 1.5 kg. A fragment of a stone meteorite weighing 745.47 g was found 50 km east of the Noyon Somon (43°13′11.8″N, 102°39′56.7″E) in a mountainous stony desert area consisting mainly of sedimentary rocks of a white or light-gray color (1500 m above sea level). The second group of finds has comprised the fragments of meteor shower (total weight 693.42 g). This is evidenced by the similarity of the fragments found 10 km north-west of the Shinejinst Somon (44°37′15.6″N 99°12′38.1″E) at a distance of 100–500 m from each other (Fig. 2). The terrain is characterized by sloping hills covered with scattered stones of light shades. Some fragments fit together perfectly at chipped sides. It should be noted that not all the fragments of this meteorite were found.

Fig. 2 One of the Shinejinst meteorite fragments

The discovered fragments correspond to chondrites according to their cleavage structure and magnetic susceptibility parameters. The meteorites exhibit various degrees of weathering, which is likely to be determined both by their different terrestrial age and different environmental conditions during their terrestrial existence.

The Noyon meteorite reveals evident chondritic texture. The amount of chondrules and their fragments is more than 90 vol%. Their sizes strongly vary from 30–50 μm to 2 mm and are usually poorly defined (especially on the contact of different chondrules), very rarely they show clear outlines. They are represented by BO, PO, POP, RP and CC textural types. Chondrules mainly consist of olivine, low-Ca-pyroxene and glassy-like matrix, diopside, and chromite and blebs of troilite and FeNi-metal. In all chondrules, the matrix does not contain fresh glass, it is rather a fine devitrified aggregate of clinopyroxene and feldspar or nepheline-like phase. BSE images for some POP and PO chondrules show strong zonation for olivine and sometimes for low-Ca-pyroxene, which can form skeletal/dendritic crystals. RP chondrules may contain SiO_2 polymorph. All these indicate the high rate of quenching. Olivine and low-Ca-pyroxene are main minerals in a fine-grained matrix; plagioclase is not observed. All petrographic features indicate petrological type 3 for the meteorite. Undulose extinction and irregular fractures in olivine reveal S2 shock stage. The majority of FeNi metal grains (30–400 μm) are mainly represented by kamacite, taenite and tetrataenite, individual kamacite grains also occur. Weathering products (hematite, goethite and other Fe-Ni-hydroxides, gypsum) are locally abundant and mainly occur as in situ partial alteration of FeNi-metals and troilite, and fill microfractures in all minerals (W2-3 weathering grade). The appearance of Ni-rich pyrrhotite and smythite may be related to troilite alteration. Clinopyroxene, chromite, ilmenite, merrillite and chlorapatite (100–300 μm) occur locally in the matrix. Merrillite is also found as rounded inclusions (up to 5 μm) in FeNi-metal and troilite.

Petrographic observation of a polished section of the Shinejinst meteorite shows a fine-grained inequigranular recrystallized matrix and chondrules (25%). Chondrite consists of olivine 50%, orthopyroxene 15%, clinopyroxene 10%, plagioclase 15%, chromite 3%, troilite 3–4%, and Fe-Ni-metal 3–4%. The chondrite also contains accessory apatite and ilmenite. Porphyritic olivine (PO) and porphyritic olivine-pyroxene (POP) chondrules predominate. They belong to petrographic type 4. An enstatite-quartz inclusion is found in a chondrite matrix. The inclusion is 100–120 μm in size, and has an irregular shape. Quartz is observed in the form of rounded inclusions in enstatite (5–25 μm). Chromite-plagioclase assemblages are found in chondrite recrystallized matrix (Fig. 3).

The assemblages range in size from 10 to 350 μm and consist of 0.2–30-μm-size rounded, euhedral, subhedral or anhedral chromite grains surrounded by plagioclase or by the glass of plagioclase composition. Moderate metal oxidation affects about 20–60%, the alteration of mafic silicates can be seen (W2 weathering grade). The samples are transected by dark shock veins (shock stage 3–4).

Classification data of the studied meteorites are shown in Table 1.

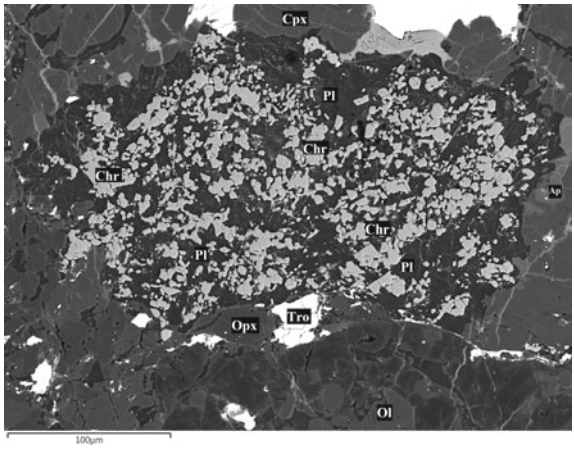

Fig. 3 Chromite-plagioclase assemblages in the chondrite recrystallized matrix of the Shinejinst meteorite (H4). Image in the back-scattered electron (BSE). Chr-chromite, Pl-plagioclase, Ol-olivine, Opx-orthopyroxene, Cpx-clinopyroxene, Tro-troilite, Ap-apatite

Table 1 Classification of the new Mongolian meteorites

Meteorite name	Class	Shock stage	Weathering grade	Fayalite (mol%)	Ferrosilite (mol%)	Wollastonite (mol%)
Noyon	LL (L)3	S2	W2-3	21.47 ± 7.10 (N = 100)	13.51 ± 7.98 (N = 63)	2.04 ± 2.45 (N = 63)
Shinejinst	H4	S3-4	W2	20 ± 2.1 (N = 37)	18 ± 0.5 (N = 17)	2 ± 2.8 (N = 6)

4 Conclusions

The first Russian-Mongolian meteorite expedition to the Gobi Desert was successfully carried out. The mineralogical composition of two new Mongolian meteorites was studied. Unfortunately, we were unable to find any DCA in this large desert, but this fact stimulates new expeditions to the Gobi Desert.

References

Bischoff A., Gerel O., Buchwald V.F. et al. Meteorites from Mongolia. Meteoritics and Planetary Sci. 1996;31:152-157. https://doi.org/10.1111/j.1945-5100.1996.tb02063.x.

Larionov M.Yu., Grokhovsky V.I., Kolunin R.N. et al. Search and recover of antarctic meteorites from Lomonosov mountains, Queen Maud Land by the first Russian meteorite expedition. Meteoritics and Planetary Sci. 2016;51:A400. https://doi.org/10.1111/maps.12698.

Muravyev L.A., Grokhovsky V.I. The history of UrFU meteoritic expeditions. Meteoritics and Planetary Sci. 2018;53:6280. https://doi.org/10.1111/maps.13145.

Pastukhovich A.Yu., Demberel S., Grokhovsky V.I. et al. Russian-Mongolian meteorite expedition to The Gobi desert. Meteoritics and Planetary Sci. 2019;54:6142 https://doi.org/10.1111/maps.13247

Pastukhovich A.Yu., Larionov M.Yu., Kruglikov N.A. et al. UrFU meteorite expedition to the Atacama Desert (Chile). Meteoritics and Planetary Sci. 2018;53:6071. https://doi.org/10.1111/maps.13145.

Pastukhovich A.Yu, Larionov M.Yu., Kruglikov N.A et al. UrFU meteorite expedition to the Lut Desert (Iran). Meteoritics and Planetary Sci. 2017;52:A265. https://doi.org/10.1111/maps.12934.

Magnetic Susceptibility and Heavy Metals in Urban Soil (Khvalynsk, Saratov Region, Russian Federation)

Mikhail V. Reshetnikov, Aleksandr S. Sheshnev, Vitaly N. Eremin, Dler S. M. Majeed, and Aleksandr S. Sheudzhen

Abstract

Magnetic susceptibility is a fast, inexpensive and reliable technique for estimating and monitoring the anthropogenic contamination of soil with heavy metals. However, it is essential to determine the factors affecting magnetic susceptibility before applying this technique to environmental studies. The objectives of this study were to investigate: the effect of parent materials and land use on the magnetic susceptibility and concentrations of Cd, Cr, Cu, Ni, Pb and Zn, and the capability of magnetic susceptibility to be an indicator of anthropogenic heavy metal contamination of soil in Khvalynsk, Saratov region, Russian Federation. 46 composite surface soil samples (0–10 cm) were taken. 1 M HNO_3 extractable concentrations of Cd, Cr, Cu, Ni, Pb and Zn were determined by atomic absorption spectroscopy. Magnetic susceptibility at low and high frequency (χlf and χhf) was measured and frequency dependent susceptibility (χfd) was calculated. The average concentrations of Cd, Cr, Cu, Ni, Pb and Zn were 0.14; 0.43; 20.82; 4.14; 3.15 and 63.24 mg/kg, respectively. Magnetic susceptibility varied from 1.81 to 77.2 $\times$ 10^{-7} m^3 kg^{-1}. Correlations between magnetic properties and mobile forms of heavy metals in the soils of Khvalynsk have not been established. Therefore, in the soils studied, magnetic susceptibility could not be employed as an indicator of anthropogenic contamination of soil with heavy metals. Magnetic susceptibility can be used to assess the degree of soil transformation in Khvalynsk.

M. V. Reshetnikov · A. S. Sheudzhen
Branch of LLC LUKOIL-Engineering "KogalymNIPIneft" in Tyumen,
19/17 Tsentralnaya str., 628486 Kogalym, Russia
e-mail: rmv85@list.ru

A. S. Sheshnev (✉) · V. N. Eremin · D. S. M. Majeed
Saratov State University - National Research University named after N.G. Chernyshevsky,
83 Astrakhanskaya str., 410012 Saratov, Russia
e-mail: sheshnev@inbox.ru

S. Votyakov et al. (eds.), *Minerals: Structure, Properties, Methods of Investigation*,
Springer Proceedings in Earth and Environmental Sciences,
https://doi.org/10.1007/978-3-030-49468-1_25

Keywords

Magnetic susceptibility · Soil · Khvalynsk · Zinc · Lead · Nickel · Cadmium · Chromium · Copper · Soil pollution

1 Introduction

In recent decades, magnetic properties were commonly used to study soil and sediment contamination with heavy metals. Studies have indicated the relationship between heavy metals and magnetic properties and used the magnetic susceptibility as an indicator to evaluate soil pollution intensity, determine the contamination depth and discriminate lithogenic and anthropogenic sources of heavy metals. Heavy metals and magnetic minerals are naturally ubiquitous in the soil parent materials which are released into the soil by weathering and pedogenic processes. With an increase of industrial activities and urbanization, considerable amounts of heavy metals in association with magnetic particles have been gradually added to the soils.

The use of magnetic parameters for the identification of pollution sources has become a widespread practice as a reliable, efficient and sensitive method for evaluating polluted sites (Blaha et al. 2008; Jordanova et al. 2003). Although the determination of total metal concentrations is a routine analysis, soil magnetic measurements can provide valuable reference information in pollution studies (Lu et al. 2012; Magiera et al. 2006; Morton-Bermea et al. 2009). Many studies have documented the correlation between magnetic properties and metal concentration in urban soils (El Baghdadi et al. 2012; Lu and Bai 2006; Lu et al. 2008).

Magnetic susceptibility mapping of soils and sediments has become one of the most important tools for estimating anthropogenic pollution (Yang et al. 2012) and has been widely used in mapping metal contamination (Hanesch and Scholger 2002; Zawadzki and Fabijanczyk 2008).

The objectives of this study were to investigate the effect of parent materials and land use on the magnetic susceptibility and concentrations of Cd, Cr, Cu, Ni, Pb and Zn, and the efficacy of magnetic susceptibility as an indicator of anthropogenic heavy metal contamination of soil in Khvalynsk, Saratov region, Russian Federation.

2 Materials and Methods

2.1 Research Area and Sampling

The research was conducted in the territory of Saratov region, Russian Federation. Saratov region is an agrarian and industrial region of Russia. There are companies for oil and gas production, transportation, storage and processing, as well as steel manufacturing, electrical energy companies and others in the territory. In recent years, urbanization and industrialization of the territory of Saratov region have led to accumulation of heavy metals in the soils of its large cities, for example, Saratov. The Khvalynsk town with a population of 12556 people (2017) was chosen as an object of this research. The primary activity of the population is agriculture and small industrial production, there are no large industrial enterprises in the settlement territory.

Parent rocks are generally presented by Cretaceous deposits. The main type of soil in this territory is black soil. The sample area was recorded by GPS. The sampling scheme is shown in Fig. 1. A total of 46 soil samples obtained using a plastic shovel were selected and put in plastic packages. Soil samples were quartered, dried and sieved through a sieve of 1 mm.

2.2 Magnetic Measurements and Chemical Analysis

In this research the set of magnetic parameters included magnetic susceptibility at low frequency (976 Hz, χLF), magnetic susceptibility at high frequency (3904 Hz, χHF) as well as their frequency dependence (frequency-dependent susceptibility, χFD, %). Measurements were taken by means of a MFK1-FB magnetic susceptibility measuring instrument.

Five grams of the total sample were taken to evaluate the concentration of mobile forms of heavy metals. The extraction of mobile forms of heavy metals was carried out using 1 M HNO_3 solution during 24 h. The concentration of Cu, Cd, Pb, Cr, Ni and Zn was determined using an atomic absorption spectrophotometer.

The actual concentration of each heavy metal was compared with its threshold limit value (TLV) while calculating its hazard index (HI) using the formula (1) for identifying environmentally hazardous levels of heavy metals in a soil cover:

$$HI = \frac{Ci}{MAC}, \tag{1}$$

where Ci is the content of a form of heavy metal in a sample, mg/kg;
MAC (maximum allowable concentration) is the threshold limit value of the heavy metal form, mg/kg.

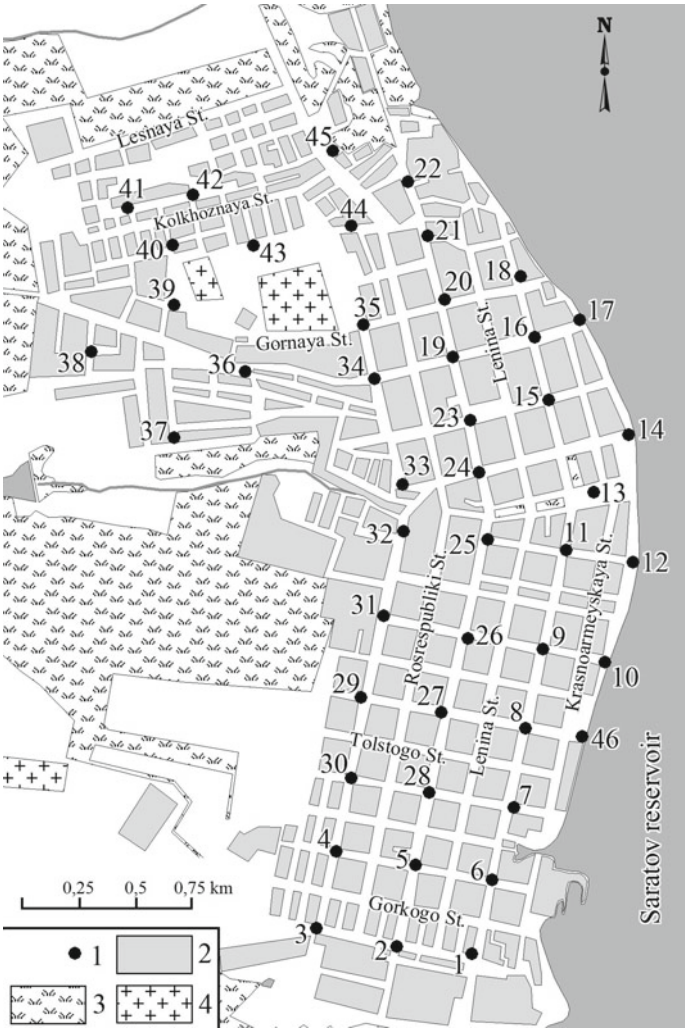

Fig. 1 Scheme of sampling: 1—sampling site, 2—urban buildings, 3—green spaces, 4—cemetery

Zc total contamination index was determined to assess the extent of geochemical transformation of a soil cover by mobile forms of heavy metals using the formula (2):

$$Zc = \sum HI_n - (n-1), \tag{2}$$

where Zc is the index of total contamination by heavy metals in test;
n is the quantity of the defined elements;
HI is the hazard index of the heavy metals defined in the sample.

When calculating Zc, we used the excess over the maximum allowable concentration (HI), but not the excess over the background (BI), unlike recommended.

The statistical processing of the experimental data was done using the Microsoft Excel 2010 (for Windows XP). The confidence limit was considered to be the difference in probable errors $p = 0.05$ (95% confidence interval). Interrelations between chemical and magnetic indicators of the soil were estimated using Pearson's correlation coefficients.

3 Results and Discussion

3.1 Results for the Khvalynsk Territory

Forty-five soil samples were selected in the territory. Below are initial results considering the concentration of heavy metals.

Chromium mobile forms were determined in all tested samples. Chromium concentration ranged from 0.13 to 1.05 mg/kg, with an average content of 0.43 mg/kg and a maximum allowable concentration of 6.0 mg/kg. Changes in the hazard index ranged from 0.02 to 0.18 with an average value of 0.07.

Nickel mobile forms were also observed in all tested samples in concentrations from 1.23 to 7.67 mg/kg, with an average content of 4.14 mg/kg and a maximum allowable concentration of 4.0 mg/kg. Changes in the hazard index ranged from 0.31 to 1.92 with an average value of 1.04.

Lead in its mobile form was found in all tested samples in concentrations ranging from 0.6 to 13.87 mg/kg, with an average content of 3.15 mg/kg and a maximum allowable concentration of 6.0 mg/kg. Changes in the hazard index ranged from 0.1 to 2.31 with an average value of 0.53.

Copper mobile forms were recorded in all the test samples in concentrations ranging from 8.41 to 213.66 mg/kg, with an average content of 20.82 mg/kg and a maximum allowable concentration of 3.0 mg/kg. Changes in the hazard index ranged from 2.8 to 71.22 with an average value of 6.94.

Zinc in its mobile form was found in all tested samples in concentrations ranging from 12.45 to 149.36 mg/kg, with an average content of 63.24 mg/kg and a maximum allowable concentration of 23.0 mg/kg. Changes in the hazard index ranged from 0.54 to 6.49 with an average value of 2.75.

Cadmium mobile forms were observed in all tested samples in concentrations ranging from 0.02 to 0.38 mg/kg, with an average content of 0.14 mg/kg and a maximum allowable concentration of 0.5 mg/kg. Changes in the hazard index ranged from 0.04 to 0.75 with an average value of 0.29.

Table 1 Correlation between geochemical and petromagnetic characteristics in Khvalynsk soils

	Cr	Ni	Pb	Zn	Cd	Cu	χ_{LF}	χ_{FD}
Cr	1.00	0.68	–	–	−0.29	–	–	–
Ni		1.00	–	–	–	–	–	–
Pb			1.00	0.48	–	–	–	–
Zn				1.00	0.72	–	–	–
Cd					1.00	–	–	–
Cu						1.00	–	–
χ_{LF}							1.00	–
χ_{FD}								1.00

n = 46, p = 0.05, r = 0.29

The geochemical order of mobile forms of heavy metals based on their concentrations in the territory of the Khvalynsk was as follows: Zn > Cu > Ni > Pb > Cr > Cd.

Changes in the specific magnetic susceptibility of Khvalynsk soils measured at low frequency (χLF) ranged from 1.81×10^{-7} to 77.2×10^{-7} m^3/kg with an average of 7.27×10^{-7} m^3/kg. The magnetic susceptibility at high frequency (χHF) changed from 1.76×10^{-7} to 74.6×10^{-7} m^3/kg with an average of 7.07×10^{-7} m^3/kg. The frequency dependence (frequency-dependent susceptibility) (χFD) changed from 0.05 to 5.65%, with an average of 2.68%.

The correlation analysis of analytical data for the identification of possible paragenetic associations between petromagnetic and geochemical parameters was carried out (Table 1).

As can be seen from Table 1, the following geochemical paragenetic associations of elements were identified in the explored territory: nickel-chromium, nickel-cadmium, lead-zinc, zinc-cadmium. Based on the correlation analysis data, it is possible to assume that the compounds of mobile forms of heavy metals were formed paragenetically in the Khvalynsk territory. Thus, these elements have a uniform mineralogical origin inherited from parent rocks or a uniform source of technogenic origin. The confirmation of these assumptions demands more detailed mineralogical research, which is not considered by us in this work.

Correlations between magnetic properties and mobile forms of heavy metals in the Khvalynsk soils have not been established.

4 Conclusions

An unusually high level of magnetic susceptibility of the soils was attributed to the presence of magnetically soft MD ferrimagnetic particles, which were originated probably from automobile exhaust and other industrial activities. Although the magnetic susceptibility of the topsoil proved to be a reliable indicator of anthropogenic pollutant input into the soil, it could not be employed as an indicator of anthropogenic contamination of soil with heavy metals in the soils studied.

Acknowledgements The study was supported by the grant of the President of the Russian Federation to support young Russian scientists (project MK-3355.2019.5).

References

Blaha U, Appel E, Stanjek H. Determination of anthropogenic boundary depth in industrially polluted soil and semi-quantification of heavy metal loads using magnetic susceptibility. Environ. Pollut. 2008;156:278–89. https://doi.org/10.1016/j.envpol.2008.02.013.

El Baghdadi M, Barakat A, Sajieddine M, Nadem S. Heavy metal pollution and soil magnetic susceptibility in urban soil of Beni Mellal City (Morocco). Environ. Earth Sci. 2012;66:141–55. https://doi.org/10.1007/s12665-011-1215-5.

Hanesch M, Scholger R. Mapping of heavy metal loadings in soils by means of magnetic susceptibility measurements. Environ. Geol. 2002;42:857–70. https://doi.org/10.1007/s00254-002-0604-1.

Jordanova NV, Jordanova DV, Veneva L, Yorova K, Petrovsky E. Magnetic response of soils and heavy metal pollution – a case study. Environ. Sci. Technol. 2003;37:4417–24. https://doi.org/10.1021/es0200645.

Lu SG, Bai SQ. Study on the correlation of magnetic properties and heavy metals content in urban soils of Hangzhou City, China. J. Appl. Geophys. 2006;60:1–12. https://doi.org/10.1016/j.jappgeo.2005.11.002.

Lu SG, Bai SQ, Fu LX. Magnetic properties as indicators of Cu and Zn contamination in soils. Pedosphere. 2008;18:479–85. https://doi.org/10.1016/S1002-0160(08)60038-7.

Lu SG, Chen DJ, Wang SY, Liu YD. Rock magnetism investigation of highly magnetic soil developed on calcareous rock in Yun-Gui Plateau, China: evidence for pedogenic magnetic minerals. J. Appl. Geophys. 2012;77:39–50. https://doi.org/10.1016/j.jappgeo.2011.11.008.

Magiera T, Strzyszcz Z, Kapicka A, Petrovsky E. Discrimination of lithogenic and anthropogenic influences on topsoil magnetic susceptibility in Central Europe. Geoderma. 2006;130:299–311. https://doi.org/10.1016/j.geoderma.2005.02.002.

Morton-Bermea O, Hernandez E, Martinez-Pichardo E, Soler-Arechalde AM, Lozano Santa-Cruz R, Gonzalez-Hernandez G, et al. Mexico City topsoils: heavy metals vs. magnetic susceptibility. Geoderma. 2009;151:121–5. https://doi.org/10.1016/j.geoderma.2009.03.019.

Yang T, Liu Q, Zeng Q, Chan L. Relationship between magnetic properties and heavy metals of urban soils with different soil types and environmental settings: implications for magnetic mapping. Environ. Earth Sci. 2012;66:409–20. https://doi.org/10.1007/s12665-011-1248-9.

Zawadzki J, Fabijanczyk P. Reduction of soil contamination uncertainty assessment using magnetic susceptibility measurements and Co_Est method. Proceedings of ECOpole. 2008;2(1):169–74.

Sulfur and Oxygen Isotopic Composition of Sulfate Minerals in the Kungur and Kinderlinskaya Caves in the Urals

Sergey A. Sadykov, Sergey S. Potapov, and Olga. Ya. Chervyatsova

Abstract

Sulfur and oxygen isotopic composition of sulfate minerals from the Kungur and Kinderlinskaya caves located in the Urals was studied. The sulfur isotopic composition has a small enrichment in a light sulfur isotope in comparison with gypsum and anhydrite of host rocks in the Kungur cave, which shows a slight fractionation during crystallization from aqueous solutions. Oxygen isotopic ratios have the average value +1.52‰, VSMOW in the Kungur cave. Secondary sulfates have approximately similar values of the oxygen isotopic composition with sulfate from the surrounding rocks. The sulfur isotopic composition has values typical for bacterial reduced sulfur compounds in the Kinderlinskaya cave. The mean value of oxygen isotopic ratios is −0.81‰ VSMOW. This can be explained by the enrichment of the heavy oxygen isotope in the process of evaporative saturation and the participation of sediment brines of marine origin contained in the host limestones.

Keywords

Sulfur isotopes · Oxygen isotopes · Sulfate · Gypsum · Kungur cave · Kinderlinskaya cave

S. A. Sadykov (✉) · S. S. Potapov
Institute of Mineralogy SU FRC MG UB RAS, 1 Ilmensky Reserve, 456317 Miass, Russia
e-mail: sergei_sadykov@mail.ru

S. S. Potapov
e-mail: s_almazov@74.ru

Olga.Ya. Chervyatsova
Shulgan-Tash State Nature Reserve, 14 Zapovednaya str., Irgizly, Burzyan District, 453585 Republic of Bashkortostan, Russia
e-mail: kittary@yandex.ru

S. Votyakov et al. (eds.), *Minerals: Structure, Properties, Methods of Investigation*, Springer Proceedings in Earth and Environmental Sciences,
https://doi.org/10.1007/978-3-030-49468-1_26

1 Introduction

The object of study is the sulfur and oxygen isotopic composition of sulfate deposits (minerals) of the Urals caves. The aim of the study is to build a model of mineral and speleogenesis based on the study of the isotopic composition of sulfur and oxygen of primary and secondary mineral formations. The samples of sulfate mineral formations were collected in the Kinderlinskaya and Kungur caves.

The study of speleogenesis is important not only from the fundamental, but also applied point of view, since speleogenesis is often associated with the formation of mineral deposits. Sulfuric acid is one of several known agents of speleogenesis.

Sulfate minerals in carbonate karst caves have one of four possible sources of sulfur for their formation: (1) oxidation of sulfides and sulfide waters, (2) transposition from marine evaporates, (3) decomposition of bat guano, (4) migration of deep gases at post-volcanic activity (Hill and Forti 1997).

The reliable determination of the substance source for the formation of gypsum, especially the formation of sulfate class minerals in caves, is in some cases problematic. One of the most informative ways to determine the source of sulfate formation is to study the sulfur isotopic composition (Egemeier 1981; Hose and Pisarowicz 1999; Seal 2006).

2 Materials and Methods

The sulfur ($\delta^{34}S$ ‰, VCDT) and oxygen ($\delta^{18}O$ ‰, VSMOW) isotope composition of mineral samples was determined using a Delta^{Plus} Advantage mass spectrometer manufactured by Thermo Finnigan, coupled with an EA Flash1112 elemental analyzer and a high temperature convector TC/EA ConFlo III interface at the Institute of Mineralogy, UB RAS, Miass, Russia. Isotope ratios were measured in a continuous gas flow. NBS-123 and NBS-18 reference materials were used for measurements.

The Kungur cave (Perm region, Kungur) is located in the Middle Urals. The main part of the cavities belongs to the Ledyanopescherskaya member of the Irenskaya Suite of the Kungurian of the lower Permian ($^{ir}_{ld}P_{1K}{}^{ir}$). Its composition is dominated by anhydrites, gypsum is less common (Dublyanskiy 2005). The cave is located on the contact of the lower horizon of the Kungurian. It is composed of limestone and dolomites, while the upper horizon is mainly composed of gypsum and anhydrite. The result of the meteoric water activity is the dissolution of sedimentary rocks (limestone, dolomite and gypsum-anhydrite rocks of the evaporite strata) and their redepositing with the formation of the newly-formed sulfate minerals: gypsum, salts, blödite, jarosite.

The Kinderlinskaya cave (Republic of Bashkortostan, Gafuriysky district) is located within the Western Ural external folding zone, laid in the West wing of the Tchastinsky synclinal fold, in the Famennian limestones of the upper Devonian

(D_3fm). It presents layered bituminous grey and dark grey limestones with siliceous intercalations in the cave area.

The Kinderlinskaya cave is characterized by abnormally broad distribution of gypsum deposits as compared to other known carbonate caves of the Urals, although the sulfate minerals are not known in the stratigraphic context of the enclosing and overlying rock sediments. The most gypsum-bearing areas are confined to dry, intensively ventilated cavities of the cave. Typical forms of gypsum are crystal-grained crusts on the walls (up to several cm), gypsum filler, fibrous crystalline aggregates ("stone flowers" or antholites), tabular and elongated-prismatic crystals (presumably grown in subaqueous conditions), various crystalline units inside the loam in the Kinderlinskaya cave. A feature of most deposits (bark, antholites, aggregates in clays) is their formation from capillary water in the evaporate barrier (Chervyatsova et al. 2016).

3 Results and Discussion

The main host rocks (gypsum and anhydrite) have a $\delta^{34}S$ sulfur isotopic composition from +10.09 to +12.32‰, VCDT in the Kungur cave, which is typical for the lower Permian sea evaporites (Scholle 1995). The isotopic composition has not shown significant changes in the system, under which sulfur migration and transformation took place: host rocks => infiltration waters => secondary sulfate deposits, which is consistent with the literature data on insignificant fractionation during crystallization from aqueous solutions (Hill and Forti 1997). A slightly lighter composition ($\delta^{34}S$ = +8.62‰) is observed for the mirabilite of the Diamond grotto, which may be due to partial sulfate reduction in capillary solutions.

The oxygen isotope composition has a wide range of $\delta^{18}O$ values from −2.70 to +8.92‰, VSMOW (Table 1) in the Kungur cave.

The mean value of oxygen isotope is +1.52‰, VSMOW. Secondary sulfates have approximately the same value as gypsum and anhydrite from host rocks, with the exception of one sample CLP-2/2008 (POL-2). If this sample is excluded from the definition of the average oxygen isotope composition, then we have a slightly enriched ^{18}O isotope (+0.53‰, VSMOW) when compared with the composition of ocean water. This isotopic composition shows that during the formation of secondary sulfates the oxygen isotope fractionation with respect to primary gypsum and anhydrite does not occur. This may be due to the fact that during sediment filtration through the roof and host rocks, isotopic oxygen balancing occurs and this is observed in the isotopic composition of secondary sulfates.

Fluctuations in $\delta^{18}O$ values can be associated with small local changes in the external environment, as well as with variations in temperature, pressure and water flow.

The Kinderlinskaya cave has a light isotope composition of sulfur in secondary gypsum deposits ($\delta^{34}S$ from −23.25 to −13.85‰, VCDT). Sulfur and oxygen isotope composition of the studied samples is given in Table 2.

Table 1 Sulfur and oxygen isotope composition of sulfate samples from the Kungur cave

Sample number	Sample name	Description, mineral composition	Sulfur isotope composition $\delta^{34}S$ ‰, VCDT	Oxygen isotope composition $\delta^{18}O$ ‰, VSMOW
Host rocks $^{ir}{}_{1d}P_{1K}{}^{ir}$ *(gypsum and anhydrite)*				
1	KLP-2/2012	Gypsum	**+10.09**	**−0.09**
2	KLP-03/2013	Gypsum	**+11.87**	**+1.10**
3	KLP-04/2013	Gypsum	**+12.26**	**+2.58**
4	KLP-06/2013	Gypsum and anhydrite rock	**+11.37**	**+0.94**
5	KLP-07/2013	White gypsum rim around the block of gypsum-anhydrite rock	**+12.32**	**−0.74**
Secondary sulfate deposits				
6	KLP-1/2012	Black cryogenic flour	+9.40 +9.57	−2.70
7	KLP-01/2013	White cryogenic flour	+10.32	+1.14
8	KLP-2/2008 (POL-2)	White fluffy needle-like formation of mirabilite with a mixture of gypsum on the roof of the grotto	+8.62	+8.92
9	KLP-02/2013	Gypsum crystals (newly formed) on the retaining wall	+10.97	+2.53

Table 2 Sulfur and oxygen isotope composition of samples from the Kinderlinskaya cave

Sample number	Sample name	Description, mineral composition	Sulfur isotope composition $\delta^{34}S$ ‰, VCDT	Oxygen isotopic composition $\delta^{18}O$ ‰, VSMOW
1	K-2/2012	Gypsum antholites	+22.31	−3.31
2	K-3/2012	Gypsum crusts	+23.25	−1.26
3	K-4/2012	Gypsum antholites	+23.03	−1.13
4	K-5/2012	Gypsum crack filler	+23.51	+3.90
5	K-13/2012	Gypsum brown crusts	+22.22	+0.18
6	K-21/2012	Gypsum crusts	+19.64	+0.07
7	K-22/2012	White gypsum growths	+17.28	−1.32
8	K-5/2013	Gypsum crusts	+13.85	−1.24
9	K-7/2013	Gypsum	+16.49	−0.45
10	K-8/2013	Gypsum antholites	+15.29	−3.55

This composition is typical for bacterially reduced sulfur compounds, and excludes the deposition of gypsum with the direct participation of marine sulfates (heavy isotopic composition) (Egemeier 1981; Onac et al. 2007; Scholle 1995; Seal 2006). The most likely source of gypsum formation is organically bound sulfur contained in the bituminous substance in the host rocks, which can be oxidized to sulfates with the participation of sulfur-oxidizing bacteria. Our isotopic studies show that the Kinderlinskaya cave sulfate minerals have sulfur isotopic composition similar to that of the most of the studied caves in the world, in which sulfates are formed by authigenic processes (oxidation of sulfides or H_2S-waters, mineralization of organic residues, etc.) (Egemeier 1981; Onac et al. 2007; Scholle 1995; Seal 2006).

The oxygen isotope composition has a lesser range of $\delta^{18}O$ values from −3.55 to +3.90‰, VSMOW in the Kinderlinskaya cave and the mean value of −0.81‰, VSMOW.

4 Conclusions

The following features can be noted:

- Lighter oxygen isotope composition ($\delta^{18}O$ up to −3.5‰, VSMOW) is observed for antholites growing by the capillary power of rock substrates. Presumably, this can be explained by the participation of atmospheric waters. The calculation using the OIPC statistical model allows the weighted average oxygen isotope composition of atmospheric waters in the cave area to be estimated as $\delta^{18}O$ = −10.9‰, VSMOW. The summer composition of atmospheric water is estimated as $\delta^{18}O$ = −5.5‰, VSMOW. Thus, antholites can inherit the composition of condensation water generated in the cave during summer.
- The oxygen isotope composition has $\delta^{18}O$ values from −1.3 to +0.18‰, VSMOW, while the most massive gypsum deposits (crusts) are characterized by a less negative $\delta^{18}O$ values as compared to antholites. The heaviest isotopic composition ($\delta^{18}O$ = +3.90‰ VSMOW) was obtained for gypsum crack filler. This feature can be explained both by the heavy isotope enrichment in the process of evaporative saturation and by the participation of sedimentation brines of marine origin contained in the host limestones. Most likely, both of these processes are realized, which, in particular, can be evidenced by skeletal halite crystals formed on the surface of gypsum crystals.

Acknowledgements The work was carried out within the state budget theme of the Institute of Mineralogy of UB RAS “Mineralogical-geochemical evolution and metallogeny of hydrothermal authigenic and supergene ore-forming systems”.

References

Chervyatsova OYa, Potapov SS, Sadykov SA. Sulfur isotopic composition of sulfur deposits in Ural karst caves. Izvestiya Ural'skogo gosudarstvennogo gornogo universiteta [News of the Ural State Mining University]. 2016; 2:37-41. https://doi.org/10.21440/2307-2091-2016-2-32-41.

Dublyanskiy VN. Kungurskaya ledyanaya peshchera: opyt rezhimnykh nablyudeniy. Kollektivnaya monografiya [Dublyanskiy VN. Kungur Ice Cave: the experience of monitoring observations. The collective monograph], Ekaterinburg, 2005; 375 p. (In Russ.).

Egemeier SJ. Cavern development by thermal waters. NSS Bulletin, 1981; 43:31–51.

Hill CA, Forti P. Cave minerals of the world (2nd ed.) National Speleological Society, Huntsville Alabama, 1997; 463 p.

Hose LD, Pisarowicz JA. Cueva de Villa Luz, Tabasco, Mexico: reconnaissance study of an active sulfur spring cave and ecosystem. Journal of Cave and Karst Studies. 1999; 61:13-21.

Onac BP, Hess JW, White WB. The relationship between the mineral composition of speleothems and mineralization of breccia pipes: evidence from Corkscrew Cave, Arizona, USA. The Canadian Mineralogist. 2007; 45 (5):1177-1188.

Scholle PA. Carbon and sulfur isotope stratigraphy of the Permian and adjacent intervals The Permian of Northern Pangea. Springer Berlin Heidelberg, 1995. P. 133-149.

Seal RR. Sulfur isotope geochemistry of sulfide minerals. Reviews in mineralogy and geochemistry 2006; 61(1): 633-677.

Chemical Composition Features of Garnets from the Bergen Arcs Eclogites (Southern Norway)

Laysan I. Salimgaraeva, Aleksey V. Berezin, and Sergey G. Skublov

Abstract

The results of a comprehensive study of the garnet chemical composition from the Bergen Arcs eclogites and their protoliths are presented in the paper. The Bergen Arcs system is a part of the Caledonian Orogen in western Norway. The eclogites are formed in shear zones. Field works were carried out in Holsnøy island (SW Norway). The study included SEM-EDS analysis and secondary-ion mass spectrometry (SIMS). The redistribution of the main and trace components occurs at the mineral level and is illustrated by the example of garnet. Major-element and REE zoning in garnets from granulites is not observed; their composition is constant. The garnets from eclogites have distinct rims: their major element and REE composition contrasts with that of the grain cores. The composition of garnet cores from eclogites is similar to that of garnets from granulites. The composition of garnet rims from eclogites is an evidence of garnet recrystallization during Caledonian eclogite metamorphism.

L. I. Salimgaraeva (✉) · S. G. Skublov
Saint Petersburg Mining University, 2 21st Line, 199106 Saint Petersburg, Russia
e-mail: fluoritecaf2@mail.ru

L. I. Salimgaraeva · A. V. Berezin · S. G. Skublov
Institute of Precambrian Geology and Geochronology RAS, 2 Makarova emb., 199304 Saint Petersburg, Russia
e-mail: berezin-geo@yandex.ru

S. G. Skublov
e-mail: skublov@yandex.ru

A. V. Berezin
Saint Petersburg State University, 7/9 Universitetskaya Emb., 199034 Saint Petersburg, Russia

S. Votyakov et al. (eds.), *Minerals: Structure, Properties, Methods of Investigation*,
Springer Proceedings in Earth and Environmental Sciences,
https://doi.org/10.1007/978-3-030-49468-1_27

Keywords

Eclogites · Garnets · Bergen Arcs complex · Metamorphism · Local methods

1 Introduction

The HP and UHP rocks formed during the Caledonian continent collision between Baltica and Laurentia are exposed along the southwestern coast of Norway, both in the Caledonian nappe pile and in the autochthonous/parautochthonous Western Gneiss Region. From P–T estimates and mineral assemblages, it can be inferred that the Lindås Nappe of the Bergen Arcs and the Western Gneiss Region (WGR) were buried to the depth corresponding to the present day crustal root zones developed under the Alps and Himalayas (Austrheim 2013). Therefore, the Bergen Arcs complex is a great object for studying metamorphic processes and properties of crustal root zones.

A great number of papers are devoted to the Bergen Arcs complex, but the redistribution of trace and rare earth components at the mineral level during the transition from granulite to eclogite has not been studied. Trace components are more sensitive to the mineral crystallization environment, recent recrystallization and redeposition processes than the main components (Hickmott 1988). Therefore, the study of redistribution of trace components is very important for polymetamorphic complexes.

The present paper is dedicated to the study of the chemical composition of garnets from eclogites of the Bergen Arcs, because garnets are rock-forming minerals of both main types of rocks of this complex: eclogites and their protoliths—granulites.

2 Materials and Methods

Samples were collected during field works on Holsnøy Island (Fig. 1) in the South-West of Norway in 2018. The distinctive textural features of the rocks and the major components of the chemical composition of their minerals, the occurrence of foreign mineral inclusions, and their composition were determined using a JEOL JSM6510LA scanning electron microscope with a JED2200 EDS spectrometer at the Institute of Precambrian Geology and Geochronology (IPGG), Russian Academy of Sciences. The concentrations of REE and other trace elements in garnets were analyzed on a Cameca IMS-4f ion probe at the Yaroslavl Branch of the Valiev Institute of Physics and Technology, Russian Academy of Sciences. Analytical spots in mineral grains were no larger than 15–20 μm in diameter, the relative errors of the analyses were 10–15% for most elements, and the average detection limits were 10 ppb. When constructing the normalized REE patterns of garnets, their REE concentrations were normalized to CI chondrite (McDonough and Sun 1995).

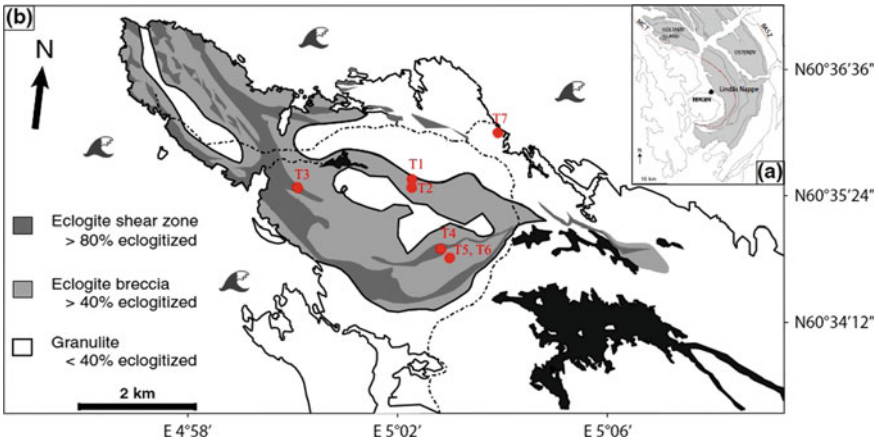

Fig. 1 **a** The location of Holsnøy Island relative to Bergen in western Norway. The Lindås Nappe is also highlighted by grey. **b** Geological map of northern Holsnøy Island modified from Austrheim et al. (1997). Red labels mark sampling points (Color figure online)

3 Geological Setting

The Bergen Arcs system is a part of the Caledonian Orogen in western Norway resulted from the convergence of Laurentia and Baltica in the late Ordovician—early Devonian (Roberts and Gee 1985). Eclogites within the Caledonian Nappes of the Bergen Arcs (upper plate) structurally overlie the eclogite bearing basement gneisses of the WGR (lower plate). The eclogites occur within one of the arcuate Caledonian Nappes of the Bergen Arcs, the Lindås Nappe, which is interpreted as a slice of the lowermost continental crust now exposed over 1000 km^2 (Austrheim and Griffin 1985).

The Lindås Nappe consists predominantly of an anorthosite complex and related rocks, which record two main phases of deformation and metamorphism. Primary metamorphism and deformation of Proterozoic garnet-granulite facies (800–900 °C, <10 kbar) occurred at lower crustal levels, followed by their secondary deformation and metamorphism during the Caledonian Orogeny that brought granulites to the eclogite facies conditions (670 °C, >15 kbar) (Austrheim and Griffin 1985; Cohen et al. 1988; Boundy et al. 1992). However, not all granulite was converted to eclogite. The localized transition from granulite to eclogite facies rocks took place over a few centimeters, apparently related to deformation and fluid interaction (Fig. 2) (Austrheim and Griffin 1985).

Fig. 2 Eclogitization zone in granulites

The eclogite facies shear zones (Fig. 2) are approximately parallel to other Caledonian structural trends in the Bergen Arcs area, including lower grade shear zones. These lower grade shear zones, which are generally characterized by the hydrous amphibolite facies mineralogy, developed locally throughout the granulite facies anorthosite terrane during the later Caledonian deformation and partially overprinted some of the eclogite facies rocks (Austrheim and Robins 1981).

4 Results and Discussion

Major element and REE zoning in garnets from granulites is not observed (Figs. 3 and 4); their composition is constant. The garnets from eclogites have distinct rims (Figs. 5 and 6): their major element and REE composition contrasts with that of the cores of grains. The composition of cores of garnets from eclogites is similar to that of garnets from granulites (Fig. 7).

The rims of garnets from eclogites are characterized by an elevated content of almandine and spessartine end-members and lower amounts of pyrope end-member (Fig. 6). This change in the chemical composition is the result of a metamorphic temperature decrease. The contrast of the core and rim composition indicates a sharp change in the metamorphism parameters and an intensive effect of fluid during garnet recrystallization processes (Pollok et al. 2008).

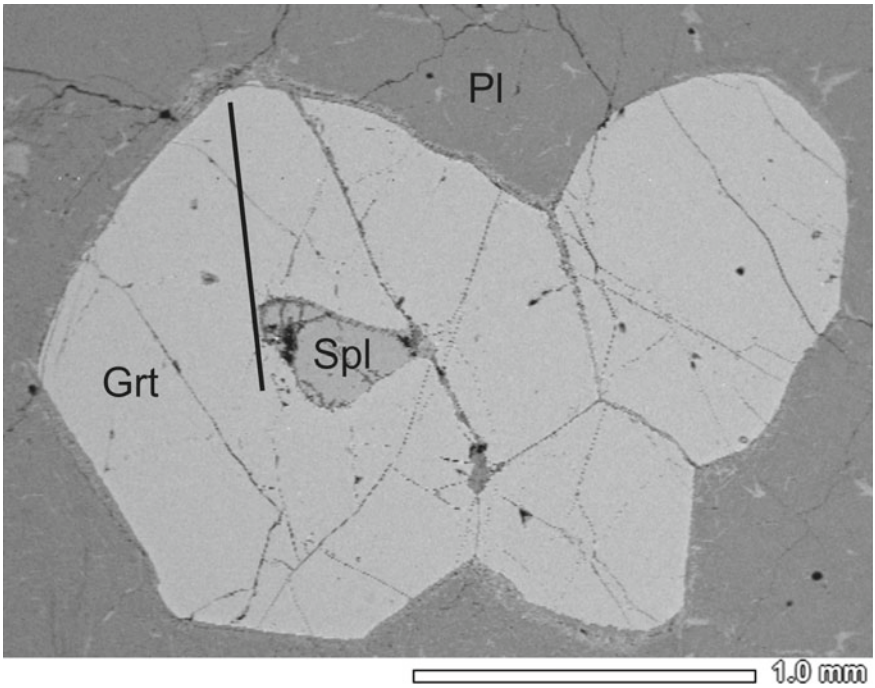

Fig. 3 Back-scattered electron image of a garnet from granulite

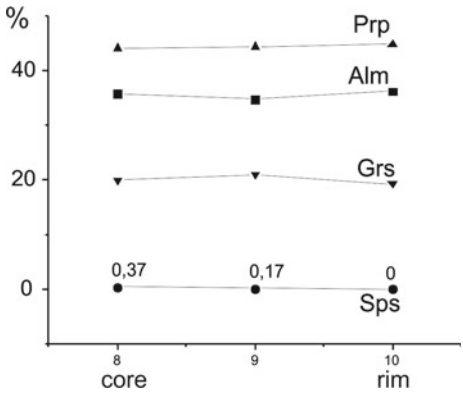

Fig. 4 Major element profiles (core–rim) of selected garnets from granulite

In addition, the rims are distinctly depleted in Ti and Cr and enriched in Y (Table 1). The Y distribution can also indicate a decrease in the metamorphism temperature (Pyle 2000). The contrast of the trace element composition of rims gives evidence to a relatively short duration of eclogite-facies metamorphism. REE patterns for rims of garnets from eclogite (Fig. 7) look like typical diagrams for garnets from eclogites (Skublov 2005).

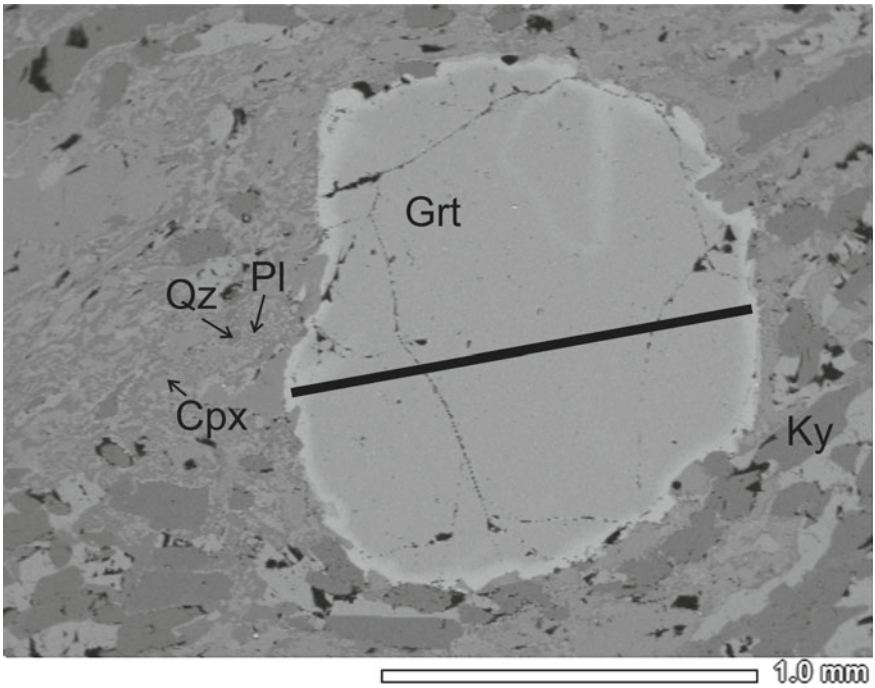

Fig. 5 Back-scattered electron image of a garnet from eclogite

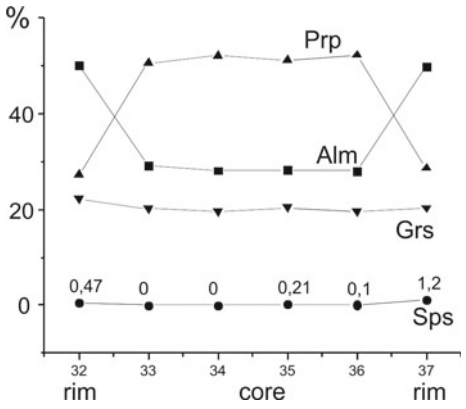

Fig. 6 Major element profiles (rim–core–rim) of selected garnets from eclogite

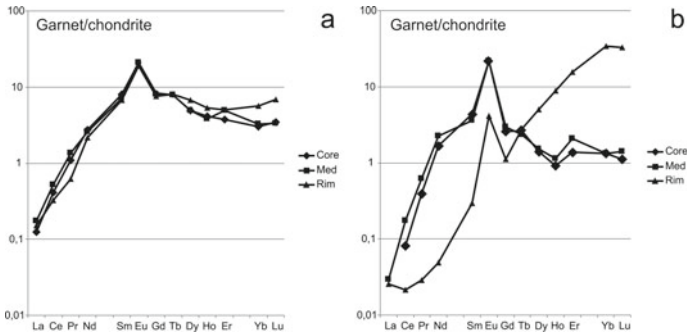

Fig. 7 REE patterns for garnet from: **a** granulites; **b** eclogites. REE composition is chondrite-normalized (Hickmott 1988)

Table 1 Major and trace element compositions of selected garnets

	Garnets from granulite				Garnets from eclogite					
	Core	Rim	Core	Rim	Core	Rim	Core	Rim	Core	Rim
Sample	1801				1802					
Point	1	3	7	9	38	36	11	14	17	22
Composition (wt% oxides)										
SiO_2	40.71	40.38	40.67	40.97	40.68	39.13	40.31	38.66	41.94	38.99
Al_2O_3	22.92	22.49	23.00	22.73	22.82	21.45	23.40	21.40	22.76	22.28
FeO	17.15	17.52	17.04	17.23	16.33	22.68	15.84	24.25	15.12	23.58
MnO	0.20	0.23	0.17	0.00	0.00	1.06	0.07	0.80	0.26	0.83
MgO	11.76	12.26	11.75	11.95	12.41	5.87	12.51	6.88	12.47	5.91
CaO	7.27	7.12	7.37	7.13	7.77	9.81	7.86	8.02	7.45	8.41
Total	100.01	100.00	100.00	100.01	100.01	100.00	99.99	100.01	100.00	100.00
Composition (ppm)										
Ti	1107	896	1034	904	715	256	538	285	613	520
V	108	112	92.5	91.7	91.5	40.8	72.1	41.8	83.3	54.6
Cr	121	161	95.9	107	108	55.5	106	62.2	107	69.6
Y	5.69	8.57	3.48	4.77	1.61	16.2	1.52	6.49	1.39	1.61
Zr	112	96.4	204	174	2.50	1.19	1.99	1.19	1.98	1.83
Nb	0.21	0.12	0.07	0.08	0.01	0.01	0.01	0.02	0.03	0.04
Ba	0.39	0.71	0.27	0.22	0.19	0.96	0.14	0.21	4.80	0.57
Hf	1.36	1.31	3.10	2.49	0.12	0.44	0.13	0.28	0.12	0.09
La	0.03	0.04	0.01	0.00	0.00	0.01	0.00	0.01	0.02	0.01
Ce	0.25	0.20	0.20	0.12	0.05	0.01	0.04	0.03	0.13	0.09
Pr	0.10	0.06	0.09	0.08	0.04	0.00	0.04	0.02	0.07	0.05
Nd	1.27	0.10	1.22	1.13	0.77	0.02	0.72	0.28	0.96	0.72

(continued)

Table 1 (continued)

	Garnets from granulite				Garnets from eclogite					
	Core	Rim	Core	Rim	Core	Rim	Core	Rim	Core	Rim
Sm	1.20	0.10	1.28	1.32	0.66	0.04	0.59	0.11	0.55	0.48
Eu	1.19	1.08	1.34	1.18	1.23	0.23	1.20	0.39	1.04	0.88
Gd	1.67	1.53	1.40	1.49	0.52	0.22	0.58	0.24	0.51	0.44
Tb	0.29	0.29	0.20	0.24	0.09	0.10	0.07	0.06	0.06	0.07
Dy	1.22	1.67	0.89	0.96	0.35	1.24	0.33	0.52	0.22	0.32
Ho	0.23	0.29	0.11	0.18	0.05	0.48	0.05	0.21	0.05	0.06
Er	0.60	0.81	0.35	0.44	0.22	2.52	0.16	1.05	0.22	0.31
Yb	0.49	0.92	0.15	0.31	0.21	5.57	0.16	1.96	0.15	0.13
Lu	0.09	0.17	0.05	0.07	0.03	0.82	0.04	0.29	0.02	0.03
Σ REE	8.63	9.04	7.28	7.53	4.21	11.28	3.97	5.16	4.00	3.59
Eu/Eu*	2.56	2.68	3.05	2.58	6.43	7.17	6.24	7.39	5.95	5.86
$(La/Lu)_N$	0.04	0.02	0.03	0.01	–	0.00	0.01	0.00	0.07	0.03
$(La/Nd)_N$	0.05	0.07	0.02	0.01	–	0.53	0.01	0.04	0.03	0.03
$(La/Sm)_N$	0.02	0.02	0.01	0.00	–	0.09	0.00	0.03	0.02	0.01

5 Conclusions

The results of geochemical studies of garnet from granulites and eclogites located in the Bergen Arcs complex (Southern Norway) using a set of microprobe and SIMS methods indicate that the garnets from granulites are not zoned by major and trace elements; the garnets from eclogites have specific rims formed during eclogite metamorphism while their cores were formed during granulite metamorphism. These features should be taken into account during the Sm–Nd dating.

References

Austrheim H. Fluid and deformation induced metamorphic processes around Moho beneath continent collision zones: examples from the exposed root zone of the Caledonian mountain belt, W-Norway. Tectonophysics. 2013;609:620–35. https://doi.org/10.1016/j.tecto.2013.08.030.

Austrheim H, & Griffin WL. Shear deformation and eclogite formation within granulite facies anorthosites of the Bergen Arcs, western Norway. Chemical Geology. 1985;50:267–81. https://doi.org/10.1016/0009-2541(85)90124-X.

Austrheim H & Robins B. Reactions involving hydration of orthopyroxene in anorthosite-gabbro. Lithos. 1981;14:275–81. https://doi.org/10.1016/0024-4937(81)90055-4.

Austrheim H, Erambert M, Engvik AK. Processing of crust in the root of the Caledonian continental collision zone: role of eclogitization. Tectonophysics. 1997;273:129–53. https://doi.org/10.1016/S0040-1951(96)00291-0.

Boundy TM, Fountain DM, Austrheim H. Structural development and petrofabrics of eclogite facies shear zones, Bergen Arcs, western Norway: implications for deep crustal deformational processes. Journal of Metamorphic Geology. 1992;10.2:127–46. https://doi.org/10.1111/j.1525-1314.1992.tb00075.x.

Cohen AS, O'Nions RK, Siegenthaler R, Griffin WL. Chronology of the pressure-temperature history recorded by a granulite terrain. Contributions to Mineralogy and Petrology. 1988;98:303–311. https://doi.org/10.1007/bf00375181.

Hickmott DD. Trace element zoning in garnets: implications for metamorphic petrogenesis. Ph. D. Thesis. Cambridge: 1988. 449 p.

McDonough WF, Sun SS. The composition of the Earth. Chemical Geology. 1995;120:223–53. https://doi.org/10.1016/0009-2541(94)00140-4.

Pollok K, Lloyd GE, Austrheim H, Putnis A. Complex replacement patterns in garnets from Bergen Arcs eclogites: a combined EBSD and analytical TEM study. Chemie der Erde – Geochemistry. 2008;68:177–91. https://doi.org/10.1016/j.chemer.2007.12.002.

Pyle JM, Spear FS. An empirical garnet (YAG)—xenotime thermometer. Contributions to Mineralogy and Petrology. 2000;138:51–8. https://doi.org/10.1007/PL00007662.

Roberts D, Gee DG. An introduction to the structure of the Scandinavian Caledonides. The Caledonide orogeny–Scandinavia and related areas. 1985;1:55–68.

Skublov SG. Geochemistry of Rare Earth Elements in Rock-Forming Metamorphic Minerals (Nauka, St. Petersburg, 2005) [in Russian].

Magmatic Hornblende in the Gabbronorites of the Kusa Intrusion (Southern Urals, Russia)

Evgeny S. Shagalov, Vladimir V. Kholodnov, and Tatyana D. Bocharnikova

Abstract

An important place in the composition of the rocks of the Kusa intrusion is occupied by the minerals of the amphibole group, mainly associated with the late magmatic processes of auto-metamorphism and skarn formation. Primary magmatic high-temperature amphiboles of the deposit have not been described. The aim of the work is to characterize the chemical composition of magmatic high-temperature hornblende of the Kusa deposit. Major element composition of amphiboles as well as the composition of halogens in apatite present in the form of fine inclusions in ore minerals was studied by electron probe microanalyzer (Cameca SX100). The chemical composition of the hornblende aggregates corresponds to titanium-enriched pargasite with weak chemical zoning. Using several geothermobarometers, the pressure and temperature during crystallization of high-titanium amphiboles was calculated, resulting in the direct evidence of the increased fluid content in the magma, which formed this intrusion at the magmatic stage. The apatite halogen composition confirmed the earlier conclusions about the deep facies of the Kusa massif as compared to the deposits situated farther south, in the Zyuratkul riftogenic fault zone, which were less deep and did not have such a high chloride specialization characterized by a different composition of ore mineralization with prevailing high-titanium titanomagnetite in ores, and the increased fluorine content in water-containing minerals.

Keywords

Magmatic hornblende · Gabbronorites · The Kusa intrusion

E. S. Shagalov (✉) · V. V. Kholodnov · T. D. Bocharnikova
Institute of Geology and Geochemistry, Ural Branch of the Russian Academy of Sciences, 15 Akademika Vonsovskogo, 620016 Ekaterinburg, Russia
e-mail: shagalov@igg.uran.ru

E. S. Shagalov
Ural State Mining University, 30 Kuibysheva str., 620144 Ekaterinburg, Russia

S. Votyakov et al. (eds.), *Minerals: Structure, Properties, Methods of Investigation*, Springer Proceedings in Earth and Environmental Sciences,
https://doi.org/10.1007/978-3-030-49468-1_28

1 Introduction

The Kusa-Kopan complex (Southern Urals, Chelyabinsk region, Russia) of layered intrusions has an extensive mineralogy. An important place in the composition of the rocks is occupied by the minerals of the amphibole group. They are mainly associated with the late magmatic processes of auto-metamorphism and skarn formation. Primary magmatic high-temperature amphiboles of the deposit have not been described.

In the study devoted to the deep borehole No. 2, which drilled the deeper part of the Kusa gabbro massif uncovered by erosion, Alekseev et al. (1992) has described a gabbronorite horizon that did not reach the day surface and was uncovered at a depth of more than 500 m. In gabbonorites, amphibole has only been mentioned as a minor mineral (up to 7%) without specifying the mineral species. Gabbronorites on separate horizons of the borehole section were mostly intensely amphibolitic with the development of pargasite-hastingsitic hornblende over pyroxene.

The aim of the work is to characterize the chemical composition of primary magmatic high-temperature hornblende from the Kusa deposit.

2 Materials and Methods

A thin section made from the sample of ore gabbronorite from the borehole No. 2 (depth 530 m) was studied.

The analyses of elemental composition were performed at the Geoanalyst Center for Collective Use at the IGG UB RAS using a Cameca SX100 electron probe microanalyzer. The thin section was carbon-sputtered prior to analysis.

3 Results and Discussion

When studying the petrographic sections of this borehole in a sample of ore gabbronorite, we have detected brown hornblende aggregations (Figs. 1 and 2). Grain sizes range from tenths of mm to 3 mm. They grow with the replacement by clinopyroxene grains. Aggregations vary from xenomorphic, filling the interstitial space between individuals of pyroxene and ore minerals, to idiomorphic, growing on pyroxene individuals. In thin sections, the mineral has a strong pleochroism in brown tones.

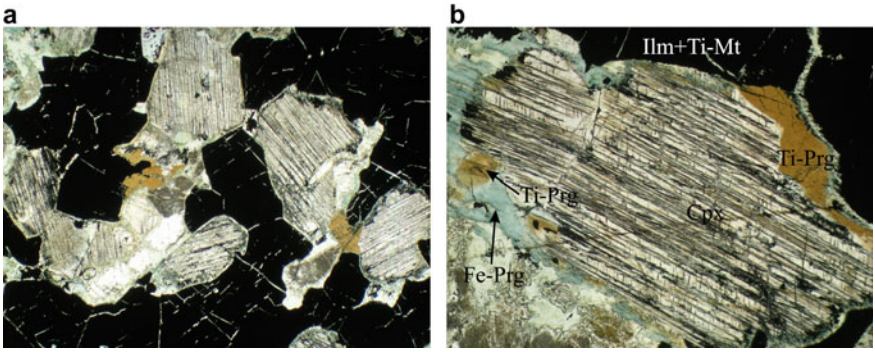

Fig. 1 Ore amphibole-containing gabbronorite. Borehole 2, depth 530.5 m. Incident light, polished thin section. Field of view 3 mm **a**, 1.5 mm **b**. Cpx—clinopyroxene, Fe-Prg—ferropargasite, Ti–Mt—titanomagnetite, Ilm—ilmenite

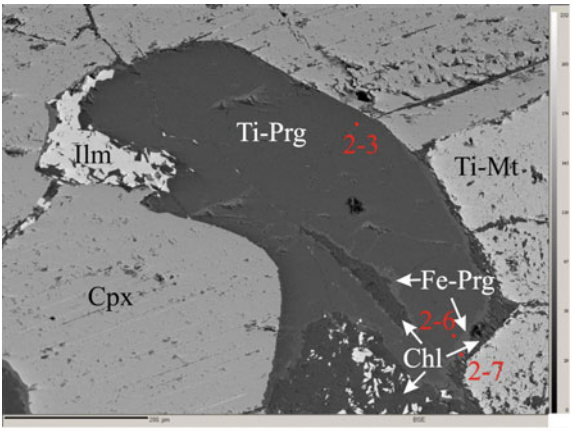

Fig. 2 Titanium-enriched pargasite (Ti-Prg) in ore gabbronorite of the Kusa intrusion. Borehole 2, depth 530.5–529.2 m. Image in backscattered electrons, Cpx—clinopyroxene, Fe-Prg—ferropargasite, Ti–Mt—titanomagnetite, Ilm—ilmenite, Chl—chlorite

The chemical composition of the mineral corresponds to titanium-enriched pargasite. The grains have a weak chemical zoning (Table 1). From the center to the edge, the content of titanium, iron and alkali metals decreases, with an increase of alumina, magnesium and manganese.

Over Ti-pargasite, a blue-green hornblende (ferropargasite) develops with an increased chlorine content (up to 0.57%), which in turn is replaced by clinochlore.

Table 1 Compositions and formulas of amphiboles in gabbronorites of the Kusa intrusion

Element/oxide	Ck-2_am_2-3	Ck-2_am_2-6	Ck-2_am_2-7
SiO_2	41.89	41.63	42.4
TiO_2	4.25	3.25	0.29
Al_2O_3	11.95	13.51	12.23
Cr_2O_3	0,00	0.02	0.07
MnO	0.04	0.13	0.14
FeO	10.81	10.2	19.01
MgO	13.24	13.83	8.59
CaO	12.22	12.2	11.7
SrO	0.38	0.32	0.38
Na_2O	3.11	2.45	2.19
K_2O	0.74	0.19	0.44
F	0.11	0.10	0.07
Cl	0.01	0,00	0.57
O=F, Cl $_{(calc)}$	0.05	0.04	0.16
Total	98.75	97.84	98.08
P	6.5–6.7	7.8–8.0	7.1–7.3
T	1005.0–1059.3	974.1–952.3	584.7–509.3
Calculated Mineral Formulae			
$(Na_{0.835}K_{0.138})_{0.973}(Ca_{1.919}Na_{0.049}Sr_{0.032})_2(Mg_{2.893}Fe^{2+}_{1.325}Ti_{0.469}Al_{0.205}Mn^{2}_{0.005}$ $^{+})_{4.897}(Si_{6.14}Al_{1.86})_8$ $O_{22}((OH)_{1.947}F_{0.051}Cl_{0.002})_2$			
$(Na_{0.659}K_{0.035})_{0.694}(Ca_{1.908}Na_{0.035}Sr_{0.027}Mn_{0.016}Fe_{0.014})_2(Mg_{3.009}Fe^{2+}_{1.083}Al_{0.401}Ti_{0.357}Fe^{3}_{0.148}$ $^{+}Cr_{0.002})_5$ $(Si_{6.076}Al_{1.924})_8O_{22}((OH)_{1.954}F_{0.046})_2$			
$(Na_{0.609}K_{0.085})_{0.694}(Ca_{1.901}Na_{0.035}Sr_{0.033}Mn_{0.018}Fe_{0.012})_{1.999}(Fe^{2+}_{2.181}Mg_{1.942}Al_{0.617}Fe^{3}_{0.218}$ $^{+}Ti_{0.033}$ $Cr_{0.008})_{4.999}(Si_{6.431}Al_{1.569})_8O_{22}((OH)_{1.82}Cl_{0.147}F_{0.034})_{2.001}$			

Note Ck-2_am_2-3 is the center, Ck-2_am_2-6 is the edge, Ck-2_am_2-7 is the rim

Based on the aluminum content measured in the central and marginal parts of Ti-pargasite, the pressure during crystallization of high-titanium amphiboles increased from 6.5 to almost 8 kbar with a temperature drop of 100 °C from 1060 °C. With further cooling (about 550 °C, a blue-green hornblende developed), the pressure decreased (geothermobarometers (Hammarstrom and Zen 1986; Otten 1984; Putirka 2016; Schmidt 1992)). Thus, we have a direct evidence of the increased fluid content in the magma, which formed this intrusion at the magmatic stage. In the same thin section of ore two-pyroxene gabbro (borehole 2, depth 530 m), the composition of halogens in apatite was studied. 4 apatite grains were analyzed. In all cases, the

apatite is present in the form of fine inclusions in ore minerals. The chlorine content in apatites is 0.15–0.49%, and the fluorine content is 1.36–1.57%. In terms of chlorine content, the apatite is close to blue-green hornblende—ferropargasite.

4 Conclusions

Thus, the amphibolization of gabbronorite occurred with the development of pargasite-hastingsitic hornblende over pyroxene. Blue-green ferropargasite is a subsolidus phase of the interaction of intergranular fluid with the frame of early high-temperature igneous minerals. Chlorine accumulates in this fluid, which has an important effect on ore formation during the formation of the Kusa magnetite-ilmenite deposit; magnetite is poor in titanium (Kholodnov et al. 2016; Borodina 2001 and others). This also confirms earlier conclusions about the deep facies of the Kusa massif, while the deposits situated farther south, in the Zyuratkul riftogenic fault zone, are less deep and do not have such a high chloride specialization. Therefore, they are characterized by a different composition of ore mineralization with prevailing high-titanium titanomagnetite in ores, and the increased fluorine content in water-containing minerals.

Acknowledgements This work was financially supported by the Project of the Ural Branch of the Russian Academy of Sciences No. 18-5-5-8 (state registration No. AAAA-A18-118052590034-0). EPMA analyses were performed at the Geoanalyst Center for Collective Use within the framework of topic No. AAAA-A18-118053090045-8 of the IGG UB RAS state assignment.

References

Alekseev AA, Alekseeva GV, Kovalev SG. Kusinsko-Kopanskii rassloennyi kompleks: novye dannye, predstavleniya i perspektitvy. [Alekseev AA, Alekseeva GV, Kovalev SG. The Kusa-Kopan layered complex: new data, ideas and perspectives. Ufa, 1992. 20 p. (in Russ.)].

Fershtater GB, Kholodnov VV, Borodina NS. Usloviya formirovaniya i genezis rifeiskikh il'menit-titanomagnetitovykh mestorozhdenii Urala. Geologiya rudnykh mestorozhdenii. 2001;43(2):112–128. [Fershtater GB, Kholodnov VV, Borodina NS. Formation conditions and genesis of Riphean ilmenite-titanomagnetite deposits in the Urals. Geology of ore deposits. 2001;43(2):112-128. (in Russ.)].

Hammarstrom JM, Zen E. Aluminum in hornblende: an empirical igneous geobaro-meter. Am. Min. 1986;71:1297–1313.

Kholodnov VV, Shagalov ES, Bocharnikova TD, Konovalova EV. Sostav i usloviya formirovaniya Ti-Fe-V orudeneniya v dvupiroksenovom gabbro Medvedevskogo mesto-rozhdeniya (Yu. Ural). Chast' II. Stadiinost' rudoobrazovaniya—kak rezul'tat evolyutsii rudonosnogo rasplava. Litosfera. 2016;2:48–69. [Kholodnov VV, Shagalov ES, Bocharnikova TD, Konovalova EV. Composition and conditions for the formation of Ti-Fe-V mineralization in the two-pyroxene gabbro of the Medvedevsky deposit (S. Ural). Part II. Staged ore formation as a result of the evolution of an ore-bearing melt. Litosfera. 2016;2:48–69. (in Russ.)].

Otten MT. The origin of brown hornblende in the Artfjallet gabbro and dolerites. Contrib Mineral Petrol. 1984;86:189–99.

Putirka K. Amphibole thermometers and barometers for igneous systems and some implications for eruption mechanisms of felsic magmas at arc volcanoes. American Mineralogist. 2016;101 (4):841–858.

Schmidt MW. Amphibole composition in tonalite as a function of pressure: an experimental calibration of the Al-in-hornblende barometer. Contrib Mineral Petrol, 1992;110:304–10.

Atomic and Electronic Structure of Zircon According to High-Resolution X-Ray Photoelectron Spectroscopy: Methodological Aspects

Yuliya V. Shchapova, Dmitry A. Zamyatin, Sergey L. Votyakov, Ivan S. Zhidkov, Andrey I. Kukharenko, and Seif O. Cholakh

Abstract

A new XPS methodology to analyze the atomic and electronic structure of a wide-gap dielectric zircon has been developed. A high spectral resolution with the O1s-line width of 1.3 eV and volume (near surface) sensitivity have been achieved by using a spectrometer with a dual charge compensation system and monochromatic AlK_α-excitation as well as by the measurement (electron exit angle 90°, spot diameter 100 μm) and sample preparation (fresh cleavage) conditions. The possibility of analysing the structure of short-range order, in particular, diagnosing the formation of Si-O-Si and Si-OH fragments occurring in the bulk and/or surface layers of zircon under the influence of external (e.g., radiation, chemical) factors, is shown.

Keywords

X-ray photoelectron spectroscopy · Zircon · Oxygen sublattice

Y. V. Shchapova (✉) · D. A. Zamyatin · S. L. Votyakov
Institute of Geology and Geochemistry, Ural Branch of the Russian Academy of Sciences, 15 Vonsovskogo Street, 620016 Ekaterinburg, Russia
e-mail: shchapova@igg.uran.ru

Y. V. Shchapova · D. A. Zamyatin · I. S. Zhidkov · A. I. Kukharenko · S. O. Cholakh
Ural Federal University named after the First President of Russia Boris Yeltsin, 19 Mira Street, 620002 Ekaterinburg, Russia

S. Votyakov et al. (eds.), *Minerals: Structure, Properties, Methods of Investigation*, Springer Proceedings in Earth and Environmental Sciences,
https://doi.org/10.1007/978-3-030-49468-1_29

1 Introduction

X-ray photoelectron spectroscopy (XPS) is based on recording the energy spectrum of electrons emitted from the surface layers of solid samples under the impact of X-ray radiation. The method along with the quantitative analysis of the chemical composition of the layer, allows the measurements of E_b binding energies of core level and valence band electrons to be carried out. The latter depends on the structure of short-range order, effective charge and chemical bond characteristics (Zigban et al. 1971; Nefedov and Vovna 1987). The layer thickness analysed by XPS depends on the photoelectron energy and does not exceed several hundred atomic layers (~20 nm) (Zigban et al. 1971). Photoelectrons from various depths can be recorded in the spectra by choosing the measurement conditions (see, for example, reviews by (Hochella 1988; Fadley 2010)). It has been shown that, when using AlK_α X-ray radiation and high values of the photoelectron collection angle, over 90% of the measured intensity is provided by the layers lying deeper than the surface monolayer (Nesbitt and Bancroft 2014). When analysing appropriately prepared mineral surfaces (fresh cleavage), the information obtained can be correlated with their bulk properties (Zakaznova-Herzog et al. 2005, 2006).

Photoionization and emission of both Auger and secondary electrons lead to positive charging of the dielectric material surface layer, thus resulting in a decrease in the kinetic energy of photoelectrons and overestimation of the calculated binding energy. A serious problem is the uneven charging of imperfect surfaces resulting in the broadening and distortion of the XPS peak shape and, as a result, the impossibility of separating the contributions from atoms with small differences in chemical shift. In modern spectrometers, high-energy resolution is provided by the use of monochromatic X-ray radiation and efficient charge compensation systems (Nesbitt and Bancroft 2014), as well as by specific surface preparation.

In mineralogy, XPS has so far been primarily used to study the surface properties and reactivity of natural oxides, sulfides and silicates and, to a lesser extent, to study the composition, structure and chemical bonds in the mineral bulk (see, for example, reviews by Hochella (1988); Fadley (2010)). It has been shown that the XPS spectra of silicates and phosphates in the amorphous and crystalline state (with typical O1s oxygen line widths in the order of 2 eV or greater, using an ESCALAB-MKII spectrometer and the analysis of mechanically processed or natural surfaces) reflect qualitatively the changes in the short-range order in the mineral bulk (Gubanov et al. 1991; Zatsepin et al. 1997; Shchapova et al. 2010; Votyakov et al. 2012). This approach was developed in connection with the introduction of high-resolution spectrometers (Zakaznova-Herzog et al. 2005, 2006; Fadley 2010; Nesbitt et al. 2011). Similar values of O1s, Si2p, Mg2p and Ca2p line FWHM (~1.3 eV) were obtained for quartz, olivine, diopside and bronzite, and their vibrational broadening was suggested. Three structurally nonequivalent oxygen atoms were assigned in the diopside: bridging and non-bridging MgOSi and CaOSi/FeOSi (Zakaznova-Herzog et al. 2005, 2006). The leaching of olivine, bronzite, and diopside was studied by Zakaznova-Herzog et al. (2008). The high

resolution of the O1s spectrum allowed an additional type of OH^- oxygen to be diagnosed, arising from the exchange of H^+ with near-surface cations. Different types of oxygen in silicate glasses were studied (Nesbitt et al. 2011; Sawyer et al. 2015); the concentration dependences of the energy of oxygen O1s levels of various types and Si2p levels were used to interpret the concentration changes in the Raman spectra of stretching vibrations of SiO_4 tetrahedra; their relationship with the electron density on oxygen atoms was revealed (Nesbitt et al. 2017).

For zircon, the XPS method was previously used to study the E_b elemental chemical shifts relative to SiO_2 and ZrO_2 simple oxides, with the possibility of using O1s E_b values to assess the Si-O covalence in silicates being discussed (Guittet et al. 2001). The effect of argon ion irradiation (8 keV) on the chemical composition of the $ZrSiO_4$ surface layers was studied, and a significant loss of SiO_2 and a strong reduction of Zr after irradiation was observed (Iacona et al. 1999). The effect of weathering of the zircon surface with various degrees of metamictization on the XPS spectra was considered; no significant changes in the chemical composition were detected, and the relationship between the changes in the O1s spectra was attributed to kaolinite particles (Balan et al. 2001). The XPS was used to study the flotation properties of zircon after plasma cleaning (Marshall et al. 2014) and surface modification by non-thermal treatment with electromagnetic pulses due to a change in the ratio of different types of hydroxyl groups (Chanturia et al. 2017). In (Shchapova et al. 2010), changes in the zircon O1s, Si2p and the valence band spectra due to radiation damage of its structure were observed; the changes were attributed to the partial polymerization of silicon-oxygen tetrahedra in the damaged structure. It should be noted that there are XPS studies of radiation damage of other natural orthosilicates, in particular, olivine, for which radiation-induced reduction of metallic Fe has been reported (Dukes et al. 1999; Loeffler et al. 2009).

Thus, XPS is a promising method for the analysis of structural and chemical transformations of the surface and bulk (sub-surface) layers of minerals. Modern equipment allows the spectra to be obtained with high-spectral resolution and the atomic and electronic structures of the bulk minerals to be analyzed using appropriate measurements and sample preparation techniques. The application of XPS to study the structure and chemical bonding of dielectric silicate minerals requires a detailed consideration of methodological issues.

This work is aimed at solving methodological issues of surface preparation, selecting XPS spectral measurement modes with the use of a PHI XPS Versaprobe 5000 high-resolution spectrometer, as well as processing and analysing the results to study the oxygen sublattice of silicate minerals, in particular zircon; minimizing the influence of surface states and the differential surface charge on O and Si spectral shape; and testing the methodology using highly crystalline zircon as an example.

2 Materials and Methods

2.1 Samples and Sample Preparation

Highly crystalline Ratanakiri zircon aged 0.92 ± 0.07 Ma (Zeug et al. 2018) from Cambodian secondary deposits of alkaline basalt rocks having a low (<0.1 wt%) amount of trace elements except hafnium (~0.7 wt% HfO_2) was studied. The test sample was previously annealed under reducing conditions at 900–1000 °C. According to our data from the electron microprobe and Raman analyses, the sample was homogeneous in the major and trace element composition and structure. In order to reduce the contribution of the modified surface layers, the measurements were performed on a fresh cleavage, after which the sample was immediately placed in the vacuum chamber of the spectrometer. The orientation of the sample surface was not taken into account.

2.2 Analytical Equipment and Measurement Modes

The studies were performed using a PHI XPS 5000 VersaProbe spectrometer (ULVAC-Physical Electronics, USA, 2011). The spectrometer was operated according to the classical X-ray optical scheme using a quartz monochromator with a working range of the binding energy analyser of 0–1500 eV. The device used an electrostatic type of focusing and magnetic shielding of the main camera. The mentioned features of the spectrometer provided high energy resolution (ΔE 0.5 eV for AlK_α excitation), high spatial selectivity (minimum diameter of X-ray AlK_α probe d ≤ 10 μm) and high elemental sensitivity with a significant signal-to-noise ratio when studying a wide range of objects. An important feature of the spectrometer was a system of two-channel neutralization of the electrostatic charge arising during the registration of XPS spectra of dielectric samples. The neutralization was carried out using both an electron source with a thermal cathode (~1 eV) and low-energy ions (≤200 eV). The spectrometer had an oil-free two-stage vacuum pumping system based on turbomolecular and magnetic discharge pumps, which effectively maintained a working vacuum not exceeding 10^{-7} Pa. In this case, sample contamination with fore-vacuum oil vapour in the preparation chamber, which usually occurs when the standard vacuum-pumping scheme is used for vapour-oil fore-pumps, was completely excluded.

The measurements were performed at an electron exit angle of 90°, corresponding to the maximum bulk sensitivity. The X-ray spot diameter was 100 μm. The X-ray radiation power on the sample did not exceed 25 W. In the survey spectral mode, the energy window width was equal to 187.85 eV, in the high-resolution mode in the region of O1s, Si2p, Zr3d, C1s lines it was 23.5 eV. The accumulation time at one point in a single pass was 50 ms. The measurements were carried out in vacuum with a residual pressure of argon ions used for neutralizing of about 1×10^{-6} Pa. The typical signal-to-noise ratio was of the order of

10,000/3 for core level lines. The spectrometer energy scale was calibrated using the Au $4f_{7/2}$ and Cu $2p_{3/2}$ lines; the effect of the energy window width on the FWHM was calibrated using Ag $3d_{5/2}$line. The initial processing of the spectra was carried out using the ULVAC-PHI MultiPak 9.8 software. The charge of the sample was taken into account by the C1s level binding energy of 284.8 eV (Moulder et al. 1992; https://xpssimplified.com/elements/carbon.php).

3 Results and Discussion

The survey spectrum of Ratanakiri zircon is shown in Fig. 1; electron binding energies of 525–535 eV (O1s), 425–445 (Zr 3 s), 325–355 (Zr $3p_{3/2}$, $3p_{1/2}$), 275–290 (C1s), 176–190 (Zr $3d_{5/2}$, $3d_{3/2}$), 145–160 (Si2s), 95–110 (unresolved Si $2p_{3/2}$, $2p_{1/2}$), <60 eV (Zr valence band 4s, 4p, 4d; Si3s, 3p; O3s, 3p) are typical for crystalline zircon (Iacona et al. 1999; Guittet et al. 2001; Shchapova et al. 2010). The chemical composition of the surface cleavage, determined by the ratio of the Zr3d, Si2p, O1s, and C1s lines using photoionization cross sections (Moulder et al. 1992), is close to stoichiometric with the exception of uncontrolled surface carbon: 14, 15.3, 61.6, 9 at. % for Zr, Si, O and C, respectively.

The O1s, Si2p, and $Zr3d_{5/2}$ spectra of zircon are presented in Figs. 2, 3 and 4; the binding energies of O1s, Si2p, and $Zr3d_{5/2}$ are shown in Table 1. The O1s spectrum is represented by a narrow, slightly asymmetric line with a tail in the high-energy region (Fig. 2a). The approximation of the entire line by one Voigt profile (R = 0.99487) gives the values of E_b(O1s) = 530.86 ± 0.01 eV and FWHM (O1s) = 1.32 ± 0.02 eV, but does not reproduce the line shape accurately. O1s binding energy is close to that obtained previously (531.3 and 530.95 eV) for

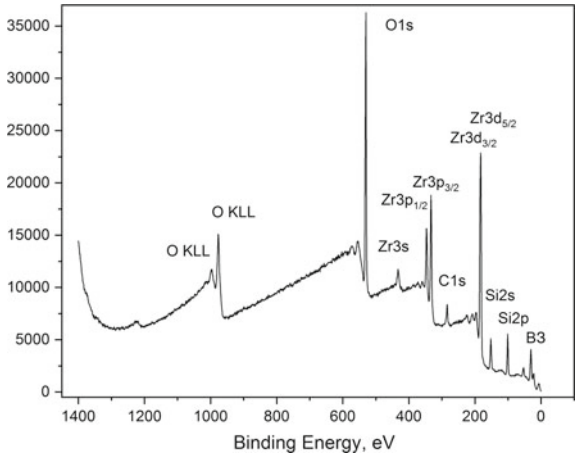

Fig. 1 Survey XPS spectrum of Ratanakiri zircon

the three-coordinated O (Si, Zr, Zr) atom in synthetic and highly crystalline zircon from kimberlites, respectively (Guittet et al. 2001; Shchapova et al. 2010), as well as to 531.0 eV in Mg olivine (Zakaznova-Herzog et al. 2005), in the structure of which, similar to zircon, isolated SiO_4 tetrahedra are identified. Small discrepancies in zircon E_b(O1s) can be partially explained by small differences in the reference C1s binding energy (Greczynski and Hultman 2018). The obtained FWHM (O1s) of full contour ~1.3 eV in zircon is close to FWHM (O1s) = 1.24–1.27 eV in quartz, pyroxene and olivine (Kratos Axis Ultra spectrometer with magnetic retention charge compensation system, AlK_α—radiation, spectrometer spectral resolution 0.35 eV) (Nesbitt et al. 2004, Zakaznova-Herzog et al. 2005, 2006; Bancroft et al. 2009). In the cited papers, the nature of the O1s and Si2p spectral broadening has been discussed in detail and the following main factors have been named in conclusion: (i) phonon broadening (decrease in the lifetime of the excited state) leading to a temperature-dependent symmetric Gaussian diffusion of the contour, and (ii) vibronic splitting of the excited state (FSVB—final state vibrational broadening) first noted by (Siegbahn 1974), which leads to temperature-independent asymmetric broadening of the contour. It has also been noted that FWHM (O1s) ~1.3 eV is the minimum possible measured value for silicates at spectral resolution of ~0.35 eV at room temperature. Taking into account these considerations and the Versaprobe spectral resolution (not exceeding ~0.5 eV), the obtained zircon FWHM (O1s) = 1.32 ± 0.02 eV confirms that the selected measurement and sample preparation conditions truly provide the effective compensation of the surface differential charge, and the technique can be used further to study the effects of changes in line profile.

To obtain the information on the possible contribution of any other O atoms in different from O (Si, Zr, Zr) coordination to the high-energy O1s spectral tail, we have used the procedure for approximating the spectrum in its low-energy part

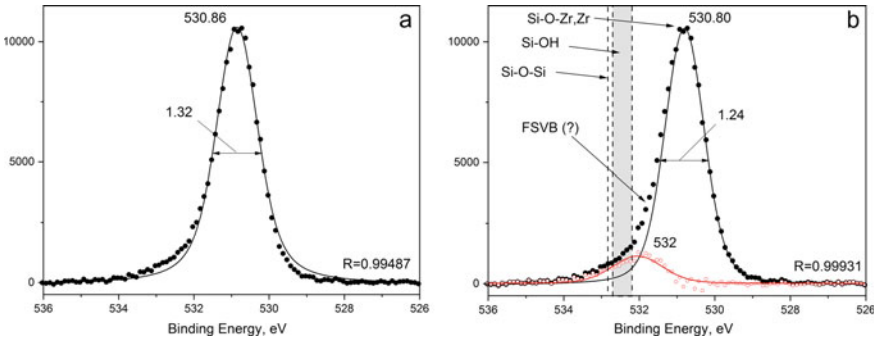

Fig. 2 Zircon O1s spectrum (filled circles) and its approximation over full profile **a** and over its low-energy part (526.00–530.86 eV) by Voigt profile (black line) **b**. Empty circles—difference between experimental spectrum and approximation; red line—approximation of the difference spectrum by Voigt profile. Vertical dotted lines—binding energy E_b range (filled) of O1s for Si-OH coordination in olivine (532.2–532.7 eV) and E_b value of O1s for Si-O-Si coordination in quartz (530.8 eV) according to (Duval et al. 2002; Zakaznova-Herzog et al. 2008; Guittet et al. 2001)

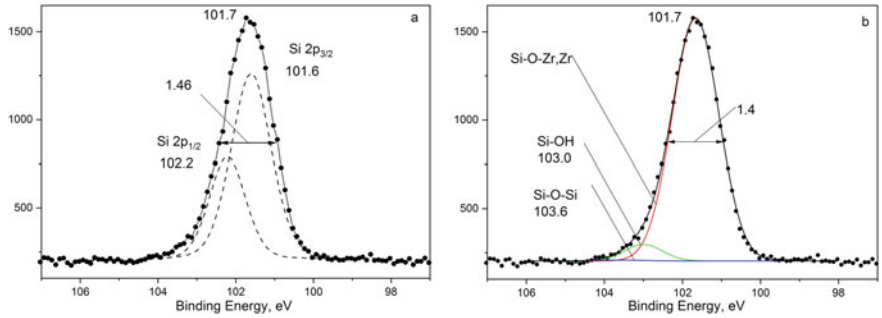

Fig. 3 Zircon Si2p spectrum (filled circles) and its approximation by one (black line) and two Voigt profiles corresponding to $Si2p_{3/2}$ and $Si2p_{1/2}$ contributions with fixed maxima at 101.6 and 102.2 eV (profiles and envelope curve—grey dotted lines) **a** and by three Voigt profiles corresponding to Si-O-Zr, Zr; Si-OH and Si-O-Si contributions (red, green and blue lines) with fixed values of the two latter maxima at 103.0 and 103.6 eV **b**. Black line—envelope curve

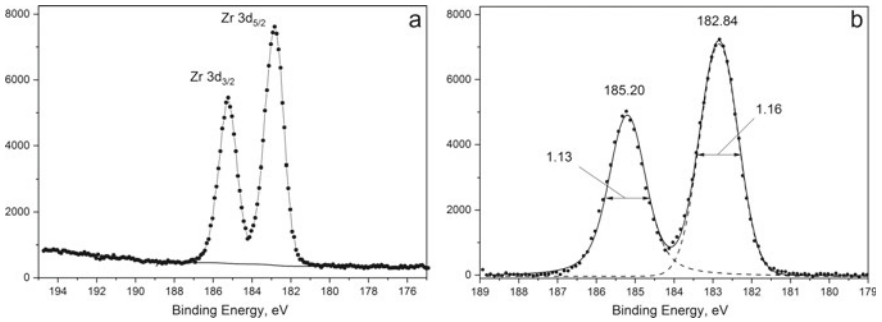

Fig. 4 Zircon Zr3d spectrum (filled circles) and Shirley background approximation **a**; the spectrum after background correction (filled circles) and its approximation by two Voigt profiles corresponding to $Zr3d_{5/2}$ and $Zr3d_{3/2}$ contributions (dotted lines) and envelope curve (solid line) **b**

(Fig. 3b) described in (Nesbitt and Bancroft 2014). An approximation by the Voigt profile (R = 0.99931) in the range of 526.00–530.86 eV gives maximum values of 530.80 ± 0.01 eV and FWHM = 1.24 ± 0.02 eV and clearly reveals the asymmetry of the O1s line. The additional high-energy part (~10% of the total integrated O1s intensity) is described by the Voigt profile with a maximum of 532.0 eV and FWHM 1.6 eV. A similar "additional" spectrum with a maximum at 532.2–532.7 eV and FWHM 1.2–1.6 eV has been observed in the initial and leached olivine, where it is assigned to Si—OH fragments (Zakaznova-Herzog et al. 2008). According to the type of the O1s spectrum in Ratanakiri zircon, it can be assumed that the additional high-energy part of the band is associated with both the FSVB effect of asymmetric line broadening (Bancroft et al. 2009) and the possible

Table 1 E_b binding energy (eV) and FWHM (eV) of O1s, Si2p, $Zr3d_{5/2}$ spectral bands in zircon and a number of silicate minerals

Sample	O1s		Si2p (3/2 and 1/2)		$Zr3d_{5/2}$		$C1s_{meas}$	$C1s^{a}_{ref}$
	E_b	FWHM	E_b	FWHM	E_b	FWHM	E_b	E_b
Ratanakiri zircon	530.86 ± 0.01	1.32 ± 0.02[b]	101.67 ± 0.01	1.47 ± 0.01[b]	182.84 ± 0.01	1.16 ± 0.01[b]	284.81 ± 0.05	284.8
Z1 zircon[c]	530.95	2.06	101.5	1.8	182.7	1.77	–	284.5
Zircon[d]	531.3	2.3	101.8	2.0	182.95	1.8	–	284.6
Quartz[d]	532.7	2.0	103.15	2.0	–	–	–	284.6
Olivine[e]	531.0	1.26	101.7	1.29			–	285.0
Quartz[e]	532.8	1.23	103.6	1.38	–	–	–	285.0

Note [a]reference C1s binding energy used for calibration; [b]FWHM before deconvolution into components; [c]high-crystalline zircon from the Mir kimberlite pipe (Shchapova et al. 2010); [d]synthetic analogs (Guittet et al. 2001); [e]olivine and quartz (Zakaznova-Herzog et al. 2005)

contribution of O atoms to Si-OH coordination (E_b = 532.2–532.7 eV (Duval et al. 2002; Zakaznova-Herzog et al. 2008). The latter can occur on the surface of the cleaved sample in the atmosphere. The contribution of O atoms to the coordination of Si–O–Si (E_b = 530.8 eV (Guittet et al. 2001)), if present, is at a very low amount. Thus, the application of the fresh cleavage technique makes it possible to identify the contributions of (i) sub-surface "bulk" and (ii) surface zircon layers altered by adsorption. Therefore, this technique is acceptable for studying the changes in the state of oxygen atoms induced by various factors (genetic features of the mineral).

The Si2p spectrum can be approximated by one Voigt profile with a maximum of E_b(Si2p) = 101.69 ± 0.01 eV and FWHM (Si2p) = 1.46 ± 0.01 eV, however, the line shape is not exactly reproduced (Fig. 3a). The peak parameters are close to those for olivine 101.7 and 1.29 eV (for comparison, 103.6 and 1.38 eV in quartz) (Zakaznova-Herzog et al. 2005). The spectrum is slightly asymmetric, but to a lesser extent, as compared to O1s. This may be due to the masking of asymmetry caused by the non-elementary nature of the band, because it represents an unresolved (splitting ~0.6 eV) $Si2p_{3/2}$ and $Si2p_{1/2}$ spin—orbit doublet (Bancroft et al. 2009). The deconvolution into two components, schematically simulating $Si2p_{3/2}$ and $Si2p_{1/2}$ contributions ($Si2p_{3/2}$ and $Si2p_{1/2}$ binding energies for olivine are taken from (Zakaznova-Herzog et al. 2005)) gives good agreement with the experiment, but does not contain useful information. Therefore, by analogy with Iacona et al. (1999); Balan et al. (2001); Chanturia et al. (2017), hereinafter, the $Si2p_{3/2}$ and $Si2p_{1/2}$ doublet is simulated by one profile. In this case, an additional intensity in the high-energy region can be related to the integral contribution of Si2p of Si atoms being in a certain new coordination. Figure 3b shows the approximation of the spectrum by three Voigt profiles: Si-O-Zr, Zr (parameters determined by fitting), Si-OH (fixed binding energy of 103.0 eV (Zakaznova-Herzog et al. 2008; Chanturia et al. 2017)) and Si-O-Si (fixed binding energy of 103.6 eV (Zakaznova-Herzog et al. 2005)). In this approximation, the Si–O–Zr, Zr linewidth is 1.40 eV, which is close to the data for olivine (see table). The contribution of Si-OH is ~5%, while the contribution of Si-O-Si is negligible. The result obtained is consistent with the analysis of the Ratanakiri zircon O1s spectrum. It confirms the absence of a significant differential surface charge and shows the presence of an insignificant amount of OH groups that can occur on the surface of the cleaved sample in the atmosphere.

The Zr3d spectrum is represented by two lines from the well-resolved components of the $Zr3d_{5/2}$ and $Zr3d_{3/2}$ spin-orbit splitting (Fig. 4a). The Voigt approximation gives $E_b(Zr3d_{5/2})$ = 182.84 ± 0.01 eV (Fig. 4b), which is in good agreement with Guittet et al. (2001); Shchapova et al. (2010). FWHM ($Zr3d_{5/2}$) = 1.16 ± 0.01 eV is significantly lower than in the cited works. There are no signs of OH groups. It has been noted by Balan et al. (2001) that chemical exposure and weathering have a weak effect on the shape of the Zr3d line in zircon; however, a strong effect of Ar ion irradiation on the line shape has been found by Iacona et al. (1999) due to a change in the charge state of some Zr atoms. The high

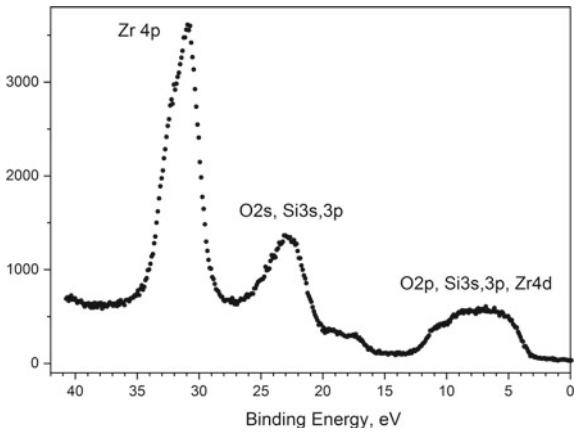

Fig. 5 Zircon valence band spectrum and the assignment of electronic state contributions according to Shchapova et al. (2010)

resolution of the Zr3d spectrum achieved in this work allows the possibility of detecting radiation damage to be predicted not only in the silicon-oxygen, but also in the zirconium sublattice of zircon.

The valence band spectrum (Fig. 5) reproduces the known features of the zircon electronic structure (Rignanese et al. 2002; Shchapova et al. 2010; Du et al. 2012). Note that high kinetic energies of valence electrons (1446–1486 eV) provide the greatest depths of electron exit; in this case, the contribution of the surface layers is less than that for the core electrons. The achieved high spectral resolution allows subsequently tracing changes in chemical binding under the influence of external factors (zircon genetic characteristics). The contribution of bulk layers can be considered dominant.

4 Conclusions

The XPS analysis methodology of the atomic and electronic structure of a wide-gap dielectric zircon has been developed. The minimization of the influence of surface states and the differential surface charge has been achieved by: (1) using a spectrometer with a dual charge compensation system and monochromatic AlK_α-excitation; (2) the selection of measurement conditions, in particular, a maximum increase in the exit angle of the measured electrons and a small spot diameter of 100 μm; (3) a surface preparation technique—fresh cleavage in the atmosphere immediately before measurement. Various processing options of O1s, Si2p and Zr3d spectra have been tested using highly crystalline Ratanakiri zircon (Cambodia) from secondary deposits of alkaline basalt rocks, annealed under reducing conditions at 900–1000 °C. FWHM (O1s) = 1.3 eV measured using the developed

methodology corresponds to the minimum possible for silicates when operating on high-resolution serial spectrometers. Such a result has been obtained for zircon for the first time. The possibility of analyzing the structure of short-range order, in particular, diagnosing the formation of Si-O-Si and Si-OH fragments occurring in the bulk and/or surface layers of zircon under the influence of external (e.g., radiation, chemical) factors, has been shown.

Acknowledgements This work was supported by the Russian Foundation for Basic Research, project No. 18-15-01153. The implementation of electron microprobe analysis was supported by the theme of state assignment of IGG UB RAS (number AAAA-A19-119071090011-6). The authors are grateful to Christoph Lenz for providing a zircon sample for research.

References

Balan E, Trocellier P, Jupille J, Fritsch E, Muller J-P, Calas G. Surface chemistry of weathered zircons. Chemical Geology. 2001;181(1–4):13–22.

Bancroft GM, Nesbitt HW, Ho R, Shaw DM, Tse JS, Biesinger MC. Toward a comprehensive understanding of solid-state core-level XPS linewidths: Experimental and theoretical studies on the Si 2p and O 1 s linewidths in silicates. Physical review B. 2009;80:075405.

Chanturia VA, Bunin IZh, Ryazantseva MV, Chanturia EL, Khabarova IA, Koporulina EV, Anashkina NE. Modification of Structural, Chemical and Process Properties of Rare Metal Minerals under Treatment by High-Voltage Nanosecond Pulses. Journal of Mining Science. 2017;53(4):718–733.

Du J, Davanathan R, René CL, Weber WJ. First-principles calculations of the electronic structure, phase transition and properties of ZrSiO4 polymorphs. Computational and Theoretical Chemistry. 2012;987:62–70.

Dukes CA, Baragiola RA, McFadden LA. Surface modification of olivine by H+ and He+ bombardment. Journal of Geophysical Research: Planets. 1999;104(E1):1865–1872.

Duval Y, Mielczarski JA, Pokrovsky OS, Mielczarski E, Ehrhardt JJ. Evidence of the existence of three types of species at the quartz-water solution interface at pH 0–10: surface group quantification and surface complexation modelling. J. Phys. Chem. 2002;B202:2937–2945.

Fadley CS. X-ray photoelectron spectroscopy: Progress and perspectives. Journal of Electron Spectroscopy and Related Phenomena. 2010;178–179:2–32.

Greczynski G, Hultman L. Reliable determination of chemical state in x-ray photoelectron spectroscopy based on sample-work-function referencing to adventitious carbon: Resolving the myth of apparent constant binding energy of the C 1s peak. Applied Surface Science. 2018;451:99–103.

Gubanov VA, Zatsepin, AF, Kortov VS, Novikov DL, Friedman SP, Cherlov GB, Shchapova UV. Electronic states spectrum for lead silicate glasses with different short-range order structures. Journal of Non-Crystalline Solids. 1991;127(3):259–266.

Guittet MJ, Crocombette JP, Gautier-Soyer M. Bonding and XPS chemical shifts in $ZrSiO_4$ versus SiO_2 and ZrO_2: Charge transfer and electrostatic effects. Physical Review B. 2001;63:125117-1–125117-7.

Hochella MF. Auger electron and X-ray photolectron spectroscopies. Reviews in Mineralogy. 1988;18:573–637.

https://xpssimplified.com/elements/carbon.php.

Iacona F, Kelly R, Marletta G. X-ray photoelectron spectroscopy study of bombardment-induced compositional changes in ZrO_2, SiO_2, and $ZrSiO_4$. Journal of Vacuum Science and Technology A: Vacuum, Surfaces, and Films. 1999;17(5):2771–2778.

Loeffler MJ, Dukes CA, Baragiola RA. Irradiation of olivine by 4 keV He+: Simulation of space weathering by the solar wind. Journal of Geophysical Research. 2009;114:E03003.

Marshall GM, Patarachao B, Moran K, Mercier PHJ. Zircon Mineral Solids Concentrated from Athabasca Oil Sands Froth Treatment Tailings: Surface Chemistry and Flotation Properties. Minerals Engineering. 2014;65:79–87.

Moulder JF, Stickle WF, Sobol PE, Bomben KD. Handbook of X-ray Photoelectron Spectroscopy. Perkin-Elmer Corp.: Eden, Prairie, MN, US. 1992.

Nefedov VI, Vovna VI. Elektronnaya struktura khimicheskikh soedinenii. M.: Nauka, 1987. 347 p. [Nefedov VI, Vovna VI. Electronic structure of chemical compounds. Moscow: Nauka, 1987. 347 p. (In Russian)].

Nesbitt HW, Bancroft GM. High resolution core- and valence-level XPS studies of the properties (structural, chemical and bonding) of silicate minerals and glasses. Reviews in Mineralogy and Geochemistry. 2014;78:271–329.

Nesbitt HW, Bancroft GM, Davidson R, McIntyre NS, Pratt AR. Minimum XPS core-level line widths of insulators, including silicate minerals. Am Mineral. 2004;89:878–882.

Nesbitt HW, Bancroft GM, Henderson GS, Ho R, Dalby KN, Huang Y, Yan Z. Bridging, non-bridging and free (O^{2-}) oxygen in Na_2O-SiO_2 glasses: An X-ray Photoelectron Spectroscopic (XPS) and Nuclear Magnetic Resonance (NMR) study. Journal of Non-Crystalline Solids. 2011;357(1):170–180.

Nesbitt HW, Henderson GS, Bancroft GM, O'Shaughnessy C. Electron densities over Si and O atoms of tetrahedra and their impact on Raman stretching frequencies and Si-NBO force constants. Chemical Geology. 2017;461:65–74.

Rignanese G-M, Detraux F, Gonze X, Bongiorno A, Pasquarello A. Dielectric Constants of Zr Silicates: A First-Principles Study. Phys. Rev. Letters. 2002;89(11):117601(4).

Sawyer R, Nesbitt HW, Bancroft GM, Thibault Y, Secco RA. Spectroscopic studies of oxygen speciation in potassium silicate glasses and melts. Canadian Journal of Chemistry. 2015;93 (1):60–73.

Siegbahn K. Electron spectroscopy-an outlook. Journal of Electron Spectroscopy and Related Phenomena. 1974;5(1):3–97.

Shchapova YuV, Votyakov SL, Kuznetsov MV, Ivanovsky AL. Influence of Radiation Defects on Electronic Structure of Zircon from X-Ray Photoelectronic Spectroscopy Data. Zh. Strukt. Khimii. 2010;4:687–692.

Votyakov SL, Schapova YuV, Hiller VV, Vinogradova NS, Glavatskikh SP, Porotnikov AV, Galakhova OL, Vovkotrub EG, Strekalovsky VN, Ivanovsky AL, Kuznetsov MV, Ryzhkov MV, Shalaeva EV. Spektroskopiya i fizika monatsita: sostoyanie i perspektivy ispol'zovaniya v reshenii geokhronologicheskikh problem Urala. Litosfera. 2012;4:158–172. [Votyakov SL, Schapova YuV, Hiller VV, Vinogradova NS, Glavatskikh SP, Porotnikov AV, Galakhova OL, Vovkotrub EG, Strekalovsky VN, Ivanovsky AL, Kuznetsov MV, Ryzhkov MV, Shalaeva EV. Spectroscopy and physics of monazite: state and prospects of use in solving the geochronological problems of the Urals. Litosfera. 2012;4:158–172. (In Russ.)].

Zakaznova-Herzog VP, Nesbitt HW, Bancroft GM, Tse JS, Gao X, Skinner W. High-resolution valence-band XPS spectra of the nonconductors quartz and olivine. Physical review B. 2005;72:205113.

Zakaznova-Herzog VP, Nesbitt HW, Bancroft GM, Tse JS. High resolution core and valence band XPS spectra of non-conductor pyroxenes. Surf Sci. 2006;600:3175–3186.

Zakaznova-Herzog VP, Nesbitt HW, Bancroft GM, Tse JS. Characterization of Leached Layers on Olivine and Pyroxenes Using High-Resolution XPS and Density Functional Calculation. Geochimica and Cosmochimica Acta. 2008;72:69–86.

Zatsepin AF, Kortov VS, Shchapova YuV. Electronic structure of phosphate glasses with a complex oxygen sublattice structure. Phys. Solid State. 1997;39(8):1212–1217.

Zeug M, Nasdala L, Wanthanachaisaeng B, Balmer WA, Corfu F, Wildner M. Blue Zircon from Ratanakiri, Cambodia. The journal of gemmology. 2018;36(2):112–132.

Zigban K, Nordling K, Falman A. i dr. Electronnaya spektroskopiya. M.: Mir, 1971. 495 p. [Siegbahn K, Nordling K, Fahlman A. et al. Electron spectroscopy. Moscow: Mir. 1971. 495 p. (In Russ.)].

Mineral Composition of the Zun-Torey Lake (Eastern Siberia) Bottom Sediments Studied by X-Ray Diffraction

Roman V. Smelyy, Ekaterina V. Kaneva, Anastasia V. Oshchepkova, Tatiana S. Aisueva, and Aleksandr L. Finkelstein

Abstract

Three methods for determining the mineral and mineral-group content in carbonate-silicate bottom sediments are compared. Two methods are based on the powder X-ray diffraction. The first one uses the processing of diffraction patterns by the Rietveld method. The second one relies on the method of reference intensity ratios (corundum ratios). The third method is based on physical and chemical modeling with the use of data on the elemental composition obtained by XRF and XRD. Thirty core samples of bottom sediments of the Zun-Torey Lake (Eastern Siberia) were analyzed. The contents of the mineral groups (feldspars, quartz, phyllosilicates, carbonates) varied in the range of about 10–40 wt%. The differences between the results obtained by three methods had a standard deviation in the range of 2–9 wt%. The relative standard deviation, as a rule, was less than 30%, therefore such analyses can be considered quantitative. The obtained data has allowed us to estimate the X-ray powder analysis error when determining the content of mineral groups in carbonate-silicate sedimentary rocks in the absence of reference materials.

Keywords

Quantitative XRD · Bottom sediments · Zun-Torey lake

R. V. Smelyy (✉) · E. V. Kaneva · A. V. Oshchepkova · T. S. Aisueva · A. L. Finkelstein
Vinogradov Institute of Geochemistry SB RAS, 1A Favorsky str., 664033 Irkutsk, Russia
e-mail: srv47@yandex.ru

S. Votyakov et al. (eds.), *Minerals: Structure, Properties, Methods of Investigation*,
Springer Proceedings in Earth and Environmental Sciences,
https://doi.org/10.1007/978-3-030-49468-1_30

1 Introduction

The bottom sediments of continental lakes serve as the "natural archives". They provide information on changes in the sedimentation regime associated with changes in the natural environment and climate in the past. The study of sediments of Eastern Siberian lakes for paleoclimatic reconstructions of continental regions is of particular interest. The indicators of changes in the sedimentation regime can be mineral groups such as carbonate minerals, quartz, clay minerals, phyllosilicates, feldspars and some others.

The mineral composition of sediments is determined, as a rule, by an X-ray diffraction method. Quantitative determination of the mineral composition of sedimentary rocks by X-ray diffraction is a significantly more complex task. The reasons include the uncertainty of identification of individual minerals that are included in mineral groups (clay minerals, carbonate minerals, feldspars, and others), and the absence of reference materials of sedimentary rocks with the certified mineral composition. The error in determining the mineral composition remains, as a rule, unknown, despite the fact that the error of the X-ray diffraction method established in the interlaboratory experiment for artificial mixtures of well-characterized minerals may be less than 3%.

The aim of this work is to compare various methods for determining the mineral composition of carbonate-silicate lake sediments. The study was performed using an X-ray diffraction analysis by the Rietveld method and the method of reference intensity ratio (RIR, corundum ratios). To compare the results, a calculation analysis (physical and chemical modelling) based on elemental composition data was also applied.

2 Materials and Methods

The object of this study is the bottom sediments of the Zun-Torey lake, located within the Torey Basin in the south of Eastern Siberia and included in the Lake Torey system. Zun-Torey is a salt lake without drainage. The water surface of the lake is 302 km^2, the depth is about 7 m. A core with a diameter of 6–8 cm and a length of 94 cm was selected by a drum-type gravity corer and divided into parts with a step of 1 cm. Each centimeter of the core was distributed among various methods of analysis.

The mineralogical composition of the core sediment was determined by X-ray diffraction, and the quantitative determination of the identified phases in the powder sample was performed. Powder X-ray diffraction data were obtained using a D8 ADVANCE diffractometer (Bruker) equipped with a scintillation detector and a Göbel mirror. The radiation source was CuKα. The data were recorded in a step scan mode in the range of diffraction angles 2θ from 3 to 80°. Experimental conditions were as follows: 40 kV, 40 mA, time per step—1 s and step size—0.02° 2θ. Rotation of sample—15 rpm. Samples for measurement were prepared by

packing and leveling the powder in a special cuvette. Data processing was performed using two software packages. The first one, the TOPAS 4 (Bruker 2008), deals with the Rietveld method. The second one, IPS (Yakimov 2009), uses the method of reference intensity ratio (RIR) and the optimization of the model powder patterns of the X-ray phase reference materials from PDF-2 database and the element balance equations with regularized least squares.

The determination of the content of the main rock-forming elements was performed on an S8 Tiger wavelength dispersion X-ray fluorescence spectrometer (Bruker AXS). The physical and chemical modeling (PCM) was performed using the "Selector" software (Chudnenko 2010).

3 Results and Discussion

The following phases were identified in the samples of the Zun-Torey lake bottom sediments (the number in the PDF database (ICDD Products) is indicated in parentheses): quartz SiO_2 (86–1560); carbonates: dolomite $Ca(Mg,Fe)(CO_3)_2$ (34–517), ankerite $Ca(Fe,Mg)(CO_3)_2$ (84–2066, 84–2067), calcite $CaCO_3$ (72–1651, 86–2336); feldspars: anorthoclase $(Na,K)(Si_3Al)O_8$ (9–478), albite $NaAlSi_3O_8$ (9–466); phyllosilicates: illite $KAl_2(Si_3Al)O_{10}(OH)_2$ (9–343, 29–1496, 43–685), clinochlore $(Mg,Fe)_6(Si,Al)_4O_{10}(OH)_8$ (29–701) and palygorskite $Mg_5(Si_4O_{10})_2(OH)_2(H_2O)_8$ (88–1951).

The results of calculations of the dependence of the mineral group content on the core depth using three methods mentioned (TOPAS 4 and IPS software as well as the physical and chemical modeling based on elemental composition), demonstrate a satisfactory agreement of the behavior of the dependence of the quartz, carbonates and feldspar content on the depth (Figs. 1, 2 and 3). Figures show that the mineral content varies by a factor of 3–5 depending on the core depth. The mineral contents

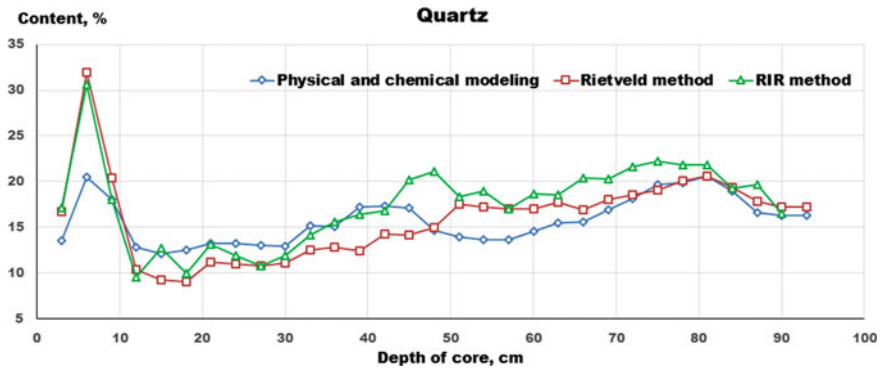

Fig. 1 The distribution of the content of quartz over the core depth

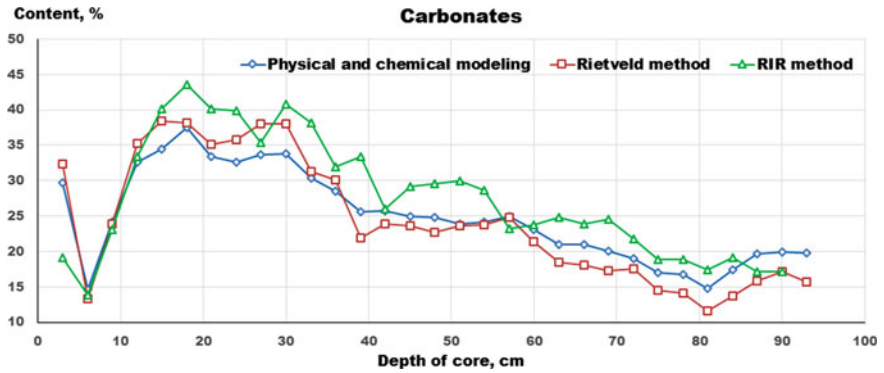

Fig. 2 The distribution of the content of carbonate minerals over the core depth

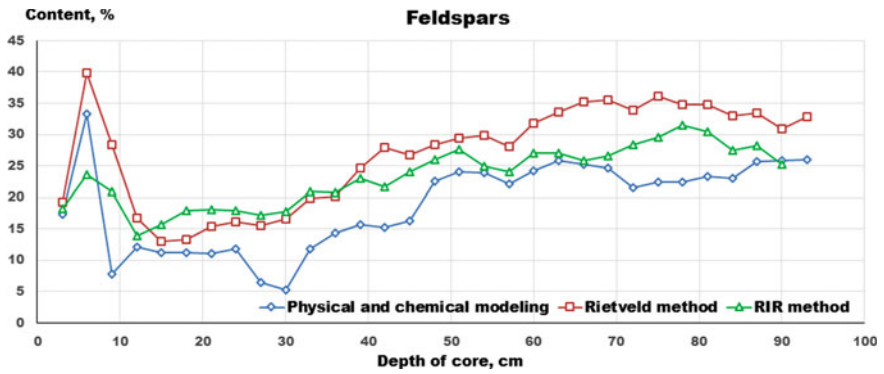

Fig. 3 The distribution of the content of feldspars over the core depth

are significantly more sensitive to changes in the environmental conditions of the catchment area and are obviously the preferred marker for their changes (Fig. 2).

The discrepancy between the results of the content determination is greater for feldspar than for quartz and carbonates. Feldspar identification is a difficult task due to the frequently present isomorphic impurities, changing the ordering of the Al and Si cation positions in plagioclase, and the superposition of quartz peaks.

As expected, the greatest discrepancy between the definitions is observed for phyllosilicates (Fig. 4). The routine for processing the results of X-ray diffraction analysis of phyllosilicates, especially clay minerals, is a complex task and requires the use of special sample preparation procedures and a specialized mathematical apparatus (Solotchina 2009).

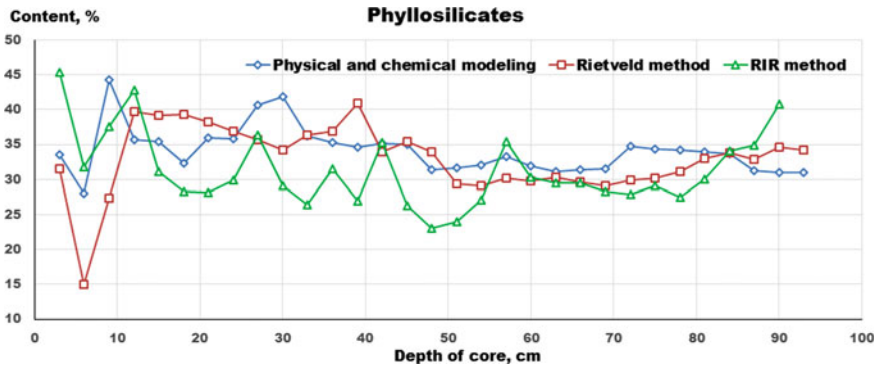

Fig. 4 The distribution of the content of phyllosilicates over the core depth

Standard deviations (SD) and relative standard deviations (RSD) for the three methods used for determining the mineral composition are given in Table 1. The table also shows the average content of mineral groups (Av. cont.). Based on the above data, it is difficult to give preference to any of the considered methods for assessing the mineral composition. The standard deviation between the determination of the quartz and carbonate content is 2–5 wt%, for feldspars and phyllosilicates it is slightly greater—5–9 wt% with variations in the range of 10–40 wt%. The relative standard deviation of the results of determination for most pairs of methods is less than 30%. Such determinations should be considered quantitative. A relative standard deviation of more than 30% is observed between the results of X-ray diffraction and physical and chemical analysis for the feldspar analysis. It corresponds only to an approximate-quantitative determination.

As a result, it could be noted that the three considered methods for determining the mineral composition are not completely independent. The same experimental data, but different computational algorithms and processing procedures for diffraction patterns are used in methods based on the measurement of X-ray diffraction (TOPAS 4 (Bruker 2008), IPS (Yakimov 2009)). In the method based on physical and chemical modeling, the data on the qualitative mineral composition obtained by X-ray powder diffraction are used together with the data of elemental X-ray fluorescence analysis. In addition, the variations in the content of some elements have a pronounced correlation with variations in the content of mineral groups. In general, in the absence of an alternative method for estimating the error, the data obtained allow the error of the X-ray powder analysis in determining the mineral group content in carbonate-silicate sedimentary rocks to be estimated.

Table 1 The standard deviation between the three methods of mineral composition determination

Pairs of methods to estimate mineral composition	Quartz Av. cont.—16 wt%		Carbonates Av. cont.—25 wt%		Feldspars Av. cont.—23 wt%		Phyllosilicates Av. cont.—33 wt%	
	SD, wt%	RSD	SD, wt%	RSD	SD, wt%	RSD	SD, wt%	RSD
TOPAS 4—PCM	3.1	19%	2.6	11%	9.0	33%	5.2	16%
IPS—PCM	2.8	18%	4.4	18%	6.3	33%	6.0	18%
TOPAS 4—IPS	2.2	12%	5.0	20%	5.7	21%	6.0	18%

4 Conclusions

The obtained data allow us to estimate the error of X-ray powder diffraction analysis in determining the content of mineral groups in carbonate-silicate sedimentary rocks in the absence of reference samples with a certified mineral composition. Therefore, an alternative possibility is proposed for estimating this error. The error estimation in determining the mineral composition is important for paleoclimatic reconstructions based on the results of the analysis of lake sediments. Such mineral species as quartz and carbonate minerals in lake carbonate-silicate sediments can be determined with an accuracy of 2–5 wt%. The content of feldspar and phyllosilicates can be determined with an accuracy of 6–9%. It should also be noted that the method of physical and chemical modeling provides satisfactory estimates of the mineral group content, based on XRF data.

Acknowledgements The study was performed using the equipment at the "Isotopic-geochemistry investigation centre" of Collective Use Center of A.P. Vinogradov Institute of Geochemistry SB RAS.

References

Bruker AXS. Topas V4: General profile and structure analysis software for powder diffraction data (User's Manual, Bruker AXS, Karlsruhe, Germany). 2008.

Chudnenko KV. Thermodynamic modeling in geochemistry: theory, algorithms, software, applications. Academy Publishing "Geo". Novosibirsk. 2010. (In Russ).

ICDD Products, http://www.icdd.com/products/.

Solotchina EP. Structural typomorphism of clay minerals of sedimentary sections and cores. Academy Publishing "Geo", Novosibirsk. 2009. (In Russ).

Yakimov IS, Dubinin PS, Piksina OE. Regularization of the Reference Intensity Ratio method for X-ray quantitative phase analysis of powders. J. SibFU. Chemistry 1. 2009; 2:71–80. (in Russ.). http://elib.sfu-kras.ru/handle/2311/1302.

Crystal Chemical Features and Color Nature of Sapphire from the Naryn-Gol Deposit (Buryatia)

Vasilina F. Sotnikova, Anatoliy G. Nikolaev, Evgeny V. Kislov, Vladislav V. Vanteev, and Anna V. Aseeva

Abstract

This paper is devoted to the studies of the crystal chemical characteristics and color nature of sapphires from the Naryn-Gol deposit (Republic of Buryatia, Russia). A brief geological description of the sapphire occurrence and the results of $\delta^{18}O$ isotope analysis are presented, which have shown a magmatic genesis of these sapphires. The color of sapphires is associated with the ions of ferric and ferrous iron, which is isomorphically replaced by Al^{3+} ions in the structure of corundum. It has been found that blue and green sapphires have different color centers, which were formed under different conditions of mineral formation. Studies of the color of sapphires in polarized light have been carried out and the features of absorption depending on the crystallographic direction in crystals have been shown. The calculation of chromaticity coordinates was carried out using the International Commission on Illumination CIE—1931.

V. F. Sotnikova (✉) · A. G. Nikolaev
Kazan (Volga Region) Federal University, 18 Kremlyovskaya str., Kazan, Russia
e-mail: vasilina0917@gmail.com

E. V. Kislov · V. V. Vanteev
Geological Institute of the Siberian Branch of the Russian Academy of Sciences, 6a Sakhyanovoy str., Ulan-Ude, Russia
e-mail: evg-kislov@ya.ru

E. V. Kislov · V. V. Vanteev
Buryat State University, 24a Smolina str., Ulan-Ude, Russia

A. V. Aseeva
Far East Geological Institute of FEB RAS, 159 Pr-t 100-Letiya Vladivostoka, Vladivostok, Russia
e-mail: aseeva@fegi.ru

S. Votyakov et al. (eds.), *Minerals: Structure, Properties, Methods of Investigation*, Springer Proceedings in Earth and Environmental Sciences,
https://doi.org/10.1007/978-3-030-49468-1_31

Keywords

Sapphires · Optical spectroscopy · Coloring of minerals · Gemology

1 Introduction

The purpose of this work is to study the nature of the color of sapphires from the Naryn-Gol deposit.

Sapphire is included in the group of jewelry stones, it has a bright deep blue color and high hardness. This variety belongs to the corundum mineral species. Corundum is a trigonal modification of α-Al_2O_3 crystalline alumina. Common impurities are Cr, Fe, Ti, Mn, Ni, V, etc. The crystal structure of corundum is a dense hexagonal packing of O^{2-} anions, in which two thirds of the octahedral voids are occupied by Al^{3+} ions. The octahedral layers are arranged in such a way that two filled octahedrons and one empty one (Platonov et al. 1984) alternate in the chains of octahedra stretched along the C axis.

The deposits of noble corundum are diverse in origin. Magmatic (in alkaline basalts and lamprophyres), contact-metasomatic (endoskarns in marbles and plagioclasite in mafic-ultramafites), metamorphogenic and placer deposits are distinguished. The main role in the extraction of jewelry rubies and sapphires belongs to eluvial (residual), eluvial-deluvial (slope) and alluvial placers, formed due to magmatic and contact-metasomatic indigenous sources (Kievlenko 2001).

2 Materials and Methods

Sapphires for research were selected from alluvial deposits of the Naryn-Gol river. Geologically, this territory is represented by metamorphosed sedimentary rocks of the Upper Ordovician Dzhida Formation (O_3Dz) and effusive formations consisting of lava flows and covers volcanic rocks of Neogene-Quaternary age β_{alt} (βN_2-Q_1). Holocene-Quaternary alluvial-deluvial deposits (Q) are the most widespread in the study area (Fig. 1) (Aseeva et al. 2018).

The study of the isotopic composition of megacryst has shown that the content of $\delta^{18}O$ for corundum and other minerals of the megacryst association varies within narrow limits of +4.6–+6.4‰ (Fig. 2). As shown in (Giuliani et al. 2007; Vysotskiy et al. 2015), according to the isotope characteristics of corundum, it is possible to determine their genetic identity. Thus, metamorphic minerals are located in the field of negative $\delta^{18}O$ values relative to SMOW, while $\delta^{18}O$ in corundums of hydrothermal origin varies from ~+8 to +19‰. The points obtained for Naryn-Gol corundum fall in the field of igneous rocks (Fig. 2).

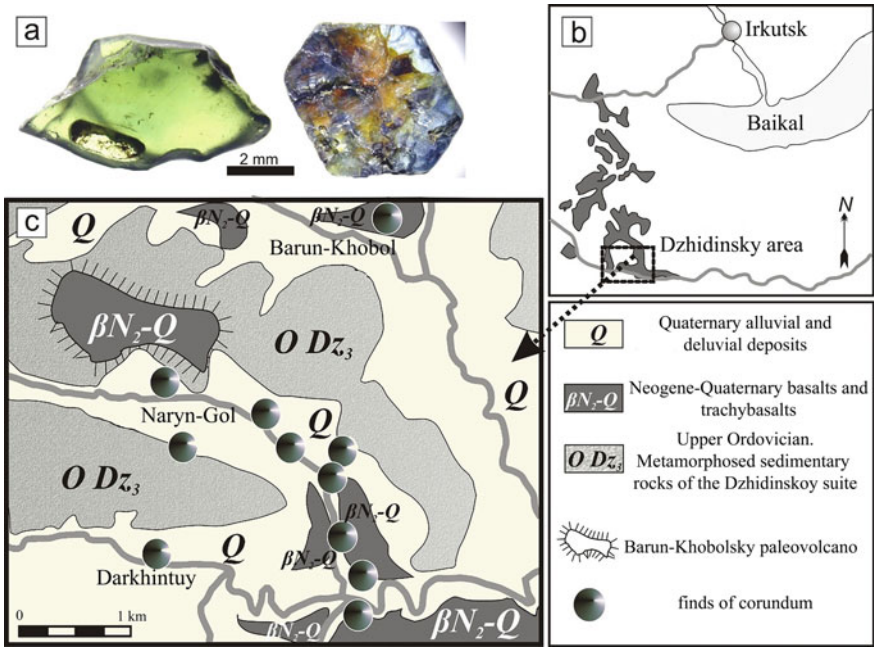

Fig. 1 **a**—Naryn-Gol corundum, **b**—layout of the Dzhida volcanic field, **c**—geological structure of the Naryn-Gol section

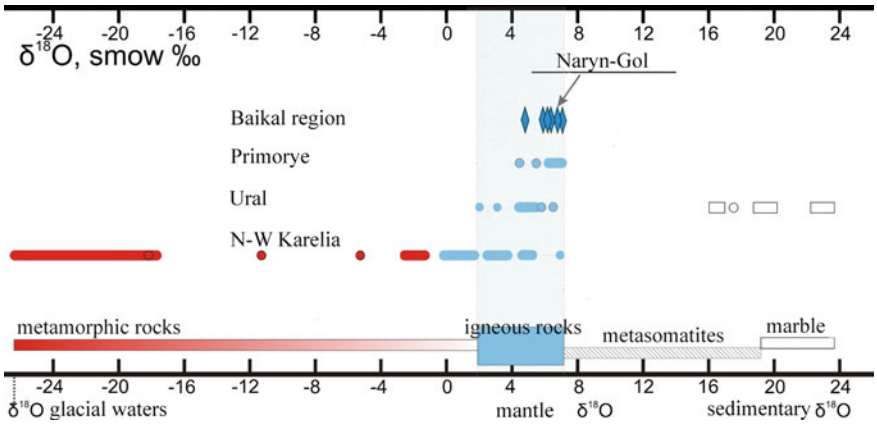

Fig. 2 Oxygen isotopic ratios in corundum of various genesis

The main research method in this paper is optical absorption spectroscopy. Optical absorption spectra were recorded on a specialized SHIMADZU UV-3600 spectrophotometer in the wavelength range of 185–3300 nm.

Additionally, optical absorption spectra of sapphires were obtained using a standardized MSFU-K spectrophotometer in the wavelength range of 400–800 nm with a step of 1 nm. The calculation of chromaticity coordinates using the XYZ international colorimetric system was used for an objective measurement and description of the sapphire color. Colorimetric results on the interpretation of the optical absorption spectra were placed on the standard color triangle (CIE—1931). Specialized Spectrum software was used for the calculation of colorimetric parameters of the studied sapphires (x, y, z chromaticity coefficients; λ wavelength, p density, L the brightness of the main color tone) with D65 light source taken as the basis for the calculations. Optical absorption spectra were recorded from sapphire plane-parallel preparations in ordinary and polarized light at room temperature.

3 Results and Discussion

In the visible range, several types of different groups of absorption bands are observed. According to the results of analyses of the optical absorption spectra of sapphires, they were divided into two different groups. One group of sapphires has a green color with a blue tint, and the second group has a bright blue color. The color is often zonal, sometimes spotted. The main impurity element in corundum is iron, its content varies from 0.61 to 1.93 wt% (Aseeva et al. 2018).

The optical absorption spectra of the first group have absorption lines at wavelengths of 455 and 575 nm (Fig. 3). When interpreting the nature of the absorption band at a wavelength of 455 nm, electronic transitions were calculated using the Tanabe-Sugano diagram of the configuration of the d^5 system ions in the octahedral field for Fe^{3+}.

The results of the analysis have shown that this absorption band at a wavelength of 455 nm is associated with the spin-forbidden transition $^6A_1 \rightarrow {}^4A_1,{}^4E$ (^4G) in the electron d-shell of Fe^{3+} ions (Burns 1993; Platonov et al. 1984). In the region of 575 nm, a broad intense absorption band is observed, which changes the intensity from the direction of polarized light, and in this case, this absorption band is associated with the charge transfer mechanism, which has the nature of Fe^{3+}–Fe^{3+}. This line has an absorption maximum when light is polarized along the C axis, which does not contradict the earlier studies on the color of sapphires (Platonov et al. 1984).

The optical absorption spectra of the second group have similar in nature absorption lines at wavelengths of 455 and 586 nm. The difference from the first group of spectra, in this group, the long-wavelength part of the spectrum has a sharp rise in the near infrared region and has a maximum at a wavelength of 874 nm (Fig. 4). According to the literature analysis, the absorption line at a wavelength of

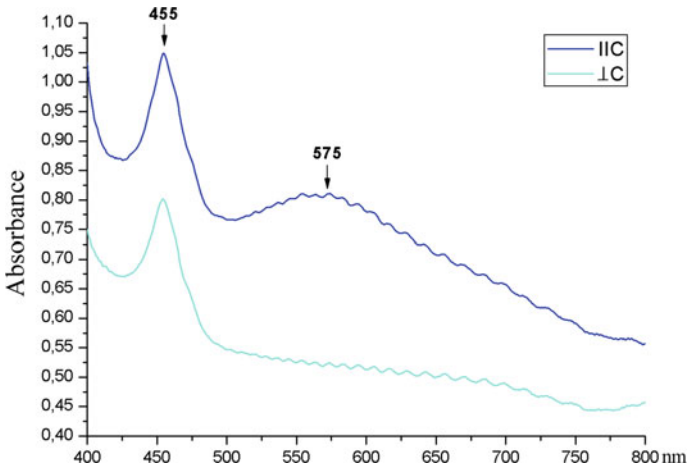

Fig. 3 Optical absorption spectra of green sapphires with a blue tint in the visible region

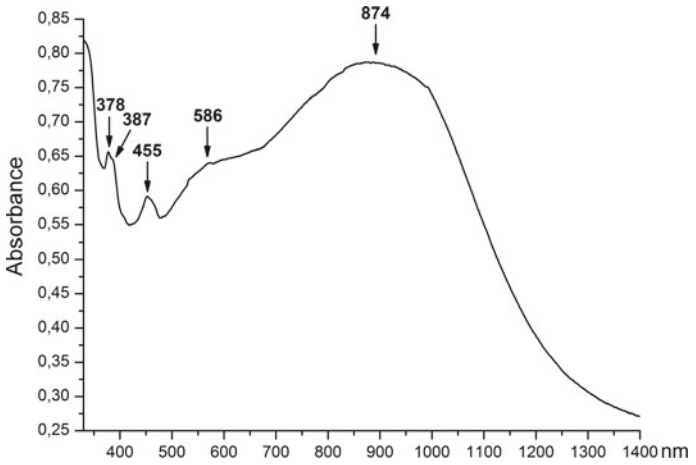

Fig. 4 Optical absorption spectra of blue sapphires in the UV-Vis-NIR region

874 nm in sapphires is associated with the Fe^{2+}–Fe^{3+} charge transfer mechanism; it can be concluded from this that the bright blue color in sapphires of this type is associated with the appearance of Fe^{2+} ions in the corundum structure.

Additionally, in the UV region, the absorption bands at the wavelengths of 378 and 387 nm, formed due to spin-forbidden transitions $^6A_1 \rightarrow {}^4A_2, {}^4E$ (D), which are also associated with Fe^{3+} ions, have been detected (Burns 1993). Calculations of the Racah parameter (B) have shown that the value for the energy of electronic

transitions at 378, 387 and 455 nm is the same and is 686 cm^{-1}, which indicates that these absorption bands belong to the same optically active center. The point symmetry of Al^{3+} ions in corundum is close to $C_3\nu$, which leads to the splitting of the electronic transition of optically active centers in the form of broadening of the absorption bands (Platonov et al. 1984).

According to the results of interpretation of the optical absorption spectra of sapphire crystals, the chromaticity coordinates were calculated using the International colorimetric system CIE—1931. The dominant wavelength of the main color tone was $\lambda = 477.5-572.9$ nm, and the saturation value of the main color tone changed within 15.11–41.78%.

4 Conclusions

As a result of the research, it has been found that the color of sapphires from the Naryn-Gol deposit is associated with ions of ferric and ferrous iron. Fe ions isomorphically replace Al^{3+} ions in the corundum crystal structure. The color of green sapphires with blue hues is associated with the optical centers Fe^{3+} and Fe^{3+}–Fe^{3+}. In blue sapphire, in addition to the centers described above, there are also exchange-coupled pairs of Fe^{2+}–Fe^{3+}. From this we can conclude that the formation of blue sapphires occurred under more reducing conditions, while under more oxidative conditions of mineral formation Fe ions were oxidized to the trivalent state, which led to the formation of an intense green tint in sapphires.

Acknowledgements This study was made in the context of the Russian Government Program of Competitive Growth of Kazan Federal University and state task of Geological Institute SB RAS No. AAAA-A17-117011650012-7.

References

Aseeva AV, Kislov EV, Vysotsky SV, Velivetskaya TA, Ignatiev AV. Sapfiry Naryn-Gol (Dzhidinskoye vulkanicheskoye pole, Buryatiya): mineral'nyye assotsiatsii i izotopnyye kharakteristiki. V Vserossiyskaya nauchno-prakticheskaya konferentsiya, posvyashchennoy 45-letiyu Geologicheskogo instituta SO RAN, August 27–31, 2018, Ulan-Ude, Rossiya, ss. 34–36. [Aseeva AV, Kislov EV, Vysotsky SV, Velivetskaya TA, Ignatiev AV. Sapphires of Naryn-Gol (Dzhidinsky volcanic field, Buryatia): mineral associations and isotopic characteristics. V All-Russian Scientific and Practical Conference dedicated to the 45th anniversary of the Geological Institute of the SB RAS, August 27–31, 2018, Ulan-Ude, Russia, pp. 34–36. (In Russ.)]

Burns RG. Mineralogical Applications of Crystal Field Theory. Cambridge: Cambridge University Press; 1993.

Giuliani G, Ohnenstetter D, Garnier V, Fallick AE, Rakotondrazafy F, Schwarz D. The geology and genesis of gemcorundum deposits. In: Groat A, Editor. Geology of Gem Deposits. Mineralogical Association of Canada. Quebec: Mineralogical Association of Canada; 2007. P. 23–78.

Kievlenko EY. Geologiya samotsvetov. M.: Zemly; 2001. [Kievlenko EY. Geology of gems. M.: Zemly; 2001. (In Russ.)]

Platonov AN, Taran MN, Balitsky VS. Priroda okraski samotsvetov. M.: Nedra; 1984. [Platonov AN, Taran MN, Balitsky VS. The nature of the gem coloring. M.: Nedra; 1984. (In Russ.)]

Vysotskiy SV, Nechaev VP, Kissin AY, Yakovenko VV, Ignat'ev AV, Velivetskaya TA, Sutherland FL, Agoshkov AI. Oxygen isotopic composition as an indicator of ruby and sapphire origin: a review of Russian occurrences. Ore Geol Rev. 2015;68:164–170.

BHVO-2, AGV-2 and BCR-2 Certified Reference Materials in the Method Validation for Zinc Stable Isotope Analysis of Environmental Samples

Maria V. Streletskaya, Maria V. Chervyakovskaya, Tatyana G. Okuneva, and Daria V. Kiseleva

Abstract

The intense growth in the number of studies aimed at assessing the contribution of natural and anthropogenic sources of pollution suggests Zn isotope analysis to be promising for identifying sources and pathways of environmental pollution. The method for zinc stable isotope analysis including the chromatographic purification stage and multicollector ICP-MS measurements using the standard-sample bracketing (SSB) technique is described in detail. The procedure validation, as well as the assessment of its performance characteristics (accuracy and precision) for the analysis of environmental samples, was performed using BHVO-2, BCR-2 and AGV-2 USGS certified reference materials. The method described combines both high accuracy and simple implementation demonstrating good agreement with reported data from other laboratories.

Keywords

Zinc stable isotopes · MC ICP-MS · CRM · Environmental samples

M. V. Streletskaya (✉) · M. V. Chervyakovskaya · T. G. Okuneva · D. V. Kiseleva
A.N. Zavaritsky Institute of Geology and Geochemistry UB RAS, 15 Vonsovskogo Street, 620016 Ekaterinburg, Russia
e-mail: isotop-igg@mail.ru

S. Votyakov et al. (eds.), *Minerals: Structure, Properties, Methods of Investigation*, Springer Proceedings in Earth and Environmental Sciences,
https://doi.org/10.1007/978-3-030-49468-1_32

1 Introduction

Recently, the number of studies aimed at assessing the contribution of natural and anthropogenic sources of pollution has grown intensively (Vasic et al. 2012; Grebenshchikova et al. 2017; Gustaytis et al. 2018). The sources of trace elements and metalloids in atmospheric emissions are associated not only with natural processes, such as rock weathering, mineralization and dust storms, but also with industrial activities, i.e. smelting, metal processing and other technological processes. Large volumes of smelting activities cause significant spatial and temporal variability in the concentrations of heavy metals in the lower atmosphere (Melaku et al. 2008). In this regard, Zn isotopes appear to be promising for identifying the sources and pathways of the environmental pollution. However, the data on the δ^{66}Zn values in liquid and solid precipitation forms turn out to be strongly insufficient (Novák et al. 2016; Voldřichová et al. 2014), especially when the Urals region is considered. Moreover, the potential for determining zinc isotope variations in environmental studies is more than obvious.

The first measurements of zinc isotope composition were performed by thermal ionization mass-spectrometry (TIMS) (Moynier et al. 2017). This method is recognized as quite suitable for measuring isotopes, predominantly in combination with the double spike technique. However, most studies on zinc isotope measurements consider the inductively coupled plasma ionization in combination with bracketing or double spike technique as the most applicable method of isotopic analysis. Moreover, in this case, the mass bias correction is viable using the method of internal normalization with copper as an internal standard.

In zinc isotope measurements, both the method of accounting for mass bias and the quality of preliminary sample preparation have a direct impact on the precision of the analytical procedure. The basic sample preparation requirements include a high degree of purification and a high quantitative yield of the target element, as well as a low blank value as compared to the zinc content in the sample. This procedure usually consists in chromatographic separation of pure analyte fractions on ion-exchange resins in one or several stages (repeated purification) (Borrok et al. 2007; Dirks et al. 2010; Maréchal et al. 1999; Marechal and Albarede 2002). Additionally, possible interferences, in particular ^{64}Ni, are necessary to be monitored during mass spectrometric measurements.

The aim of this study includes the refinement and validation of the method for measuring zinc stable isotope ratios covering the whole analytical process from the sample digestion to MC ICP-MS measurements. For this reason, as well as to assess the suitability of the methodology for the analysis of similar environmental samples, Zn isotope analysis of BHVO-2, BCR-2 and AGV-2 USGS certified reference materials was performed.

2 Materials and Methods

2.1 Reagents and Certified Reference Materials

All chemical preparation procedures were performed in cleanrooms (class 1,000) and laminar boxes (class 100) of the Zavaritsky Institute of Geology and Geochemistry, Ekaterinburg, Russia. ACS grade acids (HCl, HNO_3 and HF) were additionally purified twice using sub-boiling distillation systems (Savillex, USA; Berghof, Germany). Deionized water (18.2 $M\Omega cm^{-1}$) was obtained from Arium®pro unit (Sartorius, Germany). All the labware and materials contacting the reagents and samples were made of PFA (Savillex, USA) or PTFE (Nalgene, USA). Prior to the analysis, extra cleaning was applied to columns, pipette tips and PFA vials (Savillex®). The pipette tips and columns were washed with HCl:H_2O (1:1) on a hotplate overnight and then rinsed with deionized water. The vials were pre-cleaned by boiling in 1:3 mixture of HNO_3 and HCl overnight with subsequent boiling in deionized water. JMC-Lyon Zn isotopic reference solution was used for the standard-sample bracketing (SSB) technique. The multi-element calibration Standard No. 2 (Perkin Elmer, USA) containing 31 elements, including Zn, was used for the column calibration procedure. USGS BHVO-2 and BCR-2 basalts and AGV-2 andesite certified reference materials were applied for the validation of analytical procedure, including sample digestion, chromatographic separation and isotopic measurements.

2.2 Sample Digestion

CRM replicates of 0.01 g (2 samples in replicate) were sampled in PFA vials, admixed with 3 mL HNO_3 and 1 mL HF (both concentrated). The vials were screwed up and left in the drying furnace at 120 °C for 3 days. After evaporating to dryness, a mixture of 1 mL HNO_3 and 3 mL HCl (concentrated) was added and one more evaporation was performed. Then the residue was re-dissolved in 4 mL of concentrated HCl and dried. After the dissoluton in 0.5 mL of 10 M HCl, each sample was centrifuged at 6,000 rpm for 15 min.

2.3 Ion Exchange Column Calibration

The modified chromatography technique proposed by (Chapman et al. 2006) was applied for zinc isolation. Bio-Rad AG MP-1 resin (100–200 mesh) was loaded into pre-cleaned polypropylene column (Triskem®) fitted with two 35 μm PE frits with the following layer configuration: D = 0.7 cm, h = 4 cm, V = 1.6 mL. Figure 1 demonstrates the scheme of Zn elution.

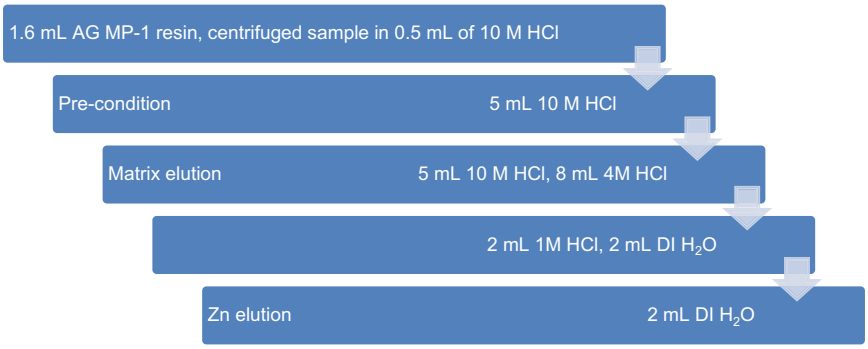

Fig. 1 The scheme of Zn chromatographic separation using Bio-Rad AG MP-1 resin

The extraction protocol included 5 mL of 10 M HCl as a resin pre-condition followed by matrix elution sequentially in 11 mL of 10 M HCl, 5 mL of 1 M HCl and 2 mL of deionized water. After that, Zn was eluted in 2 mL of deionized water. Considering the fact that Zn concentrations in pure fractions were sufficient to assure the ion beam stability and satisfactory precision of isotopic ratios, the elution of zinc was followed by adding concentrated HNO_3 in order to obtain the HNO_3 concentration in final solution equal to 3%. The recovery of Zn was assessed by measuring Zn concentrations in multi-element calibration standard through the elution curve plotting. A NexION 300S (Perkin Elmer, USA) quadrupole ICP mass-spectrometer was applied for the measurement of elemental concentrations to construct the elution curves.

2.4 Zn Isotope Measurements

Both isotope and elemental concentration measurements were conducted in cleanrooms (class 10,000) of the Zavaritsky Institute of Geology and Geochemistry, Ekaterinburg, Russia. Zinc isotope measurements were carried out using a MC ICP-MS Neptune Plus (Thermo Fisher Scientific). The sample introduction system consisted of a PFA micro-flow nebulizer (50 μL min^{-1}) connected to a quartz spray chamber. Each individual acquisition consisted of 60 ratios collected at 8-second integrations and followed by a 30 s baseline measurement. Blank correction was obtained using 3% HNO_3 solution, with a configuration of 20 cycles with 8 s integration. The main parameters and Faraday cup configuration are provided in Table 1.

The measurement of samples was performed using a standard-sample bracketing technique (SSB) in terms of a mass bias correction. JMC-Lyon Zn isotopic reference solution was used for reporting the sample results in δ-values according to the equation below.

Table 1 Neptune Plus instrumental parameters for Zn isotope measurement

Instrumental parameters		Faraday cup configuration	
Ar cooling	15 L min^{-1}	L3	^{63}Cu
Ar auxiliary	0.9 L min^{-1}	L2	^{64}Zn
Ar sample	1.08 L min^{-1}	L1	^{65}Cu
Nebulizer flow	50 µL min^{-1}	C	^{66}Zn
Torch power	1050 W	H1	^{67}Zn
Sensitivity for ^{64}Zn	7.3 V ppm^{-1}	H2	^{68}Zn

$$\delta^{66}Zn = \left[\frac{\left(^{66}Zn/^{64}Zn\right)_{sample}}{\left(^{66}Zn/^{64}Zn\right)_{JMC-Lyon}} - 1 \right] \times 1000, \text{‰}$$

The measurement results of each CRM were characterized by the standard deviation (2 SD). The expanded method uncertainty, U (k = 2), was calculated as U_{Rw} within-laboratory standard uncertainty combined for all CRMs (RMG 2010; Handbook for calculation 2017).

3 Results and Discussion

3.1 The Column Calibration for Zinc Chromatographic Isolation

The elution curves obtained for multi-element calibration standard using our modified chromatographic technique are presented in Fig. 2. As can be seen from the figure, only Cd (up to 19.7%) is observed in the Zn fraction. However, an additional isotope ratio measurement of Zn has proved this amount of Cd to have no impact on the measured value. Zn yield comprises up to 97% in the collected fraction.

3.2 Accuracy and Precision for Zn Isotope Measurements

Accuracy and precision obtained for CRMs (BHVO-2, BCR-2 and AGV-2) in Zn isotope measurements are reported in Table 2. The results of the current study demonstrated good agreement with the previously published data. The expanded uncertainty of performed methodology was estimated proceeding from the average within-laboratory standard uncertainty obtained to all CRMs and was ±0.1‰ $\delta^{66}Zn$. The precision and accuracy obtained with our analytical procedure have demonstrated that it is appropriate for application in environmental investigations of Zn isotope compositions.

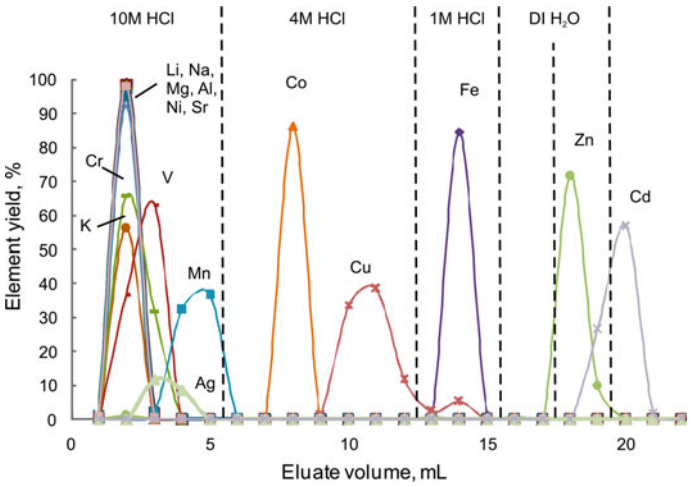

Fig. 2 Multi-element elution curves. The concentrations of Zn and matrix elements (Li, K, Na, Mg, Mn, Al, V, Cr, Ni, Fe, Ag, Sr, Cu, Cd, Co) were obtained for 1.0 mL eluate portions

Table 2 Comparison of geological reference material to $\delta^{66}Zn_{JMC}$ value obtained in this study and reported in the literature

Material	Reference	$\delta^{66}Zn_{JMC}$ (‰)	2 SD
BCR-2	**This study**	**0.24**	**0.06**
	Souto-Oliveira et al. (2019)	0.29	0.07
	Archer and Vance (2004)	0.20	0.09
	Chapman et al. (2006)	0.29	0.12
	Cloquet et al. (2006)	0.32	0.13
	Toutain et al. (2008)	0.26	0.04
	Sonke et al. (2008)	0.25	0.04
	Herzog et al. (2009)	0.33	0.09
	Bigalke et al. (2010)	0.23	0.08
	Moeller et al. (2012)	0.33	0.13
	Sossi et al. (2015)	0.25	0.01
	Araújo (2016)	0.25	0.08
BHVO 2	**This study**	**0.20**	**0.08**
	Souto-Oliveira (2019)	0.33	0.06
	Herzog (2009)	0.29	0.09
	Moeller (2012)	0.48	0.13
	Sossi (2015)	0.27	0.06
	Araújo et al. (2016)	0.25	0.09

(continued)

Table 2 (continued)

Material	Reference	$\delta^{66}Zn_{JMC}$ (‰)	2 SD
AGV 2	**This study**	**0.21**	**0.06**
	Souto-Oliveira (2019)	0.27	0.03
	Moeller et al. (2012)	0.50	0.06
	Araújo et al. (2016)	0.29	0.06

*The number of replicate measurements provided (2 samples in replicate)

4 Conclusions

A modified analytical procedure is presented combining Zn purification and MC ICP-MS isotopic analysis. An application of the procedure to various environmental rock samples has substantiated its robustness and efficiency. This accurate and uncomplicated procedure is characterized by both the yield of chromatographic separation close to 100% and complete elimination of interfering elements. The expanded uncertainty of performed method obtained for all CRMs is ±0.1‰ for $\delta^{66}Zn_{JMC}$. The USGS certified reference materials, namely AGV-2 andesite and BCR-2 and BHVO-2 basalts, used for the accuracy assessment, have demonstrated good agreement with the reported data from other laboratories.

Acknowledgements The work was carried out at the UB RAS "Geoanalitik" Center for Collective Use and supported by RSF grant no. 16-17-10283.

The authors express their deep gratitude to Valery N. Udachin, Doc. Sci. (Geol.-Min.), (Institute of Mineralogy UB RAS, Miass, Russia) for the kindly provided JMC-Lyon Zn isotope reference solution.

References

Vasic MV, Mihailovic A, Kozmidis-Luburic U, Nemes T, Ninkov J, Zeremski-Skoric T, Antic B. Metal Contamination of short-term snow cover near urban crossroads: correlation analysis of metal content and fine particles distribution. Chemosphere. 2012;85:585–592.

Grebenshchikova VI, Efimova NV, Doroshkov AA. Chemical composition of snow and soil in Svirsk city (Irkutsk Region, Pribaikal'e). Environ Earth Sci. 2017;76(20):A712.

Gustaytis MA, Myagkaya IN, Chumbaev AS. Hg in snow cover and snowmelt waters in high-sulfide tailing regions (Ursk tailing dump site, Kemerovo region, Russia). Chemosphere. 2018;202:446–459.

Melaku S, Morris V, Raghavan D, Hosten C. Seasonal Variation of Heavy Metals in Ambient Air and Precipitation at a Single Site in Washington DC. Environ Pollut. 2008;155:88–98.

Novák M, Šípková A, Chrastný V, Štěpánová M, Voldřichová P, Veselovský F, Přechová E, Čuřík J, Farkaš J, Bohdálková L, Pašava J, Míková J, Erbanová L, Bláha V, Komárek A, Krachler M. Cu-Zn isotope constraints on the provenance of air pollution in Central Europe: Using soluble and insoluble particles in snow and rime. Environ Pollut. 2016;218:1135–1146.

Voldřichová P, Chrastný V, Šípková A, Farkaš J, Novák M, Štěpánová M, Krachler M, Veselovský F, Bláha V, Přechová E, Komárek A, Bohdálková L, Čuřík J, Míková J, Erbanová L, Pacherová P. Zinc isotope systematics in snow and ice accretions in Central European mountains. Chemical Geology. 2014;388:130–141.

Moynier F, Vance D, Fujii T, Savage P. The Isotope Geochemistry of Zinc and Copper. Reviews in Mineralogy & Geochemistry. 2017;82:543–600.

Borrok D, Wanty RB, Ridley WI, Wolf R, Lamothe PJ, Adams M. Separation of copper, iron, and zinc from complex aqueous solutions for isotopic measurement. Chemical Geology. 2007;242:400–414.

Dirks C, Scholten B, Happel S, Zulauf A, Bombard A, Jungclas H. Characterisation of a Cu selective resin and its application to the production of 64Cu. J Radioanal. Nucl. Chem. 2010;28:671–674.

Maréchal C, Télouk P, Albarède F. Precise analysis of copper and zinc isotopic compositions by plasma-source mass spectrometry. Chemical Geology. 1999;156:251–273.

Marechal C, Albarede F. Ion-exchange fractionation of copper and zinc isotopes. Geochimica et Cosmochimica Acta. 2002;66:1499–1509.

Chapman JB, Mason TFD, Weiss DJ, Coles BJ, Wilkinson JJ. Chemical separation and isotopic variations of Cu and Zn from five geological reference materials. Geostand. Geoanal. Res. 2006;30:5–16.

RMG 61-2010 Accuracy, trueness and precision measures of the procedures for quantitative chemical analysis. Methods of evaluation. Moscow: Standardinform, 2013. 58 pp. [In Russ.].

Handbook for calculation of measurement uncertainty in environmental laboratories. Ed. 4. Nordtest NT TR 537, 2017. 51 pp.

Souto-Oliveira CE, Babinski M, Araújo DF, Weiss DJ, Ruiz IR. Multi-isotope approach of Pb, Cu and Zn in urban aerosols and anthropogenic sources improves tracing of the atmospheric pollutant sources in megacities. Atmospheric Environment. 2019;198:427–437.

Archer C, Vance D. Mass discrimination correction in multiple-collector plasma source mass spectrometry: an example using Cu and Zn isotopes. J. Anal. At. Spectrom. 2004;19:656–665.

Cloquet C, Carignan J, Libourel G. Isotopic composition of Zn and Pb atmospheric depositions in an urban/periurban area of northeastern France. Environ. Sci. Technol. 2006;40:6594–6600.

Toutain JP, Sonke J, Munoz M, Nonell A, Polvé M, Viers J, Freydier R, SortinoF, Joron JL, Sumarti S. Evidence for Zn isotopic fractionation at Merapi volcano. Chem. Geol. 2008;253:74–82.

Sonke J, Sivry Y, Viers J, Freydier R, Dejonghe L, Andre L, Dupre B. Historical variations in the isotopic composition of atmospheric zinc deposition from a zinc smelter. Chem. Geol. 2008;252:145–157.

Herzog GF, Moynier F, Albarède F, Berezhnoy AA. Isotopic and elemental abundances of copper and zinc in lunar samples, Zagami, Pele's hairs, and a terrestrial basalt. Geochem. Cosmochim. Acta. 2009;73:5884–5904.

Bigalke M, Weyer S, Kobza J, Wilcke W. Stable Cu and Zn isotope ratios as tracers of sources and transport of Cu and Zn in contaminated soil. Geochem. Cosmochim. Acta. 2010;74:6801–6813.

Moeller K, Schoenberg R, Pedersen RB, Weiss D, Dong S. Calibration of the new certified reference materials ERM-AE633 and ERM-AE647 for copper and IRMM-3702 for zinc isotope amount ratio determinations. Geostand. Geoanal. Res. 2012;36:177–199.

Sossi PA, Halverson GP, Nebel O, Eggins SM. Combined Separation of Cu, Fe and Zn from rock matrices and improved analytical protocols for stable isotope determination. Geostand. Geoanal. Res. 2015;39:129–149.

Araújo D, Boaventura GR, Viers J, Mulholland DS, Weis D, Araújo D, Lima B, Ruiz I, Machado W, Babinski M, Dantas E. Ion exchange chromatography and mass bias correction for accurate and precise Zn isotope ratio measurements in environmental Reference Materials by MC-ICP-MS. J. Braz. Chem. 2016;00:1–11.

Crystal-Chemical Features and Color Nature of Emeralds from the Khench Deposit (Afghanistan)

Valeria I. Tarakanova, Anatoliy G. Nikolaev, and Georgiy A. Yurgenson

Abstract

This paper describes the studies carried out on the crystal-chemical features and nature of the color of emeralds from the Khench deposit (Afghanistan). A brief geological characteristic of the emerald deposit is presented and the geochemical features of the host rocks, in which the veins are located, are shown. The color of emeralds is associated with Cr^{3+}_{VI} ions, which are isomorphic to Al^{3+} ions in the structure of the mineral. Using optical absorption spectra, electronic transitions in Cr^{3+} ions were calculated. Mostly electronic spin transitions that are allowed for $^4T_1(^4F)$ and $^4T_{2g}(^4F)$ spins are responsible for coloring. The studies on the color of emeralds in polarized light and the features of absorption depending on the crystallographic direction in crystals were performed. The calculation of chromaticity coordinates was carried out using the International Commission on Illumination CIE—1931.

Keywords

Emeralds · Optical spectroscopy · Coloring of minerals · Gemology

V. I. Tarakanova (✉) · A. G. Nikolaev
Kazan (Volga Region) Federal University, 18 Kremlyovskaya str., Kazan, Russia
e-mail: valera.tarakanova.2000@mail.ru

G. A. Yurgenson
Institute of Natural Resources, Ecology and Cryology, Siberian Branch of the Russian Academy of Sciences, 16a Nedorezova str., Chita, Russia
e-mail: yurgga@mail.ru

S. Votyakov et al. (eds.), *Minerals: Structure, Properties, Methods of Investigation*, Springer Proceedings in Earth and Environmental Sciences,
https://doi.org/10.1007/978-3-030-49468-1_33

1 Introduction

Emerald is a rare chromium-containing variety of beryl and is found in various industrial and genetic types of deposits. The aim of this work was to study emerald samples by optical absorption spectroscopy, as well as their crystal chemical characteristics and the nature of the color of emeralds from the Khench deposit, which is one of the fragments of the Panjshir emerald zone in Afghanistan. The deposit was studied by one of the authors in 1978–1980 (Yurgenson et al. 1980; Yurgenson and Pasekov 1982).

2 Materials and Methods

Optical spectra of emeralds were recorded on a standardized MSFU-K spectrophotometer. Optical absorption spectra were recorded in the wavelength range of 400–800 nm, with a step of 1 nm. For the objective measurement and description of color of emeralds, the method of calculation of XYZ chromaticity coordinates according to the international colorimetric system was used. All colorimetric results on the interpretation of the optical absorption spectra of minerals were placed on the standard color triangle of the International Commission on Illumination (CIE—1931). Colorimetric parameters of the studied minerals (x, y, z color indices; λ—wavelength, R—density, L—the brightness of the main color tones) were calculated using the specialized Spectrum software. D65 light source was taken as the basis for calculations. Optical absorption spectra were recorded from plane-parallel preparations in ordinary and polarized light. All experimental studies were conducted at room temperature.

The Panjshir emerald zone is located in the suture zone between the Hercynian folded structures and the Central Afghan middle massif. It has a width of 5–10 km and is composed of black shales, quartzites, marbles, rarely metasandstones, probably Paleozoic-Mesozoic, and Cretaceous broken biotite gabbro-diorites, diorites and monzodiorites. Beryllium, rare-earth and copper mineralization is associated with the introduction of small intrusions of Myocene alkaline-earth-sodium syenites and quartz porphyres of Alpine activation. Emeralds are confined to the ankerite-quartz veins and zones of quartzified schistosity in black shales or to the marble contact zones with dikes, monzodiorites, diorites and gabbro-diorites. Areas of contact alterations contain phlogopite, albite, tourmaline, fuchsite and pyrite. Some emeralds are found in stockwork veinlets, which cut the metasomatically altered gabbro and metadolomites. Schists, marbles and gabbro-diorite hosting emerald-bearing veins of the Khench deposit are enriched in chromium and beryllium and sometimes tantalum (Table 1).

Table 1 The range of beryllium, chromium and tantalum content in the hydrothermally altered host rocks

Rock	Number of samples	Content limits, %		
		Be	Cr	Ta
Schists	4	0.0003–0.01	0.003–0.021	Up to 0.003
Marbles	4	0.0003–0.1	0.005–0.019	Up to 0.003
Gabbro-diorites	3	0.0008–0.39	0.006–0.018	Up to 0.003

The emeralds from the Khench deposit contain 0.247–1.453% Cr_2O_3 and 0.025–0.433% V_2O_3 according to the data of 29 analyses.

Beryl is an annular silicate of beryllium and aluminum $Be_3Al_2[Si_6O_{18}]$, the structure of which consists of $[Si_6O_{18}]^{12-}$ rings connected through Be and Al atoms. The rings form columns elongated along the axis of the sixth order, connected by beryllium-oxygen tetrahedra and aluminum-oxygen octahedra (Kornilov and Solodova 1987).

A characteristic feature of the mineral structure is the presence of sufficiently capacious cavities—channels, which explain the possibility of a wide manifestation of heterovalent isomorphism with the entry of compensator ions. The channels are large enough to accommodate water molecules, large alkaline and alkaline earth cations. The structure of beryl is characterized by partial substitution of Be^{2+} atoms by Li^+ and Mg^{2+}. Al^{3+} ions in octahedral positions of the structure are also subject to isomorphism, which can be replaced by three- and divalent cations: $Al^{3+} \rightarrow Fe^{3+}$, Cr^{3+}, Mg^{2+}, Ni^{2+}, Fe^{2+}, Si^{4+}. As ions-compensators, the channels of the structure include large alkali metal cations (Na^+, Cs^+), as well as $(OH)^-$ groups, H_2O molecules, F^- ions, and others (Egorov-Tismenko 2005).

3 Results and Discussion

A common feature of the optical spectra of emeralds is the presence of two broad intense absorption bands in the visible region (Fig. 1). The configuration of the absorption spectra and the energy value of the absorption bands allow the observed bands to be attributed to electron transitions in Cr^{3+} ions, which isomorphically replace Al^{3+} ions in the octahedral positions of the beryl structure. The presence of trigonal distortion of Al^{3+} octahedra (local symmetry D_3) leads to the splitting of excited levels of Cr^{3+} ions. The splitting from the ground level to the sublevels is allowed for different polarization directions, which is manifested through the optical spectra. The emerald spectral absorption bands in the region of 422–437 nm and 604–643 nm are due to spin-resolved transitions from the $^4A_2(^4F)$ ground state to higher $^4T_1(^4F)$ and $^4T_2g(^4F)$ energy levels, respectively (Platonov et al. 1984; Sviridov et al. 1976).

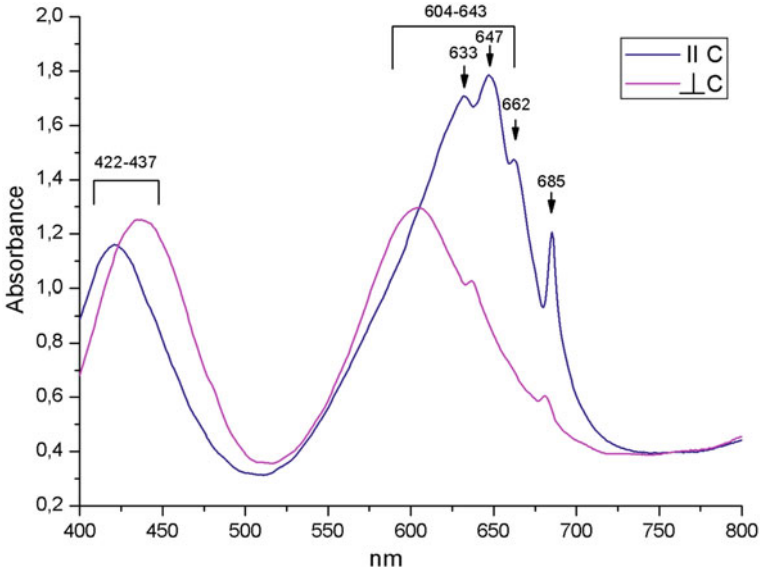

Fig. 1 Optical absorption spectrum of an emerald from the Khench deposit

Additionally, weak narrow absorption bands are observed at wavelengths of 633, 647, 662 and 685 nm, also associated with Cr^{3+} ions. The group of lines 633, 647 and 662 nm is formed by spin-forbidden transitions $^4A_2(^4F) \rightarrow {}^2T_1(^2G)$. As mentioned above, due to the distortion of the octahedral position, this electronic transition is split into three components, and they have different intensity in different polarization directions in the emerald. The line at 685 nm is associated with an electronic transition $^4A_2(^4F) \rightarrow {}^2E(^2G)$ in $Cr^{3+}{}_{VI}$ ions (Balitsky 1984).

Based on the results of the interpretation of the optical absorption spectra of emeralds, the chromaticity coordinates were calculated using the CIE—1931 international colorimetric system. For emeralds, the dominant wavelength of the primary color tone was λ = 525.5–539.8 nm, and the amount of saturation of the main color tone changed in the range of 32.1–53.83%.

4 Conclusions

The optical absorption spectra of emeralds from the Khench Deposit in Panjshir province were analyzed, and the nature of their color was investigated. The nature of coloring is connected exclusively with trivalent chromium, which isomorphically replaces aluminum in the structure of beryl. The role of vanadium in this regard remains to be studied. The obtained results provide a new material for determining the nature of the color of green beryl crystals from the Sherlovaya Gora deposit in Transbaikalia.

Acknowledgements This study was performed within the Russian Government Program of Competitive Growth of Kazan Federal University. The work was performed under state assignment (No. 0386-2019-0004) project of SB RAS IX 137.1.2.

References

Yurgenson GA, Izmailov VN, Garmal GA. Peculiarities of the emerald-bearing mineralogy of the Kherskand site. VIII scientific and methodical conference, May 5–7, 1980, Kabul, Afghanistan, pp. 116–119.

Yurgenson GA, Pasekov YM. Mineralogy of productive emerald-bearing complexes. Materials of the XIII Congress of IMA, January 10–17, 1982, Varna, Bulgaria, pp. 56–57.

Kornilov NI, Solodova YP. Yuvelirnyye kamni. M.: Nedra; 1987. [Kornilov NI, Solodova YP. Jewelry stones. M.: Nedra; 1987. (In Russ.)].

Egorov-Tismenko YK. Kristallografiya i kristallokhimiya. M.: Publishing House "Book House University"; 2005. [Egorov-Tismenko YK. Crystallography and crystal chemistry. M.: Publishing House "Book House University"; 2005. (In Russ.)].

Platonov AN, Taran MN, Balitsky VS. Priroda okraski samotsvetov. M.: Nedra; 1984. [Platonov AN, Taran MN, Balitsky VS. The nature of the gem coloring. M.: Nedra; 1984. (In Russ.)].

Sviridov DT, Sviridova RK, Smirnov YF. Opticheskiye spektry ionov perekhodnykh metallov v kristallakh. M.: Publishing house of Science; 1976. [Sviridov DT, Sviridova RK, Smirnov YF. Optical spectra of transition metal ions in crystals. M.: Publishing house of Science; 1976. (In Russ.)].

Mineral Composition Features of the Sediments at the Saradj-Chuko Grotto

Vladimir A. Tselmovich, Anastasiia S. Korzinova, Ekaterina V. Doronicheva, Liubov V. Golovanova, and Vladimir B. Doronichev

Abstract

The first stratified Neanderthal site in the Elbrus region (Central Caucasus) was found in the Saradj-Chuko grotto. The minerals identified in the sediments of the grotto can be used as indicators of paleoclimatic conditions. The lack of terrigenous minerals contributes to the grotto uniqueness.

Keywords

Mineral composition · Climate change · Human settlement · Magnetic microparticles

1 Introduction

Information about the Paleolithic of the Central Caucasus is very limited, but the interest has recently increased due to the discovery of a Neanderthal settlement in the Saradj-Chuko grotto in the Elbrus region (Doronicheva et al. 2017).

The grotto deposits are represented mainly by loam. Their average thickness is 120 cm. In the stratigraphic column of the Saradj-Chuko grotto, 11 layers are distinguished (from top to bottom: 1, 1A, 1B, 1C, 2, 3, 4, 5, 6A, 6B and 7), the

V. A. Tselmovich (✉) · A. S. Korzinova
Borok Geophysical Observatory, Shmidt Institute of Physics of the Earth, Russian Academy of Sciences (BGO IPE RAS), Borok 142, Nekouz District, Yaroslavl Region, Russia
e-mail: tselm@mail.ru

E. V. Doronicheva · L. V. Golovanova · V. B. Doronichev
ANO "Laboratory of Prehistory", 14th liniya 3-11, St. Petersburg, Russia
e-mail: labprehistory@yandex.ru

S. Votyakov et al. (eds.), *Minerals: Structure, Properties, Methods of Investigation*, Springer Proceedings in Earth and Environmental Sciences,
https://doi.org/10.1007/978-3-030-49468-1_34

period of the Middle Paleolithic includes layers 6A and 6B, as well as, possibly, layer 3, in which few artifact were found. In layer 6B, an active habitat site existed in the Saradj-Chuko grotto, where tools were manufactured from flint and obsidian and hunting prey was butchered.

The Saradj-Chuko grotto is located on the territory of the Republic of Kabardino-Balkaria, 4 km south of Zayukovo, in the valley of the river Fanduko (local name—Saradj-Chuko). The grotto is located in the massif of volcanic rocks, previously dated as the Pliocene (Kizivalter 1947). The volcanic rocks are represented mainly by rhyolites, which occur in the form of lava flows and dome-shaped structures. This grotto was discovered in one of these dome-shaped structures.

Climate changes often result in the change of magnetic properties of the buried layers (Noveyshiy I sovremenny vulkanizm na territorii Rossii 2005). Electron microprobe studies and X-ray phase analysis make it possible to determine the causes of the events studied, using minerals and their associations as the indicators of various events.

The aim of this work was to identify climatic factors, such as global cooling or warming, which could have influenced the grotto population by ancient people.

2 Materials and Methods

A Tescan Vega II scanning electron microscope was used to determine the morphology and composition of the microparticles in 126 samples taken in the grotto. Magnetic and nonmagnetic fractions were studied separately. The results were compared with the results of analyses of similar objects, selected by other researchers as indicators of the climatic situation (Mozherovsky 2016).

Powder X-ray diffraction was carried out using a STADI—MP diffractometer (STOE, Germany) with a primary curved germanium monochromator, Co Kα radiation with a wavelength of 1.788965 Å. For further quantitative analysis, the survey was carried out with the addition of a standard (CaF_2). With the help of X-ray phase analysis, 60 samples were taken sequentially every 2 cm from the section.

3 Results and Discussion

Sedimentary rocks are composed of mineral components different in composition and origin. There are five main types of components that make up sedimentary rocks: terrigenous, authigenic, biogenic, pyroclastic, and cosmogenic (Yapaskurt 2008). The uniqueness of the Saradj-Chuko grotto is that it completely lacks the terrigenous component associated with the long-range transport of matter.

In cave sediments, authigenic minerals can either be the products of mechanical destruction (relict) or the result of chemical transformation of the original rock (newly formed). The relict includes: quartz, microcline, albite, muscovite, biotite, zircon, monazite, rutile, apatite, ilmenite, magnetite, and titanomagnetite. They are found in all layers. The newly formed minerals include those that were formed during the destruction of the original igneous rocks. Halite, sylvite and various clay minerals were formed during the destruction of feldspar. The revealed clay minerals can be attributed to the group of kaolinite, hydromica, and chlorite. Secondary minerals such as palygorskite and barite are also found in some layers. When biotite was destroyed, lepidocrocite was formed, which was partially transformed into maghemite during oxidation.

Melted particles of titanomagnetite can be a marker of volcanic activity, low and high titanium (up to ulvospinel), or ilmenite (Fig. 1) (Noveyshiy I sovremenny vulkanizm na territorii Rossii 2005).

Melted particles of titanomagnetite and ilmenite are not present in all layers and correlate well with the presence of volcanic ash. The greatest number of them is noted in layer 6. Often, the same sample contains both melted grains of titanomagnetites and ilmenites, as well as well-crystallized titanomagnetites with growth steps (Fig. 2). The presence of two generations of titanomagnetite and ilmenite may indicate several sources of their origin.

The biogenic minerals include hydroxyapatite from bones found in the grotto. Some magnetite individuals (microspheres) may be of cosmogenic origin (Fig. 3).

Native iron, nickel and their alloys can be attributed to cosmic dust as well (Fig. 4) (Grachev et al. 2005).

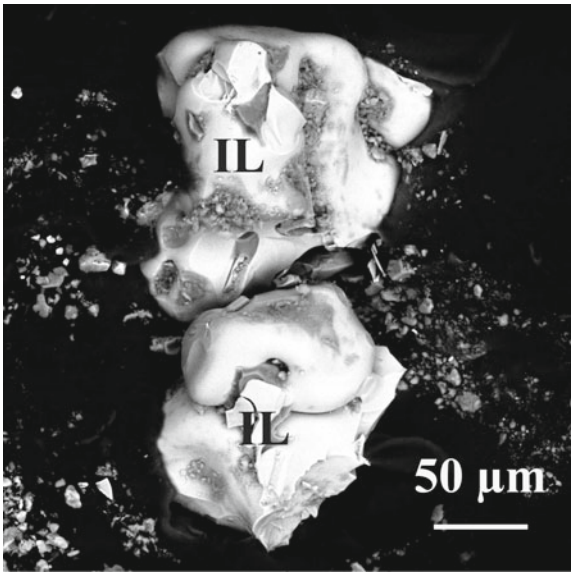

Fig. 1 Melted ilmenite. SEM image

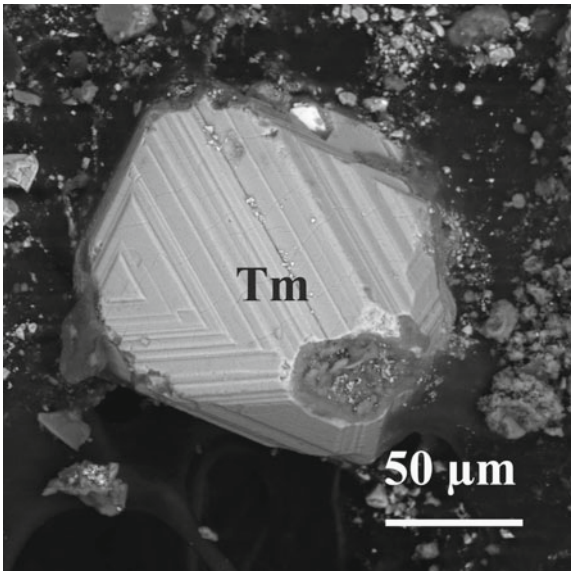

Fig. 2 Titanomagnetite with growth steps. SEM image

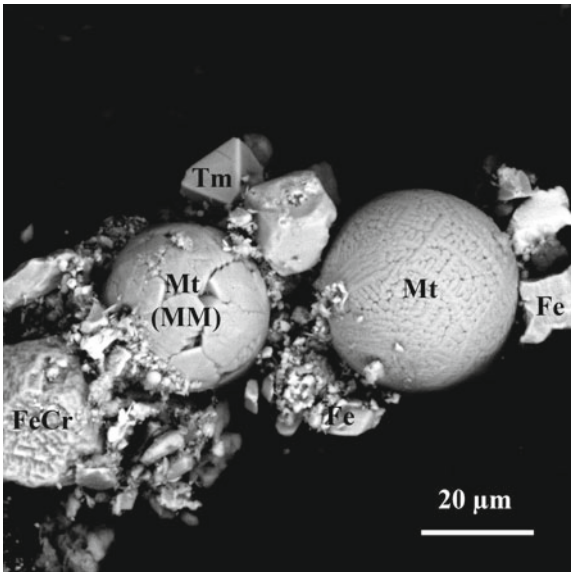

Fig. 3 Cosmogenic magnetite. SEM image

The abundance of cosmogenic particles in layer 1 is probably due to a slowdown in sedimentation rate.

A different ratio of magnetic to nonmagnetic fraction is observed in the layers. An increase in the content of the magnetic fraction can be associated with an increase in the moisture content of the grotto during local periods (Kerkis 1975).

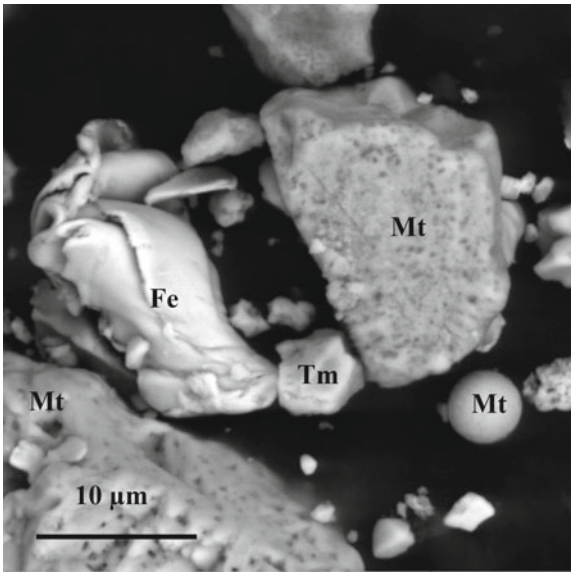

Fig. 4 Native iron. SEM image

In layers 6B and 7, the γ-FeOOH lepidocrocite grains, partially converted to Fe_2O_3 maghemite, which are 10 microns in size or less, serve as an additional source of the magnetic fraction (Gapeev et al. 2010). The initial formation of hydroxides was facilitated by the fact that the lower layers in the section were looser and more heterogeneous than the overlying ones, and water easily circulated through them.

The chain of transformations of lepidocrocite-maghemite-hematite occurs in 1 million years at 90 °C, but it can also be at a lower temperature if the minerals have impurities and a small grain size (Gapeev et al. 2010).

According to the results of X-ray phase analysis and scanning electron microscopy, the following mineral associations were chosen as climate indicators:

1. High content of minerals of the hydromica and chlorite group indicates progressive cooling.
2. High content of palygorskite, barite, halite and sylvite, and minerals of the kaolinite group indicates a hot climate (Mozherovsky 2016).

As a result of determining the relative content of authigenic minerals, the boundaries of the most significant climatic events were identified.

It can be assumed that during the accumulation period of layer 7, the climate was warm (closer to hot) and dry. During the accumulation of layer 6, the climate changed alternately from warm and humid to cold and humid. Each of the 4 and 3 layers began to deposit in a cold and humid climate, but then the climate changed to warm and humid, with a transition to warm and dry. In the second layer, high content of minerals of the hydromica group with relatively low content of the

minerals of the kaolinite and chlorite group, does not allow one to unambiguously interpret the paleoclimatic environment of accumulation of this layer, although most likely the climate was warm and humid. The same considerations apply to the accumulation time of layer 1.

4 Conclusions

As a result of our study, mineral associations that are indicators of climate change, which include clay minerals, palygorskite, halite, sylvite, and barite, have been identified. This made it possible to identify the sections of the incision formed during the periods of cooling and warming.

In the sediments of the Saradj-Chuko grotto, climatic changes have been recorded and well interpreted according to authigenic indicators, which makes the grotto significant not only in archaeological, but also in geological terms.

The diagnostic signs of climatic and volcanic events proposed during the study of the section, as well as the diagnosis of cosmic matter can be used in practice when analyzing similar archaeological objects and interpreting the causes of extinctions and local and global environmental changes that occurred in the Pleistocene and Holocene.

Acknowledgements This work was supported by the grant of the Russian Science Foundation (project No. 17-78-20082, "The interaction of man and nature in antiquity in the Central Caucasus: the dynamics of changes in the natural environment and technological innovations, adaptation of life support systems").

References

Doronicheva EV, Golovanova LV, Doronichev VB, Nedomolkin AG, Shackley MS. The first Middle Paleolithic site exhibiting obsidian industry on the northern slopes of the Central Caucasus. Antiquity. 2017;91(359):1–6. https://doi.org/10.15184/aqy.2017.171.

Kizivalter DS. Geologicheskaya karta SSR. Masshtab 1:20 000. Seriya Kavkazskaya. K-38-II. Ministerstvo geologii i ochrany nedr SSR. 1947. [Kizivalter DS. Geological Map of the USSR. Scale 1: 20 000. Series Caucasian. K-38-II. Ministry of Geology and Mineral Protection of the USSR. 1947. (In Russ)].

Noveyshiy I sovremenny vulkanizm na territorii Rossii. Pod redakciey Lavrova NP, M.: Nauka; 2005. s. 604. [The newest and modern volcanism in the territory of Russia. Under the editorship of Lavrov NP. M.: Nauka; 2005. p. 604. (In Russ)].

Mozherovsky AV. Autigennoe miniraloobrazovanie kak indicator usloviy formirovaniya mezokaynozoyskich vulkanogenno-osadochnych komplexsov Dal'nevostochnych morey. Dissertacya na soiskanie uchenoy stepeni doktora geologo-mineralogicheskich nauk. Vladivostok, 2016. p. 251. [Mozherovsky AV. Authigenic mineral formation as an indicator of the formation conditions of the Meso-Cenozoic volcanogenic-sedimentary complexes of the Far Eastern seas. Thesis for the degree of Doctor of Geological and Mineralogical Sciences. Vladivostok, 2016. p. 251. (In Russ)].

Yapaskurt OV. Geneticheskaya mineralogiya i stadinyi analiz processov osadochnogo porodo- I rudoobrazovaniya. Ucheb. Posobie. M.: ESLAN, 2008, p. 356. [Yapaskurt OV. Genetic mineralogy and the stage analysis of the processes of sedimentary rock and ore formation. Training allowance. M.: ESLAN. 2008, 356 p. (In Russ)].

Grachev AF, Korchagin OA, Kollmann HA, Pechersky DM, Tselmovich VA. A New Look at the Nature of the Transitional Layer at the K/T Boundary near Gams, Eastern Alps, Austria, and the Problem of the Mass Extinction of the Biota. Rus. J. Earth Sci. 2005;7(6):1–45.

Kerkis EE. Metody izucheniya filtracionnych svoistv gornych porod. L.: Nedra, 1975, 231 p. [Kerkis EE. Methods for studying the filtration properties of rocks. L.: Nedra, 1975, p. 231. (In Russ)].

Gapeev AK, Gribov SK, Dolotov AV. Kinetika tamperaturnych fazovych prevrasheni prirodnych lepidokrokitov. Geofizicheskie issledovania. 2010;11(2):5–26 [Gapeev AK., Gribov SK., Dolotov AV. Kinetics of temperature phase transformations of natural lepidocrocites. Geophysical surveys. 2010;11(2):5–26. (In Russ)].

Morphologycal Types of Zircons from Granites of the Polar Urals

Nataliya S. Ulyasheva

Abstract

Small intrusions of the Late Vendian muscovite granites of the Polar Urals penetrating the Late Proterozoic deposits have been studied. By chemical composition, the granites belong to the potassium-sodium calc-alkaline highly aluminous rocks of the normal series. The study of the morphological features of zircon from granites using the method proposed by J. Pupin and G. Turco has shown that the mineral is crystallized when the temperature drops from 800 to 650 °C. The average temperature is 700–750 °C. A sharp increase in environmental alkalinity occurs at a temperature of 750 °C. These data have been confirmed by the results obtained (T = 739–751 °C) using zircon saturation thermometry according to E. Watson and T. Harrison.

Keywords

Granite · Zircon · Polar urals · Temperature

1 Introduction

In the western tectonic zone of the Polar Urals within the Kharbey antiform, ancient rocks are on the surface. According to many researchers, the central part of the antiform consists of deeply metamorphosed volcanogenic-sedimentary and magmatic formations that have completed their development cycle in the early

N. S. Ulyasheva (✉)
Institute of Geology of Komi Science Center of Ural Branch of the Russian Academy of Sciences, 54, Pervomayskaya, Syktyvkar 167000, Russia
e-mail: nsulasheva@geo.komisc.ru

S. Votyakov et al. (eds.), *Minerals: Structure, Properties, Methods of Investigation*, Springer Proceedings in Earth and Environmental Sciences,
https://doi.org/10.1007/978-3-030-49468-1_35

Proterozoic (Pystin 1994; Pystina and Pystin 2002; Kusnetsov et al. 2005). The wings of the protrusion consist of green shale rocks of presumably Riphean (Nyarovei series, Nemuryugan suite) with magmatites of acidic and basic composition breaking through them, whose age is determined from Middle Riphean to late Paleozoic. Most opinions tend to suggest that Middle Riphean-Cambrian rocks have formed at various stages (rift, island-arc, collisional) of the Paleo-Asian ocean evolution.

As is known, granitoids are a good indicator of geodynamic settings of the formation, and zircon is a good indicator of petrogenesis, a reliable geochronometer and geothermometer (Pupin and Turco 1972; Watson and Harrison 1983; Lyakhovich and Chervinskaya 1961; Denisova 2015; Denisova 2016). The purpose of this work is to establish the conditions for the formation of small bodies of granitoids, which break through the Upper Proterozoic deposits of the Nyarovei series based on the study of their chemical composition and morphological features of zircons derived from them.

2 Materials and Methods

Granite samples were taken along the banks of the Nemuryegan river basin (Polar Urals) (Fig. 1). The chemical composition of rocks was determined by a complex method of titrimetry with X-ray fluorescence analysis in the Geology Center of the Komi Scientific Center IG, Ural Branch of the Russian Academy of Sciences (Syktyvkar, Russia). The content of rare and rare earth elements was determined by ICP-MS at the Institute of Geology and Geochemistry named after A. N. Zavaritsky (Ekaterinburg, Russia). The morphological features of zircons from granites were studied using a Tescan Vega 3 LMH scanning electron microscope with X-Max energy dispersive spectrometer at the Geo-Scientific Center for Collective Use of the Komi IG Research Center, the Ural Branch of the Russian Academy of Sciences. The methods proposed by Puipin and Turco (1972) and Watson and Harrison (1983) were used.

3 Results and Discussion

Petrography and Chemical Composition of Muscovite Granites

Muscovite granites have a light gray color, a foliaceous structure and a porphyritic, slightly cataclastic structure. Porphyry secretions are represented by potassium feldspar and felsic plagioclase. Xenomorphic elongated and irregularly shaped sericitized potassium feldspar grains more often form a pertite structure. Microcline up to 4 mm in size is observed with edges corroded with quartz. Plagioclase is represented by albite. The bulk of the rocks is represented by crushed and partially

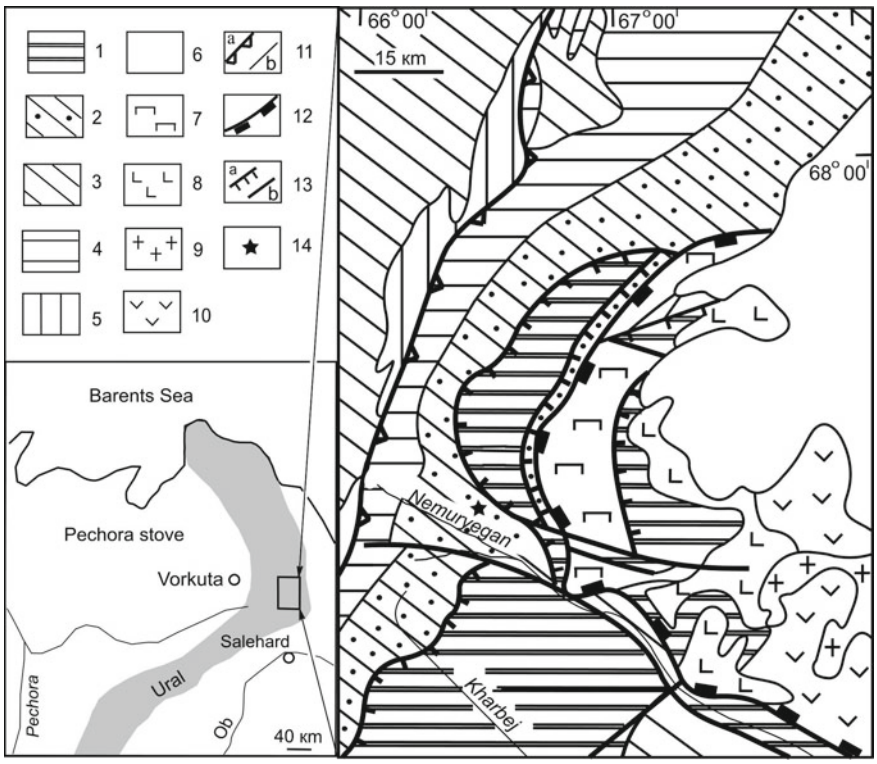

Fig. 1 Schematic geological map of the Kharbey antiform. 1—Archean-Lower Proterozoic complexes; 2—Nyarovei series (RF); 3—Upper Precambrian complexes; 4—volcanogenic-sedimentary complexes ($Є_3$-P_1) of the Lemva structural-facial zone; 5—terrigenous-carbonate complexes ($Є_3$-C) of the Elets structural-facial zone; 6—slab complex (MZ); 7—Ray-Iz—Voikar dunite-hazburgite complex ($O_{1\text{-}2}$?); 8—Kershorsky gabbroid complex (O_3-S_1); 9—Sobsky diorite-plagiogranite complex (S_2-D_1); 10—Yunyaginsky volcanogenic complex: basalts, andesite-basalts, rhyolites, tuffs: 11—geological boundaries: a—thrust boundary of Lemva and Elets structural-facies zones, b—boundaries of complexes, suites; 12—Main Ural deep fault (thrust); 13—other faults: a—thrusts and reverse faults, b—steeply dipping faults, 14—place of granite collection

recrystallized quartz (0.1–0.8 mm), and muscovite and chlorite up to 5 mm in size with scales oriented in one direction.

By chemical composition, granites belong to the potassium-sodium calc-alkaline highly aluminous rocks of the normal series. They are characterized by silica content of 70.64–73.55% and agpaitic index of 0.67–0.75. The granites are close to S and I types according to the content of the following indicator elements and their ratios: Zr (69–88 ppm), Nb (16–21 ppm), Ga (13–15 ppm), Y (25–29 ppm), Rb/Sr (0.5–1.2), Fe/Fe + Mg (0.45–0.5) and the number of alkalis (7.14–7.22%).

Muscovite granite on the chondrite diagram is characterized by a practically undifferentiated flat spectrum of the rare-earth element distribution. The content of La and Yb is 80 and 15 times higher than chondrite, respectively. The spider diagram has high contents of Rb, U, and Th, low quantities of highly charged elements and negative anomalies for Nb, Sr, P and Ti. The Nb content in the rocks under consideration is higher than that in the island-arc formations. High Ta content and low Sr amounts in muscovite granites indicate their formation in collision situations during the contamination of mantle magmas with crustal melts.

The weighted average concordant age of 41 zircon grains from granite according to U-Pb LA-SF-ICP-MS dating is 545.6 million years (Ulyasheva and Grakova 2016).

Morphological Features of Zircon

According to the method of J. Pupin and G. Turko, there is a clear relationship between the zircon morphology, crystallization temperature and chemical composition of the environment. The presence and development of prism faces is controlled by temperature, and the presence of certain faces of dipyramids is associated with the influence of the environment chemism. According to the method of E. Watson and T. Harrison, the melt crystallization temperature depends on the chemism of the protolith and the amount of zirconium in the rock. During zircon typification, the mineral's color and elongation coefficient have also been taken into account.

By the color and transparency degree, zircons from granite are divided into pink transparent (40%); pink, yellowish-pink translucent (40%); colorless, and slightly pink transparent (20%). The development of {100}, {110}, {101}, {211} faces is typical for these three types of zircons (Fig. 2).

Pink transparent zircons are prismatic and long prismatic grains 0.1–0.2 mm in size; they have a smooth surface and an elongation factor of 1.5–3. According to the classification of Pupin, P1, P2, P3, S13-18 forms are common among these zircons (Fig. 2), which indicates zircon formation at temperatures from 800 to 650 °C.

Pink and yellowish-pink translucent zircons have prismatic grains 0.1–0.25 mm in size and an elongation factor of 1.5–3. Among these zircons, there are grains with rough and curvilinear faces. S15, P2 and P1 forms prevail, which correspond to crystallization temperatures of 750, 700 and 650 °C.

Colorless transparent zircons have smooth edges, prismatic and long prismatic crystals 0.5–0.18 mm in size with an elongation factor of 1.5–3.5. Common forms are S13, S14, P3, P2 and P1, which correspond to melt crystallization in the range of 750–650 °C.

Also, for comparison, the crystallization temperature of the igneous melt was calculated using the zircon saturation thermometry according to E. Watson and T. Harrison. The calculated temperature of granite formation is 739–750 °C. This value corresponds to the average temperature obtained by Pupin (700–750 °C), at which the most common forms of zircons S13, S14, S15 and P3 are formed and a sharp increase in alkalinity occurs.

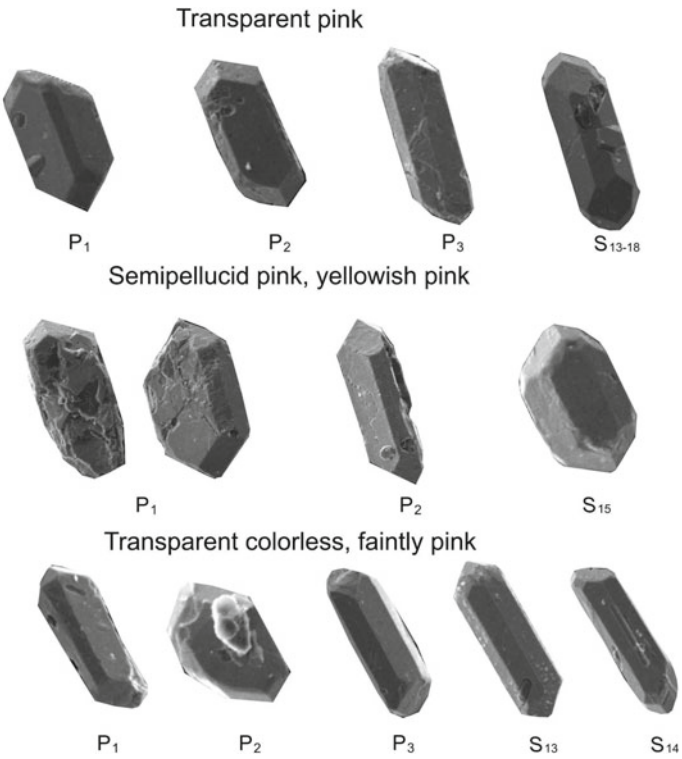

Fig. 2 Types of zircons from muscovite granite determined by the method of J. Pupin and G. Turko

4 Conclusions

The studies of the Late Vendian small bodies of granites of the Polar Urals has shown that they were most likely formed in collision situations. According to the method of J. Pupin and G. Turco, P1, P2, P3, S13, S14, S13-18, and S15 forms are common among the zircon types from granites. Zircons crystallized when the temperature decreased from 800 to 650 °C. The average temperature was 700–750 °C. A sharp increase in the environment alkalinity occurred at 750 °C. These data have been confirmed by the results (T = 739–751 °C) obtained using zircon saturation thermometry according to E. Watson and T Harrison.

References

Pystin AM. Polymetamorficheskiye komplexy zapadnogo sklona Polyarnogo Urala. Spb: Nauka. 1994. 208 s. [Pystin AM. Polymetamorphic complexes of the western slope of the Polar Urals. Spb.: Science, 1994. 2008. 208 p. (In Russ.)].

Pystina YuI, Pystin AM. Tsirkonovaya letopis' ural'skogo dokembriya. Yekaterinburg: UrO RaN, 2002. 167 s. [Pystina YuI, Pystin AM. The zircon chronicle of the Ural Precambrian. Ekaterinburg: Ural Branch of RAS, 2002. 167 p. (In Russ.)].

Kusnetsov NB, Soboleva AA, Udoratina OV, Gertseva MV. Doordovikskiye granitoidy Timano-Ural'skogo regiona i evolyutsiya protouralid-timanid. Syktyvkar: Geoprint, 2005. 100 s. [Kuznetsov NB, Sobolev AA, Udoratina OV, Gertseva MV. Preordovik granitoids of the Timan-Ural region and the evolution of the Protouralids-Timanids. Syktyvkar: Geoprint, 2005. 100 p. (In Russ.)].

Pupin JP, Turco G. Le zircon accessoire en géothermométrie. C.R. Acad. Sci. Paris. 1972; 274; 2: 212–214 (In French).

Watson EB, Harrison TM. Zircon saturation revisited: temperature and composition effects in a variety of crustal magma types. Earth Planet Sci. Lett. 1983; 64: 295–304.

Lyakhovich EB, Chervinskaya AD. Aktsessornye mineraly v granitoidakh Tyrny-Auza i ikh petrogeneticheskoye znacheniye. Trudy IMGRE. 1961; 7: 156–181. [Lyakhovich VV, Chervinskaya AD. Accessory minerals in the granitoids of Tyrny-Auz and their petrogenetic significance. Trudy IMGRE. 1961; 7: 156–181. (In Russ.)].

Denisova YuV. Petrogeneticheskoye znachenie ZrO2/HfO2 otnocheniya v akzessornom zirkone granitov Pripolyarnogo Urala. Vestnik Instituta geologii Komi NZ UrO RAN. 2015; 2: 23–31. [Denisova YuV. Petrogenetic value of the ZrO2/HfO2 ratio in the accessory zircon of granites of the Subpolar Ural. Vestnik of the Institute of Geology, Komi Science Center, Ural Branch of the Russian Academy of Sciences. 2015; 2: 23–31. (InRuss.)].

Denisova YuV. Termometriya zirkona iz granitoidov Pripolyarnogo Urala. Vestnik Instituta geologii Komi NZ UrO RAN. 2016; 12: 37–44. [Denisova YuV. Thermometry of zircon from the granitoids of the Subpolar Urals. Vestnik of the Institute of Geology of Komi Science Center, Ural Branch of the Russian Academy of Sciences. 2016; 12: 37–44. (In Russ.)].

Ulyasheva NS, Grakova OV. U-Pb LA-SF-ICP-MS-vozrast i geokhimicheskie osobennosti melkikh tel granitov zapadnogo kryla kharbeyskogo vystupa (Polyarnyj Ural). "Struktura, veshshestvo, istoriya litosfery Timano-Severoural'skogo segmenta": materialy 25 nauchnoj konferenzii. 29 dekabrya – 1 noyabrya, 2016, Syktyvkar, Rossiya. ss.185–189. [Ulyasheva NS, Grakova OV. U-Pb LA-SF-ICP-MS-age and geochemical features of small bodies of granites of the western wing of the Harbey projection (Polar Urals). "Structure, substance, history of the Timan-Severouralsky lithosphere segment": materials of the 25th scientific conference. December 29–November 1, 2016, Syktyvkar, Russia. pp. 185–189. (in Russ.)].

Capacity of Fullerenes for Doping Atoms

Yury L. Voytekhovsky and Dmitry G. Stepenshchikov

Abstract

The results of computer modeling of fullerenes in both quasi-spherical and Bartell's approximations are presented in the paper. The cavity volumes of all the C_{60} to C_{100} fullerenes have been calculated. The numbers of doping Au, Ag, Pt, and Pd atoms have been found for the most stable (symmetrical with no adjacent pentagons) fullerenes. The cavity volume is stated to be dependent on the number of fullerene-forming atoms, as well as their combinatorial type and symmetry. The elongated and flattened but not spherical fullerenes are the most appropriate for the doping atoms, given the number of carbon atoms.

Keywords

Doped fullerene · Cavity volume · Quasi-spherical and Bartell's approximations · Computer modeling

1 Introduction

Fullerene structures are common in nature. In crystal structures, they are known as cavities in clathrate compounds (Ripmeester and Ratcliff 1999), capable of containing doping atoms. Thus, it is of interest to systematically calculate their volumes. All the combinatorial types of fullerenes in the C_{20} to C_{60} range are listed and

Y. L. Voytekhovsky (✉)
Saint-Petersburg Mining University, 21st Line Vasilyevsky Ostrov, 199106 Saint-Petersburg, Russia
e-mail: Voytekhovskiy_YuL@pers.spmi.ru

D. G. Stepenshchikov
Geological Institute KSC RAS, 14 Fersman Str., 184209 Apatity, Russia
e-mail: Stepen@geoksc.apatity.ru

S. Votyakov et al. (eds.), *Minerals: Structure, Properties, Methods of Investigation*,
Springer Proceedings in Earth and Environmental Sciences,
https://doi.org/10.1007/978-3-030-49468-1_36

characterized by point symmetry groups (Voytekhovsky and Stepenshchikov 2001; Voytekhovsky and Stepenshchikov 2002). Their diversity grows with the number of vertices faster than the exponent, while high symmetry and the smallest possible number of contacting pentagons contribute to their stability (Kroto 1987; Schmalz et al. 1988). Therefore, in the C_{62} to C_{70} and C_{72} to C_{100} ranges, the authors have listed and characterized by point symmetry groups only fullerenes with pairs (Voytekhovsky and Stepenshchikov 2002) and without contacting pentagons (Voytekhovsky and Stepenshchikov 2003), respectively. The article proposes an averaged parameter estimating C_n cavity volume of the fullerene as a function of n.

For fullerene of any combinatorial type, its metric implementations can vary widely. Using computer simulation, metric realizations and the capacities of fullerenes with respect to Au, Ag, Pt, and Pd atoms have been studied in Bartell's approximation. In most cases, the doping atoms enter the bonds with the carbon shell (Shpak et al. 2001). The authors have considered the simplest situation when the metal atoms do not interact with the shell. The problem is reduced to finding the volume of the cavity and counting the maximum number of doping atoms. They are considered as spheres with a radius equal to the atomic radius of the chemical element. The cavity is calculated as the range of action of the van der Waals forces.

A similar approach was implemented in (Adams et al. 1994) without an involvement of doping atoms. The latter do not form chemical bonds with the carbon shell and can be considered as the densest ball packing in quasi-spherical volume. The problem is divided into three tasks: the construction of 3D frames for potentially stable fullerenes from previously generated varieties (Voytekhovsky and Stepenshchikov 2002; Voytekhovsky and Stepenshchikov 2003); the calculation of the cavity volumes; filling them with atoms and counting their maximum number.

2 Quasi-Spherical Approximation

Let a_m be the edge of a regular m-gon. Then, its perimeter, the radii of inscribed and circumscribed circles equal, respectively,

$$P = m\,a_m\,,\ \mathrm{r} = a_m/2\,\mathrm{tg}(\pi/m)\ \text{and}\ \mathrm{R} = a_m/2\sin(\pi/m).$$

For any m, we have

$$\mathrm{r} < \rho < \mathrm{R}$$

where $\rho = \mathrm{P}/2\pi$ is the radius of a circle with length P. But,

$$\mathrm{r}/\mathrm{R} \to 1\ \text{as}\ m \to \infty$$

Hence,

$$\rho/r \to 1 \text{ and } \rho/R \to 1 \text{ as } m \to \infty$$

i.e. ρ simultaneously estimates r and R.

The most symmetric fullerenes C_{60} (–3–5*m*) and C_{70} (–10*m*2) are usually characterized by the radii of inscribed and circumscribed spheres. The above-said leads to an idea to use $\wp$ radius of an equiareal sphere to characterize any C_n fullerene as an "almost regular" polyhedron of 12 nearly regular 5-gonal and *n*/2–10 6-gonal facets. Let us consider a fullerene with all vertices being on a sphere. Then,

$$R^2 = r^2 + r_6^2,$$

where r and R are the radii of inscribed and circumscribed spheres while

$$r_6 = a/2 \sin(\pi/6) = a$$

is the circumradius of a 6-gonal facet of fixed finite edge length *a*. Then

$$r/R = \left[1-(a/R)^2\right]^{1/2} \to 1$$

as $R \to \infty$ caused by $n \to \infty$. Hence, $\wp$ asymptotically estimates r and R. The areas of 5-gonal and 6-gonal facets equal

$$S_m = m\,a^2 \text{ ctg } (\pi/m)/4,$$

where m = 5 or 6. So, the surface area of a C_n fullerene equals

$$S_{ful} = a^2[15 \text{ ctg } (\pi/5) + 3(n/2-10) \text{ ctg } (\pi/6)/2].$$

Finally, it follows from the equation $S_{ful} = 4\pi\wp^2$ that

$$\wp = a\{[15 \text{ ctg } (\pi/5) + 3(n/2-10)\text{ctg}(\pi/6)/2]/4\pi\}^{1/2} \approx$$

$$\approx a(0.103374\,n-0.424548)^{1/2} = a\varphi(n).$$

It follows from the above formula that *a* is nothing but a scaling coefficient, while φ(*n*) non-linearly defines $\wp$ as a function of *n*. It is tabulated for n = 60 to 100 in Table 1.

Let us compare our results with previous data. It is known for the ideal truncated icosahedron that R = 2.478*a*, h_5 = 2.327*a* and h_6 = 2.267*a*, where *a*, R, h_5 and h_6 are the edge, radius of circumscribed sphere and apothems (*i.e.* distances from the centre to 5-gonal and 6-gonal facets), respectively. Our estimate φ(60) ≈ 2.404 is in a good agreement with this model. It is reported for the real C_{60} fullerene that

Table 1 φ(*n*) values for *n* = 60 to 100

n	φ(*n*)	*n*	φ(*n*)	*n*	φ(*n*)
60	2.403725	74	2.687960	88	2.944888
62	2.446352	76	2.726147	90	2.979784
64	2.488250	78	2.763806	92	3.014276
66	2.529454	80	2.800959	94	3.048378
68	2.569997	82	2.837626	96	3.082103
70	2.609910	84	2.873825	98	3.115462
72	2.649222	86	2.909573	100	3.148468

a = 0.14 and R = 0.35 nm (Haymet 1986). It is also reported for this case that partial double and double C = C bonds equal 0.144 and 0.139 with R = 0.357 nm (Eletsky and Smirnov 1995). It follows from our formula that R = 0.346 and 0.344 for a = 0.144 and 0.139 nm, respectively. So, our estimates are close to both an ideal model and experimental data even for the small n = 60 value. They are getting much more precise with increasing n even with C-C bonds being slightly different. This is true in particular for the most symmetric shapes, which can be characterized in addition along the symmetry axes. If the shape is not too elliptic, the estimated radius may also be a reasonable approximation.

3 Bartell's Approximation

For a fixed combinatorial type, a fullerene admits different metric realizations, especially for low point symmetry groups. Even these forms are of interest, since they are possible as stable doped structures and nanoscale crystalline cavities. To obtain the spatial coordinates, a simplified Bartell's model (Dashevsky 1974) was used. The set of atoms is considered as a mechanical system of points and elastic bonds between them. Its main properties are:

1. Non-adjacent atoms in a molecule do not interact.
2. Single and double bonds between atoms are indistinguishable.
3. $F_L = K_L$ (L–L_0) force acts between a pair of adjacent atoms, tending to arrange them at L_0 distance from each other and is proportional to the L–L_0 displacement. It is accepted that L_0 = 1.42 Å as the bond length between adjacent atoms in the graphite layer. F_L force is applied to each atom along the bond (Fig. 1a).
4. $F_A = K_A$(A–A_0) force acts between a pair of adjacent bonds and tends to turn them at an A_0 angle proportional to the A–A_0 angular displacement. It is accepted that A_0 = 120° as the angle between adjacent bonds in the graphite layer. The F_A force is applied to an atom at a common vertex along the bisector of A angle (Fig. 1b).
5. It is assumed that in the infinite graphite layer the indicated forces are absent and its structure is stable.

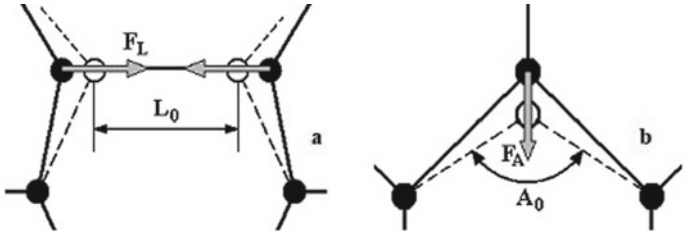

Fig. 1 Forces between atoms **a** and bonds **b** in the fullerene model

At the first step, all atoms are located on a sphere with a radius being approximately equal to that of the future fullerene (Voytekhovsky 2003). Five or six atoms forming a facet are located on a sphere along a small circle. The area of the fullerene facet is approximately equal to the area of the circle $8\pi R^2/(n + 4)$, where R is the radius of C_n fullerene. The rest of the atoms are located on a sphere at a point being opposite to the facet. Such a condition prohibits the formation of twisted or creased structures.

At the second step, all atoms, except those entering the original facet, are pulled apart over the sphere by an iterative process, namely, the coordinates of each atom are equated to the average of the coordinates of adjacent atoms. Thus, the arrangement of atoms is achieved, at which the distances between them are approximately equal.

At the third step, the atoms are removed from the sphere. Between them and between the bonds, the F_L and F_A forces act. This process is also iterative. Each atom shifts in the direction of the resultant force until all atoms are in equilibrium positions.

The F_L and F_A coefficients are chosen so as to ensure the best correspondence of the structures obtained to the known parameters of fullerenes (Dashevsky 1974). Icosahedral C_{60} with a radius of 3.57 Å and ellipsoidal C_{70} with a diameter along the equator of 6.94 and a height of 7.8 Å are taken as standards (Shpak et al. 2001). The sizes of the fullerenes obtained correspond well to these values: the C_{60} radius is 3.51 Å, the diameter of C_{70} is 6.87, and the height is 7.87 Å. An error of <2% may be caused by the assumption that the fullerene bonds are identical and cannot be eliminated within this model.

4 Cavity Volume of a Fullerene

When calculating the cavities of fullerenes, the data of (Adams et al. 1994) were used. Surrounded by van der Waals spheres, the carbon atoms form a region inside the fullerene, in which the doping atoms do not chemically bond to the carbon envelope. In this work, the extreme values of the radii of the spheres 1.47 and 1.76 Å are considered. In our calculations, their radii are half the distance between the

layers of graphite 1.7 Å. Such an assumption is natural if we consider multilayer, roll-like nanotubes or onion-like fullerenes (Kroto and McKay 1988). Their surfaces look like curved graphite layers, and the interaction of neighboring layers is due to weak van der Waals forces. With an increase in the diameter of molecules, the neighboring surfaces flatten and more correspond to the graphite structure.

The fullerene cavity was built from its similarity to the outer shell. A segment was drawn from the geometric center of the molecule to each atom, which then decreased by the radius of the van der Waals sphere. At the obtained points of intersection of a segment with spheres, an "internal" fullerene was constructed, having a combinatorial type of the outer shell. The volume of the cavity was calculated as the sum of the volumes of the pyramids with the vertices in the center of the molecule and 5- or 6-carbon bases corresponding to 5- or 6-membered rings of carbon atoms (Fig. 2). The resulting volume was less than the actual one, because between the van der Waals spheres there remained a relatively small volume, the calculation of which was rather laborious.

Another integration method was used in (Adams et al. 1994). The area that is known to cover the cavity was scanned with a step of 0.1 Å, with all the "cubes" falling into the cavity being summed. Thus, a high accuracy of calculations was achieved, which seems to be inexpedient because of the dubious accuracy of the data. At least, this is indicated by the range of changes in the van der Waals radius of the carbon atom. Secondly, even a good estimate of the volume is still insufficient for a reliable determination of the degree of filling of the cavity with atoms because its shape must also be taken into account.

The authors found cavities for icosahedral C_{60}, all C_{62} to C_{70} with pairs of adjacent pentagons, and all C_{72} to C_{100} without adjacent pentagons (Voytekhovsky and Stepenshchikov 2002; Voytekhovsky and Stepenshchikov 2003). For icosahedral C_{60} in our calculations, V = 21.3 $Å^3$. Attention is drawn to the stepwise character of the increase in volume V with an increase in the n number of atoms in the C_n fullerene (Figs. 3 and 4). For a given n, the capacity of C_n isomers fluctuates

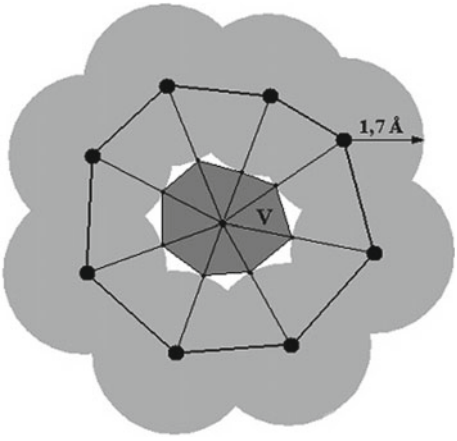

Fig. 2 Cavity volume of a fullerene

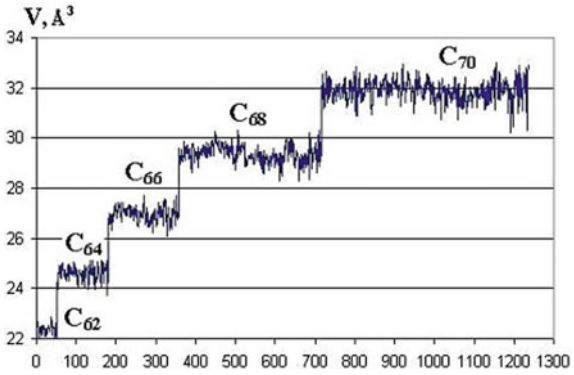

Fig. 3 Fullerenes C_{62} to C_{70} cavity volumes. Horizontal axis—numbers of fullerenes in (Voytekhovsky and Stepenshchikov 2002)

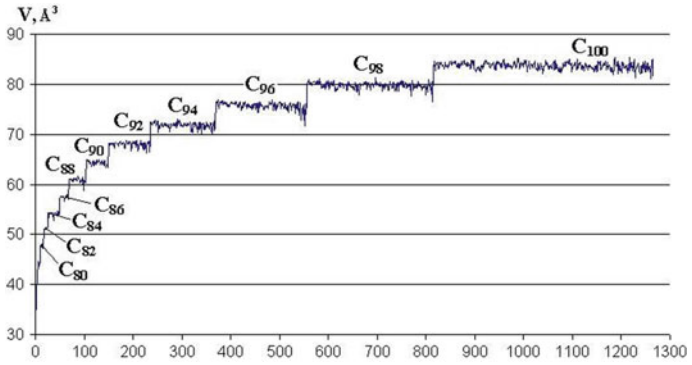

Fig. 4 Fullerenes C_{72} to C_{100} cavity volumes. Horizontal axis—numbers of fullerenes in (Voytekhovsky and Stepenshchikov 2003)

around a certain value. This is because of the different combinatorial types of fullerenes, *i.e.* different distributions of bonds between carbon atoms. The cavity volume is less dependent on the symmetry of fullerene. Local maxima and minima belong to symmetric as well as asymmetric molecules. Thus, the maximum peak for C_{66} corresponds to asymmetric fullerene No. 270 (Fig. 3).

Highly symmetric and potentially stable fullerenes (Kroto 1987) are shown in Fig. 5. Their cavity volumes are given in Table 2. For them, the radius R of the cavity is calculated, which makes it possible to estimate the maximum size of the atom that fits inside the fullerene. The sphericity of the fullerene cavity can be judged by the ξ ratio of the ball volume of R radius to the V cavity volume. By this criterion, the most spherical fullerenes are C_{60}, C_{80} (–3–5*m*), C_{80} (–10*m*2), and C_{96}

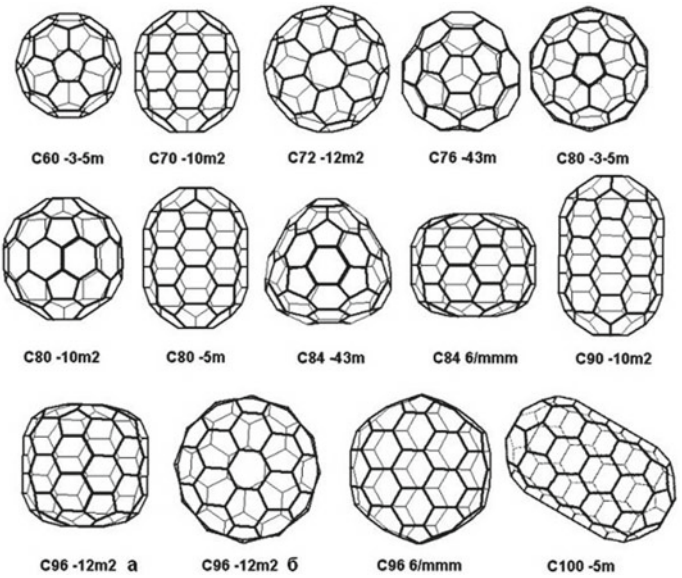

Fig. 5 Highly symmetric C_{20} to C_{100} fullerenes (automorphism group orders ≥ 20)

Table 2 The V cavity volume, R radius, and ξ sphericity coefficient for highly symmetric C_{20} to C_{100} fullerenes (Fig. 5)

n	Symmetry	V, Å^3	R, Å	ξ
60	–3–5*m*	21.3	1.8	1.1
70	–10*m*2	32.9	1.65	0.6
72	–12*m*2	35	1.31	0.3
76	–43*m*	41.8	1.88	0.7
80	–3–5*m*	48.1	2.24	1.0
80	–10*m*2	48	2.09	0.8
80	–5*m*	47.1	1.75	0.5
84	–43*m*	53.7	1.83	0.5
84	6/*mmm*	54.1	1.93	0.6
90	–10*m*2	63.3	1.59	0.3
96	–12*m*2 a	76.1	2.39	0.8
96	–12*m*2 b	74.9	1.72	0.3
96	6/*mmm*	75.3	1.75	0.3
100	–5*m*	81.4	1.72	0.3

(–12*m*2 a). For C_{60}, the value $\xi > 1$. This is explained by the peculiarities of the calculations: the V cavity volume is found as the volume of the polyhedron, and the R radius of the cavity means the radius of the sphere inscribed in its framework.

The knowledge of cavity volumes allows us to obtain an upper estimate of the number of doping atoms. For this, the V cavity volume is divided by the volume of a sphere of R_a radius equal to the atomic radius of the chemical element. The estimate is the more accurate, the more spherical the fullerene is and the smaller the radius of the doping atoms is. In the case of non-intersection of the spheres of atoms with each other, their maximum number is obviously smaller and depends on its shape. Spherical fullerenes, having the maximum cavity volumes among all fullerenes with a given number of atoms, are not the most capacious, because significant voids are between the doping atoms, especially at the boundary with the shell.

5 The Number of Doping Atoms

Analytical determination of the maximum number of atoms inside a fullerene is laborious and inefficient because of the complex configuration of the cavity. The authors used a computational experiment based on the principles of interaction of atomic shells. When modeling the atoms with spheres, it is necessary to ensure that they do not overlap each other inside the cavity. At the same time, the overlap of carbon atoms with the doping atoms is not allowed. If one atom is placed in a fullerene, the criterion is reduced to a simple comparison of its radius with the cavity radius.

For a given number of atoms near the geometric center of the fullerene, the coordinates of the centers of the corresponding spheres of R_a radius are randomly set. Under the action of repulsive forces of the doping atoms from the carbon skeleton and from each other, an equilibrium position is reached, for which the criterion of successful placement is determined. When atomic spheres do not intersect each other, the repulsive forces are weaker than in the case of overlap. Assuming several possible arrangements of atoms in a cavity, multiple repetitions (100 in our case) of placements are carried out until their maximum number is exceeded or the criterion of successful placement is fulfilled.

Computer experiments were performed for Au and Ag (1.44 Å), Pt (1.38 Å), and Pd (1.37 Å) (Weinstein et al. 1979). The range 1.3–1.5 Å was scanned with a step of 0.01 Å. For research, obviously and potentially stable fullerenes were taken (Fig. 5). The results are given in Table 3. As R_a increases in each row, the values represent a non-increasing sequence. This cannot be said about the sequences in the columns. Thus, the C_{84} isomers contain one atom in the entire range of R_a, which is less than the fullerene C_{80} (–5*m*) capacity. In this case, the shape of the cavity has a greater effect than the size. From Table 3 and Fig. 5, we can conclude that elongated fullerenes C_{80} (–5*m*), C_{96} (–12*m*2) b, and C_{100} (–5*m*) have a better capacity than spherical C_{60} (–3–5*m*), C_{80} (–3–5*m*), and C_{80} (–10*m*2).

Figure 6 shows some fullerenes doped with Au, Ag, Pt, and Pd atoms. For each structure, the fullerene cage and the cavity, van der Waals shell and doping atoms are shown. The varying degree of fullerene filling is clearly visible from high (2, 6)

Table 3 Maximum numbers of doping atoms

n	Symmetry	R_a, Å																				
		1.3	1.31	1.32	1.33	1.34	1.35	1.36	1.37	1.38	1.39	1.4	1.41	1.42	1.43	1.44	1.45	1.46	1.47	1.48	1.49	1.5
60	–3–5*m*	1	1	1	1	1	1	1	1	1	1	1	1	1	1	1	1	1	1	1	1	1
70	–10*m*2	1	1	1	1	1	1	1	1	1	1	1	1	1	1	1	1	1	1	1	1	1
72	–12*m*2	1	1	1	1	1	1	1	0	0	0	0	0	0	0	0	0	0	0	0	0	0
76	–43*m*	1	1	1	1	1	1	1	1	1	1	1	1	1	1	1	1	1	1	1	1	1
80	–3–5*m*	1	1	1	1	1	1	1	1	1	1	1	1	1	1	1	1	1	1	1	1	1
80	–10*m*2	1	1	1	1	1	1	1	1	1	1	1	1	1	1	1	1	1	1	1	1	1
80	–5*m*	2	2	2	2	2	2	2	2	2	2	2	2	2	2	2	2	2	2	2	2	2
84	–43*m*	1	1	1	1	1	1	1	1	1	1	1	1	1	1	1	1	1	1	1	1	1
84	6/*mmm*	1	1	1	1	1	1	1	1	1	1	1	1	1	1	1	1	1	1	1	1	1
90	–10*m*2	2	2	2	2	2	2	2	2	2	2	2	2	2	2	2	2	2	2	2	2	2
96	–12*m*2 a	2	2	2	2	2	2	2	2	2	2	2	1	1	1	1	1	1	1	1	1	1
96	–12*m*2 b	3	3	3	3	3	3	3	3	3	3	3	3	3	3	2	2	2	2	2	1	1
96	6/*mmm*	3	3	3	3	3	3	3	3	3	3	3	3	3	3	3	3	3	3	3	2	2
100	–5*m*	3	3	3	3	3	3	3	3	3	3	3	3	3	3	3	2	2	2	2	2	2

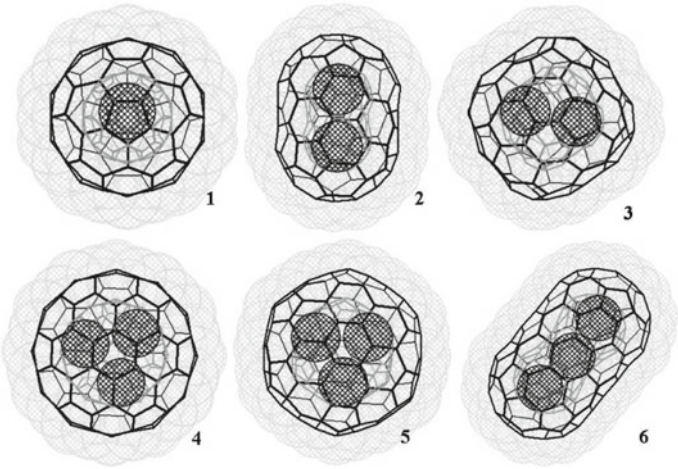

Fig. 6 Doped fullerenes 1. C_{80} (–3–5*m*). 2. C_{80} (–5*m*). 3. C_{96} (–12*m*2) a. 4. C_{96} (–12*m*2) b. 5. C_{96} (6/*mmm*). 6. C_{100} (–5*m*). R_a = 1.44 Å for 1, 2, 5, 6. R_a = 1.39 Å for 3, 4

to low (1, 3). Knowing the maximum number of atoms in a fullerene, one can find the ratio of the sum of the volumes of balls of R_a radius to the V cavity volume. The closer it is to 1, the better the fullerene is filled.

6 Conclusion

In the quasi-spherical approximation, a formula has been obtained for the cavity volume of a fullerene C_n as a function of n, which shows a good match for real C_{60}. With increasing n for quasi-spherical and potentially stable fullerenes, the estimate is getting more and more accurate.

For icosahedral C_{60}, fullerenes C_{62} to C_{70} with pairs of adjacent pentagons and fullerenes C_{72} to C_{100} without adjacent pentagons, the cavity volumes have been found. The cavity volume of the fullerene C_n depends more on the n number than on the combinatorial type and symmetry.

Computer simulations in Bartell's approximation have shown that the most capacious for doping atoms are not quasi-spherical, but elongated and flattened fullerenes. Up to three doping atoms with radii of 1.3–1.5 Å (Au, Ag, Pt, Pd, etc.) can be found in highly symmetric C_{60} to C_{100} fullerenes.

References

Ripmeester JA, Ratcliff KI. Vklad spektroskopii YAMR v issledovaniye klatratov. Zhurnal strukturnoy khimii. 1999;40(5):809–821. [Ripmeester JA, Ratcliff KI. The contribution of NMR spectroscopy to the study of clathrates. J Struct Chem 1999;40(5):809–821. (In Russ.)].

Voytekhovsky YL, Stepenshchikov DG. C_{20} to C_{60} fullerenes: combinatorial types and symmetries. Acta Cryst. 2001;A57:736–738.

Voytekhovsky YL, Stepenshchikov DG. Fullereny C_{20} – C_{60}: katalog kombinatornykh tipov i tochechnykh grupp simmetrii. Apatity: K & M. 2002 [Voytekhovsky YL, Stepenshchikov DG. Fullerenes C_{20} – C_{60}: catalog of combinatorial types and point symmetry groups. Apatity: K & M. 2002. (In Russ.)].

Kroto HW. The stability of the fullerenes C_n, with n = 24, 28, 32, 36, 50, 60 and 70. Nature. 1987;329:529–531.

Schmalz TG, Seitz WA, Klein DJ, Hite GE. Elemental carbon cages. J Am Chem Soc. 1988;110:1113–1127.

Voytekhovsky YL, Stepenshchikov DG. On the spectrum of fullerenes. Acta Cryst. 2002; A58:295–298.

Voytekhovsky YL, Stepenshchikov DG. Fullereny C_{62} – C_{100}: katalog kombinatornykh tipov i tochechnykh grupp simmetrii. Apatity: K & M. 2003. [Voytekhovsky YL, Stepenshchikov DG. Fullerenes C_{62} – C_{100}: catalog of combinatorial types and point symmetry groups. Apatity: K & M. 2003. (In Russ.)].

Shpak AP, Kunitsky YA, Karbovsky VL. Klasternyye i nanostrukturnyye materialy. Kiev: Akademperiodika. 2001. [Shpak AP, Kunitsky YA, Karbovsky VL. Claster and nanostructural materials. Kiev: Academperiodica. 2001. (In Russ.)].

Adams GB, O'Keeffe M, Ruoff RS. Van der Waals areas and volumes of fullerenes. J Phys Chem. 1994;98(38): 9465–9469.

Haymet ADJ. Footballene: a theoretical prediction for the stable, truncated icosahedral molecule C_{60}. J Am Chem Soc. 1986;108:321–322.

Eletsky AV, Smirnov BM. Fullereny i struktury ugleroda. Uspekhi fizicheskikh nauk. 1995;165 (9):977–1009. [Eletsky AV, Smirnov BM. Fullerenes and carbon structures. Advances in Phys Sci. 1995;165(9):977-1009. (In Russ.)].

Dashevsky VG. Konformatsii organicheskikh molekul. Moscow: Khimiya. 1974. [Dashevsky VG. Conformation of organic molecules. Moscow: Chemistry. 1974. (In Russ.)].

Voytekhovsky YL. A formula to estimate the size of a fullerene. Acta Cryst. 2003;A59:193–194.

Kroto H, McKay K. The formation of quasi-icosahedral spiral shell carbon particles. Nature 1988;331:328–331.

Weinstein BK, Fridkin VM, Indenbom LM. Sovremennaya kristallografiya. T. 2. Struktura kristallov. Moscow: Nauka. 1979. [Weinstein BK, Fridkin VM, Indenbom LM. Modern crystallography. Vol. 2. Structure of crystals. Moscow: Nauka. 1979. (In Russ.)].

Accessory Sulfides from the Chromitites of the Ergaksky Ultramafic Massif (The Western Sayan)

Alexey N. Yurichev

Abstract

The object of study is accessory sulfide mineralization found in massive chromitites of the Ergaksky ultramafic massif, which is the north-eastern fragment of the Kurtushibinsky ophiolite belt of the Western Sayan. Three paragenetic associations of ore minerals related to various processes of formation and transformation of enclosing chromitites have been identified. The typomorphic and chemical features of ore minerals have been characterized.

Keywords

Western Sayan · Ergaksky massif · Ultramafites · Chromitites · Accessory sulfides · Chemistry · Genesis

1 Introduction

The ultramafites of ophiolitic complexes are an integral part of mafic-ultramafic belts of folded regions. They attract great attention of researchers both from the point of view of their genesis, taking into account their mantle nature of formation and connection with early stages of development of folded structures, and the ore content position, i.e. industrial chromite ores including PGE minerals, an asbestos-bearing deposit and a nickel-bearing laterite type deposit (weathering crust).

A. N. Yurichev (✉)
Tomsk State University, 36 Lenina Avenue, 634050 Tomsk, Russia
e-mail: juratur@sibmail.com

S. Votyakov et al. (eds.), *Minerals: Structure, Properties, Methods of Investigation*,
Springer Proceedings in Earth and Environmental Sciences,
https://doi.org/10.1007/978-3-030-49468-1_37

Of the ore mineralization found in restitic ultramafites, only the mineralogy of spinelides and PGE minerals is currently studied to a greater extent. Other ore minerals, in particular, sulfides, are much less covered in the literature.

Difficulties in the diagnosis of accessory sulfides in restitic ultramafites are associated with their extremely small sizes (5–20 μm, rarely up to 2 mm), and also with their low content in these rocks (0.01–0.2%). The study of accessory sulfidic mineralization in chromitites of the Ergaksky ultramafic massif, which is part of the Kurtushibinsky ophiolite belt, located in the north-eastern part of the Western Sayan, was carried out by X-ray microanalysis.

The Ergaksky massif has an oval shape with dimensions of 14 × 8 km and is elongated in submeridional direction. It is divided into two blocks of different sizes by tectonic violation of the sublatitudinal strike: the southern—Lysansky (~75 km^2) and the northern—Maloergaksky (~10 km^2). The ultramafites of the dunite-harzburgite banded complex occur in the structure of the Lysansky block (Katanov et al. 2002). It is composed of rhythmically alternating dunites and harzburgites, which underwent intense plastic deformation (Chernyshov et al. 2016). The dunites and harzburgites of the Maloergaksky block are often converted into regenerated serpentine-olivine ultrametamorphites and olivinites. Most of the known chromite manifestations vary from densely disseminated to massive in their structure. They are mainly associated with dunites and olivinites and are controlled by the banded inner structure of the massif. The serpentinites are widely spread on the peripheral of both blocks.

2 Materials and Methods

In accordance with the objectives of this study, the traditional approach of mineralographic study of ore minerals was used with the determination of the phase chemical composition by X-ray microanalysis, using scanning electron microscopy (Reed 2005). The latter included the study of individual sulfide grains and their aggregates by a scanning electron microscope with subsequent energy dispersive and wavelength dispersive microanalysis. The following equipment was used: TESCAN Vega 3 SBH and Tescan Vega II LMU scanning electron microscopes equipped with an energy dispersive (Si(Li) detector, Oxford INCA Energy 350) and wavelength dispersive (Oxford INCA Wave 700) spectrometers. Before the study, plane-parallel 3–4 mm thick polished sections from the selected samples of chromitites were made, followed by carbon sputtering of their surfaces (~25–30 nm). Measurements were carried out on a tungsten cathode at an accelerating voltage of 20 kV, current of 15 nA and spectrum acquisition time of 120 s. The probe beam diameter was ~2 μm. The reference sample for comparison was MAC (55 standard Universal Block Layout+F/Cup № 6835).

All analyses were performed at the Analytical Center of geochemistry of natural systems, TSU (Tomsk), analyst E.V. Korbovyak. The calculations of sulfide chemical composition were carried out using INCA-Issue 18b software and original in-house software.

3 Results and Discussion

In the course of the present study, the following sulfides were identified: nickelous pentlandite, millerite, ferruginous millerite, heazlewoodite, ferruginous heazlewoodite, galena, pyrite, chalcopyrite and ferruginous chalcocite. Nickelous pentlandite, millerite and galena are the most common of the sulfides listed above.above.

Nickelous pentlandite is observed mainly in chlorite-serpentine cement between the grains of chromospinelide in the form of individual small (up to 0.03 mm) round grains with jagged edges (Fig. 1a). The chemical composition of the mineral is characterized by high Ni content (41–43%) with lower Fe content (21–23%) (Table 1). The development of millerite on the individual grains of pentlandite is observed (Fig. 1b).

Millerite is noted mainly in the grains of chromospinelide in the form of independent rounded or elongated grains up to 0.01 mm in size, rarely in the form of granular aggregate secretions along nickelous pentlandite (Fig. 1b–c). The

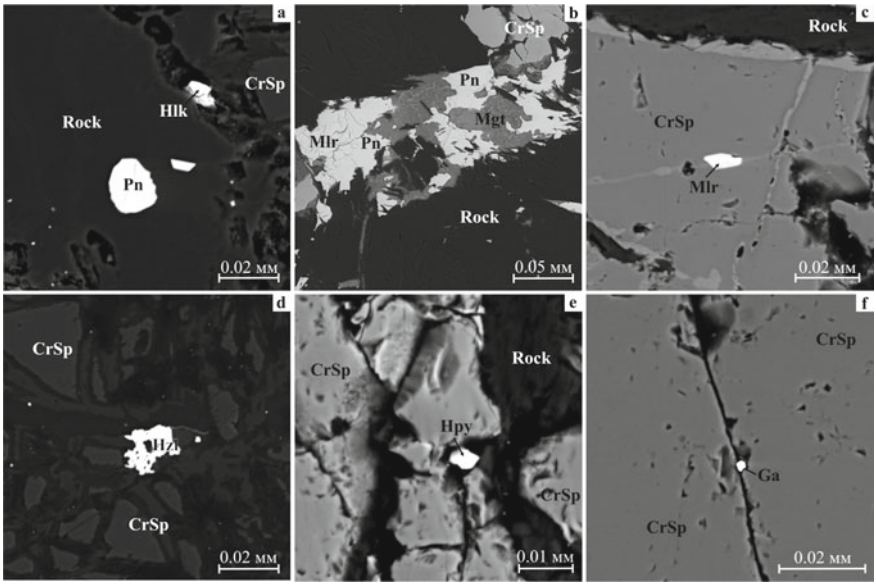

Fig. 1 Sulfidic accessory mineralization from chromitites of the Ergaksky massif (BSE mode): Pn—nickelous pentlandite; Hlk—ferruginous chalcocite; Mlr—millerite; Hzl—heazlewoodite; Hpy—chalcopyrite; Ga—galena; Mgt—magnetite; CrSp—chromospinelide; Rock—chlorite-serpentine aggregate

Table 1 The average chemical compositions of accessory sulfides from chromitites of the Ergaksky ultramafic massif, wt.%

Mineral	Number of analyzes	Ni	Co	Fe	Pb	Cu	S	Sum
Nickelous pentlandite	5	41.95	2.24	22.53	–	–	33.29	100
Millerite	7	63.37	0.18	0.52	–	–	35.72	99.79
Ferruginous millerite	3	50.55	3.02	12.23	–	–	33.40	99.20
Heazlewoodite	3	70.91	–	1.37	–	–	27.72	100
Ferruginous heazlewoodite	2	64.40	–	10.92	–	–	24.63	99.95
Galena	8	–	–	0.22	85.80	–	13.66	99.68
Pyrite	2	–	–	45.09	–	–	54.90	100
Chalcopyrite	1	–	–	29.49	–	34.02	35.79	99.31
Ferruginous chalcocite	2	–	–	11.16	–	63.15	25.31	99.63

admixtures of Fe (up to 1.33%) and Co (up to 1.23%) are often diagnosed in the chemical composition of millerite (Table 1). In the course of the study, the author has identified millerite grains with high content of Fe (up to 13.5%) and Co (3.1–5.9%), which are attributed to *ferruginous millerite*. The latter is often found in close association with PGE minerals.

Heazlewoodite has been found in the form of small (up to 0.02 mm) granular aggregate secretions of irregular shape in chromite cement (Fig. 1d). The admixture of Fe (up to 2.5%) is constantly diagnosed in the chemical composition of heazlewoodite. Samples with the high content of Fe (up to 11%) are attributed by the author to *ferruginous* variety (Table 1).

Galena is widespread. It is noted in the form of small (up to 0.01 mm) isolated grains of rounded, irregular shape in the heterogeneity of chromoshinelide grains (Fig. 1f). Its chemical composition is close to stoichiometric and is practically sterile. An exception is rare presence of Fe impurity (up to 1.4%) (Table 1).

The remaining sulfides (*pyrite, chalcopyrite, ferruginous chalcocite*) are extremely rare. They were identified and studied only by the example of several small ($\sim$5–10 μm) independent occurrences localized in cataclastic zones of chromite grains (Fig. 1a, e). This group of sulfides is characterized by "pure" compositions close to stoichiometric. Obviously, ferruginous chalcocite is a product of primary chalcopyrite replacement.

4 Conclusions

Thus, according to the chemical composition and typomorphic features, the studied accessory sulfides from chromospinelides of the Ergaksky massif can be divided into three paragenetic associations related to various processes of formation and transformation of ultramafic rocks enclosing them. According to the author, sulfides

of the first genetic group, “primary mantle”, consists of pyrite and chalcopyrite. The sufides of the second paragenetic association are represented by nickelous pentlandite, millerite, ferruginous millerite, heazlewoodite, ferruginous heazlewoodite and ferruginous chalcocite. Their formation is associated with mass lizarditization of chromitites and enclosing them dunites during regressive regional metamorphism (Yurichev 2018; Economou and Naldrett 1984), when nickel and cobalt released during the serpentinization of olivine were combined with sulfur of hydrothermal solutions and crystallized mainly as Fe-Ni-Co-S sulfides.

Standing aside, galena is attributed to the third paragenetic association, which is characterized by the accumulation of rare, “atypical” for restitic ultramafites elements, which act not as impurities, but become mineral-forming. The author suggests the emergence of this association to be related to the process of remobilization of elements under the influence of leaking and subsequently superimposed fluids rich in volatile (S, As) and non-ferrous metal elements.

The results obtained are in good agreement with earlier studies on this subject (Makeev 1992; Yurichev 2015).

References

Krivenko AP, Podlipskii MYu, Kubyshev AI, Katanov SG. Perspektivy khromitonosnosti i platinonosnosti giperbazitov Verkhne-Amyl’skogo raiona v Zapadnom Sayane. Mineral’nye resursy Krasnoyarskogo kraya. 2002:314–324. [Krivenko AP, Podlipsky MYu, Kubyshev AI, Katanov SG. Prospects for chromite-bearing and platinum-bearing hyperbasites of Upper-Amylsky district in the Western Sayan. Mineral resources of Krasnoyarsk area. 2002:314–324. (In Russ.)].

Chernyshov AI, Kicheeva AV, Podlipskii MYu. Petrostrukturnye neodnorodnosti ul’tramafitov Ergakskogo khromitonosnogo massiva (Zapadnyi Sayan). Zapiski Rossiiskogo mineralogicheskogo obshchestva. 2016;145(5):25–38. [Chernyshov AI, Kicheeva AV, Podlipsky MYu. Petrostructural heterogeneities of ultramafites of Ergaksky chromite-bearing massif (the Western Sayan). Notes of Russian Mineralogical Society. 2016;145(5):25–38. (In Russ.)].

Reed SJB. Electron microprobe analysis and scanning electron microscopy in geology. N.Y.: Cambridge University Press, 2005.

Yurichev AN. Aktsessornye sul’fidy Kempirsaiskogo ul’tramafitovogo massiva, Yuzhnyi Ural. Rudy i metally. 2018;4:67–75. [Yurichev AN. Accessory sulfides of the Kempirsai ultramafic massif, Southern Ural. Ores and metals. 2018;4:67–75. (In Russ.)].

Economou MI, Naldrett AJ. Sulfides associated with podiform bodies of chromite at Tsangli, Ermetria, Greece. Miner. Deposits. 1984;19(4):289–297.

Makeev AB. Mineralogiya al’pinotipnykh ul’trabazitov Urala. SPb.: Nauka; 1992. [Makeev AB. Mineralogy of alpine-type ultrabasites of the Urals. SPb.: Science; 1992. (In Russ.)].

Yurichev AN. Aktsessornye sul’fidy iz restitovykh ul’tramafitov. Rudy i metally. 2015;2:29–35. [Yurichev AN. Accessory sulfides from restitic ultramafites. Ores and metals. 2015;2:29–35. (In Russ.)].

Visualization of Elastic Anisotropy in Crystals

Anastasia I. Zamkovskaya and Elena M. Maksimova

Abstract

This paper presents the method for the calculation of elastic anisotropy of single crystals and 3D graphical display of the results. For illustration, the elastic properties of quartz were visualized. The symmetry elements of the indicatory surface of elastic stiffness and elastic compliance include symmetry elements of the point group of the crystal according to Neumann's principle.

Keywords

Anisotropy · Elastic properties · Neumann's principle

1 Introduction

The picture of the Earth's deep interior is rapidly improving owing to seismic tomography and indicates greater complexity than it was previously thought. Seismic anisotropy of the Earth requires extensive knowledge of anisotropic elasticity of mineral phases. A quantitative understanding of elastic properties in the minerals that likely compose the deep Earth is crucial for geosciences as it facilitates the interpretation of seismological observations in terms of composition, evolution, dynamics and thermal state of the Earth's interior. This motivates a strong interest in elasticity of several scientific disciplines, including geosciences, solid state physics and chemistry (Kantor 169).

A. I. Zamkovskaya (✉) · E. M. Maksimova
V.I. Vernadsky Crimean Federal University, 4 Vernadsky ave., 295033 Simferopol, Russia
e-mail: trabem.z@gmail.com

S. Votyakov et al. (eds.), *Minerals: Structure, Properties, Methods of Investigation*,
Springer Proceedings in Earth and Environmental Sciences,
https://doi.org/10.1007/978-3-030-49468-1_38

The purpose of this work was visualization of the anisotropy of the elastic properties of minerals.

2 Materials and Methods

An ideal elastic body becomes strained when subjected to stress, and when stress is relieved, the strains disappear. Moreover, in the limit of small stresses and strains, these two quantities are linearly related. Linear relations between the components of stress and strain are known generally as Hooke's law. Each stress component, in general, depends on all the strain components, and vice versa. The materials or definitive relationship can be written in two ways,

$$\varepsilon_{ij} = S_{ijlm}\sigma_{ij} \tag{1}$$

and its inverse

$$\sigma_{ij} = C_{ijlm}\varepsilon_{ij}. \tag{2}$$

In Eqs. (1) and (2), S_{ijlm} is the tensor of elastic compliance and is a measure of the ease of deformation, and C_{ijlm} is the tensor of elastic stiffness of the material and is a measure of the resistance of the material to elastic deformation (Maksimova 2002). Stress and strain are field quantities, i.e., they can vary from point to point in a body and also depend on time, whereas the compliance and stiffness are material properties, being constants for a particular homogeneous solid. The expanded form of (1) and (2) is represented by nine equations with 81 coefficients S and C. The complex (S_{ijlm}, C_{ijlm}) forms a fourth-rank tensor. Both the strain and stress tensors are symmetrical with respect to interchange of i and j indices, and thus, there are only six independent components of stress and strain. Therefore, there are only $6^2 = 36$ independent variants of stiffness and compliance.

Using only two suffixes makes it possible to use a matrix notation. Both the stress and strain components are written with a single suffix running from 1 to 6 simply by replacing each pair of indices *ij* with a single index $\alpha = 1, 2, 3 \ldots 6$ as follows:

$$11 \to 1; 22 \to 2; 33 \to 3; \left.\begin{matrix}32\\23\end{matrix}\right\} \to 4; \left.\begin{matrix}13\\31\end{matrix}\right\} \to 5; \left.\begin{matrix}21\\12\end{matrix}\right\} \to 6$$

The arrays of S and C are 6th order square matrices:

$$S_{mn} = \begin{pmatrix} S_{11} & S_{12} & S_{13} & S_{14} & S_{15} & S_{16} \\ S_{21} & S_{22} & S_{23} & S_{24} & S_{25} & S_{26} \\ S_{31} & S_{32} & S_{33} & S_{34} & S_{35} & S_{36} \\ S_{41} & S_{42} & S_{43} & S_{44} & S_{45} & S_{46} \\ S_{51} & S_{52} & S_{53} & S_{54} & S_{55} & S_{56} \\ S_{61} & S_{62} & S_{63} & S_{64} & S_{65} & S_{66} \end{pmatrix}$$

$$C_{mn} = \begin{pmatrix} C_{11} & C_{12} & C_{13} & C_{14} & C_{15} & C_{16} \\ C_{21} & C_{22} & C_{23} & C_{24} & C_{25} & C_{26} \\ C_{31} & C_{32} & C_{33} & C_{34} & C_{35} & C_{36} \\ C_{41} & C_{42} & C_{43} & C_{44} & C_{45} & C_{46} \\ C_{51} & C_{52} & C_{53} & C_{54} & C_{55} & C_{56} \\ C_{61} & C_{62} & C_{63} & C_{64} & C_{65} & C_{66} \end{pmatrix}$$

To transform them to other axes it is necessary to go back to the full tensor notation, S_{ijlm} and C_{ijlm}. The components of these matrices satisfy the symmetry condition $C_{mn} = C_{mn}$and $S_{mn} = S_{mn}$ (Aleksandrov and Prodaivoda 2000). Consequently, the number of independent compliance and stiffness reduces from 36 to 21, and the number of coefficients is further reduced by the material's symmetry.

A single crystal elastic tensor can be visualized by indicatory surfaces, whose radius vector is proportional to the value of the property in the n direction. For the coefficient of elastic compliance and the coefficient of elastic stiffness, the equation of the indicatory surface has the following form:

$$S_n = S_{ijkl} n_i n_j n_k n_l \tag{3}$$

$$C_n = C_{ijkl} n_i n_j n_k n_l \tag{4}$$

where n_i, n_j, n_k, n_l are the unit components of the n direction vector.

For the construction of 3D revolving models of indicatory surfaces it would be convenient to use the MathCad software. Great mathematical capabilities of this software make it a convenient tool for physical research (Polulyakh 1998).

Within this package, a program was created allowing indicatory surfaces of elastic properties to be constructed. The analysis of the obtained indicatory surfaces allows the symmetry and the anisotropy of the properties to be defined and, if necessary, the directions of its extreme value to be determined.

3 Results and Discussion

As an example, let's consider the elastic coefficients of quartz. Quartz is the second most abundant mineral in the Earth's continental crust after feldspar. It is made up of a continuous framework of SiO_4 silicon-oxygen tetrahedra, with each oxygen

atom being shared between two tetrahedra, giving an overall formula SiO_2. Below T = 847 K, quartz belongs to the 32 symmetry class. It is characterized by the presence of a triple symmetry axis, taken along the x_3 direction, three equivalent mirror planes containing this axis, and three double axes perpendicular to these planes, with the x_1 axis being parallel to one of these axes. The elastic constant matrix is a hexagonal solid, but with the sixth independent elastic constant $C_{14} = -C_{24} = C_{56}$.

The quartz symmetry class corresponds to the following matrix of elastic stiffness coefficients:

$$C_{mn} = \begin{pmatrix} C_{11} & C_{12} & C_{13} & & C_{14} & 0 & 0 \\ & C_{11} & C_{13} & & -C_{14} & 0 & 0 \\ & & C_{33} & & 0 & 0 & 0 \\ & & & C_{44} & 0 & & 0 \\ & & & & C_{44} & & C_{14} \\ & & & & & & \frac{1}{2}(C_{11} - C_{12}) \end{pmatrix},$$

where

$C_{11} = 84,84\ Gpa,$
$C_{12} = 5,31\ GPa$
$C_{13} = 12,24\ GPa$
$C_{14} = -17,66\ GPa,$
$C_{33} = 105,44\ GPa,$
$C_{44} = 57,55\ GPa, (T = 300\,\mathrm{K})$ (de Boer et al. 1996).

Quartz belongs to the trigonal crystal system. The equations giving the S_{ij} compliances in terms of the C_{ij} stiffness constants for the trigonal crystal systems are as follows:

$$S_{11} + S_{12} = \frac{C_{33}}{C}$$

$$S_{11} - S_{12} = \frac{C_{44}}{C'}$$

$$S_{13} = -\frac{C_{13}}{C}$$

$$S_{14} = -\frac{C_{14}}{C'}$$

$$S_{33} = \frac{C_{11} + C_{12}}{C}$$

$$S_{44} = \frac{C_{11} - C_{12}}{C'}$$

where

$$C = C_{33}(C_{11} + C_{12}) - 2C_{13}^2,$$
$$C' = C_{44}(C_{11} - C_{12}) - 2C_{14}^2.$$

The resulting expression in spherical coordinates describes the indicatory surface of quartz elastic compliances:

$$r = S_n = S_{11}\left(1 - n_3^2\right) + S_{33}n_3^4 + \left(1 - n_3^2\right)n_3^2 + (S_{66} + 2S_{12})n_1^2n_2^2 + 2S_{14}\left(3n_1^2 - n_2^2\right)n_2n_3,$$

where

$$n_1 = \sin\ \theta\ \cos\ \varphi,$$
$$n_2 = \sin\ \theta \sin\ \varphi,$$
$$n_3 = \cos\ \theta.$$

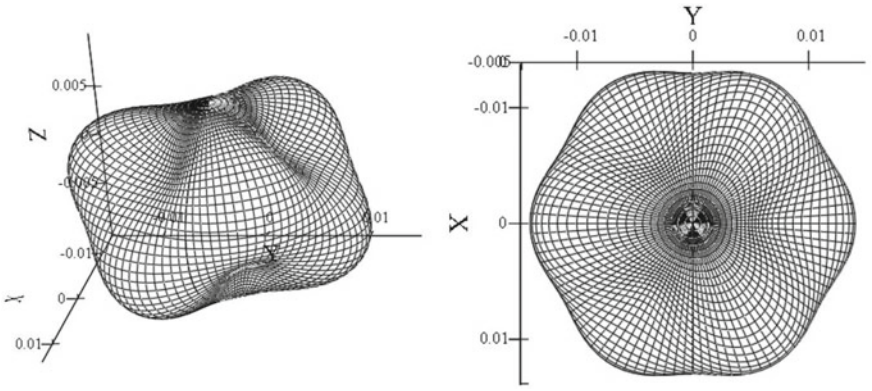

Fig. 1 The indicatory surface of elastic compliance of quartz and its projection onto the plane (XOY)

The indicatory surfaces of elastic stiffness and elastic compliance of quartz are shown in Figs. 1 and 2.

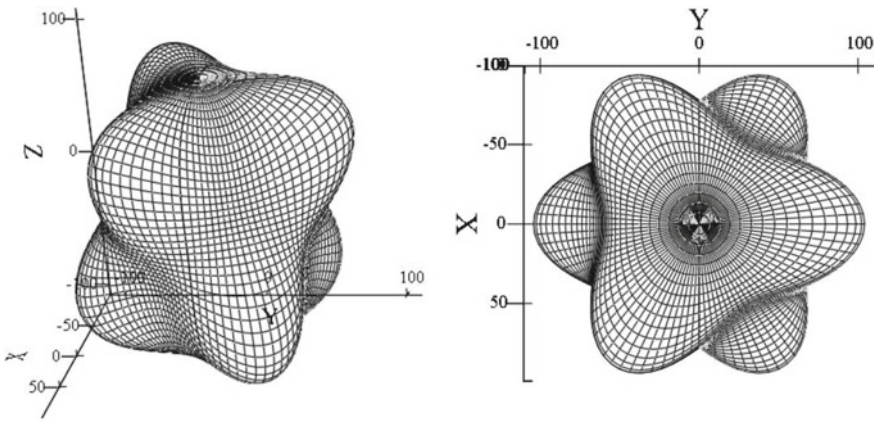

Fig. 2 The indicatory surface of elastic stiffness of quartz and its projection onto the plane (XOY)

4 Conclusions

A MathCad-based computer program was developed, which gives the possibility to construct 3D revolving models of indicatory surfaces of a fourth-rank tensor of elastic coefficients. As an example, the elastic properties of quartz were considered.

The shape and orientation of the indicatory surfaces of elastic stiffness and elastic compliance of quartz are described by the 3 m symmetry class and are related to their symmetry according to Neumann's principle: symmetry elements of any physical property of a crystal must include symmetry elements of the point group of the crystal.

The analysis of the shape of indicatory surfaces allows the directions of the extreme value of properties to be defined.

References

Kantor AP. Izuchenie uprugikh svoistv mineralov pri vysokikh davlenii i temperature na primere vyustita i zhelezo-nikelevogo splava. Moscow; 169. [Kantor AP. The study of the elastic properties of minerals at high pressure and temperature on the example of wustite and iron-nickel alloy. Moscow; 169 (In Russ)].

Maksimova EM. Tenzornye svoistva kristallov. Simferopol: TNU, 2002; 23 [Maksimova EM. Tensor properties of crystals. Simferopol: TNU, 2002; 23 (In Russ)].

Aleksandrov KS, Prodaivoda GT. Anizotropiya uprugikh svoistv mineralov i gornykh porod. SB RAS, 2000; 347. [Aleksandrov K.S., Prodaivoda G.T. Anisotropy of the elastic properties of minerals and rocks SB RAS, 2000; 347. (In Russ)].

Polulyakh SN. Application packages in physics. Simferopol: Pyramid Crimea; 1998.
de Boer K, Jansen APJ, van Santen RA, Watson GW, Parker SC. Free-energy calculations of thermodynamic, vibrational, elastic, and structural properties of a-quartz at variable pressures and temperatures. Condens Matter. 1996, 54:826–835.